DEVELOPMENT OF CAD SYSTEM FOR DETECTION, CLASSIFICATION, RETRIEVAL AND 3D RECONSTRUCTION OF BRAIN AND LIVER TUMORS ON MRI AND CT IMAGES

Thesis

Submitted in partial fulfillment of the requirements for the degree of

DOCTOR OF PHILOSOPHY

by

MEGHA. P. ARAKERI

DEPARTMENT OF INFORMATION TECHNOLOGY

NATIONAL INSTITUTE OF TECHNOLOGY KARNATAKA,

SURATHKAL, MANGALORE – 575025

DECEMBER, 2013

Dedicated

To

My Husband and Daughter

For their

Love, Sacrifice, Encouragement and Best Prayers

DECLARATION

By the Ph.D. Research Scholar

I hereby *declare* that the Research Thesis entitled **DEVELOPMENT OF CAD SYSTEM FOR DETECTION, CLASSIFICATION, RETRIEVAL AND 3D RECONSTRUCTION OF BRAIN AND LIVER TUMORS ON MRI AND CT IMAGES** which is being submitted to the **National Institute of Technology Karnataka, Surathkal** in partial fulfillment of the requirements for the award of the Degree of **Doctor of Philosophy** in **Information Technology** is a *bonafide report of the research work carried out by me.* The material contained in this Research Thesis has not been submitted to any University or Institution for the award of any degree.

(IT10F01, Megha. P. Arakeri)

Department of Information Technology

Place: NITK, Surathkal.

Date:

CERTIFICATE

This is to *certify* that the Research Thesis entitled **DEVELOPMENT OF CAD SYSTEM FOR DETECTION, CLASSIFICATION, RETRIEVAL AND 3D RECONSTRUCTION OF BRAIN AND LIVER TUMORS ON MRI AND CT IMAGES** submitted by **MEGHA. P. ARAKERI**, (Register Number: IT10F01) as the record of the research work carried out by her, is *accepted as the Research Thesis submission* in partial fulfillment of the requirements for the award of degree of **Doctor of Philosophy**.

Prof. G. Ram Mohana Reddy

(Research Guide)

Prof. Ananthanarayana V. S.

(Chairman- DRPC)

Acknowledgements

I would like to thank all those people who have made this research work possible. First and foremost, I would like to express my sincere thanks to my research guide *Prof. G. Ram Mohana Reddy*, Information Technology Department, for his guidance, suggestions and kind hearted support throughout my research work.

I would like to express heartfelt thanks to my research progress assessment committee members *Prof. Ananthanarayana V. S.* and *Prof. A. Kandasamy* for their valuable suggestions and constant encouragement to improve the research work.

I would like to express my gratitude to *Dr. B. M. Vadhiraj*, *Dr. M. S. Vidyasagar*, and *Dr. S. Pramod* for their assistance in collecting medical images from various hospitals for carrying out experiments of the research work.

I would like to extend my thanks to all teaching, technical and administrative staff of the Information Technology Department for their help during my research work. I am grateful to all those people, who supported me in any kind during the completion of my research work.

Last but not the least, I would like to thank my family for their constant support, understanding and patience throughout my research work. Without them, surely, this research work would not have been possible.

Place: NITK, Surathkal Megha. P. Arakeri
Date:

ABSTRACT

Brain and liver tumors are the life-threatening diseases due to low survival rate. Hence, accurate diagnosis of brain and liver tumors is necessary to provide effective treatment. Medical imaging techniques like Computed Tomography (CT) and Magnetic Resonance Imaging (MRI) help in acquiring images of the tumor. The visual analysis of these medical images by the radiologist is time consuming, subjective and inaccurate. The needle biopsy of the tumor provides accurate diagnosis but it is an invasive technique and generally not recommended. In order to overcome these drawbacks, there is a need to develop Computer-Aided Diagnosis (CAD) system for assisting the radiologist in fast and accurate diagnosis of tumors. Therefore, this thesis proposes an effective and efficient CAD system for tumor detection, classification, Content-Based Image Retrieval (CBIR), and 3D reconstruction to provide complete assistance to the radiologist in the diagnosis of brain and liver tumors.

In the first methodology, this thesis aims at tumor detection, by proposing automatic, effective and efficient segmentation methods for brain and liver tumors on medical images. The brain tumor is detected using the proposed segmentation technique based on Modified Fuzzy C-Means (MFCM) clustering algorithm. The liver tumor is detected using the proposed segmentation technique based on the automatic region growing algorithm.

In the second methodology, this thesis targets at identification of the type of brain/liver tumor as benign or malignant, by proposing an effective and efficient tumor classification scheme. Precisely, the proposed scheme represents the tumor characteristics using its significant features, selects most discriminating features using a two-level feature selection technique consisting of Information Gain (IG) based feature ranking and Independent Component Analysis (ICA) based feature section methods. Then, the tumor is classified using an ensemble classifier consisting of Support Vector Machine (SVM), Artificial Neural Network (ANN) and k-Nearest Neighbor (k-NN) classifiers.

In the third methodology, this thesis proposes two CBIR methods based on image rotation correction and rotation invariant features to assist the radiologist in brain/liver tumor diagnosis based on past resolved cases. In order to provide fast retrieval of tumor images from the database, the tumor features in the database are indexed using the proposed indexing technique called as Cluster with IG-ICA and KD-tree (CIKD). The features in the database are partitioned into different groups

using modified k-means clustering which identifies the number of clusters and initial cluster centers automatically.

In the fourth methodology, this thesis aims to build the 3D model of the brain/liver tumor, by proposing an effective and efficient 3D reconstruction scheme. Precisely, it proposes an enhanced shape-based interpolation algorithm to estimate missing slices in a given set of brain/liver tumor slices. Further, the 3D mesh simplification algorithm is proposed to reduce the number of triangles in the reconstructed mesh and accelerate the rendering phase. The tumor volume is also computed to assist the radiologist in estimating the stage of cancer.

Experiments are carried out on a dataset consisting of MRI images of the brain tumor and CT images of the liver tumor. Experimental results demonstrate that the proposed CAD system is automatic, effective and efficient in the diagnosis of brain and liver tumors.

Keywords: Computer-aided diagnosis, Brain tumor, Liver tumor, Segmentation, Classification, Content-based image retrieval, 3D reconstruction.

Table of Contents

List of Figures

List of Tables

Abbreviations

ANN	Artificial Neural Network
CAD	Computer Aided Diagnosis
CBIR	Content Based Image Retrieval
CCP	Cluster Center Proximity
CSF	Cerebro Spinal Fluid
CSS	Curvature Scale Space
CT	Computed Tomography
DT	Distance Transform
DWT	Discrete Wavelet Transform
EFCM	Enhanced Fuzzy C Means
EHD	Edge Histogram Descriptor
FCM	Fuzzy C Means
FD	Fourier Descriptors
FFCM	Fast Fuzzy C Means
FLIRT	FMRIB's Linear Image Registration Tool
FMRIB	Functional Magnetic Resonance Imaging Brain
FOS	First Order Statistics
GA	Genetic Algorithm
GLCM	Gray Level Co-occurrence Matrix
GM	Gray Matter

HD	Haussdorff Distance
HH	High High
HL	High Low
ICA	Independent Component Analysis
IG	Information Gain
k-NN	k Nearest Neighbor
LBP	Local Binary Pattern
LH	Low High
LL	Low Low
LMP	Local Multiple Pattern
LOO	Leave One Out
LTP	Local Ternary Pattern
MC	Marching Cubes
MFCM	Modified Fuzzy C Means
MRI	Magnetic Resonance Imaging
MS	Memoryless Simplification
PACS	Picture Archiving Communication System
PBR	Pathology Bearing Region
PCA	Principal Component Analysis
PET	Positron Emission Tomography
RBF	Radial Basis Function
ROC	Receiver Operating Characteristic
SBS	Sequential Backward Selection
SFS	Sequential Forward Selection
SHD	Symmetric Haussdorff Distance
SIFT	Scale Invariant Feature Transform

SMD	Symmetric Mean Distance
SOS	Second Order Statistics
SPECT	Single Photon Emission Computed Tomography
SURF	Speeded Up Robust Features
SVM	Support Vector Machine
US	Ultra Sonography
VO	Volume Overlap
WFD	Wavelet Fourier Descriptors
WHO	World Health Organization
WM	White Matter

Chapter 1

Introduction

This chapter introduces concepts of brain and liver tumors, and their types. Further, this chapter also gives an overview of the role of various medical imaging techniques and Computer-Aided Diagnosis (CAD) system in the analysis of cancer. In addition to this, challenges in the development of a CAD system and motivations for the present research work are discussed.

1.1 Medical Background on Cancer

The human body is made up of several types of living cells. Most cells in the body grow and then divide in an orderly way to form new cells as they are needed to keep the body healthy. When cells become old or damaged, they die and replaced with new cells; however, sometimes this orderly process goes wrong. The genetic material of a cell can be damaged or changed, producing mutations that affect normal cell growth and division. When this happens, cells do not die when they should and new cells form when the body does not need them. The extra cells form an abnormal mass of tissue called a tumor which becomes cancerous when it invades and destroys healthy tissues of organs (DeVita et al. 2012).

For years, cancer has been one of the biggest threats to human life. It is expected to become the leading cause of death over the next few decades. Based on the statistics from the World Health Organization (WHO)[1], cancer accounted for 7.6 million deaths which are around 13% of all deaths worldwide in the year 2011. Deaths caused by

[1] *World health organization cancer fact sheets.* `http://www.who.int/mediacentre/factsheets/fs297/en/index.html`

cancer are projected to increase in the future, with an estimated 11 million people dying from cancer in the year 2030. Brain and liver tumors are the most dangerous type of cancers. This is because the brain controls various organs and thus the brain cancer impairs the functionality of other organs. Whereas the liver processes the blood of the entire body and thus the cells of the liver tumor may travel along with the blood and affect many other organs. According to the statistics published by American Society of Clinical Oncology, the five year relative survival rate of people with brain/ liver cancer is lesser (10-20%) when compared to tumors of other organs. Hence, early detection and accurate diagnosis of these cancers is important to cure deadly disease (Jemal et al. 2011). Liver tumor is the fifth most common cause of cancer related death among men and ninth most among women. Brain tumor is the second most common cause of cancer related death among men and fifth most among women. Although brain tumors can occur at any age, studies show that they are most common in two age groups. The first group is children 3 to 12 years old; the second is adults 50 to 70 years old. Liver tumor occurs most often in people older than 60 years.

1.1.1 The Brain and Tumor

Brain contains billions of nerves that can simultaneously process the information in our body, operate on internal organs, generate thoughts, store and recall memories and, control movements (Sporns 2011). The brain is made of mainly gray and white matter arranged in distinct layers; the nerve cells in the brain known as neurons make up the gray matter. The neurons transmit and gather electrochemical signals that are communicated via a network of millions of nerve fibers; the glial cells of nerve fibers make up the white matter. The brain is protected by the skull, covering of three thin membranes called meninges, and cerebrospinal fluid. Brain has three major parts: the cerebrum, the cerebellum, and the brain stem (Crossman and Neary 2010). These parts work together, but each has special functions. The cerebrum is the largest part of the brain which synthesizes the sensory information into perceptions of the world around us. It also controls speech and emotions as well as reading, thinking, and learning. The cerebellum lies behind and below the cerebrum and controls the complex actions like walking, talking, etc. The brain stem connects the brain with the spinal cord and controls the basic body functions.

The brain tumor is composed of cells that exhibit unrestrained growth of the brain. Brain tumors can arise either from the brain itself, or its coverings, or the nerves at the base of the brain, or even from outside the brain (Greenberg et al. 1999). The risk factors and symptoms of brain tumor are given as follows:

Risk Factors

The following are the risk factors that may raise an individual's chance of developing a brain tumor (Cook et al. 2011):

- *Exposure to Radiation:* Exposure to ionizing radiation can cause cell damage and increase the likelihood of developing brain cancer.
- *Age:* Brain tumors are more common in children 3 to 12 years old and adults 50 to 70 years old.
- *Weakened Immunity:* People with Acquired Immunodeficiency Syndrome (AIDS) have a slightly increased risk of brain cancer.
- *Heredity:* Brain tumors occur in people with a family history of brain tumors or genetic syndromes.
- *Exposure to Chemicals:* Exposures to solvents, pesticides, oil products, rubber, or vinyl chloride may increase the risk of developing a brain tumor.
- *Other Factors:* Exposure to electromagnetic fields from power lines and transformers, and infection with certain viruses can cause brain tumors.

Symptoms

As the tumor grows it damages the nearby brain tissue. The functions of the different parts of the body are controlled by different parts of the brain. Therefore, the symptoms depend on the affected part of the brain and the size of the affected part. For example, one or more of the following symptoms may develop in a patient having the brain tumor (Freedman 2009; DeVita et al. 2012):

- Weakness of muscles in the arm, leg, part of the face, or eyes.
- Problems with balance, vision, hearing, speech or communication.
- Loss of smell.
- Dizziness or unsteadiness.

- Numbness or weakness in a part of the body.
- Personality changes.
- hormone variations.

1.1.2 The Liver and Tumor

The liver is the largest organ in the body located in the upper right side of the abdomen and is responsible for numerous metabolic, regulatory, transport, and immune functions and thus maintains the body's overall health (Clavien 2011). The liver consists of two main lobes: right and left lobes. There are networks of tubes inside the two lobes that carry bile from the liver to the intestine. Bile is a substance that helps carry away wastes and is needed for the breakdown and absorption of dietary fats. The liver filters both toxic chemicals and bacteria from the blood and it uses nutrients in the blood to provide energy to the body.

Liver tumor is due to the growth and spread of unhealthy cells in the liver. The liver can be affected by primary liver cancer, which arises in the liver, or by secondary cancer which forms on other sites and then spreads to the liver (Scheppach et al. 2004). The liver is more susceptible to cancer cells traveling in the blood stream as it processes the blood of the entire body. Thus, most of the liver tumors are secondary or metastatic tumors. The risk factors and symptoms of liver tumor are given below.

Risk Factors

The following are the risk factors that may raise an individual's chance of developing liver tumors (Clavien 2011; Scheppach et al. 2004):

- *Cirrhosis:* This progressive and irreversible condition causes scar tissue to form in the liver and increases the chance of developing liver tumor.
- *Diabetes:* People with blood sugar disorder have a high risk of liver tumor.
- *Alcohol Abuse:* Consuming high amounts of alcohol daily over many years can lead to irreversible liver damage and increase the risk of liver tumor.
- *Obesity:* Having an unhealthy body mass index increases the risk of liver tumor.
- *Hepatitis:* Chronic infection with hepatitis B or C virus increases the risk of liver cancer.

- *Other Factors:* Less common risk factors for liver cancer include exposure to arsenic in drinking water, certain chemicals in plastics, or abuse of anabolic steroids. Also, a food contaminant called aflatoxin and genetic diseases such as hemochromatosis increases a person's risk for liver cancer.

Symptoms

The symptoms of liver tumor may be different for each person. Cancer of the liver does not usually show noticeable symptoms until it has reached an advanced stage. Thus, liver cancer can go undetected for many days before there are any indications that something might be wrong. Most of the following symptoms are a result of liver damage (Scheppach et al. 2004):

- Weight loss
- Decrease in appetite
- Nausea and vomiting
- General weakness and/or fatigue
- Fever
- Enlarged liver
- Abdominal pain
- Jaundice

1.1.3 Types of Tumor

Tumors of the brain/liver are categorized according to several factors, including where they are located, the type of cells involved, and how quickly they grow (DeVita et al. 2012; Westphal 2009). The general categories of tumors are as follows:

- **Benign vs. Malignant:** Benign tumors are slow growing, non-cancerous and do not spread to the surrounding tissue. Malignant tumors, on the other hand, are cancerous, fast growing, aggressive, invade nearby tissue and also are more likely to recur after treatment.
- **Primary vs. Secondary:** A primary tumor is a tumor growing at the anatomical site where tumor progression began and proceeded to yield a cancerous mass. A secondary tumor is made of cells that have spread to the organ from

other parts of the body. Primary tumors may be benign or malignant, whereas secondary tumors are always malignant.

- **Localized vs. Invasive:** A localized tumor is confined to one area of the organ, whereas an invasive tumor spreads to the surrounding areas.

Following are the examples of brain and liver tumors:

- *Benign Brain Tumor:* Chrodomas, Schwannomas, Craniopharyngiomas, Meningiomas, Pituitary adenoma, etc.
- *Malignant Brain Tumor:* Gliomas, Astrocytomas, Ependymomas, Medulloblastomas, Oligodendrogliomas, etc.
- *Benign Liver Tumor:* Adenoma, Hemangioma, Focal Nodular Hyperplasia, Fibroma, Lipoma, etc.
- *Malignant Liver Tumor:* Hepatocellular Carcinoma, Angiosarcomas, Hepatoblastoma, Cholangiocarcinoma, etc.

1.1.4 Cancer Treatment

There are three main types of tumor treatments, namely chemotherapy, radiotherapy and surgery (Haskell 2001), and these are used alone or in various combinations. The physician chooses the appropriate treatment for an individual based on the type of tumor, its grade, and the patient's age and general state of health. Following are the treatments used for curing brain/liver tumor (Greenberg et al. 1999; Clavien 2011):

- **Chemotherapy:** It is a treatment which uses anti-cancer medicines to kill cancer cells, or to stop them from multiplying. Some of the anti-cancer medicines are taken orally, others are given via a drip into the veins. Chemotherapy is mainly used for the treatment of malignant tumors.
- **Radiotherapy:** It uses high-energy X-rays to kill tumor cells and it is often used following a surgery when it is not possible to remove the entire tumor with surgery. Radiotherapy is occasionally used for treating benign tumors, but mostly used for treating malignant ones.
- **Surgery:** The surgical treatment involves the removal of the tumor without damaging the surrounding healthy tissue. Surgery is often the main treatment for benign tumors and primary malignant tumors.

1.1.5 Medical Imaging Techniques

Once a brain/liver tumor is clinically suspected based on symptoms, radiologic evaluation is required to determine the location, the type, the extent of the tumor and its relationship to the surrounding structures. This information is very important in deciding between the different forms of therapy, such as surgery, radiotherapy, and chemotherapy. It also helps in monitoring treatment response as well as patient's prognosis.

Medical imaging has played a major role in clinical diagnosis and treatment for years, allowing radiologists to examine specific sections of the human body without resorting to invasive surgical procedures. Current technologies provide a wide range of possibilities for brain/liver imaging, chief among them being Magnetic Resonance Imaging (MRI), Computed Tomography (CT), Ultrasonography (US), Positron Emission Tomography (PET), and Single Photon Emission Computed Tomography (SPECT) (Freedman 2009; Clavien 2011). Images may be enhanced by introducing contrast agents during image acquisition to provide clear information about the tumor region on the organ being scanned. The working principles, benefits and drawbacks of the imaging methods (Bushberg et al. 2002) used in the diagnosis of brain and liver tumors are explained below:

Ultrasonography

Ultrasonography is a fundamental technique for imaging the liver and its working principle is based on high frequency sound waves called ultrasound whose frequency lies above the audible range of normal human hearing, about 20 kHz. The frequency used in diagnostic ultrasound is typically in the range of 2 to 18 MHz (Cobbold 2007). In order to acquire the image of the organ, a transducer sends a small pulse of ultrasound into the body. As the ultrasound waves penetrate tissues of different acoustic impedances along the path of transmission, some are reflected back to the transducer (echo signals) and some continue to penetrate deeper. The echo signals returned from many sequential coplanar pulses are processed and combined to generate an image.

The advantages of ultrasonography are: good soft tissue contrast, availability, relatively low cost and absence of ionizing radiation. It also provides real-time scanning of soft tissue structures. The limitations of ultrasonography are: operator dependency, and poor spatial resolution of the image due to blurring.

Computed Tomography

The CT imaging technique can be used to detect brain/liver tumors and its working principle is based on passing multiple x-ray beams at different angles through the body to build up a cross-sectional image of the organ (Seeram 2010). The CT imaging system is comprised of a motorized table that moves the patient through a circular opening and an X-ray machine that rotates around the patient as he moves through. Detectors record the radiation exiting the patient's body and this creates an X-ray snapshot. Many different snapshots are collected during one complete rotation of the X-ray machine and then the computer assembles the series of X-ray images into a cross section. Thus, a CT scan produces a series of cross-sectional images of the organ being scanned. In the conventional CT, the X-ray tube rotates around the patient while the table is immobile. After one scan is over, the table moves and the procedure is repeated; thus it requires more image acquisition time. Recent technological advances in CT technology, such as spiral and multi-detector CT have further improved the performance of conventional CT scanners in terms of image acquisition speed and resolution. In spiral CT, X-ray tube rotation and patient table translation are performed simultaneously. Multi-detector CT uses multiple detector rows as opposed to one detector row in spiral CT, and thus it can obtain multiple slices in a single rotation.

The advantages of CT are fast image acquisition, imaging soft tissues as well as bones, and less expensive. The main limitation is that it uses ionizing radiations to generate images of the organ and hence cannot be used for scanning the pregnant women. Also, sometimes the contrast agents used during the CT imaging lead to allergic reactions in patients (Huang et al. 2006).

Magnetic Resonance Imaging

The MRI technique can be used to acquire a set of cross-sectional images of the brain as well as liver. It makes use of magnetic field and radio waves to acquire the image of the organ being scanned (Hashemi et al. 2012). The MRI unit consists of a large cylindrical shaped tube surrounded by circular magnet. An electric current passes through the coils of the unit to create a magnetic field. In order to perform the MRI scan, the patient is made to lie within the electromagnetic field created. The human body is mainly composed of water containing hydrogen atoms. Normally, the nuclei

of the body's atoms spin on axes aligned in different directions. But, the MRI's powerful magnetic field realigns the protons of the body's hydrogen atoms so that they all spin along the same axis. The MRI machine sends radio waves in the area of the body being scanned and causes the atoms to change from low energy to high energy states. When radio waves are switched off, the atoms fall back to their low energy states. As they do this, they lose their energy giving off signals which are then picked up by the MRI machine. A computer processes these signals and produces an image of the organ being scanned.

MRI uses many different types of images, such as T1-weighted, T2-weighted, diffusion-weighted, and magnetic susceptibility-weighted. These images are produced with different types of imaging parameters, such as repetition time (TR) and echo time (TE). T1-weighted and T2-weighted are the most commonly used MRI images for diagnosing brain/liver tumors. On T1-weighted image, water appears dark and fat appears bright, whereas on T2-weighted image, water appears bright and fat appears dark. Advantages of MRI are: absence of ionizing radiations, high resolution and soft tissue contrast. The contrast material used in MRI exams is less likely to produce an allergic reaction. Disadvantages of MRI are: long examination time, relatively high cost, and limited availability. MRI is rarely used as the first diagnostic modality, except for the brain and soft tissue tumors. Indications for MRI are usually difficult clinical cases that are not resolved after US or CT examinations.

Nuclear Imaging

Nuclear imaging uses low doses of radioactive substances to detect tumors. During a nuclear imaging, the radioactive tracer, which is formulated to collect in specific organs, bones or tissues, is injected into the body (Greenberg et al. 1999; Clavien 2011). Sensors in the scanner detect the radioactivity as the tracer accumulates in different regions of the organ. A computer uses the data gathered by the sensors to construct multicolored images that show where the compound acts in the organ. Allergies, side effects and other reactions are extremely rare in nuclear imaging, as very small doses of tracer are used.

Two major instruments used in nuclear imaging for detection of cancer are PET and SPECT scanners. PET and SPECT rely on similar principles to produce images of the organ. The important differences in instrumentation, radiochemistry, and experimental applications are dictated by differences in their respective physics of

photon emission. Generally, SPECT tracers deteriorate more slowly than PET tracers. Hence, SPECT requires longer scan periods than PET. The PET is more versatile than SPECT and produces more detailed images with a higher degree of resolution.

In the present research work, MRI and CT images are used to analyze the brain and liver tumors, respectively due to their superior image quality. MRI is used in the analysis of brain tumor because MRI has a much greater soft tissue contrast, depict anatomy in greater detail and is more sensitive to abnormalities within the brain when compared to CT. CT is used in the analysis of liver tumor because it allows better evaluation of the involvement of extra-hepatic tissues, including bones, bowel and lymph nodes when compared to MRI. The presence of cancer can be suspected on the basis of symptoms and findings on the medical images obtained through non-invasive imaging techniques such as US, CT, MRI PET, or SPECT. Definitive diagnosis of cancer can be made only based on the needle biopsy which involves taking a sample of the abnormal tissue of the organ for examination under a microscope. However, needle biopsy is an invasive technique and hence generally not recommended by the radiologist (Huo et al. 2009). Therefore, non-invasive diagnosis of the cancer can be provided by the CAD system and the diagnosis process involves identifying the region, type and severity of the cancer.

1.2 Computer-Aided Diagnosis (CAD)

The benefit of medical image examination in terms of its ability to yield an accurate diagnosis of the cancer depends on the quality of both the image acquisition and image interpretation. During the past century, the role and contribution of radiology to medical diagnosis has expanded tremendously due to the advances in the imaging modalities, such as CT and MRI. The medical images obtained by various imaging techniques are interpreted by the radiologists. However, images interpreted by humans are limited due to non-systematic search patterns of humans, the presence of noise in the image, and the complex disease states requires the integration of a vast area of image data and clinical information (Kopec et al. 2003). Hence, manual interpretation of medical images for diagnosis of cancer is laborious, time consuming and subjective.

With the advancement of computer technology, radiologists have an opportunity to improve their image interpretation capabilities. Many attempts have been made

by computer scientists to assist a radiologist in detection and diagnosis of cancer by developing CAD systems. CAD is multidisciplinary which integrates diagnostic imaging with computer science, image processing, pattern recognition, and artificial intelligence technologies (Stoitsis et al. 2006). CAD can be defined as a diagnosis made by a radiologist who uses the output from a computerized analysis of medical images as a second opinion in detecting tumors and making diagnostic decisions (Doi 2007). The radiologist's image reading sensitivity can be increased and accurate diagnosis can be provided with the support of CAD system. Hence, cancer can be detected in early stages and cured without much difficulty with the help of CAD system.

As shown in Figure 1.1, computer-aided diagnosis of tumors on medical images consists of five steps: image acquisition, preprocessing, segmentation, feature extraction and selection, and classification (Kim et al. 2011)). The medical images acquired through imaging techniques, such as US, CT, MRI, PET, or SPECT are input to the CAD system for diagnosis of cancer. The steps of CAD are explained as follows:

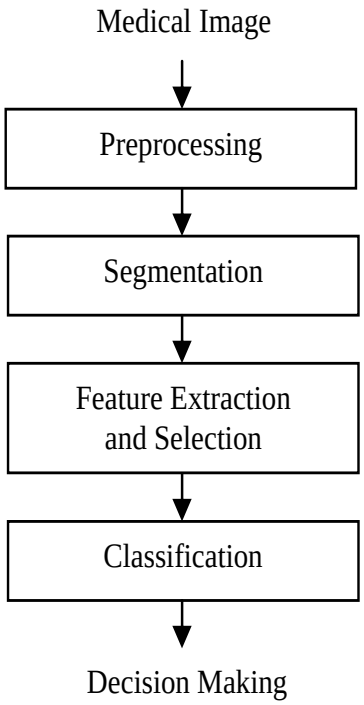

Figure 1.1: Computer-Aided Diagnosis of Tumor

Preprocessing

Images acquired by medical imaging devices may contain artifacts and noise and this makes the image analysis very difficult. Thus, preprocessing step makes the image suitable for further processing by improving the quality of the image. It involves various tasks such as elimination of artifacts, noise reduction and contrast enhancement.

Segmentation

In order to characterize the tumor, the location of the tumor on the given medical image has to be identified. Thus, the segmentation step subdivides the image into different regions based on certain properties to delineate the region of interest in the given image.

Feature Extraction and Selection

In this step, various features of the segmented tumor are extracted to represent the characteristics of the tumor. The features extracted may be shape, size, texture, average gray level, etc. However, a large number of features degrade the performance of the classifier. Thus, the feature selection step is required to reduce the dimensionality of the feature space and keep only a set of features which are most discriminating and helpful for the classifier in identifying the type of tumor.

Classification

The selected features of the tumor are fed to the classifier to determine the class of the segmented tumor, and the classifier used can be supervised or unsupervised. Supervised classifier identifies the type of the tumor based on the given examples, whereas unsupervised classifier does not need any examples or training to identify the type of tumor. Finally, the radiologist makes the diagnostic decision on the suspicious region in the medical image based upon the output of the CAD system.

1.3 Challenges

The challenges that must be addressed for the development of an effective and efficient CAD system are as follows:

- **Cancer Detection**
  The detection of tumor on a given medical image is challenging as the medical image shows other tissues or organs adjacent to the tumor. Some of the organs are very closely located and have similar intensities in medical images. In such cases it becomes difficult to segment the tumor, since the organ has to be extracted and then its tumor. Hence, to properly delineate the tumor region on the medical image one should have the knowledge about the characteristics of a medical image, anatomy of the organ, and the difference between normal and abnormal tissues.
- **Automation**
  Since the aim of the CAD system is to provide computer assisted characterization of tissues, all phases in the CAD system starting from preprocessing to classification should be automatic. However, achieving this goal is difficult, since in some phases like segmentation it requires the input from the radiologist. Automating the segmentation task is challenging due to the complex anatomy and the diverse shapes of organs.
- **Accuracy**
  The important characteristic desired in the CAD system is to achieve high sensitivity in cancer diagnosis with the fewest number of false positives. If the information given by the CAD system is flawed, then the radiologist's decision that is based on such information has the potential to be flawed as well. Thus, a large number of false positives would reduce the efficiency of the radiologist and clinical acceptance of the CAD system. But, to make the system more accurate, it needs to be trained with various types of tumor cases, which is a difficult process.
- **Efficiency**
  In addition to accuracy, efficiency is also an important feature of the CAD system. In a clinical environment, routinely a large number of images are generated and thus the analysis of these images should be fast. If the CAD system is slower than the manual interpretation of images, then the radiologist does

not find it useful. Early diagnosis of the cancer helps in providing the appropriate treatment at the right time and hence improves the survival chance of the patient.

- **Noisy Images**
  Images acquired from medical imaging modalities such as CT or MRI are usually affected by noise. The presence of noise corrupts the information in the image and thus increases the false positive rate in cancer diagnosis. Hence, CAD system must have denoising algorithms which eliminate the noise as well as retain the border and shape of regions in the medical image.
- **Learning from Radiologist**
  A radiologist uses multiple criteria for diagnosing tumors on medical images. Although algorithms could be developed by learning from positive and negative cases (training by example), algorithms are likely to be more successful if based on features that are proven clinically relevant (i.e., based on anatomy or pathology). The features which radiologists find useful include: anatomic knowledge, image characteristics, shape, and texture. Hence, incorporating the knowledge of the radiologist into the CAD system is a challenging task.

1.4 Motivation

The CAD system can offer better diagnosis support to physicians by automatically identifying the presence of pathology using quantitative features of disease. There are several papers published (Zhang et al. 2008; Fujita et al. 2010; Wu et al. 2012) on the development of CAD systems for diagnosis of brain and liver tumors. There is, however, still a long way to go before CAD systems become widely used in clinics and screening centers. The most important need is to demonstrate that the accuracy of interpretation of medical images with the CAD system is better than the accuracy without the CAD system. The research work in this thesis focuses on the development of the CAD system for the diagnosis of brain and liver tumors and is motivated by the following factors:

⋆ Curing the malicious disease like cancer requires early detection and diagnosis. But, the cancer characteristics are not much emphasized in the early stage and

hence difficult for the radiologist to understand the pathology by image reading.

- ⋆ Brain and liver cancers are the most serious type of cancers as brain and liver are related to the most important functions of the body. Also, survival rate of patients with brain/liver cancer is very low. Hence, accurate diagnosis is required to provide appropriate treatment at the right time.
- ⋆ Medical images are too complex due to varied textures, overlapping tissues, and substantial variation across the screening population. This leads to difficulty in detection and diagnosis of cancer.
- ⋆ Direct analysis of the medical images by the physician is less accurate (Kopec et al. 2003). But, 100% accuracy is expected in the medical field for effective diagnosis of tumors and to provide optimal treatment.
- ⋆ A large number of images have to be analyzed by the radiologist each day which requires fast processing. But, visual analysis of medical images is tedious and exhaustive.
- ⋆ Analysis of medical images is subjective; one radiologist may choose a particular lesion as a candidate, while another radiologist may find this lesion insignificant. Consequently, some lesions are being missed or misinterpreted.
- ⋆ The automated software tools of the CAD system provide several benefits in the clinical environment, such as accurate diagnosis, improved training in diagnostic techniques, increased diagnostic speed and reduced cost.

1.5 Outline of the Thesis

The remainder of this thesis is organized as follows. Chapter 2 includes the review of the existing CAD methods for brain/liver tumor segmentation, classification, Content-Based Image Retrieval (CBIR), and 3D reconstruction. Followed by this literature review, we highlight the research issues in the exiting CAD methods. Then the problem statement, objectives and the research framework derived based on the identified research issues in the development of CAD system are presented. Further, the description of the brain and liver tumor datasets used in the experiments of our research work is presented.

In Chapter 3, we describe our proposed methods for automatic brain tumor segmentation based on Modified Fuzzy C-Means (MFCM) clustering algorithm and liver tumor segmentation based on an automatic region growing algorithm. The validation

of the proposed tumor segmentation methods is performed by comparing the results of the proposed methods with the radiologists' segmentation results.

In Chapter 4, we present the proposed tumor classification scheme for identifying the type of brain/liver tumor in the medical image as benign or malignant. This involves the explanation of the various phases of the approach, such as feature extraction for representation of the tumor, two-level feature selection for deriving most salient features, and tumor classification by ensemble classifier. The performance evaluation of the proposed tumor classification scheme is presented in terms of effectiveness and efficiency.

In Chapter 5, we introduce two proposed CBIR methods based on the hierarchical framework for retrieving similar pathology bearing brain/liver tumor images from the medical database to assist the radiologist in the diagnosis of brain and liver tumors. The first method uses an image rotation correction technique, and the second method uses the rotation invariant features to handle the misalignment of images. The proposed indexing structure called as Cluster with IG-ICA and KD-tree (CIKD) for fast retrieval of images is also presented. The proposed modified k-means clustering algorithm automatically initializes the number of clusters and their centers. Experimental results demonstrate the effectiveness and efficiency of the proposed CBIR methods.

In Chapter 6, we present the proposed enhanced shape-based interpolation algorithm and mesh simplification algorithm for 3D reconstruction of brain/liver tumor. In this chapter, we also discuss the method for computation of tumor volume in order to assist the radiologist in predicting the stage of cancer. Experimental results illustrate the accuracy and efficiency of the proposed methods.

Finally, Chapter 7 summarizes the contributions of the research work and highlights possible directions for future work. Appendix I presents the GUI designed for the proposed CAD system.

1.6 Summary

This chapter introduced brain and liver tumors, their treatment methods, medical imaging techniques for acquiring the images of the brain/liver, and the role of the CAD system in the diagnosis of cancer. The research challenges and the motivations in the development of CAD system were discussed. This chapter also gave details on the organization of the thesis.

Chapter 2

Literature Review

This chapter presents the review of the existing CAD methods for analysis of brain and liver tumors on medical images. Further, the chapter also gives the problem statement, objectives, and the research framework to solve the challenging issues present in the existing CAD methods. The CAD system can consist of different subsystems such as tumor detection, classification, image retrieval, and 3D reconstruction to provide complete assistance to the radiologist in the diagnosis of tumors. Each subsystem is associated with different functionalities useful in diagnosis of tumors. Tumor detection helps in identifying the cancer affected region on medical image and tumor classification determines the type of the segmented tumor. The image retrieval subsystem retrieves similar images of the tumor from the medical database to assist the radiologist in diagnosing the tumor based on the relevant cases. Further, 3D reconstruction builds the 3D model of the tumor to provide information on the complexity and severity of the tumor. Following are the details of the various state-of-the-art approaches of computer-aided tumor detection, characterization, image retrieval, and 3D reconstruction.

2.1 Tumor Detection

The segmentation subdivides an image into its constituent parts to extract the region of interest. Segmentation is the important task in medical image analysis to detect the region or boundary of anatomical structures. The tumor segmentation helps the radiologist in locating the pathology, quantification of tumor volume and surgical planning (Liu et al. 2011). Hence, accurate tumor segmentation is a key

issue in analyzing the cancer. The manual labeling of tumor on medical image is a time consuming task and considerable variation is observed between different labelers. Hence, clinical researchers are focusing on computer-aided automatic image segmentation techniques to achieve high segmentation accuracy. Several brain/liver tumor segmentation techniques are proposed in the literature. Some of them are semi-automatic and some are fully automatic. Semi-automatic methods require user intervention, whereas automatic methods provide fast and user independent segmentation. Automatic segmentation of the brain tumor on MRI images is the challenging task as brain consists of various regions such as White Matter (WM), Gray Matter (GM), Cerebrospinal Fluid (CSF) (Cobzas et al. 2007). Automatic segmentation of liver tumor is also another challenging task because of variations in shape and scales of the organ across different patients, existence of neighboring structures with similar intensity and the unclear boundary between adjacent organs in the abdominal CT image (Priyadarshini and Selvathi 2012). A variety of brain/liver segmentation methods are proposed in the literature and these can be classified into different categories: threshold-based, region-based, cluster-based, deformation-based, and model-based.

2.1.1 Threshold-Based Segmentation

The threshold-based segmentation method determines intensity values, called thresholds which separate pixel intensities in the image into different regions. The threshold selection is a major task in this method of segmentation for properly partitioning the image into several regions. However, threshold selection from the medical image is a difficult process due to the presence of noise in the image and complex distribution of tissue intensities. Thus, thresholding is combined with other methods for tumor segmentation and it can be used as the pre-processing and/or post-processing step of segmentation. Park et al. (2005) computed optimal threshold for liver tumor segmentation based on statistical analysis of histogram under the liver mask, but this method fails on poorly contrasted or inhomogeneous lesions. Another similar threshold based method but in combination with active contour is proposed by Taheri et al. (2010) for brain tumor segmentation. However, this method is based on the assumption that the histograms of the tumor and adjacent non-tumor regions slightly overlap with each other; such an assumption seldom holds for the medical image. Moltz et al. (2008) utilized the pixel intensity thresholding to extract the liver region from

the abdominal CT image for the analysis of liver metastases. However, the threshold value is selected in the confidence interval and hence segmentation results are not effective. Seo et al. (2005) segmented the liver tumor using the optimal threshold calculated by composite hypotheses and minimum total probability error. Promising results are shown, even if the approach produces diverse false positives, especially for small tumors. Choudary et al. (2008) segmented the liver tumor using a multi-thresholding algorithm and further refined the segmentation with region growing and level set based methods. This method is semi-automatic, since the slice and threshold are selected manually for tumor segmentation.

2.1.2 Region-Based Segmentation

The region-based segmentation subdivides the image into several homogeneous regions based on certain properties of the regions. There exist several region-based methods for tumor segmentation such as region growing, split and merge, watershed segmentation, etc. The region growing method (Adams and Bischof 1994) requires two parameters namely seed point and threshold. Given a seed point, the region grows by extracting all pixels connected to the initial seed point with their intensity value within the threshold. The tumor segmentation methods based on region growing (Venkatachalam et al. 2004; Qi et al. 2008; Weglinski and Fabijanska 2011) are semi-automatic, since these methods require the manual selection of the seed point and threshold value. Hence, they consume a lot of time to arrive at accurate results. Fan et al. (2005) improved the region growing algorithm with automatic seed selection. But, the threshold selection was manual and the resulting over-segmentation problem was solved using region merging, which is computationally expensive. Hence, the method consumes more time. Poonguzhali and Ravindran (2006) automated the seed selection based on image texture, but the threshold value was selected based on iterative thresholding of the image. Hence, this method cannot effectively segment tumors in case of overlapping tissue intensities.

Wu et al. (2009) proposed complete automatic texture based region growing algorithm for segmentation of organs in the abdominal MRI image. The authors have assumed that the regions in MRI image have texture homogeneity, and thus their algorithm incorrectly classifies the pixels in a complex textured surface of the organ. Dongxiang and Tiankun (2009) used split and merge technique called a quad tree

decomposition method for segmentation of the liver. This method is computationally expensive, since it involves many splits and merges to extract the complete region of interest. The watershed algorithm (Beucher and Meyer 1992) is widely used in medical analysis due to its ability to produce complete division of the image into regions (Ng et al. 2006); however, its main limitation is over-segmented image. Liu et al. (2009) addressed this problem by combining watershed segmentation with region merging. The gray level threshold used in the region merging process was not adaptive and thus it affected the accuracy of segmentation results. Hamarneh and Li (2009) proposed enhanced watershed segmentation by utilizing prior shape and appearance knowledge to segment the medical image. Though this method eliminates the over-segmentation problem, it cannot provide accurate segmentation results for low contrast images.

2.1.3 Cluster-Based Segmentation

Clustering is the most popularly used method for medical image segmentation which groups patterns in such a way that the samples of the same group are more similar to each other than samples in different groups. The most commonly used clustering techniques for the medical images are k-means (MacQueen 1967) and Fuzzy C-Means (FCM) (Bezdeck 1981) methods. Juang and Wu (2010) presented brain tumor segmentation based on k-means clustering. Since k-means clustering provides crisp partitioning of the image pixels, it cannot capture the uncertainty present in MRI images of the brain. Further, k-means clustering is sensitive to cluster center initializations and as a result, it may lead to the misrepresentation of image regions. The FCM algorithm can handle the overlapping tissue intensities in MRI images, but consumes a lot of time to partition the image into desired number of clusters (Cannon et al. 2010). Recently, several methods have been proposed to improve the efficiency of FCM. Al-Zoubi et al. (2007) proposed Fast FCM (FFCM) clustering method by eliminating those points with membership value lower than a threshold value. The choice of the threshold value is manual; hence this method is not very efficient.

Hemanth et al. (2009) proposed the effective FCM method to accelerate the segmentation process based on the quantization and the aggregation of the data set. However, there was not much improvement in the efficiency, since the data reduction is based on clustering large feature set. Cai et al. (2007) presented a generalized

framework for FCM clustering which guarantees robustness to noise and preserves edge details. But, the main drawback is that it computes neighborhood term in the each iteration and hence it is a time consuming process. The computationally efficient FCM algorithm has been proposed by Murugavalli and Rajamani (2006) using parallel processing technique, but the hardware implementation is not effective. Further, de Vargas et al. (2011) reduced the number of iterations required for convergence by presenting a new method of computing cluster centers based on crisp matrix derived from the fuzzy membership matrix. Though this method could reduce total iterations for convergence, there was not much improvement in the efficiency of the algorithm; This is due to the computation of a crisp membership matrix in addition to the fuzzy membership matrix in each iteration. Though several methods have been proposed to accelerate the FCM algorithm, still the efficiency of the FCM could not be drastically improved.

2.1.4 Deformation-Based Segmentation

The deformation-based method of image segmentation utilizes closed curves that deform under internal and external forces to delineate object boundaries. Lu et al. (2005) segmented tumor from the abdominal CT image of the liver using an active contour model. Initial boundary required by the algorithm was manually placed outside the tumor region. Thus, this method is semi-automatic and does not deform to the exact boundary of the tumor in the presence of blurred edges. Krishnamurthy et al. (2004) eliminated the drawback of manual placement of the contour by forming the initial contour using the canny edge detection technique. However, this scheme suffers from over-dependence on the edge detection step, which is unreliable in the presence of noise and low contrast. Bhat and Kunte (2010) developed a mixed model by combining watershed and active contour algorithms to get the initial contour automatically in segmentation of the brain tumor. However, this method suffers from the over-segmentation problem of the watershed algorithm. The level set method is the popular deformation-based segmentation method, because of its ability to handle complex geometries. However, the level set formulation entails tuning of parameters with the help of user (Prastawa et al. 2004; Xie et al. 2005).

2.1.5 Model-Based Segmentation

In model-based segmentation, the information extracted from medical images is incorporated into a supervised approach that uses labeled data and automatically learns a model for segmentation. Moon et al. (2002) identified the tumor region by estimating the distributions of normal tissue, tumor and edema from T1- and T2-weighted MR image channels. This method fails in the case of large deformations in the brain and it also requires multi-modal images for segmentation. Corso et al. (2008) proposed a multi-scale framework based on Bayesian integration model to segment the tumor and edema. However, image context information at different scales may have distinctive characteristics, which cannot be successfully captured by a single statistical model. Furthermore, the trained class model may also suffer from the inter-subject image inconsistency. Menze et al. (2010) identified brain tumors based on the registration of the brain image to a probabilistic brain atlas; but, the presence of the tumor makes the registration a difficult task.

The classification techniques such as neural network (Zhu and Yan 1997) and support vector machine (SVM) (Zhou et al. 2008; Bauer et al. 2011) are also employed to segment brain and liver tumors on medical images (Verma et al. 2008; Ghanavati et al. 2012). Lee et al. (2003) combined neural network and fuzzy rules to segment the liver on abdominal CT image. All these classification methods require manually selected data from various tissue types. Therefore, the accuracy of segmentation technique depends on the accuracy and repeatability of the necessary manual intervention. Wels et al. (2008) proposed a discriminative model based on Markov random field to identify pediatric brain tumor on 3D MRI. But, their model is not trained to identify all tissue types that occur within a pediatric brain tumor.

2.2 Tumor Classification

An accurate diagnosis of the tumor can be provided by assisting the radiologist with computerized tissue characterization. It involves the use of computer analysis to characterize or classify the tumor as benign or malignant based on the extracted features. This process consists of three steps: feature extraction, feature selection and classification. The feature extraction step is meant for describing the tumor characteristics by extracting various features of the tumor. The feature selection

step, then selects the most discriminating features from the extracted feature set in order to improve the performance of the classifier. Finally, the classification step determines the type of tumor as benign or malignant based on the selected features.

2.2.1 Feature Extraction and Classification Methods

Several feature extraction and classification methods have been proposed for tissue characterization of brain and liver tumors on medical images. Fazel Zarandi et al. (2011) developed a CAD system for diagnosing brain tumors using fuzzy rules to handle the ambiguity in a set of symptoms, diagnosis, and phenomena of disease. Further, the authors have also considered mass effect and age of the brain as vital features for identifying benign and malignant tumors. This method resulted in 83.15% tumor classification accuracy. Moreover, tumors also possess other important properties such as texture and shape, which will help in better characterization of tumors. Since the malignant tumor grows aggressively, its boundary is more irregular compared to benign tumor. Thus, Martin-Landrove et al. (2007) proposed a method for characterization of lesions in the brain based on the analysis of irregularities of the lesion contour on MRI images. The drawback of the method is that it is dependent on the gradient-based edge detection algorithm which fails to extract the lesion contour in the presence of noise and blurry edges. Huang et al. (2006) developed a CAD system for classification of liver tumors on non-enhanced CT image based on auto-covariance texture features and SVM classifier. This method achieved classification accuracy of only 81.7% because of dependency on a single type of feature.

Mougiakakou et al. (2007) proposed a CAD system for characterization of liver lesions on non-enhanced CT images using three distinct feature sets extracted using first order statistics, spatial gray level dependence matrix and gray level difference method. The classification of liver lesion was performed using ensemble classifier consisting of multilayered neural networks; this method obtained classification accuracy of 84.96%. However, the learning process of neural network is computationally intensive due to multiple stages of training with initial parameters. Several methods based on multichannel and multi-resolution analysis have been developed over the years for texture representation of the tumor using Gabor filters and wavelet transform (Ahmadian et al. 2004; Mala et al. 2006; Kumar et al. 2011). These are capable of representing texture at multiple scales and resolutions, and thus help in

the detailed analysis of images. Arizmendi et al. (2011) developed a method for binary classification of brain tumors using wavelet energy features and Bayesian neural network; this method resulted in classification accuracy of 90%. But, this technique is computationally expensive due to wavelet decomposition and analysis of the image at multiple levels. Georgiadis et al. (2008) proposed a CAD system for discriminating between brain tumors on the MRI image by employing textural features and probabilistic neural network, and obtained 94% classification accuracy. However, the tumor could be better characterized by representing it with several features instead of a single feature. Hence, to improve the diagnosis performance, several CAD systems have been proposed to classify brain/liver tumors by integrating shape, intensity and texture features from multiple sequences of medical images into pattern classification methods such as SVM, neuro-fuzzy classifier, k-Nearest Neighbor (k-NN), and decision trees (Zacharaki et al. 2009; Zacharaki et al. 2011; Xu et al. 2011). However, the classification performance obtained is not much effective, since these methods are dependent on single classifiers.

2.2.2 Feature Selection Methods

Feature selection presents a key issue in many classification problems (Guyon and Elisseeff 2003; Zöllner et al. 2012). Several feature selection methods have been proposed for selecting discriminative features from a feature set (Saeys et al. 2007; Jiang 2011) and the most popular among them are Sequential Forward Selection (SFS), Sequential Backward Selection (SBS), Principal Component Analysis (PCA), Independent Component Analysis (ICA), and Genetic Algorithm (GA). The SFS method first selects the best single feature from the total set of features, and then adds one feature at a time, which in combination with the previously selected features maximizes the classifier performance. The SFS procedure discontinues when a feature subset of fixed cardinality is selected or the classifier performance begins to degrade. The SBS is the inverse of SFS, since in each step it deletes one feature from the feature set (Pudil et al. 1994). Both SFS and SBS methods are computationally expensive, since these are exhaustive approaches to feature selection.

PCA transforms the high-dimensional input feature space into a lower dimensional feature space using eigenvectors corresponding to largest eigenvalues of the covariance matrix (Fukunaga 1990). It gives a set of features that are uncorrelated but not sta-

tistically independent. Hence, Hyvärinen et al. (1999) proposed ICA method, which transforms the original input space into a feature space with dimensions that are independent of each other, and thus provides more significant features for classification. GA searches for optimal set of features by assessing the search results based on an evaluation function, which measures fitness of the selected features for the classification (Raymer et al. 2000). However, GA-based feature selection is computationally expensive due to the involvement of many complex operations and this method may have a tendency to converge toward local optima rather than global optimum of the problem.

2.3 Content-Based Image Retrieval

Medical image retrieval is an important component of CAD system, since it provides the physician a decision support for disease diagnosis by retrieving relevant cases (Quellec et al. 2011). Medical images of various patients suffering from brain/liver tumors are maintained by the hospitals in the medical image database known as Picture Archiving and Communication System (PACS) along with the diagnosis and treatment information (Yuan et al. 2008). Text-based retrieval techniques are widely used in PACS; these techniques use keywords from lab reports and associated text from images for querying the image database. Although this approach can offer much flexibility in query formulation, it suffers from several drawbacks, such as difficulty in manual annotation of every image in the database and subjective description of image based on human perception (Agarwal et al. 2009); thus, the text-based retrieval leads to inaccurate retrieval results. Content-Based Image Retrieval (CBIR) retrieves similar images from the database based on visual contents of the image such as shape, texture, region location and gray level features (Muller et al. 2004). The success of the CBIR system is mainly dependent on three factors, namely visual features, semantic gap, and database indexing techniques.

2.3.1 Visual Features

The visual features of the image represent the knowledge or the content in the image. The visual features used to retrieve general images may not apply to medical images. The knowledge of the acquired medical images and disease characteristics is essential

to extract appropriate features of the medical images. Color has got limited expressive power in medical image retrieval as these images are in gray scale and the most vital features in medical images are shape and texture. Traina et al. (2004) presented an image retrieval system, where shape information about the various regions in the brain is extracted to retrieve similar images from the database. This system was not able to retrieve similar images in all the cases as it is based on global features of the image. In medical radiology, the clinically useful information consists of variations in the highly localized region of the image. Hence, attributes characterizing the local regions are required and the Pathology Bearing Region (PBR) has to be segmented on the medical image to extract local features. Fauzi et al. (2008) experimented with both global features obtained from whole image and local features obtained from manually segmented non-overlapping image blocks in retrieving similar CT brain images from the database and achieved retrieval precision of 94%. Automatic segmentation of PBR is necessary in CAD system for accurate and consistent results of diagnosis. During medical image acquisition, there can be misalignment or rotation of images due to movement of the patient and this misalignment problem can limit the application of automated tools for image analysis. Thus, rotation invariant features are necessary to develop robust and accurate medical CBIR systems.

Shape is an important visual feature for describing objects in the medical image. Hence, the shape of the tumor can be characterized by region-based or contour-based shape descriptors (Shahabi and Safar 2010). The region-based shape descriptors like geometric moments (Shen et al. 2000), Legendre moments (Teague 1980) and Zernike moments (Liao and Panlak 1997) describe the shape by considering the whole area of the region of interest. While the contour-based techniques such as chain codes (Freeman 1961), Curvature Scale Space (CSS)(Abbasi et al. 1999), and Fourier Descriptors (FD) (Zhang and Lu 2002) concentrate only on the object contour for shape description. Among these shape descriptors, FD is the most effective and compact shape descriptor and it is also considered as the robust shape descriptor due to its rotation invariance.

Various texture description methods have been proposed in the literature of CBIR, such as Gray Level Co-occurrence Matrix (GLCM) (Haralick et al. 1973), Tamura (Tamura et al. 1978), wavelets (Yu et al. 2010), and Gabor filters (Manjunath et al. 2001). The multichannel analysis algorithms such as wavelets and Gabor filters have gained a lot of attention due to their ability to represent texture features at

different frequencies and orientations, but these methods are not rotation invariant. The Scale Invariant Feature Transform (SIFT) features proposed by Lowe (2004) are widely used local descriptors in image retrieval tasks, since these features are invariant to scale, rotation, and translation transformations. However, a significant drawback with SIFT features is the large number of features generated and the computational cost involved. The Speeded Up Robust Features (SURF) proposed by Bay et al. (2008) are faster than SIFT features, but these are less effective when compared to SIFT features in describing the image. There exist several other rotation invariant texture descriptors like Local Binary Pattern (LBP) (Ojala et al. 2002), contourlet transform (Arun and Menon 2009), polarograms (Davis 1981), and Markov random field (Portar and Canagarajah 1997).

LBP is the most effective and simple texture descriptor as it filters out the noise in the texture analysis (Ojala et al. 2002). But, the LBP fails in the presence of flat areas, where all pixels in the neighborhood have nearly equal gray values. Also, LBP does not consider the complete texture information in the image as it gives more weightage to uniform patterns than non-uniform patterns. There exist several methods to overcome the flat area problem of LBP such as Local Ternary Patterns (LTP) (Tan and Triggs 2007) and Local Multiple Patterns (LMP) (Zhu and Wang 2012). But, these methods are computationally intensive due to texture analysis at many complex levels. The similarity measure used for comparing images in CBIR also has an impact on image retrieval results. Tsang et al. (2005) experimented with various similarity measures and achieved a highest retrieval precision of 91.7% with Jeffrey divergence and local texture features. Napel et al. (2010) utilized both texture and boundary features for the retrieval of CT images of liver tumor, and obtained retrieval precision of 95%. However, this method is not fully automatic as segmentation of the liver tumor on CT image was performed manually and it also suffers from inter- and intra-observer variability.

2.3.2 Semantic Gap

One of the inherent problems in CBIR systems is the semantic gap due to the inconsistency between the features extracted and the user interpretation of an image. In the recent years, several methods have been proposed to eliminate the semantic gap based on supervised classification, unsupervised classification and relevance feedback

(Trpovski 2008). Suganya and Rajaram (2012) developed a CBIR system for liver tumor diagnosis by incorporating relevance feedback to fill the semantic gap. But, the relevance feedback consumes a lot of time to fine tune the system parameters, since it involves the user feedback. Emmanuel et al. (2007) extracted multiple features to characterize the tumor completely; but, a large number of features leads to "curse of dimensionality" problem. Dube et al. (2006) retrieved brain tumors based on classification and obtained accuracy of 87% as the system could not match the images of subclasses. In order to enhance similarity learning, Rahman et al. (2007) combined classification with clustering. But, the same feature set was used both for classification and retrieval, and thus this method could not achieve high performance in retrieving most similar medical images.

The k-means clustering algorithm (MacQueen 1967) is the widely used unsupervised classification method because of its simplicity. However, it is sensitive to initial cluster centers and thus it may give unstable and empty clusters in case of random initialization (Bishnu and Bhattacherjee 2012). There exist several methods for cluster center initialization such as genetic programming-based (Babu and Murthy 1993), binary splitting-based (Linde et al. 1980), KD-tree based (Likas et al. 2003). But, these are computationally intensive and parameter dependent. Further, k-means clustering requires the user to specify the number of clusters in the dataset and this becomes the difficult task if the user does not have any prior knowledge about the data. The existing methods such as the one proposed by Kothari and Pitts (1999), Zhao et al. (2011), and Fang et al. (2012) solved this problem by running the clustering algorithm for a wide range of clusters and selecting the number of clusters that optimize the cluster validity index. However, a single index may not give optimum results in all the cases (Arbelaitz et al. 2013).

2.3.3 Feature Database Indexing Techniques

In addition to accuracy, efficiency is also the important performance factor to be considered in the development of CBIR system. The radiologists are interested in a fast retrieval of images relevant to the query image to accelerate the diagnosis process. But, the advent of medical imaging techniques such as CT and MRI has lead to the production of large amount of images in the hospitals every day, and thus the medical image databases are steadily increasing in size. Hence, retrieval speed becomes an

important issue in CBIR systems. In order to improve the retrieval performance, the multi-dimensional features of the image must be indexed, and thus the existing CBIR systems make use of various indexing schemes such as KD-tree, R-tree, R*-tree and quad trees for fast retrieval of images from the database (Lu 2002). The indexing techniques retrieve images similar to the query image without comparing each image in the database and thus reduce the retrieval time. All these indexing structures give worse performance in case of large-dimensional feature vectors. Extracting a large number of visual features of an image leads to the "curse of dimensionality" problem, where the indexing, retrieval and similarity matching techniques collapse (Wu et al. 2004). Thus, the retrieval accuracy and efficiency can be improved by applying a feature reduction technique on the feature vectors.

2.4 3D Reconstruction of Tumor

Medical imaging techniques such as CT and MRI present the anatomic details of 3D tumor as a set of 2D parallel cross sectioned images. Representation of a 3D data in the form of 2D projected slices results in loss of information and may lead to erroneous interpretation of results (Crossingham et al. 2009). The radiologist may have difficulty in imagining the 3D anatomy based on a set of 2D images. Hence, there is a need for 3D reconstruction of the tumor from the set of 2D parallel cross sectioned images of the tumor. 3D visualization enables better understanding of the topology of the tumor, and enables measurements of tumor geometrical characteristics. Further, the 3D model of the tumor is helpful in estimating the stage of tumor, surgical planning, and biological research (Archip et al. 2006). Therefore, how to reconstruct a trustworthy surface from the set of parallel 2D cross sections becomes a crucial issue in biomedical 3D visualization. The 3D reconstruction of tumor involves several steps such as inter-slice interpolation, 3D surface mesh generation, and rendering. Several methods have been proposed for improving the steps of 3D reconstruction with respect to effectiveness and efficiency.

2.4.1 Inter-Slice Interpolation Methods

Generally, MRI or CT imaging systems provide a limited number of slices of the anatomical structure being scanned and these slices are not closely spaced. This

limited number of slices is due to the technical limitations of the imaging device and to reduce the patient's exposure and examination time. However, it is not possible to reconstruct accurate surfaces with such limited set of slices, and thus inter-slice interpolation is a vital step in 3D reconstruction for estimating missing slices (Pan et al. 2012). Inter-slice interpolation methods are divided into two groups: scene-based and object-based. The scene-based methods interpolate gray values of the present slices to fill the gray values of the missing slices. Examples of methods belonging to this group are: nearest-neighbor interpolation (Lehmann et al. 1999), linear interpolation (Goshtasby et al. 1992) and cubic spline interpolation (Meijering et al. 2000). These methods have several drawbacks, such as generation of large amounts of data for segmentation, artifacts are produced when contour locations on adjacent slices shift considerably, and inability to handle branching between two slices. In order to alleviate these problems, dynamic elastic interpolation schemes were proposed by Lin et al. (1988) and Chen et al. (1990). The key concept in these methods is to identify force field acting on one contour and distort it to make it similar to the other contour. This method has a wide adaptability, but the complicated implementations and the computing effort involved prevent it from extensive practical applications.

In object-based methods, object information extracted from the given scene is used in guiding the interpolation process and thus, the amount of time required by segmentation task is significantly reduced. The popular example for object-based method is shape-based interpolation proposed by Raya and Udupa (1990). This method interpolates distance between image pixels and object boundary instead of gray values, and therefore maintains better geometric changes. However, the method fails to interpolate slices when there is no overlapping area between two objects and it is dependent on the city-block distance transform, which provides a bad approximation to the Euclidian distance. In order to overcome the non-overlapping problem, a level set reformulation of the shape-based method was presented by Morigi and Sgallari (2004). However, this method fails when the boundaries of the corresponding structures in adjacent slices are not well defined. Several morphology-based interpolation methods were proposed to handle non-overlapping regions (Guo et al. 1995; Albu et al. 2008; Liao et al. 2011). These methods interpolate non-overlapping regions using dilation and/or erosion operations (Shih 2010), but cannot handle objects with heavy perturbations and thin structures. Object-based methods have been further

extended by registration-based interpolation techniques (Penny et al. 2004, Frakes et al. 2008), where the registration is performed prior to interpolation to provide correspondence between adjacent slices. However, these methods have high computational cost and hence limited clinical applications.

2.4.2 Mesh Generation Methods

The mesh generation methods reconstruct the surface mesh of the medical object using a set of cross-sectional images of the object, and operate either on the original pixel data or on organ boundaries. The 3D mesh generation methods that simply join contours together suffer from branching and correspondence problem (Meyers et al. 1992). Some methods handle this problem by matching contour segments (Shih and Tseng 2000) and other methods by constructing the areas of difference (Oliva et al. 1996; Klein et al. 2000). These methods fail to provide reasonable results for some particular patterns of contour pairs. 3D deformable models such as level sets have also been used to perform the surface reconstruction in the medical field. The main advantage of the level set method is its ability to handle changes of surface topology implicitly. However, the main drawback of this method is its high computation complexity due to several levels of deformations.

Another important class of algorithms for 3D model reconstruction is based on Delaunay triangulation (You et al. 2008; Boissonnat et al. 2009). These algorithms reconstruct object surface with a collection of geometric structures defined from the Delaunay triangulation. But, these algorithms produce a flat silver tetrahedron when the data points are irregularly spaced and also computationally expensive due to involvement of complex operations. Marching Cubes (MC) (Lorensen and Cline 1987) is a popular algorithm for generating 3D surface meshes due to its simplicity and effectiveness. This algorithm generates surface mesh with a set of triangles based on several cube-surface intersection configurations. However, the MC algorithm generates a large number of triangles and thus rendering the 3D model becomes computationally expensive. Further, the algorithm reconstructs mesh with holes due to ambiguous faces of the cubes. Hence, several methods have been proposed in the literature to improve the accuracy of the MC algorithm (Newman and Yi 2006; Dietrich et al. 2009; Masala et al. 2013).

2.4.3 Mesh Simplification Methods

The 3D mesh models generated using surface reconstruction algorithms often consist of a large number of triangles. Rendering such complex meshes at an interactive rate in real-time applications such as treatment planning or virtual surgery becomes difficult. Thus, many researchers have focused on developing mesh simplification algorithms to improve the rendering efficiency and save the storage space. Mesh simplification methods can be divided into three categories: vertex clustering, vertex decimation and edge collapse. Methods in all these three categories are based on different error metrics for measuring the geometric deviation of the mesh during simplification. Mesh simplification methods based on vertex clustering (Rossignac and Borrel 1993; Low and Tan 1997) simplify the mesh by replacing a cluster of vertices in a given grid cells with a single vertex. This helps in selective refinement for view-dependent simplification, but can drastically alter the topology of the input mesh and the quality of the output is low as the size of the grid cells does not provide a geometric error bound. The vertex decimation methods (Schroeder et al. 1992; Franc and Skala 2002; Insu et al. 2006) iteratively selects the vertex for removal, eliminates all the adjacent faces and re-triangulates the resulting hole. These methods preserve the mesh topology, but require a re-triangulation procedure to fill the hole on each vertex removal.

The edge collapse operation has become popular in the graphics community in the last several years. It collapses an edge by merging two vertices into a single vertex based on the error metrics. The edge collapse was first used by Hoppe et al. (1993) to create progressive meshes based on an energy function for measuring the quality of simplified mesh. This scheme can create a high-quality approximation, but finding an optimal solution of the energy function is computationally expensive. Further, many edge collapse-based algorithms have been proposed and the most popular methods among them are QSlim and Memoryless Simplification (MS) methods proposed by Garland and Heckbert (1997), and Lindstrom and Turk (1998), respectively. The QSlim method computes the geometric deviation of the edge collapse as the squared distance of a vertex to incident planes and stores it as a 4x4 symmetric matrix with a vertex. While this method is computationally efficient and gives high quality approximations, it is not memory efficient as with each vertex it stores a 4x4 symmetric matrix. Further, it cannot preserve the sharp details of the mesh as its error metric is based on the distance measure. The mesh simplification algorithms by Yoshizawa

et al. (2005), Lee et al. (2005), and Li et al. (2012) incorporated additional heuristics to QSlim for tackling its drawbacks. Although these algorithms preserve the salient features of the model, the execution time increases drastically. The MS method selects the position of the new vertex for edge collapse such that volume of the mesh is not distorted. This method is memory efficient and fast as it does not maintain a geometric history of the mesh; but, it fails to retain the sharp details of the mesh during simplification. In another method called FSIMP (Hussain 2008), normal field of the local neighborhood of a vertex is used as a measure of geometric fidelity to guide the vertex-based edge collapse operation. The simplified meshes generated by this method are not of good quality because of the significant volume loss.

2.4.4 Model Rendering Methods

Rendering algorithms apply lighting models to shade over surfaces in a scene. The commonly used rendering techniques for shading the polygonal surfaces are: flat shading (Foley et al. 1996), Gouroud shading (Gouroud 1971), and Phong shading (Phong 1975). In flat shading method, the intensity value for the polygon in the mesh is calculated once and the whole polygon is shaded with the same intensity value. This method is fast and simple, but produces intensity discontinuities because the light intensity is computed based on the normal of each polygon surface. Gouraud shading model renders a polygon surface by first computing the intensity value at the vertices of the polygon and then interpolates vertex intensity values across the surface to shade the polygon. With this, the intensity values of each polygon are matched with the values of the adjacent polygons and thus the intensity discontinuities are eliminated. However, the linear interpolation of intensity values produces a Mach band effect, which is the appearance of dark and bright intensity streaks on the surface. Phong shading model eliminates the Mach band effect by interpolating the normal vectors between the vertices instead of intensity values. The intensity value is then calculated at each pixel using the interpolated normal vector and realistic highlights are displayed on the surface. Thus, the Phong shading model is considered as the accurate method for rendering the polygon surface.

2.5 Outcome of Literature Review

After extensive review of tumor detection, classification, CBIR and 3D reconstruction methods, the following open issues and challenges are identified for developing an automatic, effective and efficient CAD system for analysis of brain and liver tumors.

The tumor segmentation accuracy determines the eventual success or failure of computerized medical image analysis tasks like diagnosis, volume analysis and surgical planning. Most of the brain/liver tumor segmentation methods in the existing literature are manual or semi-automatic. These methods are time consuming and do not automate the entire diagnosis process of the CAD system, since they require the manual intervention in the tumor segmentation. But, the hospitals are in need of fully automatic diagnosis system with better accuracy compared to the analysis of the disease by the physician. Though some automatic segmentation techniques exist, they do not provide the accuracy required in the medical domain. Further, most of the automatic methods do not focus on the tumor and edema separation, which is most required to properly delineate the region of a tumor on the medical image. Hence, there is a need to develop a fully automatic, accurate and efficient segmentation method for detection of brain and liver tumors on medical images.

In an effort to deliver more effective treatment, clinicians are continuously seeking for greater accuracy in pathological characterization of the tumor tissues from imaging investigations. Hence, to build an effective CAD system for correctly classifying brain and liver tumors, it is necessary to present all the available information of the tumor region to the CAD system. The existing methods employ few features for characterizing the pathology of the tumor and no method uses all the features in a comprehensive manner. However, the use of all the heterogeneous information, leads to high-dimensional feature vector and in turn degrade the diagnostic accuracy of CAD systems significantly. Therefore, the reliable feature selection technique is needed for providing compact and discriminating tumor descriptors. Another observation is that the majorities of the existing techniques investigate the performance of different classifiers independently and discuss their merits and demerits under certain contexts. However, a decision support system based on the fusion of multiple classifiers would be more effective compared to individual classifier alone (Ponti 2011).

Although several studies are already being conducted with respect to content-based medical image retrieval, many challenging problems still exist. The main fac-

tors that judge the success of a CBIR system are the visual features used for retrieval, the size of the database and the retrieval speed. Achieving these objectives becomes difficult in large medical image databases. The performance of the CBIR system can be improved by using the appropriate feature set. A single feature descriptor like texture alone may not retrieve the most relevant images, and hence the challenge is to find the combination of several features that adequately represent the tumor on medical image. The existing CBIR systems rely on multiple features, classification and clustering techniques to eliminate the semantic gap. However, multiple feature set may not alone give good retrieval results, but instead leads to problems of high dimensionality. Classification finds good similarity within the class, but fails to match subclass items. Though clustering helps in performing unsupervised classification, it requires specification of number of clusters and their centroids. Hence, there is a need for CBIR framework that learns well the similarity between images and inherent structure of the data. Further, the CBIR system must be made robust to misalignments of images that occur during MRI/CT image acquisition to retrieve most similar images from the database. Existing indexing structures give good efficiency in low-dimensional feature vectors and perform worse than exhaustive search in case of high-dimensional feature vectors. Hence, the indexing structures with reduced feature vectors are needed for the efficient CBIR system.

The existing 3D reconstruction methods do not provide the high quality surfaces and efficient 3D visualization of brain/liver tumors on medical images. Shape-based interpolation is suitable for medical applications, but it cannot handle shifts in the tumor cross sections, and the use of city-block distance transform fails to provide a good approximation to the Euclidian distance transform. Thus, shape-based interpolation should be enhanced with respect to accuracy and efficiency. The most popular marching cubes algorithm can yield high quality surfaces, but generates a large amount of triangles due to processing of small sized cubes. Thus, the number of triangles in the 3D surface mesh of the tumor must be reduced to accelerate the rendering phase and save storage space. The existing mesh simplification algorithms cannot preserve important shape features of the mesh such as highly curved regions, and thus there is a need to develop a mesh simplification algorithm that preserves the quality of the simplified mesh.

2.6 Problem Statement

In order to solve the open issues and challenges discussed in the previous section, there is a need to develop an accurate and efficient CAD system for assisting the radiologist in the diagnosis of brain and liver tumors on medical images. Accordingly, the research problem is stated as follows:

"To develop an effective and efficient computer-aided diagnosis system for detection, classification, content-based image retrieval and 3D reconstruction of brain and liver tumors using MRI and CT images, and thereby assisting the radiologist in making an accurate diagnostic decision".

2.7 Research Objectives

The objectives of this research work are as follows:

- To develop automatic, effective and efficient segmentation techniques for detecting the region of the brain and liver tumors on medical images.
- To develop an effective and efficient tumor classification scheme for identifying the type of brain/liver tumor as benign or malignant.
- To develop an effective and efficient content-based image retrieval (CBIR) method for assisting the radiologist in the diagnosis of brain and liver tumors based on relevant cases.
- To develop an effective and efficient 3D reconstruction scheme for building a 3D model of the brain/liver tumor and compute its volume for assisting the radiologist in determining the stage of cancer.

In order to accomplish the four objectives of the research work, the framework of the proposed CAD system comprising of tumor detection, classification, CBIR and 3D visualization methods is illustrated in Figure 2.1. Input to the proposed CAD system is the MRI image of brain tumor or the CT abdominal image of liver tumor. The input image is processed to determine the location, type, similar tumor images in the medical database and to build the 3D model of the tumor.

The brief description of research contributions in the development of a CAD system for analysis of brain and liver tumors is given as follows:

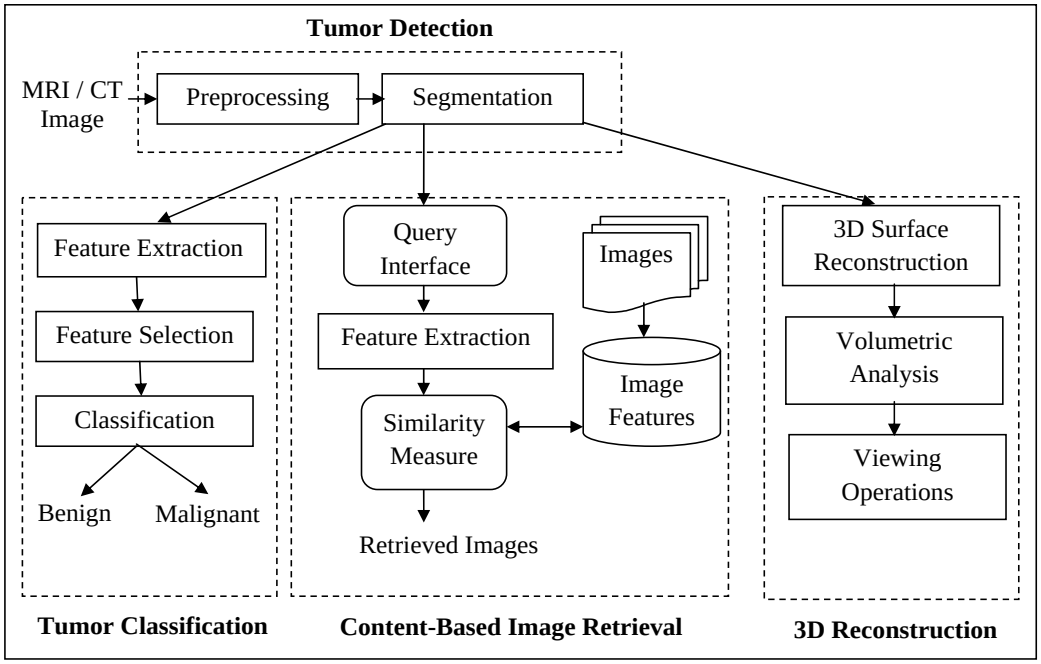

Figure 2.1: Framework of the Proposed CAD System

⋆ **Tumor Detection**

Automatic, effective and efficient segmentation techniques are proposed for the detection of brain and liver tumor on MRI and CT image, respectively. The brain tumor segmentation technique consists of the steps for identifying abnormal slices in a set of slices of the brain, extracting the tumor region using proposed Modified Fuzzy C-Means (MFCM) clustering algorithm and separation of the tumor and edema. The liver tumor segmentation technique consists of the steps for identifying abnormal slices in a set of slices of the liver, liver segmentation and extracting the tumor region using the proposed automatic region growing algorithm.

⋆ **Tumor Classification**

An effective and efficient scheme is proposed for classifying the brain/liver tumor as benign or malignant. The significant features of the brain/liver tumor such as shape, texture and boundary features are extracted to represent the tumor characteristics. The most discriminating features of the tumor are selected using the proposed two-level feature selection technique consisting of information

gain (IG)-based feature ranking and ICA-based feature selection. The accuracy of the tumor classification is improved using the proposed ensemble classifier consisting of three heterogeneous classifiers, namely SVM, artificial neural network (ANN) and k-NN.

⋆ **Content-Based Image Retrieval**

Two CBIR methods are proposed based on a hierarchical framework to retrieve similar tumor images from the database for assisting the radiologist in brain/liver tumor diagnosis: 1) CBIR using image rotation correction 2) CBIR using rotation invariant features. The indexing technique named as Cluster with IG-ICA and KD-tree (CIKD) is proposed for fast retrieval of images from the medical database. The features in the database are clustered by the proposed modified k-means clustering algorithm, in which the initialization of the number of clusters and cluster centers is performed automatically.

⋆ **3D Reconstruction of Tumor**

3D model of the brain/liver tumor is reconstructed effectively and efficiently from a set of 2D slices containing the tumor. The missing slices of the tumor are identified by the proposed enhanced shape-based interpolation technique, which handles the drastic shift of the tumor regions in the consecutive slices and incorporates chamfer distance transform for approximating Euclidian distance transform. Then, the surface mesh is generated from the set of slices using the marching cubes algorithm (Lorensen and Cline 1987). This algorithm generates a large number of triangles, and thus the reconstructed mesh of the tumor model is simplified without degrading the model quality using the proposed mesh simplification algorithm. Further, the volume of the tumor is computed in order to assist the radiologist in determining the stage of cancer.

2.8 Tumor Datasets

All MRI/CT images required for the experiments of this research work are collected from different hospitals. The verification of the experimental results related to each module of the proposed CAD system is performed with the help of the experienced radiologists. In order to maintain the privacy of the patients, the identifying infor-

mation including patients' names and initials are kept confidential throughout the research work. The proposed CAD system is implemented using MATLAB, and all the experiments are performed on a personal computer with 3GHz Pentium processor and 3GB of memory running under Windows XP operating system. The details of the brain and liver tumor datasets are given below:

Brain Tumor Dataset

The brain tumor dataset consists of T1-weighted post-contrast and T2-weighted brain MRI images of 820 patients (female: 382, male: 438) with verified and untreated tumors. The patients' ages are in the range of 15 to 74 years (mean age 48 years). The images are acquired from 1.5-T MRI clinical scanner at the Shirdi Sai Cancer Hospital, Manipal, India and M.S. Ramaiah Memorial Hospital, Bangalore, India. The scan of each patient produced a set of 22 slices having a thickness of 5 mm. All images in the dataset are gray scale images with size 640×480 and each pixel size corresponds to 0.31 mm×0.31 mm. Among 820 patients, 420 patients are diagnosed with benign tumor and 400 patients with malignant tumor based on histopathological analysis of biopsy samples. T1-weighted post-contrast and T2-weighted MRI images are used in the experiments as they provide important diagnostic information and appreciable contrast between brain regions.

Liver Tumor Dataset

The liver tumor dataset consists of non-enhanced abdominal CT images of 764 patients (female: 350, male: 414) with verified and untreated tumors. The patients' ages are in the range of 27 to 68 years (mean age 43 years). The images are acquired from CT scanner at the Kidwai Institute of Oncology, Bangalore, India and Bapuji Cancer Hospital, Davangere, India. The scan of each patient produced a set of 32 slices having a thickness of 3 mm. All images in the dataset are gray scale images with size 512×512 and each pixel size corresponds to 0.44 mm×0.44 mm. Among 764 patients, 380 patients are diagnosed with benign tumor and 384 patients with malignant tumor based on histopathological analysis of biopsy samples. Non-contrast-enhanced CT images are used in the experiments, since the contrast agent injection during CT imaging can induce the renal toxicity and allergic reactions in the patient.

2.9 Summary

The literature reviews of various techniques on computer-aided tumor detection, classification, CBIR and 3D reconstruction are summarized in the following tables.

Table 2.1: Literature Review of Tumor Detection Methods

Method	**Author**	**Description**	**Drawback**
Threshold-based	Park et al.(2005)	Threshold selected based on analysis of histogram.	Fails on poorly contrasted lesions.
	Moltz et al. (2008)	Pixel intensity thresholding.	Threshold selected in the confidence interval.
	Seo et al. (2005)	Threshold selection based on minimum total probability error.	Produces false positives for small tumors.
	Choudary et al. (2008)	Thresholding combined with region growing and level set methods.	Semi-automatic.
Region-Based	Venkatachalam et al.(2004)	Region growing with manual selection of seed point and threshold.	Semi-automatic.
	Fan et al. (2005)	Region growing with manual selection of seed point.	Computationally intensive.

Continued on next page

Table 2.1 – *Continued from previous page*

Method	**Author**	**Description**	**Drawback**
	Poonguzhali and Ravindran (2006)	Region growing with seed point selection based on texture and threshold selection based on iterative thresholding.	Inaccurate results in overlapping tissue intensities.
	Dongxiang and Tiankun (2009)	Used region split and merge method for tumor extraction.	Computationally intensive.
	Ng et al. (2006)	Used watershed algorithm to extract tumor region.	Over-segmented image.
	Liu et al.(2009)	Combined watershed and region merging methods.	Threshold used in region merging is not adaptive.
	Hamarneh and Li (2009)	Used prior shape and appearance knowledge in watershed algorithm.	Fails in low-contrast images
Cluster-Based	Juang and Wu (2010)	Tumor segmentation based on k-means clustering	Cannot capture uncertainty in medical image.
	Murugavalli and Rajamani (2006)	Used parallel FCM algorithm for tumor detection.	Hardware implementation is not effective.
	Cai et al. (2007)	FCM clustering with robustness to noise.	Computationally expensive.

Continued on next page

Table 2.1 – *Continued from previous page*

Method	**Author**	**Description**	**Drawback**
	Al-Zoubi et al. (2007)	Fast FCM clustering with number of data points reduced based on threshold.	Threshold value manually selected.
	Hemanth et al.(2009)	Effective FCM clustering based on quantization and aggregation of data.	Computationally expensive.
	De Vargas et al. (2011)	Reduced number of iterations in FCM clustering by deriving crisp membership matrix from fuzzy matrix.	Required additional time for computing crisp membership matrix.
Deformation-Based	Lu et al.(2005)	Tumor segmentation based on active contour model with manually placed initial contour around tumor.	Semi-automatic.
	Krishnamurthy et al. (2004)	Used active contour with initial contour derived using edge detection technique.	Fails in presence of noise.
	Bhat and Kunte (2010)	Combined watershed and active contour methods to get the initial contour for tumor segmentation.	Over-segmented image.

Continued on next page

Table 2.1 – *Continued from previous page*

Method	**Author**	**Description**	**Drawback**
	Prastawa et al. (2004), Xie et al. (2005)	Used level set method to segment tumor.	Requires tuning of the level set parameters with the help of user.
Model-Based	Moon et al.(2002)	Tumor detection based on distribution of normal tissue, tumor and edema.	Fails in case of large deformations.
	Corso et al. (2008)	Baysian integration model to detect tumor.	Suffers from inter-subject image inconsistency.
	Menze et al. (2010)	Identified tumors based on image registration.	Computationally expensive.
	Lee et al. (2003), Zhou et al. (2008), Verma et al. (2008), Bauer et al. (2011), Ghanavati et al. (2012)	Used classification techniques such as neural network, SVM, and fuzzy rules to detect tumor.	Accuracy of the segmentation depends on accuracy of manually selected data on tissue types.
	Wels et al. (2008)	Used discriminative model based on Markov random field to detect tumor.	Fails to detect all types of tumors.

Table 2.2: Literature Review of Tumor Classification Methods

Method	**Author**	**Description**	**Drawback**
Feature extraction and classification	Fazel Zarandi et al. (2011)	Identified tumor type based on features such as mass effect and age, and fuzzy classifier.	Inaccurate as vital features of the tumor such as texture and shape are not considered.
	Martin-Landrove et al. (2007)	Used border irregularity of the tumor and ANN classifier.	Fails in case of blurry edges.
	Huang et al. (2006)	Tumor classification based on texture features and SVM classifier.	Inaccurate due to depedency on single type of feature.
	Mougiakakou et al. (2007)	Used tumor texture features and ensemble classifier with multilayered neural network.	Computationally intensive.
	Kumar et al. (2011)	Used wavelet-based texture features and ANN classifier for identifying tumor type.	Computationally intensive.
	Georgiadis etal. (2008)	Classified tumors based on texture features and probablistic neural network.	Inaccurate due to dependency on single type of feature.

Continued on next page

Table 2.2 – *Continued from previous page*

Method	**Author**	**Description**	**Drawback**
	Zacharaki et al. (2011)	Classifier tumors based on shape and texture features, and SVM classifier.	Inaccurate due to dependency on single type of classifier.
Feature selection	Pudil et al. (1994)	Used sequential forward and backward search methods for selecting vital features.	Computationally expensive.
	Fukunaga (1990)	Principal Component analysis method for reducing the number of features.	Reduced feature set is not statistically independent.
	Hyvarinen et al. (1990)	Used ICA for feature selection	The number of vital features manually selected.
	Raymer et al. (2000)	Feature selection based on genetic algorithm.	Computationally expensive.

Table 2.3: Literature Review of CBIR Methods

Method	**Author**	**Description**	**Drawback**
Visual features extraction	Traina et al. (2004)	Used shape and texture features in CBIR	Based on global features.
	Fauzi et al. (2008)	Extracted global and local features from manually segmented tumor.	Semi-automatic.

Continued on next page

Table 2.3 – *Continued from previous page*

Method	**Author**	**Description**	**Drawback**
	Teague et al. (1980), Liao and Panlak (1997), Shen et al. (2000)	Used region-based shape descriptors in CBIR	Computationally expensive.
	Freeman (1961), Abhasi et al. (1999), Zhang and Lu (2002)	Used contour-based shape descriptors in CBIR	Less accurate in case of blurry edges.
	Yu et al.(2010), Manjunath et al. (2001)	Object representation with Gabor filters.	Extracted features are rotation variant.
	Lowe (2004)	Used SIFT features in CBIR.	Computationally expensive as large number of features are generated.
	Bay et al. (2008)	Image description with SURF features for retrieving similar image from database	Less effective in describing the image.
	Ojala et al. (2002)	LBP features for representing image texture in CBIR	Fails in the presence of flat area and provides incomplete texture description.
	Zhu and Wang (2012)	Object representation with local multiple patterns.	Computationally expensive due to image analysis at multiple levels.

Continued on next page

Table 2.3 – *Continued from previous page*

Method	**Author**	**Description**	**Drawback**
	Napel et al. (2010)	Used texture and boundary features extracted from manually segmented tumor for CBIR.	Semi-automatic.
Elimination of semantic gap	Suganya and Rajaram (2012)	Filled semantic gap using relevance feedback.	Computationally expensive due to many loops of feedback from the user.
	Emmanuel et al. (2007)	Eliminated semantic gap by using multiple features of the image.	Suffers from curse of dimensionality problem.
	Dube et al. (2006)	Filled semantic gap based on image classification.	Could not match images of subclasses.
	Rahman et al. (2007)	Filled semantic gap based on image classification and clustering.	Less accurate since same features are used for classification and clustering.
Feature database indexing	Lu (2002), Wu et al. (2004)	Reduced retrieval time based on KD-tree, R-tree, R*-tree, and quad-tree.	All these trees give worse performance in case of large-dimensional feature vectors.

Table 2.4: Literature Review of 3D Reconstruction Methods

Method	**Author**	**Description**	**Drawback**
Inter-slice interpolation	Lehmann et al. (1999), Goshtasby et al. (1992), Meijering et al. (2000)	Scene-based interpolation for estimating missing slices.	Generates large amount of data for tumor segmentation.
	Lin et al. (1988), Chen et al. (1990)	Used dynamic elastic interpolation for slice interpolation.	Computationally expensive.
	Raya and Udupa (1990)	Performed inter-slice interpolation using shape-based interpolation.	Provides bad approximation to Euclidian distance.
	Morigi and Sgallari (2004)	Estimated missing slices with shape-based interpolation and level sets.	Fails when object boundaries are not well defined.
	Guo et al. (1995), Albu et al. (2008), Liao et al. (2011)	Inter-slice interpolation by morphology-based interpolation.	Cannot handle objects with heavy perturbations.
	Penny et al. (2004), Frakes et al. (2008)	Estimated missing slices by registration-based interpolation.	Computationally expensive.
Mesh generation	Meyers et al. (1992)	Generated surface mesh by joining contours of adjacent slices.	Suffers from branching and correspondence problem.

Continued on next page

Table 2.4 – *Continued from previous page*

Method	**Author**	**Description**	**Drawback**
	Shih and Tseng (2000), Klein et al. (2000)	Generated surface mesh by matching contour segments and constructing area of difference of adjacent slices.	Could not handle all patterns of contour pairs.
	Boissonnat et al. (2009)	Surface mesh generated based on Delaunay triangulation.	Produced flat silver triangles and computationally expensive.
	Lorensen and Cline (1987)	Generated surface mesh by marching cubes algorithm.	Generates large number of triangles and holes in the surface mesh.
	Dietrich et al. (2009), Masala et al. (2013)	Modified marching cubes algorithm to eliminate hole problem.	Computationally expensive and generates silver triangles in the mesh.
Mesh simplification	Rossignac and Borrel (1993), Low and Tan (1997)	Simplified mesh based on vertex clustering.	Drastically alters the topology of the mesh.
	Franc and Skala (2002), Insu et al. (2006)	Mesh simplification by vertex decimation.	Requires retriangulation procedure to fill the hole on each vertex removal.

Continued on next page

Table 2.4 – *Continued from previous page*

Method	**Author**	**Description**	**Drawback**
	Hoppe et al. (1993)	Mesh simplification by collapsing edges based on energy function.	Computationally expensive.
	Garland and Heckbert (1997)	Reduced number of triangles in the reconstructed mesh based on quadric error metrics.	Memory inefficient and cannot preserve sharp details of the mesh.
	Lindstrom and Turk (1998)	Memoryless mesh simplification by not retaining the history of the mesh.	Cannot preserve sharp details of the mesh.
	Lee et al.(2005), Li et al. (2012)	Mesh simplification based on Qslim method with additional heuristics.	Computationally expensive.
	Hussain (2008)	Simplified mesh by collapsing an edge based on normal field of the neighborhood of a vertex.	Results in significant volume loss.
Model rendering	Foley et al. (1996)	Whole Model is shaded with same intensity value (Flat shading).	Produces intensity discontinuities.
	Gouroud (1971)	Model rendering by interpolating vertex intensity across the polygon surface (Gouroud shading).	Suffers from Mach band effect.

Continued on next page

Table 2.4 – *Continued from previous page*

Method	**Author**	**Description**	**Drawback**
	Phong (1975)	Model rendering by interpolating normal vectors between the vertices (Phong shading).	Computationally expensive since it computes intensity value based on interpolated normal vector.

This chapter provided a review of the CAD methods proposed by various researchers for detection, classification, CBIR and 3D reconstruction of brain and liver tumors. The research problem statement and objectives were framed based on the outcome of the literature review. Also, the chapter provided the description of the brain and liver tumor datasets used in the experiments of the present research work.

Chapter 3

Tumor Detection on Medical Images

The proposed CAD system consists of tumor detection, classification, CBIR and 3D reconstruction methods for effective and efficient analysis of brain and liver tumors. The tumor detection method is meant for extracting the tumor region from the given medical image. The tumor detection is necessary for diagnosis, 3D reconstruction, volumetric analysis and treatment planning. Hence, in this chapter, we discuss the proposed automatic, effective and efficient segmentation techniques for detection of brain and liver tumor on MRI and CT images, respectively. Precisely, an attempt has been made to fulfill the first objective of the research work and to overcome the drawbacks of the existing segmentation methods as discussed in Section 2.5. The research contributions towards the detection of brain and liver tumors are as follows:

- An automatic, effective and efficient brain tumor segmentation technique based on Modified Fuzzy C-Means (MFCM) clustering algorithm.
- An automatic, effective and efficient liver tumor segmentation technique based on the automatic region growing algorithm.

The proposed techniques follow a systematic approach to tumor detection by first identifying the abnormal slice from a given set of slices, and then segmenting the tumor on the abnormal slice. The proposed segmentation techniques for detection of brain and liver tumor are explained in Section 3.1 and 3.2, respectively.

3.1 Brain Tumor Segmentation Using Modified FCM Clustering

The FCM clustering algorithm (Bezdek 1981) can handle the complex distribution of tissue intensities in MRI images, but, it consumes a lot of time to partition the image into desired number of clusters. It is also sensitive to initial cluster centers and thus leads to local minima results (Alia et al. 2009). Though some existing methods (Al-Zoubi et al. 2007; Hemanth et al. 2009) accelerate the FCM algorithm, the efficiency improvement is not much effective. In order to overcome these drawbacks, we propose MFCM clustering algorithm for brain tumor segmentation on the MRI image.

3.1.1 Proposed Methodology

The framework of the proposed brain tumor segmentation technique is shown in Figure 3.1. It consists of two phases, namely, preprocessing and segmentation.

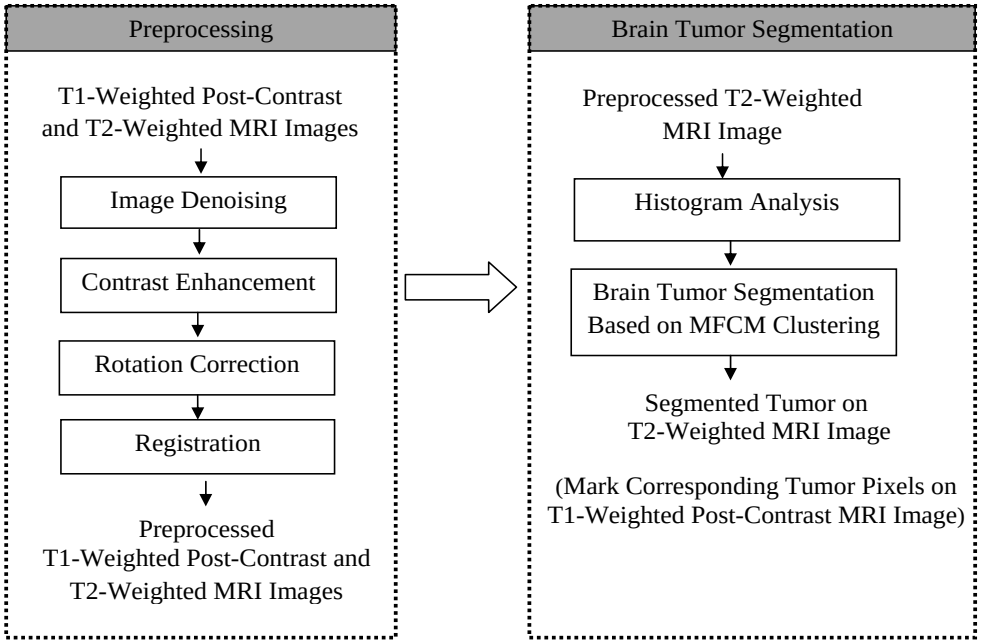

Figure 3.1: Framework of the proposed Brain Tumor Segmentation Technique

The preprocessing phase improves quality of the input T1-weighted post-contrast and T2-weighted MRI images by image denoising, contrast enhancement, rotation

correction and registration techniques. Next, in the segmentation phase histogram of the brain region on the T2-weighted MRI image is analyzed to determine whether the given image is normal (without tumor) or abnormal (with tumor). If the given image is abnormal, then the tumor is segmented on the T2-weighted MRI image using the proposed MFCM clustering algorithm and the corresponding pixels on T1-weighted post-contrast MRI image are considered as the tumor region. In case of T1-weighted post-contrast MRI image, the contrast agent not only enhances the tumor but also the blood vessels in the brain and this creates ambiguity in segmenting the brain tumor, whereas in T2-weighted MRI image the brain tumor shows higher intensity when compared to other regions in the brain. Thus, the proposed segmentation algorithm is applied on T2-weighted MRI image of the brain.

3.1.2 Preprocessing

Prior to segmentation, the preprocessing step is applied on both T1-weighted post-contrast and T2-weighted images to improve the quality of images. The noise can mask and blur the important features in the MRI image and thus further processing of medical image becomes difficult. Hence, the noise is eliminated by applying 3×3 median filter (Burger and Burge 2008). However, the edges in the resulting image are smoothed. Hence, to improve the perceptibility of the tumor and other structures in the brain, unsharp masking is used after the median filtering. A 3×3 unsharp filter is constructed using the negative of the 2D Laplacian filter (Bourne 2010). The sizes of filters are chosen empirically. Next, the image contrast is enhanced by applying histogram equalization. If the given T1- and T2-weighted images are rotated, then these images are restored to their standard position using the proposed rotation correction technique, which is discussed below. Finally, for each patient, T1-weighted post-contrast and T2-weighted images are co-registered using FMRIB's[1] Linear Image Registration Tool (FLIRT) (Jenkinson and Smith 2001).

The patient's movement during MRI image acquisition may lead to misalignment (rotation/translation) of the image. The translation will not cause problems in image analysis because the tumor can be segmented and analyzed irrespective of the location of brain region in the medical image. But, image rotation limits the application of automated tools for MRI image analysis, since rotation changes the shape and texture

[1] *The Oxford Center for Functional MRI of the Brain*

properties of the tumor. Thus, in the present work, a method has been proposed for rotation correction of misaligned MRI image of the brain. First, the orientation of the brain must be identified to know the angle by which to rotate the misaligned brain to its standard position. This is accomplished by measuring the orientation of the major axis of the brain in the MRI image with the reference x-axis (Figure 3.2).

Figure 3.2: Orientation Angle Estimation of the Brain MRI Image (a) Rotated MRI Image (b) Orientation Angle

Then, based on the orientation angle (θ), the rotation correction angle ($\theta' = 90 - \theta$) is computed. Next, the misaligned image can be restored to its standard position using the following rotation transformation equations.

$$x' = xcos(\theta') - ysin(\theta') \tag{3.1}$$

$$y' = xsin(\theta') + ycos(\theta') \tag{3.2}$$

Where, a point (x, y) in the original image is directly mapped onto the point (x', y') in the resultant image. But, this kind of forward mapping creates holes in the output image, since the target position (x', y') does not coincide with the discrete grid points. Thus, to retain the quality of the resultant image, inverse mapping is performed. For each discrete pixel position in the output image, the corresponding continuous position (x, y) is computed in the input image. This mapping hits the non-integer locations in the input image, where there is no pixel present. Hence, the pixel value at this non-integer location is computed using interpolation method. In the present work, bicubic interpolation method (Keys 1981) is used as it is more accurate com-

pared to the nearest neighbor and bilinear interpolation techniques (Amrutha et al. 2010). Bicubic interpolation determines a new pixel value by considering nearest 4×4 neighborhood of known pixels and by giving all the 4×4 pixels a weight using their distance to the new pixel. The interpolated pixel value is mapped back to the point (x', y') in the output image.

3.1.3 Brain Tumor Segmentation

After preprocessing the MRI images, the brain tumor on the T2-weighted MRI image is segmented using various steps as shown in Figure 3.3.

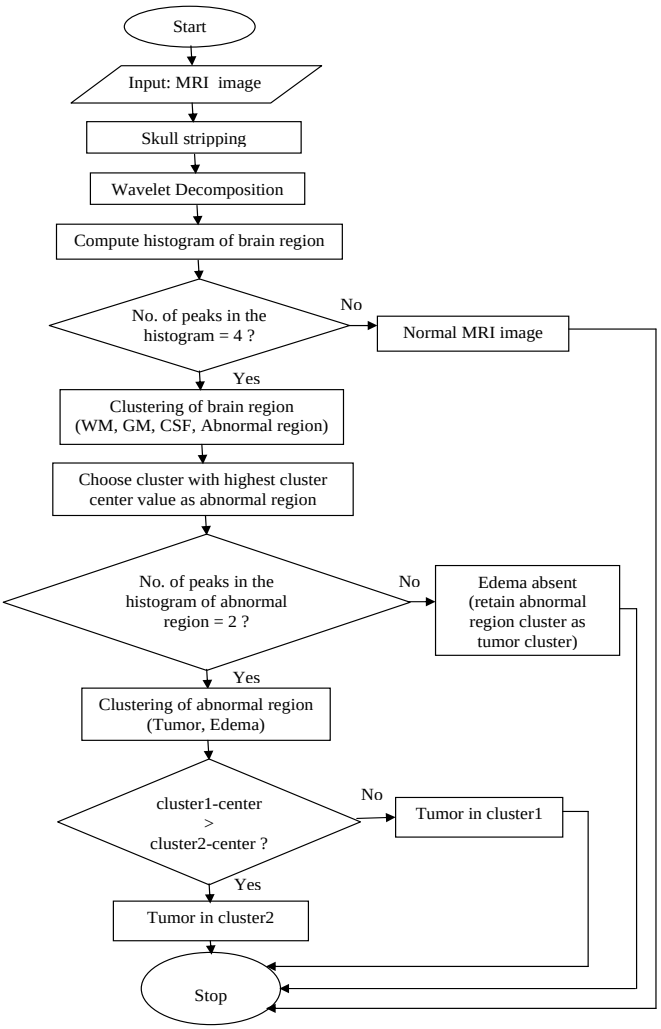

Figure 3.3: Flowchart of the Brain Tumor Segmentation Technique

The skull stripping removes the skull region from the MRI image and wavelet transform decomposes the image into various frequency bands. Then, the histogram analysis of the brain region in wavelet transformed image is carried out to determine whether the given MRI image is normal or abnormal. If the image is abnormal, then MFCM clustering is applied in order to segment the tumor region on the MRI image. The various steps in the brain tumor segmentation technique are detailed below.

Skull Stripping

Skull removal of the brain from the MRI image is an important step in the segmentation of brain tumor, since skull may cause misclassifications of pixels due to intensity similarities with brain structures (Roalsn et al. 2011). Thus, the skull region is eliminated on each slice by first converting the original T2-weighted MRI image (Figure 3.4(a)) to a binary image based on the threshold value calculated automatically using Otsu's method (Otsu et al. 1979). The resultant binary image consists of connected components as shown in Figure 3.4(b). Then, a search is made for the largest connected component corresponding to the brain, and accordingly the skull region is eliminated by retaining only the pixels in the largest connected component as shown in Figure 3.4(c).

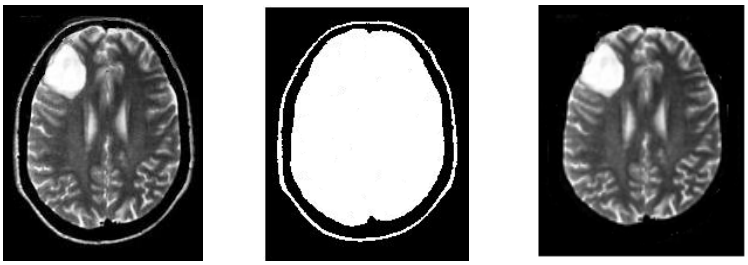

Figure 3.4: Brain Skull Stripping (a) Original MRI Image (b) Binary Image (c) Skull Stripped MRI Image

Wavelet Decomposition

In this step, the Discrete Wavelet Transform (DWT) is applied to the skull stripped MRI image to reveal the characteristics of tissues. DWT makes use of high-pass

(h(n)) and low-pass (g(n)) filters to decompose the given image into four sub-bands: Low-Low (LL), Low-High (LH), High-Low (HL), and High-High (HH) representing approximate, vertical, horizontal, and diagonal details (Acharyya et al. 2003), respectively as shown in Figure 3.5. In the present work, Haar wavelet is used to decompose the image at three levels due to its simplicity and efficiency. In the next step, MFCM clustering is applied to the approximate image to segment tumor, since the approximate image contains more details of the image when compared to other sub-bands of the image.

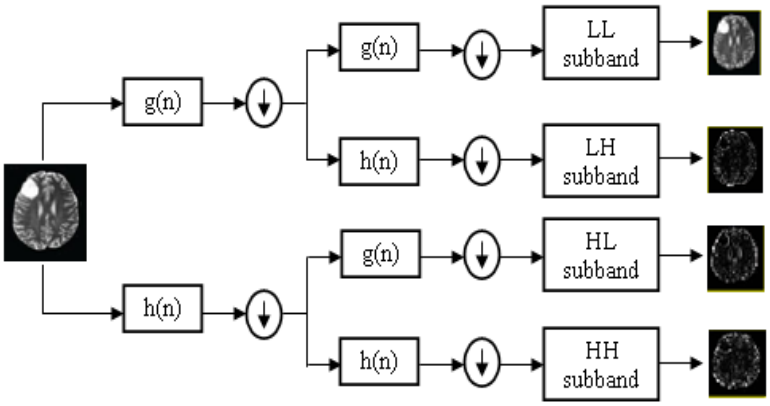

Figure 3.5: Image Decomposition Using Discrete Wavelet Transform

Tumor Identification

MRI of the brain gives a set of slices containing normal and abnormal slices; hence, identification of the abnormal slices is needed before segmentation. The normal slice consists of three regions White Matter (WM), Gray Matter (GM) and Cerebrospinal Fluid (CSF), whereas the abnormal slice consists of four regions (WM, GM, CSF and abnormal region). Thus, to determine whether the given T2-weighted MRI image of the brain is normal or abnormal, the histogram of the brain region is computed using Equation (3.3), and the number of clusters present in the brain region is determined based on the histogram analysis (Castro et al. 2007).

$$h(g) = \frac{\sum_{x=0}^{M-1} \sum_{y=0}^{N-1} \delta(I(x,y) - g)}{M \times N} \tag{3.3}$$

Where, the function $h(g)$ gives the number of pixels having a gray level equal to g in the image of size $M \times N$. The gray level g lies in the range $[0, L-1]$ and L is the maximum gray level in the image. Function $\delta(0) = 1$ and $\delta(g \neq 0) = 0$. If the histogram consists of four peaks, then the given T2-weighted MRI image is considered as the abnormal slice and in the next step, clustering algorithm is applied in order to segment the abnormal region on the T2-weighted MRI image. Otherwise, the given T2-weighted MRI image is considered as the normal slice and further processing is not carried out.

Modified FCM Clustering

After identifying that the given T2-weighted MRI image contains the abnormal region, the T2-weighted MRI image is partitioned into four clusters ($c = 4$): WM, GM, CSF and abnormal region (tumor) using the MFCM clustering algorithm. In conventional FCM clustering algorithm (Bezdek 1981), the time required to segment the image is dependent on the image size. Hence, MFCM performs clustering on the basis of gray level histogram instead of pixels in the image as the number of gray levels is less than the number of pixels in the image.

The clustering algorithm converges to a local minimum if the centers are randomly initialized and the minimal amount of improvement (e) is not small enough to allow improvements in the center positions. Hence, we initialized the cluster centers with the gray levels corresponding to four peaks in the histogram and used $e = 10^{-7}$ as the minimal amount of improvement. The weights in the membership matrix are initialized based on the distance of the gray levels to initial centers. The proposed MFCM clustering algorithm also contains an effective objective function to partition the given data into desired number of clusters such that intra-cluster distance is minimized and inter-cluster distance is maximized.

The complete steps of MFCM clustering are given in Algorithm 3.1. The MFCM clustering algorithm begins with the initialization of its parameters, such as degree of fuzziness (m) and tolerance value (e). Next, the four cluster centers (v_i) are initialized using gray levels corresponding to four peaks in the histogram of the brain region. Then, membership weight (u_{ig}) is assigned to each gray level based on its distance from cluster centers and the weights are stored in membership matrix (u). Finally, the objective function (J) is computed based on the inter-cluster distance and intra-cluster distance. If the difference between the objective function of the current

iteration and that of the previous iteration is less than the tolerance value, then the algorithm stops. Otherwise, the process is repeated with the new cluster centers and membership matrix.

Algorithm 3.1 MFCM

Input: MRI image and No. of clusters (c).
Output: Clusters in the MRI image.

1: Compute histogram of an image I of size $M \times N$ using Equation (3.3).
2: Initialize parameters required for fuzzy clustering.
Degree of fuzziness: $m = 2$; Tolerance value: $e = 10^{-7}$;
Iteration: $l = 1$;
Initialize the c cluster centers $(v_i, i = 1, .., c)$ using gray levels corresponding to c peaks identified by histogram analysis.
3: Initialize the membership matrix u.

$$u_{ig} = \frac{1}{\sum_{k=1}^{c} \left(\frac{||g - v_i||}{||g - v_k||} \right)^{\frac{2}{m-1}}} \tag{3.4}$$

4: Compute the objective function J.

$$J^{(l)} = \sum_{i=1}^{c} \sum_{g=0}^{L-1} u_{ig}^{m} h(g) ||g - v_i||^2 - \frac{1}{c(c-1)} \sum_{i=1}^{c} \sum_{k=1}^{c} ||v_i - v_k||^2. \tag{3.5}$$

5: Check for convergence: If $|J^{(l)} - J^{(l-1)}| < e$ then STOP;
Else $l = l + 1$.
6: Compute new cluster centers.

$$v_i = \frac{\sum_{g=0}^{L-1} h(g) u_{ig}^{m} g}{\sum_{g=0}^{L-1} h(g) u_{ig}^{m}}. \tag{3.6}$$

7: Compute new membership matrix using Equation (3.4) and go to step (4).

The four clusters obtained by the application of MFCM clustering on the T2-weighted MRI image are shown in Figure 3.6. The tumor shows higher intensity compared to WM, GM and CSF. Hence, the highest cluster center value indicates the presence of abnormal region in the corresponding cluster.

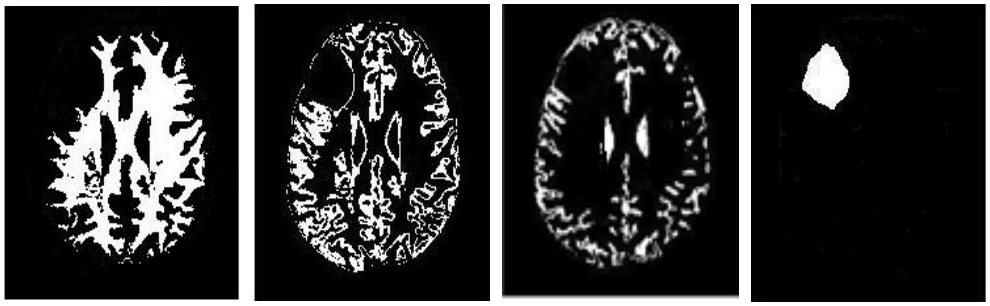

Figure 3.6: Clusters of Brain in T2-weighted MRI Image: (a) White Matter (b) Gray Matter (c) Cerebrospinal Fluid (d) Abnormal Region

Tumor and Edema Separation

Once the abnormal region is identified on the T2-weighted MRI image, a test is carried out to identify the presence of edema. This is because the tumor may not be surrounded by edema in all cases. Edema is the swelling of the brain tissue surrounding the tumor mass and the separation of the tumor from edema is necessary for diagnosis and treatment planning. The presence of edema is identified by determining the number of clusters in the abnormal region based on the histogram analysis of abnormal region (Castro et al. 2007). If it contains two peaks, then it means that the tumor is associated with edema on T2-weighted MRI image. Hence, the abnormal region is partitioned into two clusters (tumor and edema) using MFCM clustering. Edema when present, exhibits higher intensity than tumor on T2-weighted MRI image. Hence, the tumor is segmented by retaining only the pixels in the cluster whose center value is lower than the other cluster center value.

3.1.4 Experimental Results and Discussion

In order to evaluate the performance of the proposed brain tumor segmentation method, the following experiments are carried out on T1-weighted post-contrast and T2-weighted brain MRI images of 550 patients (female: 246, male: 304). Among 550 patients, 280 patients were diagnosed with benign tumor and 270 patients with malignant tumor based on histopathological analysis of biopsy samples. The detailed description of the brain tumor dataset is already given in Section 2.8.

Rotation Correction Results

In order to test the effectiveness of the rotation correction technique, some of the images in the dataset are rotated by 10^o, 15^o, 20^o, and 25^o in the clockwise and anti-clockwise directions. In the preprocessing stage, the misaligned images are corrected using inverse mapping and bicubic interpolation. Table 3.1 shows the difference between the original MRI images (images in a standard position) and the rotation corrected MRI images based on three interpolation methods: bicubic (Keys 1981), bilinear, and nearest neighbor (Gonzalez and Woods 2009). The difference between the original image and the rotation corrected image is measured by computing relative error, which is given by,

$$RelativeError(RE) = \frac{|N_r - N_o|}{N_o} \times 100 \tag{3.7}$$

where, N_o represents the number of pixels in the brain region of the original image and N_r represents the number of corresponding pixels occupied by brain region on the rotation corrected image.

Table 3.1: Performance Comparison of Interpolation Methods

Rotation Angle	**Average Relative Error(%)**		
	Nearest Neighbor	**Bilinear**	**Bicubic**
-10^0	1.36	0.98	0.00
-15^0	2.73	0.76	0.00
-20^0	2.98	1.13	0.00
-25^0	4.15	1.20	0.01
10^0	1.28	0.71	0.00
15^0	3.01	1.02	0.00
20^0	4.00	2.08	0.01
25^0	4.55	2.11	0.02

The nearest neighbor interpolation takes the intensity of the closest pixel as the intensity of new pixel and it shows least effectiveness in rotation correction with RE higher than 2% for most of the rotation angles. The bilinear interpolation considers

the 4 neighbors to estimate the intensity of a pixel and it shows the moderate effectiveness, whereas with the bicubic interpolation original image and rotation corrected image are considered similar ($RE = 0.00\%$) for most of the rotation angles. Hence, the bicubic interpolation is used in the proposed rotation correction technique.

Segmentation Results

After preprocessing, the brain tumor is segmented on the MRI image using the proposed segmentation technique based on MFCM clustering. The proposed segmentation technique is able to perfectly distinguish between normal and abnormal slices of the brain in all the cases. After identifying the abnormal slice, the tumor region is extracted. Figure 3.7 shows the segmentation results of some of the brain tumor cases in the dataset. Figure 3.7(a) shows the original T2-weighted MRI images. Images in

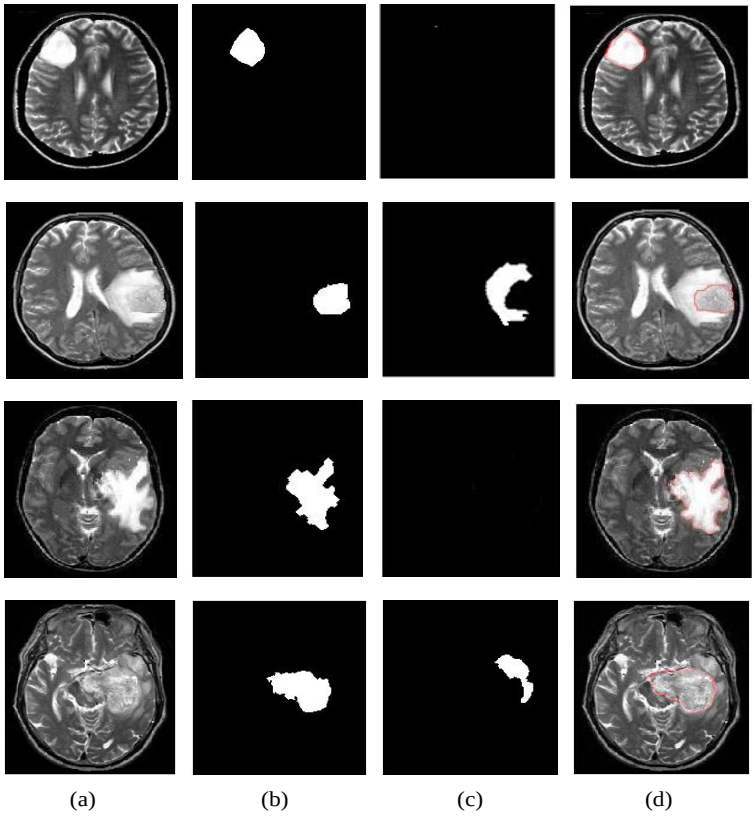

Figure 3.7: Results of Brain Tumor Segmentation on the MRI Image (a) T2-Weighted Brain MRI Image (b) Brain Tumor (c) Edema (d) Boundary of Brain Tumor on the MRI Image

the first and third row do not contain edema, whereas the images in a second and fourth row contain tumor along with edema. Figure 3.7(b) and Figure 3.7(c) shows the separation of the tumor and edema, respectively. The boundary of the segmented tumor is marked on the original image using 4-connected neighbors as shown in Figure 3.7(d).

The evaluation of the brain tumor segmentation results is performed through a quantitative comparison with the results of a manual segmentation (gold standard). The manual segmentation of brain tumor is carried out by two experienced (R1 and R2) and two inexperienced (R3 and R4) radiologists. The purpose of comparison of the segmentation results with inexperienced radiologists is to show that the accuracy of segmentation depends on radiologist's experience. Let M be the manually segmented tumor and A be the automatically segmented tumor by the proposed segmentation technique. A set of three VALMET measures (Gerig et al. 2001) is used to evaluate the segmentation results and the description of these measures is given as follows:

Volume Overlap:
It measures the extent of overlap between two segmented regions and it is computed using Equation (3.8).

$$\text{Volume Overlap}(VO) = \frac{A \cap M}{A \cup M} \times 100 \tag{3.8}$$

Hausdorff Distance:
The Hausdorff distance H_{am}, between two sets of points A and M can be obtained in two steps. First, for each point in A, the minimum distance to all points in M is obtained, and then maximum of this set of minimum distances is computed. The minimum distance for the i^{th} surface voxel in A to the set of surface voxels in M is d_i^{am} and H_{am} is the maximum value of the surface distance of all n_a surface voxels in A (Equation (3.9)). The Hausdorff distance, HD, is the maximum of the directed form for $A \rightarrow M$ and $M \rightarrow A$ (Equation (3.10)).

$$H_{am} = max(d_i^{am}), i = 1....n_a \tag{3.9}$$

$$HD = max(H_{am}, H_{ma}) \tag{3.10}$$

Symmetric Mean Absolute Surface Distance:
The symmetric mean absolute surface distance estimates the error between the surface of A and M using distances between their surface voxels. The surface distance of the i^{th} surface voxel on A (d_i^{am}) is the distance to the closest voxel on M. The symmetric mean absolute surface distance, SMD, is the mean of the absolute values of the surface distance from A and M as given in Equation (3.11).

$$SMD_{am} = \frac{1}{n_a + n_m}\left(\sum_{i=1}^{n_a} |d_i^{am}| + \sum_{j=1}^{n_m} |d_j^{ma}|\right) \tag{3.11}$$

The segmentation was performed on all 550 cases but for simplicity only 10 cases are shown in the following tables. The inter-rater variability is demonstrated by comparing radiologists' segmentation results as shown in Table 3.2.

Table 3.2: Comparison of Brain Tumor Segmentation Results of Expert Radiologists

Cases	**R1 vs.R2**		
	VO(%)	**HD(mm)**	**SMD(mm)**
1	100	0	0
2	100	0	0
3	99.86	0.53	0.16
4	100	0	0
5	100	0	0
6	100	0	0
7	99.73	0.77	0.21
8	100	0	0
9	100	0	0
10	100	0	0
Mean	99.81	0.004	0.001

The mean values of VALMET measures shown are computed by taking average over all 550 cases. Cases 1-5 contain tumor, whereas cases 6-10 contain tumor along with edema. The segmentation results of experienced radiologists R1 and R2 are almost similar due to their expertise in the segmentation of tumor. The radiologists

R1 and R2 have several years of experience in interpreting brain MRI images and hence results are similar ($VO = 100\%, HD = 0\ mm, SMD = 0\ mm$) in most of the cases. However, R1 and R2 have showed small differences (e.g., Case 3, $VO = 99.86\%, HD = 0.53\ mm, SMD = 0.16\ mm$) in segmenting the tumor, when the boundary of tumor was not clear on the MRI image.

Further, the results of R1 are compared with the inexperienced radiologists R3 and R4 as shown in Table 3.3. The segmentation results of R3 showed overall mean values of $VO = 75.68\%, HD = 13.82\,mm, SMD = 1.69\,mm$, and the segmentation results of R4 showed overall mean values of $VO = 70.63\%, HD = 16.77\ mm, SMD = 1.63\,mm$. It is observed that manual segmentation results depend on the experience of the radiologist.

Table 3.3: Comparison of Brain Tumor Segmentation Results of Experienced (R1) and Inexperienced Radiologists

Cases	**R1 vs. R3**			**R1 vs. R4**		
	VO(%)	**HD(mm)**	**SMD(mm)**	**VO(%)**	**HD(mm)**	**SMD(mm)**
1	82.31	15.12	1.62	79.71	11.36	1.44
2	80.64	16.38	1.64	83.25	14.78	1.73
3	70.21	9.35	1.87	70.69	8.49	1.98
4	78.83	17.85	1.78	76.07	15.41	1.66
5	85.16	8.50	1.58	84.27	8.07	1.54
6	79.96	12.31	1.50	70.81	15.67	1.80
7	65.79	13.11	1.83	59.34	13.05	1.58
8	69.66	10.73	1.87	72.58	9.40	1.76
9	68.20	12.80	1.75	68.06	11.89	1.73
10	57.96	18.93	1.67	53.93	19.26	1.69
Mean	75.68	13.82	1.69	70.63	16.77	1.63

Table 3.4 shows the comparison of the segmentation results of R2 with inexperienced radiologist R3 and R4. The segmentation results of R3 showed overall mean values of $VO = 73.81\%, HD = 14.51\ mm, SMD = 1.68\ mm$, and the segmentation results of R4 showed overall mean values of $VO = 71.43\%, HD = 14.83\ mm, SMD =$

1.60 mm. This shows that segmentation results of inexperienced radiologists did not match well with the expert radiologist's results. Also, the level of agreement between experienced and inexperienced radiologists for cases which contain tumor along with edema is lower than cases that contain only tumor. This is mainly due to the ambiguity in determining the edema boundary on MRI images.

Table 3.4: Comparison of Brain Tumor Segmentation Results of Experienced (R2) and Inexperienced Radiologists

Cases	**R2 vs. R3**			**R2 vs. R4**		
	VO(%)	**HD(mm)**	**SMD(mm)**	**VO(%)**	**HD(mm)**	**SMD(mm)**
1	82.31	15.12	1.62	79.71	11.36	1.44
2	80.64	16.38	1.64	83.25	14.78	1.73
3	71.52	9.20	1.83	72.01	8.52	1.91
4	78.83	17.85	1.78	76.07	15.41	1.66
5	85.16	8.50	1.58	84.27	8.07	1.54
6	79.96	12.31	1.50	70.81	15.67	1.80
7	63.80	14.23	1.88	61.76	12.92	1.51
8	69.66	10.73	1.87	72.58	9.40	1.76
9	68.20	12.80	1.75	68.06	11.89	1.73
10	57.96	18.93	1.67	53.93	19.26	1.69
Mean	73.81	14.51	1.68	71.43	14.83	1.60

The quantitative results obtained by comparing the proposed automatic segmentation (AS) with the manual segmentation performed by expert radiologists R1 and R2 are provided in Table 3.5. The mean values of VALMET measures shown in Table 3.5 are computed by taking average over all 550 cases. The results of automatic segmentation provide a good match with the expert radiologists' results. For the overlap measure, all values are greater than 95% and the distance based evaluations also show good performance in all the cases. The proposed segmentation method showed overall mean values of $VO = 98.24\%, HD = 1.37\ mm, SMD = 0.38\ mm$, when evaluated with the R1's segmentation results and $VO = 98.38\%, HD = 1.32\ mm, SMD = 0.34\ mm$, when evaluated with the R2's segmentation results.

Table 3.5: Comparison of Automatic and Manual Segmentations of Brain Tumor

Cases	**AS vs. R1**			**AS vs. R2**		
	VO(%)	**HD(mm)**	**SMD(mm)**	**VO(%)**	**HD(mm)**	**SMD(mm)**
1	97.57	1.68	0.42	97.57	1.68	0.42
2	99.05	1.13	0.27	99.05	1.13	0.27
3	98.56	1.26	0.36	98.75	1.22	0.31
4	96.82	2.13	0.50	96.82	2.13	0.50
5	99.43	1.08	0.25	99.43	1.08	0.25
6	95.03	2.96	0.64	95.03	2.96	0.64
7	96.15	2.28	0.57	96.31	2.23	0.55
8	97.18	1.78	0.45	97.18	1.78	0.45
9	96.45	2.21	0.52	96.45	2.21	0.52
10	95.26	2.21	0.50	95.26	2.21	0.50
Mean	98.24	1.37	0.38	98.38	1.32	0.34

In order to evaluate the performance of the proposed MFCM clustering in tumor segmentation, its efficiency and cluster validity are measured in terms of run time and Davies-Bouldin (DB) index (Davies and Bouldin 1979). The details of the performance evaluations are given as follows:

Time Complexity

The MFCM clustering algorithm partitions the given image into different clusters based on the gray levels in the image histogram. Let G be the number of gray levels in the image histogram, C be the number of clusters required, and I be the number of iterations required by the MFCM algorithm to converge. The basic operation of the MFCM clustering algorithm is calculating the membership weights and cluster centers. These operations take constant amount of time and hence, the time complexity of the MFCM algorithm is based on the number of times these basic operations are executed for I iterations, C clusters and G gray levels. Accordingly, the time

complexity of the MFCM clustering algorithm is given by,

$$T = \sum_{i=1}^{I} \sum_{j=1}^{C} \sum_{k=1}^{G} 1 \tag{3.12}$$

The Equation (3.12) is solved by applying the summation rules as follows:

$$\begin{aligned} T &= \sum_{i=1}^{I} \sum_{j=1}^{C} G - 1 + 1 \\ &= \sum_{i=1}^{I} (C - 1 + 1)(G) \\ &= ICG \end{aligned} \tag{3.13}$$

Hence, the time complexity of the MFCM algorithm is $O(ICG)$ and the algorithm takes about 1.12 sec to cluster the given MRI image.

Cluster Validity

The clusters resulting from MFCM algorithm are validated based on the Davies-Bouldin index, which is defined as the ratio of the sum of within-cluster scatter (intra-cluster) to between-cluster separation (inter-cluster) and is computed by,

$$DB = \frac{1}{C} \sum_{i=1}^{C} \max_{i \neq l} \left\{ \frac{d_w(v_i) + d_w(v_l)}{d_b(v_i, v_l)} \right\} \tag{3.14}$$

where, C is the number of clusters, $d_w(v_i)$ is the average distance of all elements in the cluster i to their cluster center v_i, $d_w(v_l)$ is the average distance of all elements in the cluster l to their cluster center v_l, and $d_b(v_i, v_l)$ is the distance between cluster centers v_i and v_l. The clustering algorithm that minimizes the DB index value is considered as the best algorithm. The validation of the clustering results of MFCM algorithm showed an average DB value of 0.62.

Comparison with the Existing Methods

Table 3.6 shows the performance comparison of the MFCM clustering algorithm with the following existing FCM algorithms.

- Conventional FCM proposed by Bezdek (1981).
- Fast FCM (FFCM) proposed by Al-Zoubi et al. (2007).
- Effective FCM (EFCM) proposed by Hemanth et al. (2009).

Table 3.6: Performance Comparison of Fuzzy Clustering Algorithms

FCM Methods	**Time Complexity**	**Time (sec)**	**DB Index**
FCM	$O(ICN)$	47.15	0.94
FFCM	$O(ICK) + O(TN)$	24.98	1.13
EFCM	$O(ICM) + O(FN)$	5.34	0.97
MFCM	$O(ICG)$	1.12	0.62

Where, N: Number of pixels in the image, K: Number of pixels selected based on threshold, T: Number of iterations required to select the threshold, M: Number of pixels selected based on features, and F: Number of features selected.

The conventional FCM algorithm takes more time (47.15 sec), since it is dependent on the number of pixels in the image. The FFCM and EFCM clustering algorithms improve the efficiency of the conventional FCM algorithm by reducing the amount of input data. However, the efficiency improvement provided by FFCM (24.98 sec) and EFCM (5.34 sec) is not better than the proposed MFCM algorithm (1.12 sec). This is because the FFCM and EFCM reduce the input data based on the manually selected threshold and the features extracted from the image, respectively. Whereas the MFCM algorithm clusters the image based on the number of gray levels in the image histogram and hence consumes less time for clustering.

Further, the FFCM algorithm reduces the dataset by eliminating all those points with membership weight less than the threshold and hence shows poor clustering results ($DB = 1.13$). The EFCM algorithm aggregate data points in the homogeneous areas of the image and hence its clustering results ($DB = 0.97$) do not deviate from the FCM results ($DB = 0.94$). However, in FCM, FFCM and EFCM algorithms the cluster centers are initialized manually and hence it affects the effectiveness of the clustering results. Whereas, the MFCM clustering algorithm automatically initializes the cluster centers and also focuses on maximizing the inter-cluster distance and minimizing the intra-cluster distance, and hence it gives better clustering results ($DB = 0.62$) when compared to other methods.

3.2 Liver Tumor Segmentation Using Automatic Region Growing

The region growing algorithm (Adams and Bischof 1994) is well suited for segmentation of abdominal CT image as it provides thin and well connected borders of the region. But, the region growing algorithm is semi-automatic, since it requires the manual selection of seed point and threshold (Venkatachalam et al. 2004; Qi et al. 2008) and thus, it needs a lot of time to arrive at accurate results. Though some existing methods (Poonguzhali and Ravindran 2006; Wu et al. 2009) automate the region growing algorithm, they are not computationally efficient. In order to overcome these drawbacks, in the present research work, an automatic region growing algorithm is proposed for segmentation of the liver tumor on abdominal CT image.

3.2.1 Proposed Methodology

The framework of the proposed liver tumor segmentation technique is shown in Figure 3.8. It consists of three phases, namely preprocessing, liver segmentation, and liver tumor segmentation.

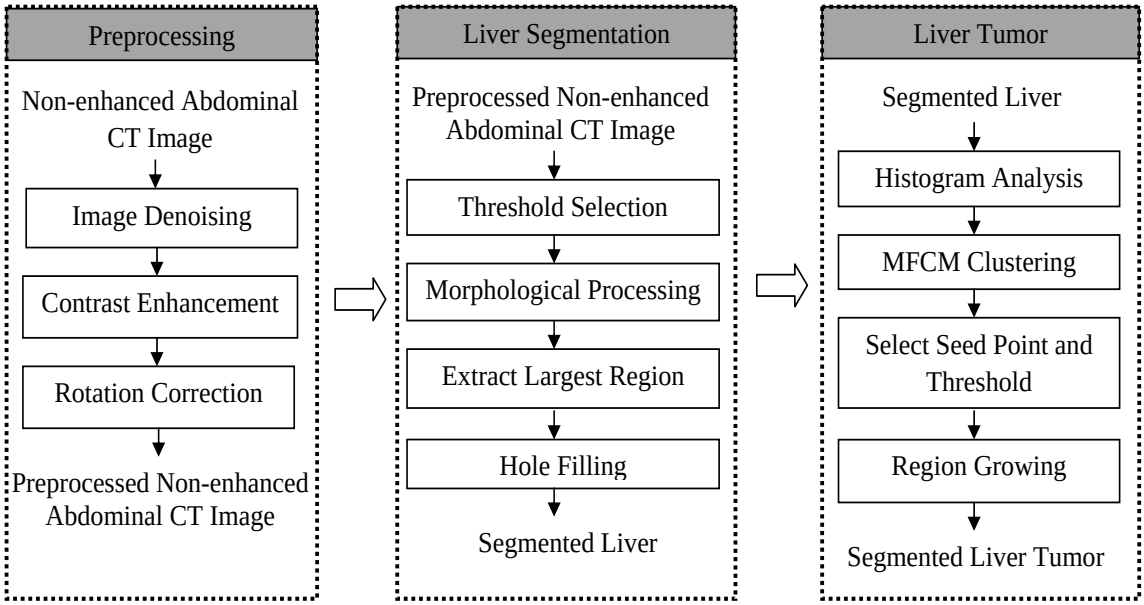

Figure 3.8: Framework of the Proposed Liver Tumor Segmentation Technique

The preprocessing phase improves quality of the input non-contrast-enhanced abdominal CT image by image denoising, contrast enhancement, and rotation correction techniques. Next, in the liver segmentation phase, liver region is extracted from the abdominal CT image based on adaptive thresholding and morphological processing. Finally, in the liver tumor segmentation phase, the histogram of the liver segmented CT image is analyzed to determine whether the liver is normal (without tumor) or abnormal (with tumor). If the liver is abnormal, then the liver tumor is segmented using the proposed automatic region growing algorithm, which selects the seed point and threshold value based on the Modified Fuzzy C-Means (MFCM) clustering algorithm.

3.2.2 Preprocessing

Similar to brain MRI image, the abdominal CT image of the liver is also preprocessed to improve the quality of the image. The noise is eliminated from the abdominal CT image using 3×3 median filter (Burger and Burge 2008) and 3×3 Laplacian filter with unsharp masking (Bourne 2010). Next, the image contrast is enhanced by applying histogram equalization. The patient's movement during CT image acquisition may lead to misalignment of the image. Hence, in order to correct the rotation of the CT image, the orientation of the CT image is determined by measuring the orientation of its minor axis with the reference x-axis. Then, based on the orientation angle (θ), the rotation correction angle ($\theta' = 90 - \theta$) is computed. The misaligned image is restored to its standard position using inverse mapping and bicubic interpolation (Arpitha et al. 2010) as discussed in Section 3.1.2.

3.2.3 Liver and Tumor Segmentation

After preprocessing step, the liver is segmented on the abdominal CT image by extracting the pixel intensities in the liver region and thereby, eliminating organs adjacent to the liver. Then, the liver tumor is segmented on the extracted liver region. The various steps for liver and tumor segmentation on the abdominal CT image are detailed below.

Liver Segmentation

The various steps of liver segmentation such as thresholding, morphological processing, largest region extraction and hole filling are explained as follows:

Thresholding: Liver occupies the largest region in the abdominal CT image as shown in Figure 3.9(a). Thus, the highest peak of the image histogram excluding background and bone values represents the mean intensity of the liver region as shown in Figure 3.9(b).

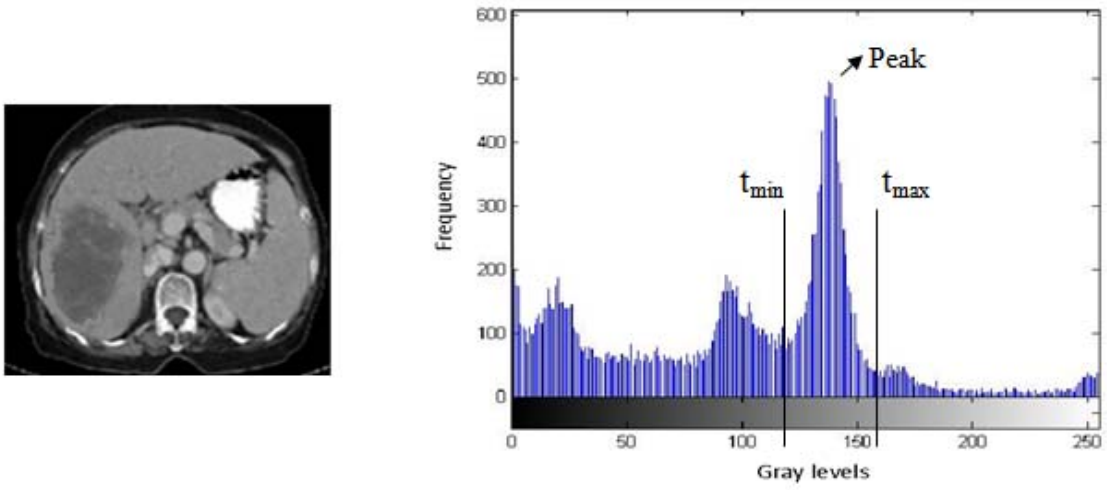

(a) (b)

Figure 3.9: Computation of Intensity Range of the Liver (a) Abdominal CT Image (b) Histogram of the Abdominal CT Image

Then, based on the identified peak, an intensity threshold is selected adaptively by including certain margin within the intensity range of the liver region as shown in Figure 3.9(b). The intensity threshold is defined by,

$$\text{Intensity Threshold}(T) = [t_{min}, t_{max}] \tag{3.15}$$

where, t_{min} and t_{max} are the two valleys of the liver region and they represent the minimum and maximum intensity of the liver region. After selecting the intensity threshold, the abdominal CT image (Figure 3.10(a)) is thresholded to extract the

pixels in the liver region as given below.

$$I(x,y) = \begin{cases} 1 & \text{if } t_{min} \leq I(x,y) \leq t_{max} \\ 0 & \text{otherwise} \end{cases} \tag{3.16}$$

Where, $I(x,y)$ is the intensity value of the pixel at location (x,y). The thresholded image consists of liver, and other organs having intensity similar to that of liver. The extracted regions contain small gaps and narrow bridges as shown in Figure 3.10(b).

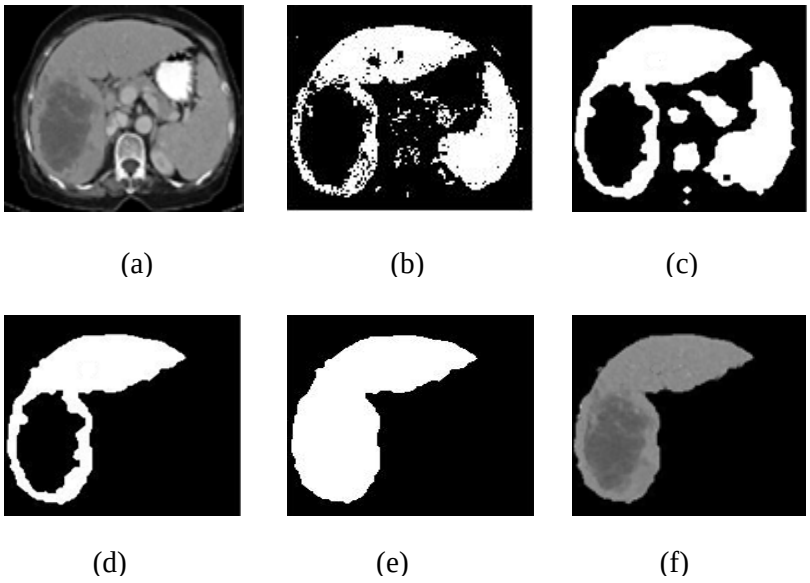

Figure 3.10: Liver Segmentation (a) Abdominal CT Image (b) Thresholding (c) Morphological Processing (d) Largest Region Extracted (e) Hole Filling (f) Segmented Liver

Morphological Processing: In order to preserve the structure of the extracted regions, the small gaps and narrow bridges are eliminated by applying morphological opening and closing operators (Gonzalez and Woods 2009) defined by Equation (3.17) and Equation (3.18), respectively. The effect of morphological processing is shown in Figure 3.10(c).

$$I \circ S = (I \ominus S) \oplus S \tag{3.17}$$

$$I \bullet S = (I \oplus S) \ominus S \tag{3.18}$$

Where, I is the threshold image and S is the structuring element. The symbols $\ominus$ and $\oplus$ are morphological dilation and erosion operators, respectively. The morphological opening operator smooths the contours, breaks narrow isthmuses, and eliminates thin protrusions in the image, whereas the morphological closing operator fuses narrow breaks and long thin gulfs, eliminates small holes, and fills gaps in the contours.

Largest Region Extraction: After morphological processing, the organs on the CT image which have the intensity similar to the liver's intensity are eliminated by retaining only the largest connected component as shown in Figure 3.10(d).

Hole Filling: The intensities of liver and tumor are different and thus the pixels of the tumor do not appear in the extracted liver region. Hence, the missed pixels create hole in the liver. In order to extract the complete region of the liver, the hole is filled by pixels with value 1 as shown in Figure 3.10(e). Finally, the resultant image is complemented and multiplied by the original abdominal CT image to obtain the segmented liver as shown in Figure 3.10(f).

Liver Tumor Segmentation

Before segmenting the liver tumor, a test is carried out to determine whether segmented liver is normal or abnormal based on the histogram analysis (Castro et al. 2007). If the liver is normal, then the histogram of the liver segmented CT image consists of two peaks corresponding to the liver and background, respectively. Otherwise, the liver segmented CT image consists of three peaks corresponding to the liver, tumor, and background, respectively. If the liver is normal, further processing of CT image is not required. Otherwise, the liver tumor is segmented on the abnormal liver using the proposed automatic region growing algorithm. The proposed algorithm combines the MFCM clustering algorithm with the region growing algorithm to automatically determine the seed point and threshold value as shown in Figure 3.11. Based on the seed point and a threshold value, certain modifications are made to the membership criteria of the conventional region growing algorithm.

First, the MFCM clustering algorithm (as discussed in Section 3.1) is applied to the abdominal CT image to partition the image into three clusters ($c = 3$), namely

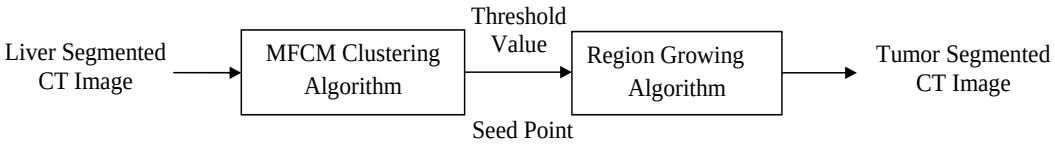

Figure 3.11: Automation of Region Growing Algorithm

tumor, liver and background. Next, the seed point and threshold value needed by the region growing algorithm are determined based on the tumor cluster. The value of the tumor cluster center is taken as the threshold (β) and the pixel in the tumor cluster with the gray level lower than β is taken as the seed point. Before proceeding with region growing, the gradient of the image is computed based on the sobel operator (Gonzalez and Woods 2009) to locate edges in the image and it is given by,

$$G_x = (z_7 + 2z_8 + z_9) - (z_1 + 2z_2 + z_3) \tag{3.19}$$

$$G_y = (z_3 + 2z_6 + z_9) - (z_1 + 2z_4 + z_7) \tag{3.20}$$

where, $|G_x + G_y|$ gives the gradient of the image $I(x, y)$ at location (x, y). For a 3×3 region around pixel (x, y), z_1, z_3, z_7 and z_9 are diagonal neighbors, z_4 and z_6 are the horizontal neighbors, and z_2 and z_8 are the vertical neighbors.

After finding the gradient, the region growing begins with the initial seed point and includes all neighborhood pixels satisfying the membership criteria of the region. Once, the pixel is included in the region, it becomes the new seed point for growing the region and this procedure is repeated until the boundary of the region is reached. The membership criteria for including a pixel in the region are based on the following intensity and gradient properties of the region: 1) The intensity values inside the tumor region are lower than the intensity values on the liver. 2) Edges of the tumor have gradient values higher than those in the middle of the tumor region.

Since, the initial seed pixel is chosen close to the center of the region, the gradient is low for the first few sets of pixels encountered during region growing. As the region growing approaches the edge, the gradient gets large. Since, edges found by the gradient are thick, pixels on the edges are included based on mean (μ) and standard deviation (σ) of the region. When a point of high gradient is reached, a check is made to determine whether the pixel's intensity is lower than the ($\mu - \sigma$). If the

pixel satisfies this condition, it is included in the region. Based on these concepts, the membership criteria for including the pixel in the region are given as follows:

- If the pixel has low gradient (less than 95% of the equalized histogram) and its gray value is less than or equal to the threshold, β.
- If the pixel has high gradient (more than or equal to 95% of the equalized histogram) and the gray level of the pixel is not more than $(\mu - \sigma)$.

The complete steps of the automatic region growing algorithm are given in Algorithm 3.2 (Automatic Region Growing).

Algorithm 3.2 Automatic Region Growing

Input: CT image, Tumor cluster, Tumor cluster center.
Output: CT image with segmented liver tumor

1: Take the value of tumor cluster as a threshold value, β.
2: Examine all the pixels in the tumor cluster and set the pixel with grey level value lower than β as the initial seed location, $p(x, y)$.
3: Calculate the gradient of the image using sobel operator.
4: Choose $N \times N$ neighborhood for the seed pixel.
5: Calculate the mean (μ), and the standard deviation(σ) of the region.

$$\mu = \frac{\sum_{i=1}^{n} k_i}{n} \tag{3.21}$$

$$\sigma = \sqrt{\frac{\sum_{i=1}^{n} (k_i - \mu)^2}{n - 1}} \tag{3.22}$$

Where, n is the total number of pixels in the region and k_i is the gray value of the i^{th} pixel.

6: Compare each neighbor pixel with the seed pixel. Add a pixel to the region if it is satisfies either one of the two criteria:

- If the gradient of the pixel is less than 95% of the equalized histogram and its gray value is less than or equal to the threshold, β.
- If the gradient of the pixel is more than or equal to 95% of the equalized histogram and the gray level of the pixel is not more than $(\mu - \sigma)$.

7: Set the neighbor pixel, which is added to the region, as the new seed location.
8: Repeat Steps 4 to 7 until the region cannot be grown.
9: Change the grey level of the pixel that cannot be grown with the value of 255 to mark the boundary of the tumor.

3.2.4 Experimental Results and Discussion

The performance of the proposed liver tumor segmentation technique is evaluated by carrying out the following experiments on non-contrast-enhanced abdominal CT images of 487 patients (female: 235, male: 252). Among 487 patients, 247 patients were diagnosed with benign tumor and 240 patients with malignant tumor based on histopathological analysis of biopsy samples. The detailed description of the liver tumor dataset is already given in Section 2.8.

Rotation Correction Results

In order to test the effectiveness of the rotation correction technique, some of the images in the dataset are rotated by 10^o, 15^o, 20^o, and 25^o in the clockwise and anti-clockwise directions. In the preprocessing stage, the misaligned images are corrected using inverse mapping and bicubic interpolation. Table 3.7 shows the difference between the original CT images (images in a standard position) and the rotation corrected CT images based on three interpolation methods: bicubic (Keys 1981), bilinear, and nearest neighbor (Gonzalez 2009). The difference between the original and the rotation corrected liver image is measured based on the relative error (Equation (3.7)). The nearest neighbor interpolation assigns the intensity of the closest pixel to

Table 3.7: Comparison of Interpolation Methods

Rotation Angle	**Average Relative Error (%)**		
	Nearest Neighbor	**Bilinear**	**Bicubic**
-10^0	1.25	0.84	0.00
-15^0	2.48	0.78	0.00
-20^0	3.67	1.46	0.00
-25^0	4.32	1.23	0.00
10^0	1.21	0.62	0.00
15^0	2.33	0.73	0.00
20^0	3.10	1.28	0.02
25^0	4.28	2.05	0.02

the new pixel and it shows least effectiveness in rotation correction with relative error higher than 2% for most of the rotation angles. The bilinear interpolation uses the 4 neighbors to estimate the intensity of a pixel and it shows the moderate effectiveness, whereas with the bicubic interpolation original image and rotation corrected image are considered similar ($Relativeerror = 0.00\%$) for most of the rotation angles, since it considerers 16 neighbors to estimate the intensity of a pixel. Hence, the bicubic interpolation is used in the proposed rotation correction technique.

Segmentation Results

After preprocessing, the liver tumor is segmented on the non-contrast-enhanced abdominal CT image using the proposed segmentation technique based on automatic region growing. The proposed segmentation technique was able to perfectly distinguish between normal and abnormal slices of the liver in all the cases. After identifying the abnormal slice, the tumor region is extracted. Figure 3.12 shows the segmentation results of some of the liver tumor cases in the dataset. Figure 3.12(a) shows the original abdominal CT image of the liver tumor.

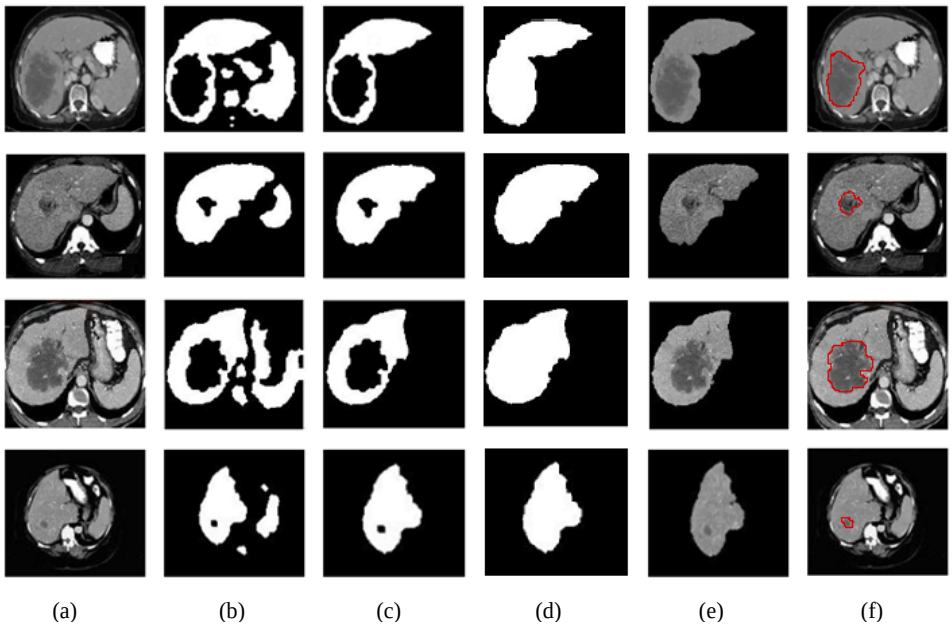

Figure 3.12: Results of Liver Tumor Segmentation on the CT Image (a) Abdominal CT Image (b) Morphological Processing (c) Largest Area Component (d) Hole filling (e) Segmented Liver (f) Segmented Liver Tumor

Pixel Intensities in the liver region are extracted by thresholding and morphological processing as shown in Figure 3.12(b). The other organs which are extracted along with the liver are eliminated by retaining only the largest region as shown in Figure 3.12(c). Next, the hole in the liver region is filled by the pixels with a value 1 in order to obtain the complete liver region as shown in Figure 3.12(d). Then, the image is complemented and multiplied with the original image to obtain segmented liver as shown in Figure 3.12(e). Next, the automatic region growing algorithm is applied on the segmented liver to obtain the tumor region as shown in Figure 3.12(f).

The results obtained by the proposed method are evaluated by comparing with manual segmentation results. The manual segmentation of liver tumor is carried out by two experienced (R1 and R2) and two inexperienced (R3 and R4) radiologists. The purpose of comparison of the segmentation results with inexperienced radiologists is to show that the accuracy of segmentation depends on radiologist's experience. In order to quantify the segmentation results, a set of three VALMET measures (Gerig et al. 2001) is used: Volume Overlap (VO), Hausdorff Distance (HD), and Symmetric Mean Absolute Surface Distance (SMD). The segmentation was performed on all 487 cases but for simplicity only 10 cases are shown in the following tables. The

Table 3.8: Comparison of Liver Tumor Segmentation Results of Expert Radiologists

Cases	**R1 vs.R2**		
	VO(%)	**HD(mm)**	**SMD(mm)**
1	99.89	0.48	0.15
2	100	0	0
3	100	0	0
4	100	0	0
5	100	0	0
6	99.65	0.82	0.24
7	100	0	0
8	99.81	0.58	0.20
9	100	0	0
10	100	0	0
Mean	99.76	0.006	0.002

inter-rater variability is shown in Table 3.8. The mean values of VALMET measures are computed by taking average over all 487 cases. The segmentation results of experienced radiologists R1 and R2 are almost similar due to their expertise in the segmentation of tumor. The radiologists R1 and R2 have several years of experience in interpreting liver CT images and hence their results are similar ($VO = 100\%, HD = 0\ mm, SMD = 0\ mm$) in most of the cases. However, R1 and R2 have showed small differences (e.g., case 1, $VO = 99.89\%, HD = 0.48\ mm, SMD = 0.15\ mm$) in segmenting the tumor when the boundary of the tumor was not clear on the image.

Further, the results of R1 are compared with inexperienced radiologists R3 and R4 as shown in Table 3.9. It can be observed that there is variation in the manual segmentation results, since the segmentation depends on the experience of the radiologist. The segmentation results of R3 showed overall mean values of $VO = 70.83\%, HD = 14.29\ mm, SMD = 1.66\ mm$ and the segmentation results of R4 showed overall mean values of $VO = 68.92\%, HD = 15.73\ mm, SMD = 1.61\ mm$.

Table 3.9: Comparison of Liver Tumor Segmentation Results of Experienced (R1) and Inexperienced Radiologists

Cases	**R1 vs. R3**			**R1 vs. R4**		
	VO(%)	**HD(mm)**	**SMD(mm)**	**VO(%)**	**HD(mm)**	**SMD(mm)**
1	76.52	11.45	1.74	74.18	10.19	1.71
2	76.38	9.40	1.51	78.26	9.21	1.47
3	81.94	11.82	1.40	82.47	10.38	1.35
4	70.51	8.43	1.86	67.51	9.10	1.80
5	68.73	8.02	1.58	65.44	7.83	1.49
6	54.17	17.24	1.63	58.65	13.46	1.60
7	80.64	10.02	1.42	73.49	9.82	1.40
8	60.02	14.03	1.89	61.73	13.20	1.93
9	58.46	13.17	1.46	55.28	15.58	1.74
10	71.45	10.39	1.45	70.89	11.64	1.52
Mean	70.83	14.29	1.66	68.92	15.73	1.61

Table 3.10 shows the comparison of the liver tumor segmentation results of R2 with inexperienced radiologists R3 and R4. The segmentation results of R3 showed overall mean values of $VO = 73.45\%, HD = 11.32\ mm, SMD = 1.52\ mm$ and the segmentation results of R4 showed overall mean values of $VO = 71.37\%, HD = 13.02\ mm, SMD = 1.57\ mm$. This shows that segmentation results of inexperienced radiologists did not match well with the expert radiologist's results.

Table 3.10: Comparison of Liver Tumor Segmentation Results of Experienced (R2) and Inexperienced Radiologists

Cases	**R2 vs. R3**			**R2 vs. R4**		
	VO(%)	**HD(mm)**	**SMD(mm)**	**VO(%)**	**HD(mm)**	**SMD(mm)**
1	79.83	10.48	1.68	80.02	10.16	1.64
2	76.38	9.40	1.51	78.26	9.21	1.47
3	81.94	11.82	1.40	82.47	10.38	1.35
4	70.51	8.43	1.86	67.51	9.10	1.80
5	68.73	8.02	1.58	65.44	7.83	1.49
6	60.89	15.51	1.60	61.73	15.08	1.63
7	80.64	10.02	1.42	73.49	9.82	1.40
8	64.58	12.45	1.78	68.08	11.43	1.62
9	58.46	13.17	1.46	55.28	15.58	1.74
10	71.45	10.39	1.45	70.89	11.64	1.52
Mean	73.45	11.32	1.52	71.37	13.02	1.57

The quantitative results obtained by comparing the proposed automatic segmentation (AS) with the manual segmentation performed by expert radiologists R1 and R2 are provided in Table 3.11. The mean values of VALMET measures shown in Table 3.11 are computed by taking average over all 487 cases. The results of automatic segmentation provide a good match with the expert radiologists' results. For the overlap measure, all values are greater than 94% and the distance based evaluations also show good performance in all the cases. The proposed liver tumor segmentation technique showed overall mean values of $VO = 96.89\%, HD = 1.52\ mm, SMD = 0.60\ mm$, when evaluated with the R1's segmentation results and

$VO = 96.95\%, HD = 1.46\ mm, SMD = 0.57\ mm$, when evaluated with the R2's segmentation results.

Table 3.11: Comparison of Automatic and Manual Segmentations of Liver Tumor

Cases	**AS vs. R1**			**AS vs. R2**		
	VO(%)	**HD(mm)**	**SMD(mm)**	**VO(%)**	**HD(mm)**	**SMD(mm)**
1	95.71	1.83	0.78	95.80	1.80	0.73
2	97.38	1.43	0.54	97.38	1.43	0.54
3	94.97	2.10	0.93	94.97	2.10	0.93
4	98.63	1.35	0.41	98.63	1.35	0.41
5	96.72	1.58	0.67	96.72	1.58	0.67
6	94.16	2.23	1.14	94.20	2.22	1.10
7	95.04	1.98	0.88	95.04	1.98	0.88
8	98.28	1.40	0.48	98.35	1.38	0.44
9	96.57	1.62	0.70	96.57	1.62	0.70
10	95.43	1.91	0.85	95.43	1.91	0.85
Mean	96.89	1.52	0.60	96.95	1.46	0.57

Time Complexity

The proposed automatic region growing algorithm for liver tumor segmentation combines MFCM clustering and region growing algorithm. The time complexity of MFCM clustering algorithm is O(ICG) as already discussed in Section 3.1.4. The region growing algorithm begins with initial seed point and includes the neighboring pixels satisfying the membership criteria into the region. The included pixels become new seed pixels and the procedure is repeated. Thus, the basic operation of the region growing algorithm is to check whether the pixel satisfies the membership criteria and this operation takes a constant amount of time. If the neighborhood size is $H \times W$, then the membership criteria are tested for each of the pixels in $H \times W$ neighborhood. This procedure is repeated for M pixels in the region, and hence the time complexity

of the automatic region growing algorithm is given by,

$$T = \sum_{i=1}^{M} \sum_{j=1}^{H} \sum_{k=1}^{W} 1 \tag{3.23}$$

The Equation (3.23) is solved by applying the summation rules as follows.

$$\begin{aligned} T &= \sum_{i=1}^{M} \sum_{j=1}^{H} W - 1 + 1 \\ &= \sum_{i=1}^{M} (H - 1 + 1)(W) \\ &= (M - 1 + 1)(HW) \\ &= MHW \end{aligned} \tag{3.24}$$

Hence, the time complexity of the automatic region growing algorithm is $O(ICG) + O(MHW)$ and the algorithm takes about 2.73 sec to segment the liver tumor on abdominal CT image.

Comparison with the Existing Methods

Table 3.12 shows the performance comparison of the proposed automatic region growing algorithm with the existing region growing algorithms for tumor segmentation.

Table 3.12: Performance Comparison of Region Growing Algorithms

Region Growing Methods	**Time Complexity**	**Time (sec)**
Venkatachalam's Method	$O(TMHW)$	720
Poonguzhali's Method	$O(MHW) + O(FN) + O(IN)$	14.03
Wu's Method	$O(MHW) + O(FN) + O(N^2)$	53.68
Proposed Method	$O(ICG) + O(MHW)$	2.73

- Venkatachalam's Method: semi-automatic region growing proposed by Venkatachalam et al. (2004).

- Poonguzhali's Method: Automatic region growing proposed by Poonguzhali and Ravindran (2006).
- Wu's Method: Automatic region growing proposed by Wu et al. (2009).

Where, T: Number of iterations required to obtain correct segmentation results, F: Number of features extracted, N: Number of pixels in the image, and I: Number of iterations required to select the threshold.

The Venkatachalam's method for liver tumor segmentation is based on the semi-automatic region growing algorithm and requires the manual input of seed point and threshold; thus, the method is computationally expensive (720 sec). The Wu's and Poonguzhali's methods automate the region growing algorithm based on the texture features, but do not show much improvement in the computational cost when compared to our method. The Wu's method selects the seed point based on texture features and performs two scans over the image to select the threshold, and for every threshold value the region growing is performed to check its effectiveness in segmentation; hence this algorithm has poor performance (53.68 sec). The Poonguzhali's method also selects the seed point based on texture features, but the threshold is selected based on iterative thresholding of the image and hence consumes more time (14.03 sec). The process of texture feature extraction in both the methods is much more complex than simple intensity features used in the proposed method. The proposed automatic region growing method is efficient (2.73 sec) when compared to other methods. This is because the proposed method selects the seed point and threshold based on the MFCM clustering algorithm, which is computationally efficient and performs clustering based on pixel intensities rather than texture features.

3.3 Summary

This chapter discussed the proposed automatic, effective and efficient brain and liver tumor detection techniques based on MFCM clustering and automatic region growing algorithms, respectively. The experimental results demonstrated that the tumor detection results obtained by the proposed techniques are close to the expert radiologists' results. The inter-observer agreement for experienced radiologists is 99.81% and 99.76% in the segmentation of brain and liver tumor, respectively; these values define the upper limit of segmentation accuracy. On the average, the automatically

segmented brain and liver tumors have more than 98% and 96% overlap with the segmentation results of the expert radiologists, respectively. This indicates that the results of the proposed segmentation technique are close to the upper limit. The proposed tumor detection techniques are also more efficient when compared to the existing methods. The proposed brain and liver tumor detection techniques take about 1.12 and 2.73 sec to detect the tumor on MRI and CT images, respectively. Hence, these techniques can assist the radiologist to accurately detect the tumor on medical images in less amount of time.

Chapter 4

Classification of Tumor on Medical Images

The proposed CAD system consists of tumor detection, classification, CBIR and 3D reconstruction methods for effective and efficient analysis of brain and liver tumors. The tumor classification determines the type of tumor as benign or malignant based on its features. The benign and malignant tumors differ by clinical behavior, prognosis and therapy; hence accurate classification of brain/liver tumors into benign or malignant category is necessary for optimal patient treatment. Therefore, in this chapter, an effective and efficient classification scheme for characterization of brain/liver tumor as benign or malignant is presented. Precisely, an attempt has been made to fulfill the second objective of the research work and to overcome the limitations of the existing tumor classification methods as discussed in Section 2.5. The research contributions towards developing an effective and efficient brain/liver tumor classification scheme are listed below:

- Tumor analysis by extracting significant features of the tumor such as shape, texture, and boundary characteristics.
- Selecting the most discriminating features by a two-level feature selection technique consisting of Information Gain (IG)-based feature ranking and Independent Component Analysis (ICA)-based feature selection methods.
- Improving the accuracy of tumor classification by developing an ensemble classifier consisting of heterogeneous classifiers, namely Support Vector Machine (SVM), Artificial Neural Network (ANN) and k-Nearest Neighbor (k-NN).

The details of the proposed tumor classification scheme incorporating the above contributions in identifying the type of brain/liver tumor as benign or malignant are given in the following sections.

4.1 Proposed Methodology

The proposed CAD system for characterization of brain/liver tumor contains various phases of the pattern recognition such as segmentation, feature extraction, feature selection and classification as shown in Figure 4.1.

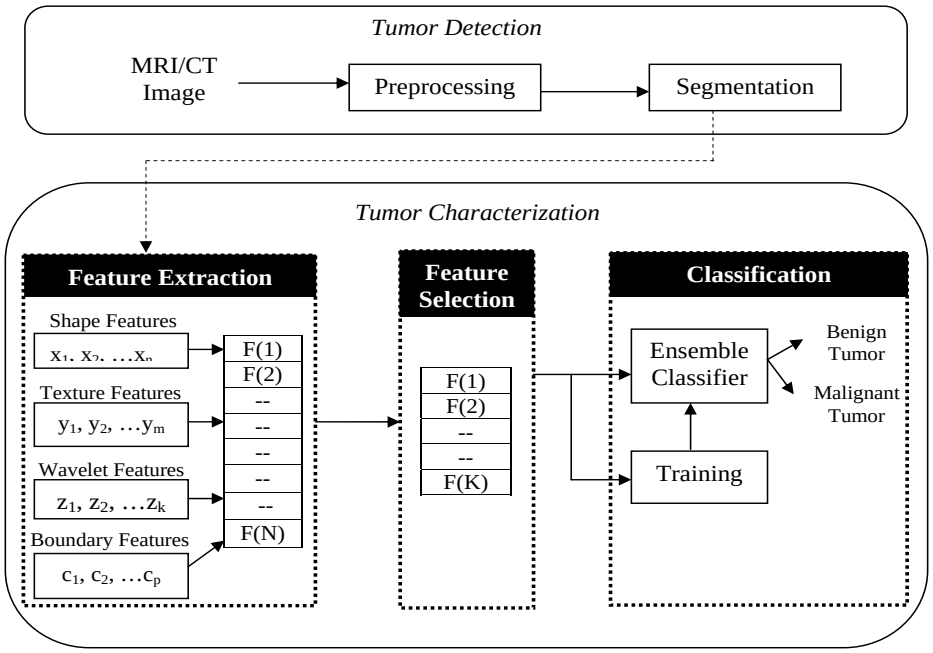

Figure 4.1: Framework of the Proposed CAD System for Characterization of Brain and Liver Tumors

In the first step, the input medical image is preprocessed to enhance its quality, and then the image is segmented to detect the tumor region using the proposed segmentation methods as discussed in Chapter 3. Next, the segmented tumor is represented by the feature vector consisting of various features of the tumor such as texture, shape and boundary characteristics. Then, the most discriminating features are derived from the high-dimensional feature vector using a two-level feature selection technique consisting IG-based feature ranking and ICA-based feature selection

methods. Finally, the selected features are fed to the ensemble classifier, which combines the output of SVM, ANN and k-NN classifiers to determine the class of the given tumor as benign or malignant.

4.1.1 Preprocessing

Prior to segmentation, the quality of MRI/CT images is enhanced by image denoising based on the median and Laplacian filters, image contrast enhancement using histogram equalization, and rotation correction of misaligned image using the proposed rotation correction technique. The T1-weighted and T2-weighted MRI images of the brain are co-registered using the FLIRT registration tool (Jenkinson and Smith 2001) as discussed in Chapter 3.

4.1.2 Segmentation

After preprocessing, the input image is segmented in order to extract the tumor region for further analysis. If the input image is the MRI image of the brain, then the image is segmented using the proposed brain tumor segmentation technique based on Modified Fuzzy C-Means (MFCM) clustering. If the input image is the abdominal CT image of the liver, then the image is segmented using the proposed liver tumor segmentation technique based on automatic region growing. The brain and liver tumor segmentation techniques are already discussed in Chapter 3.

4.1.3 Feature Extraction

The feature extraction step is used to describe characteristics of the segmented tumor by extracting its various features. In the present research, both 2D and 3D features are extracted from the tumor in order to evaluate their effectiveness in differentiating between benign and malignant tumors. Wavelets offer an inherent multi-resolution analysis that can help in representing the discriminating features at various scales. Hence, the tumor image is analyzed at three levels by decomposing the tumor image into four sub-bands (approximate, vertical, horizontal, and diagonal) using Haar wavelet. A set of 2D and 3D features such as shape, texture, and boundary characteristics are extracted from approximation and detail coefficients in each level of wavelet decomposition. Given a set of slices, the slice containing the largest cross-sectional

area of the tumor is chosen as a representative slice of the tumor, since it contains the maximum possible information of the tumor.

In case of brain tumor analysis, a representative slice is selected from both T1-weighted post-contrast and T2-weighted MRI images of the brain, and in case of liver tumor analysis, a representative slice is chosen from a set of non-contrast-enhanced abdominal CT images of the liver. Instead of processing all slices, a set of 2D features is extracted from a single representative slice in order to have a faster analysis of the tumor. 3D features are extracted from the 3D model of the tumor, which is developed by applying the marching cubes algorithm (Lorensen and Cline 1987) on a set of slices containing the tumor. The following set of features is extracted from the representative slice and 3D model of the tumor.

Shape Features

Benign tumors have more circular and regular shape when compared to malignant tumors, and hence tumor shape is one of the important features for discriminating between benign and malignant tumors. In the present work, tumor geometric parameters such as circularity, eccentricity, radial length and compactness are measured in order to identify the shape of the tumor (Mingqiang et al. 2008; Kassimi and El beqqali 2011) and the details are given below.

- *Circularity:* It is a gross shape descriptor measured using the area (A) and perimeter (P) of the tumor as given by,

$$Circularity = \frac{4\pi A}{P^2} \tag{4.1}$$

- *Radial Length:* It is computed as the Euclidian distance (d_i) from the tumor centre (x_c, y_c) to each of the boundary coordinates (x_i, y_i); the boundary is followed clockwise by 1^o increment as shown in Figure 4.2.

$$Radial\ Length = \frac{1}{N}\sum_{i=1}^{360} d_i, \tag{4.2}$$

  Where,

$$d_i = \sqrt{(x_i - x_c)^2 + (y_i - y_c)^2} \tag{4.3}$$

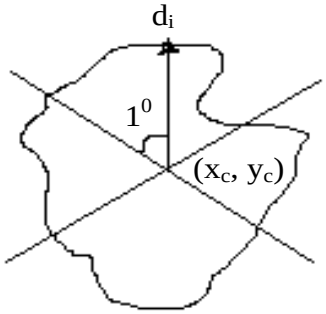

Figure 4.2: Computation of Radial Length

- *Eccentricity:* It is the ratio of the distance between the two foci ($f1$ and $f2$) to the length of the major axis (M).

$$Eccentricity = \frac{distance(f1, f2)}{length(M)}. \tag{4.4}$$

- *Compactness:* It determines the roundness of the tumor by measuring the amount of tumor outside the circular region, and it is computed using the perimeter (P) and area (A) of the tumor.

$$Compactness = \frac{P^2}{A} \tag{4.5}$$

Texture Features

Tissues have consistent and homogeneous texture along with the series of slices, and therefore the texture information can be used for tumor characterization. In the present research work, texture features are extracted using the first- and second-order statistics of the tumor region.

First-Order Statistics (FOS): It represents the texture based on the intensity level distribution in the image. In the experiment, five FOS-based texture features (average gray level, standard deviation, entropy, skewness, and kurtosis) are calculated from the histogram of the segmented tumor using the following equations (Akilandeswari et al. 2012):

$$Average\ Gray\ Level\text{: avg} = \sum_g gH(g) \tag{4.6}$$

$$\textit{Standard Deviation}\text{: std} = \sqrt{\sum_{g}(g - avg)^2 H(g)} \tag{4.7}$$

$$Entropy : ent = -\sum_{g} H(g)\ln(H(g)) \tag{4.8}$$

$$Skewness : skw = \frac{1}{std^3}\sum_{g}(g - avg)^3 H(g) \tag{4.9}$$

$$Kurtosis : kur = \frac{1}{std^4}\sum_{g}(g - avg)^4 H(g) - 3 \tag{4.10}$$

Where, g is the gray level value in the image and $H(g)$ is the number of the pixels in the image having gray level equal to g.

Second-Order Statistics (SOS): It represents the image texture based on the relative positions of the various intensity levels in the image. The texture characteristics which correspond to SOS are derived from the gray level co-occurrence matrix (GLCM) (Haralick et al. 1973). The elements of the GLCM represent the values of the probability density function P_{ij}, which counts the number of occurrences of pixel pairs having intensity values (i, j) and separated by a distance d along the direction θ. In case of the 2D image, four co-occurrence matrices are computed for each sub-band of wavelet decomposition by considering the inter-pixel distance of one, and four angular directions: $0^o, 45^o, 90^o$, and 135^o. In case of the 3D image, thirteen co-occurrence matrices (Showalter et al. 2005) are computed for each sub-band of wavelet decomposition by considering the inter-voxel distance of one, and thirteen angular directions: $(0^o, 0^o)$, $(45^o, 0^o)$, $(90^o, 0^o)$, $(135^o, 0^o)$, $(0^o, 45^o)$, $(0^o, 90^o)$, $(0^o, 135^o)$, $(90^o, 45^o)$, $(90^o, 135^o)$, $(45^o, 45^o)$, $(45^o, 135^o)$, $(135^o, 45^o)$, $(135^o, 135^o)$. Seven texture features corresponding to contrast, correlation, variance, entropy, homogeneity, cluster tendency, and inverse difference moment are extracted from each GLCM to represent the texture of the tumor using the following equations.

$$Contrast : cont = \sum_{n=0}^{N_g} n^2 \left\{ \sum_{i=1}^{N_g}\sum_{j=1}^{N_g} P_{ij} |i - j| = n \right\} \tag{4.11}$$

$$Correlation : corr = \frac{\sum_i \sum_j (ijP_{ij}) - \mu^2}{\sigma^2} \tag{4.12}$$

$$Variance : var = \sum_i \sum_j (ijP_{ij}) - \mu^2 \tag{4.13}$$

$$Entropy : ent = \sum_i \sum_j P_{ij} \ln P_{ij} \tag{4.14}$$

$$Homogeneity : hmg = \sum_i \sum_j \frac{P_{ij}}{1 + |i - j|} \tag{4.15}$$

$$Cluster\ Tendency : ctd = \sum_i \sum_j (i + j - 2\mu)P_{ij} \tag{4.16}$$

$$Inverse\ Difference\ Moment : idm = \sum_i \sum_j \frac{P_{ij}}{1 + (i - j)^2} \tag{4.17}$$

Where, P_{ij} is the $(i, j)^{th}$ element of GLCM, μ and σ are the mean and standard deviation of the GLCM, respectively, and N_g is the number of gray levels in the image. The texture information on each sub-band is represented by the average of each feature computed over different angles.

Wavelet Energy Features

The wavelet-based feature called wavelet energy reflects the energy distribution in different directions at different resolutions of the image, and thus it can effectively represent the tumor region characteristics. The wavelet energy is computed for each sub-band of the wavelet decomposed image (Jafari-Khouzani et al. 2004) and it is given by,

$$E = \frac{1}{M \times N} \sum_{i=1}^{M} \sum_{j=1}^{N} |W_{ij}| \tag{4.18}$$

where, W_{ij} is the wavelet coefficient and $M \times N$ is the size of the sub-band.

Boundary Features

The brain and liver tumors have distinct boundary characteristics (Wu et al. 2012); a typical benign tumor has a round and smooth boundary, whereas malignant tumor has a speculated and rough boundary as shown in Figure 4.3. In the present research, border irregularity of the tumor is described using fractal dimension (FD) (Iftekharuddin et al. 2003; Wu et al. 2010) as it helps in describing the geometric complexity of the objects, which do not fit into the Euclidian space and exhibit

(a) (b)

Figure 4.3: Tumor Boundary Characteristics: (a) Benign Tumor (b) Malignant Tumor

self-similarity at multiple scales. The Hausdorff-Besicovitch definition of FD is given below:

$$D_H = \lim_{r \to 0} \frac{\log(N(r))}{\log\left(\frac{1}{r}\right)} \tag{4.19}$$

where, $N(r)$ is the number of self similar pieces and $1/r$ is the magnification factor. The FD is estimated using the box counting method (Mandelbrot 1983), which partitions the image into boxes of equal size (r), and then counts the number of boxes(N) that contain at least one pixel of the region of interest (ROI); this process is repeated with different box sizes. The FD of the tumor is obtained from the slope of the best fitting straight line in the graph representing $log(N(r))$ versus $log(1/r)$ as shown in Figure 4.4.

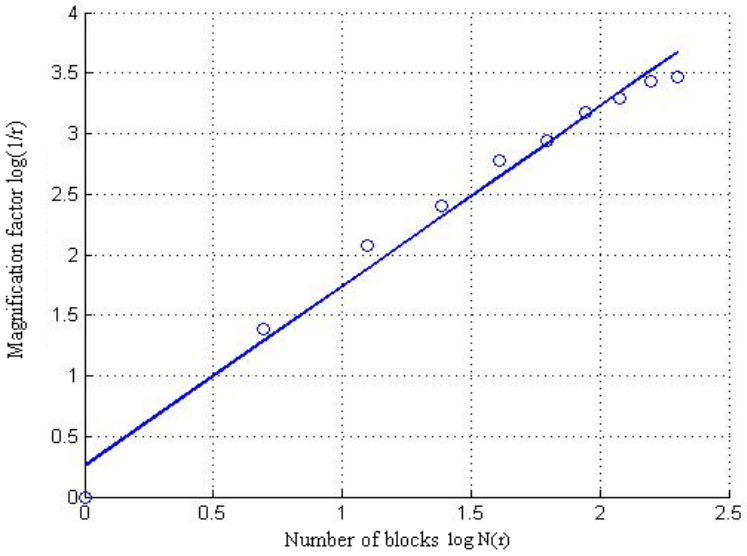

Figure 4.4: Fractal Dimension Analysis of Tumor

Table 4.1 shows the number of features extracted in each feature category from the representative slice of brain/liver tumor. In case of brain tumor analysis, a feature vector is formed by combining all features extracted from the representative slice of T1-weighted post-contrast and T2-weighted MRI images of the tumor. In case of liver tumor analysis, a feature vector is formed by extracting features from the representative slice of the non-contrast-enhanced abdominal CT images of the liver.

Table 4.1: Features of the Brain/Liver Tumor

Feature Category	**No. of Features Extracted**
Shape	48
Texture (FOS)	60
Texture (GLCM)	84
Wavelet Energy	12
Boundary	12

4.1.4 Two-Level Feature Selection

In order to improve the classification accuracy and efficiency, an optimal feature subset is selected from the original feature vector by applying a two-level feature selection technique consisting of feature ranking and feature selection methods. The feature ranking method computes a rank of each feature based on its discriminating power, and then top ranked features are retained to form a feature vector containing the most relevant features. On the contrary, the feature selection method focuses on selecting the non-redundant features of the feature set. Thus, the combination of feature ranking and feature selection results in the least number of features by eliminating both irrelevant and redundant features. This combination also improves the classification accuracy when compared to applying the feature selection method alone on the feature vector.

Feature Ranking Using Information Gain

In the first level of feature election, feature ranking is performed using the Information Gain (IG) method that selects a subset of features on the basis of the information

contribution related to the class variable. The information gain $IG(X|Y)$ of a given attribute Y with respect to the class attribute X quantifies the change in information entropy when the value of Y is revealed (Shang and Barnes 2010). The information gain of an attribute is computed using the following equation.

$$IG(X|Y) = H(X) - H(X|Y) \tag{4.20}$$

The information entropy H(X) measures the uncertainty about the value of X, and it is computed by,

$$H(X) = -\sum_{i} p(x_i) \log_2 p(x_i) \tag{4.21}$$

where, $p(x_i)$ is the prior probability of the i^{th} value of X. The conditional information entropy $H(X|Y)$ measures the value of X when the value of Y is known.

$$H(X|Y) = -\sum_{j} p(y_j) \sum_{i} (p(x_i|y_j) \log_2 p(x_i|y_j)) \tag{4.22}$$

The features that attain the highest IG value get the highest rank; thus, the features are arranged in the descending order according to their rank. A subset of M features is selected from the feature vector containing N features by choosing the top M features in the rank list. Based on the experiments, M is set to a value which results in the highest classification accuracy. However, redundant features may still exist in the selected features. Hence in the next level, statistically independent features are generated using ICA technique.

Feature Selection Using Independent Component Analysis

The Independent Component Analysis (ICA) transforms the original feature space into a set of statistically independent components, and thereby helps in finding hidden structure of the data. The basic ICA model can be expressed as follows (Hyvärinen 1999).

$$x = As \tag{4.23}$$

Where, $x = (x_1, ..., x_m)$ is the vector of observed features, which are assumed to be a linear combination of n independent features $s = (s_1, .., s_n)$ and A is the mixing matrix of dimension $m \times n$; Both A and s are unknown. The goal of ICA is to estimate independent components (ICs) from their mixture. In the present work, we

have adopted the FastICA algorithm proposed by Hyvärinen (1999) for estimating independent features.

The initial step of FastICA algorithm is whitening, where the feature vector x is linearly transformed to a vector $z = Ux$ such that its components are mutually uncorrelated and have unit variance. This linear transformation is accomplished by Principal Component Analysis (PCA) based on the eigenvalue decomposition of the covariance matrix $E\{xx^T\}$ as given below:

$$E\{xx^T\} = EDE^T \tag{4.24}$$

where, E is the orthogonal matrix of eigenvectors of $E\{xx^T\}$ and D is the diagonal matrix of its eigenvalues, $D = diag(d1, ..., d_n)$. The linear transformation matrix U is computed using the following equation.

$$U = ED^{-1/2}E^T \tag{4.25}$$

After the linear transformation, the feature vector z is represented as:

$$z = Ux = UAs = Bs \tag{4.26}$$

where, the matrix $B = UA$ is orthogonal. In the next step, independent components are estimated from the feature vector z by finding matrix W such that:

$$s = Wz \tag{4.27}$$

If $W = B^{-1}$, then the recovered features are exactly the original features s. W is estimated from the data such that the statistical independence of the estimated features is maximized using kurtosis as the non-Gaussian criterion. Thereby, feature vectors representing the tumor characteristics are projected onto independent components. Finally, the most important ICs are selected using the FS_ICA algorithm proposed by Prasad et al. (2008). Since, the absolute value of kurtosis indicates a degree of independence, the FS_ICA algorithm orders the ICs according to the absolute value of kurtosis and retains those components that have the largest absolute value of kurtosis.

4.1.5 Ensemble Classifier

Although the SVM has been proposed by Vapnik (2005) to provide a good generalization performance, the classification result of the practically implemented SVM has been often far from the theoretically expected level because their implementations are based on approximated algorithms (Kim et al. 2003). Thus, to overcome the limited generalization performance of a single classifier, we use the ensemble classifier which combines the decision of multiple classifiers to predict the class of the given brain/liver tumor as benign or malignant as shown in Figure 4.5.

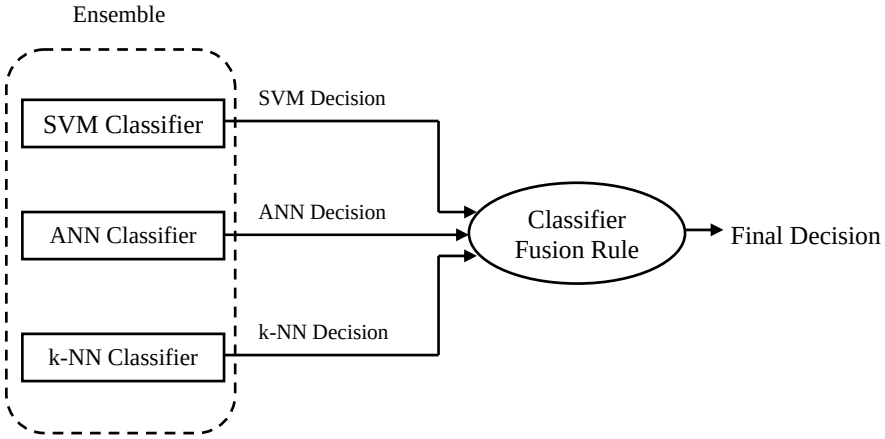

Figure 4.5: Framework of Ensemble Classifier

The fusion of decision from multiple classifiers avoids a biased decision, and hence an ensemble classifier not only improves the classification accuracy but also reduces the chance of over training. It has been shown that the strength of an ensemble is related to the diversity between the base classifiers (Bian and Wang 2007). Homogeneous ensembles built with classifiers that are generated by a single learning algorithm are highly correlated. Hence in this research, the heterogeneous ensemble is built by integrating following three different supervised classifiers: SVM, ANN and k-NN, which are trained with reduced feature vector to distinguish between benign and malignant tumors. In order to provide the ensemble decision on the tumor type, the class decision provided by SVM, ANN and k-NN are integrated using the majority voting rule (Kittler et al. 1998), and the input tumor is assigned to the class that receives the highest number of votes from the classifiers. The majority voting rule is defined as follows:

Assign sample s to the class j if

$$\sum_{i=1}^{R} \triangle_{ji} = \max_{k=1}^{M} \sum_{i=1}^{R} \triangle_{ki} \tag{4.28}$$

$$\triangle_{ji} = \begin{cases} 1 & \text{if } C_i \text{ gives the class j} \\ 0 & \text{otherwise} \end{cases} \tag{4.29}$$

Where, C_i is the i^{th} classifier, M and R represent the number of classes and classifiers, respectively. The details of the SVM, ANN and k-NN classifiers used in the ensemble classifier are given below.

Support Vector Machine: SVM is a supervised learning machine for binary classification problems. Given a training data set $\{x_i, y_i\}_{i=1}^{N}$, where $x_i \in R^d$ is a feature vector and d the dimension of the input feature vector and $y_i \in \{-1, +1\}$ is a class label, SVM seeks to define an optimal separating hyper plane which generates a maximum margin between two categories of data. By finding the maximum margin, SVM minimizes the misclassification probability of new cases (Vapnik 2005). SVM uses a kernel function to map the data from its original dimension to the higher dimension so that data vectors are linearly separable in the mapped dimension. In the present work, Radial Basis Function (RBF) is chosen as a kernel function and the parameter values of the SVM such as regularization parameter C and kernel width s are selected by trial and error procedure.

Artificial Neural Network: ANN consists of a set of interconnected neurons to map the input features to the output. A three layer feed forward neural network (Haykin 2009) is implemented with n input, h hidden and 1 output neuron indicating the characteristic of the brain/liver tumor as benign or malignant; values of n and h are determined empirically. The learning of the ANN is supervised and the weights are adjusted by the back propagation procedure with the adaptive learning rate and momentum to obtain a desired input-output relationship. The log-sigmoid and tan-sigmoid activation functions are used for the hidden and output layers, respectively.

k-Nearest Neighbor: The principle of k-NN classifier is based on the intuitive concept that data instances of the same class should be closer in the feature space.

Thus, given an input feature vector X of unknown class, it determines the k closest training vectors according to the similarity measure, such as Euclidian distance; then vector X is assigned to the class to which the majority of k nearest neighbors belong (Song et al. 2007). Based on the experiments, we set k to a value that results in the least number of tumor misclassifications.

4.2 Experimental Results and Discussion

In order to test the performance and also to tune the parameters of the classifiers for tissue characterization of brain/liver tumor, the Leave-One-Out (LOO) method (Kothavi 1995) is used. Given a dataset of n samples, the LOO-based validation is performed with n iterations, such that in each iteration the classifier is trained with $n-1$ samples and tested on the remaining one sample. The average accuracy of n iterations is used to estimate the accuracy of the classifier. Since, the LOO-based validation uses the entire dataset both in the training and testing phases of the classifier, it provides an unbiased estimation of the performance. The following performance measures: sensitivity, specificity, accuracy, and Receiver Operating Characteristic (ROC) curve are used to quantify the performance of classifiers in discriminating between benign and malignant tumors. The ROC curve demonstrates the sensitivity and specificity of the classifier's performance for the continuum of the decision threshold (Xie et al. 2009). The sensitivity, specificity and accuracy measures are defined as follows:

$$Sensitivity = \frac{TP}{TP + FN} \times 100. \tag{4.30}$$

$$Specificity = \frac{TN}{TN + FP} \times 100. \tag{4.31}$$

$$Accuracy = \frac{TP + TN}{TP + TN + FP + FN} \times 100. \tag{4.32}$$

Where, TP (True Positive): Number of malignant tumors classified as malignant; FP (False Positive): Number of benign tumors classified as malignant; TN (True Negative): Number of benign tumors classified as benign; FN (False Negative): Number of malignant tumors classified as benign. In the following experiments, we analyze the performance of the various feature section techniques, and assess the diagnostic capability of single and ensemble classifiers. Further, the classification performance

of the radiologists and time taken by the different phases of the proposed brain/liver tumor classification scheme is demonstrated. The classification results of brain and liver tumors are given in Section 4.2.1 and Section 4.2.2, respectively.

4.2.1 Brain Tumor Classification Results

The brain tumor classification experiments are carried out on T1-weighted post-contrast and T2-weighted brain MRI images of 550 patients (female: 246, male: 304). Among 550 patients, 280 patients were diagnosed with benign tumor and 270 patients with malignant tumor based on histopathological analysis of biopsy samples; the detailed description of the dataset is already given in Section 2.8.

The feature selection is performed on the features extracted from all 550 cases and the reduced feature set is used to train the individual classifiers of an ensemble classifier. The LOO-based validation is used to train and test the classifiers. The LOO-based validation is performed on a set of 550 2D representative MRI images. Each classifier is trained using 549 MRI images in the set, and then tested on the remaining single MRI image using the initialized value of the parameter. This is repeated 550 times such that each image in the set is used once as the test data. The average accuracy of these 550 iterations is used to estimate the generalization accuracy of the classifier for the parameter value used, and the parameter value that results in the highest estimated accuracy is chosen as the optimal value. This procedure provides unbiased estimation of the classifier performance and also avoids overtraining of the classifier, because the classifier is trained with features of 549 cases and the remaining one case used for testing is unknown to the classifier.

Feature Selection and Classification

The ground truth for the classification of tumors on 550 representative MRI images is obtained based on the histopathological analysis of biopsy samples. In order to determine the features leading to optimal classification performance, four types of experiments are performed, based on the use of complete 432-dimensional feature vector consisting of 2D features, and the reduced feature vectors produced by feature selection techniques, namely ICA, Principal Component Analysis (PCA), and Genetic Algorithm (GA). Further, these feature selection techniques are combined with IG-based feature ranking (IG-ICA, IG-PCA, and IG-GA). For each classifier,

the classification accuracies obtained by LOO validation based on the selected features are shown in Figure 4.6. The reduced feature vectors are estimated based on

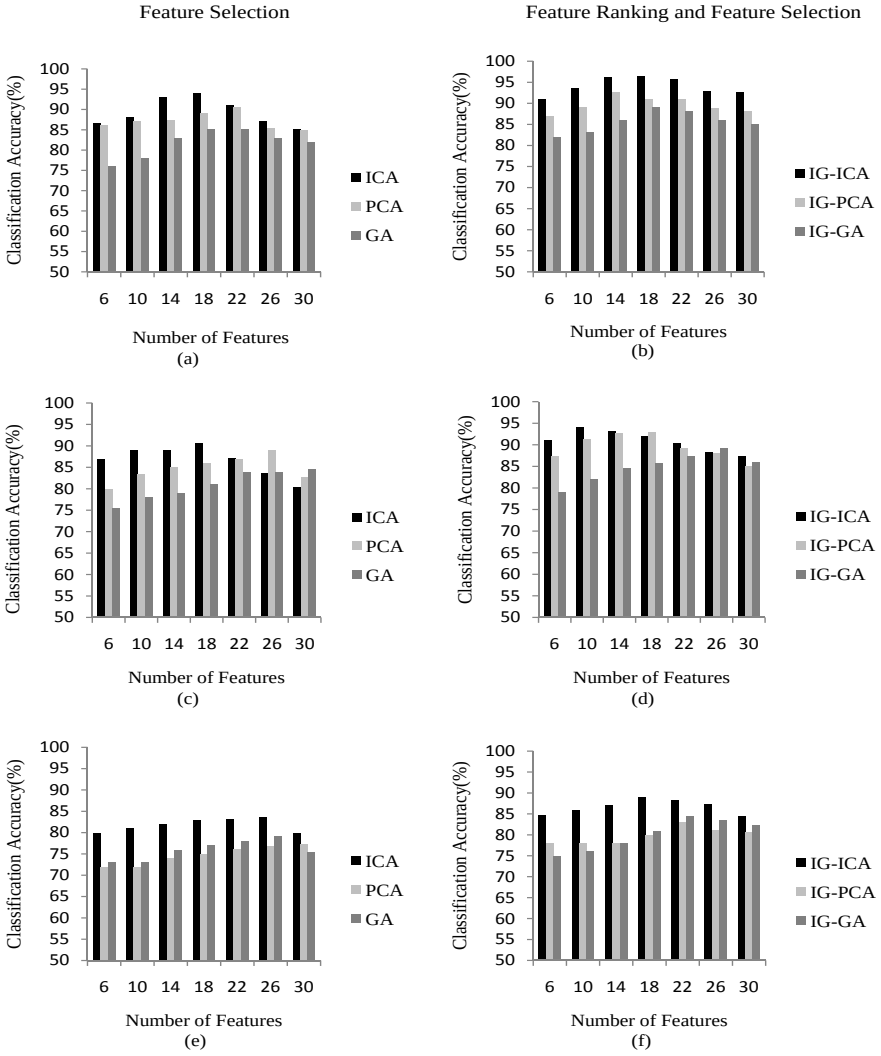

Figure 4.6: Brain Tumor Classification Performance of Individual Classifiers versus Feature Subset Dimensionality: (a) (b) SVM Classifier (c) (d) ANN classifier (e) (f) k-NN Classifier

the requirement to find small subsets with cardinality 6, 10, 14, 18, 22, 26, and 30. The feature vector produced by the feature selection technique is used for training the individual classifiers. Further details about experiments on input feature vector are presented as follows.

Complete Feature Vector: In the first experiment, each classifier is trained with the complete 432-dimensional feature vector containing extracted features from both T1-weighted post-contrast and T2-weighted MRI images. Classification accuracy of 81.37% is achieved by SVM with its parameters set as: $C = 30$ and $\sigma = 0.86$. ANN achieved classification accuracy of 75.04% with 28 hidden neurons. Classification accuracy of 70.46% is achieved by k-NN with the number of neighbors $k = 32$.

Reduced Feature Vector Using ICA: In the second experiment, feature selection is carried out for SVM, ANN and k-NN classifiers using ICA and IG-ICA techniques. In SVM classification, highest classification accuracy of 94.11% and 96.42% is achieved with 18 and 14 features obtained by ICA and IG-ICA techniques, respectively. ANN classifier resulted in the highest classification accuracy of 90.61% with 18 features obtained through ICA and 94.18% with 10 features obtained through IG-ICA technique. In k-NN, the highest classification accuracy of 83.69% and 89.09% is obtained using 26 and 18 features selected by ICA and IG-ICA techniques, respectively. The parameters resulting in optimal classification accuracies consist of $C = 6$ and $\sigma = 0.01$ for SVM classifier, 8 hidden neurons for ANN classifier and the number of neighbors $k = 13$ for k-NN classifier.

Reduced Feature Vector Using PCA: Experiments similar to ICA method are also performed with PCA and IG-PCA techniques. PCA transforms the high-dimensional input feature space into a lower dimensional feature space using eigenvectors corresponding to the largest eigenvalues of the covariance matrix (Fukunaga 1990). SVM attained the highest classification accuracy of 90.65% and 92.72% with 22 and 14 features obtained through PCA and IG-PCA techniques, respectively. In ANN classifier, 26 and 18 features led to the highest classification accuracy of 88.98% and 93.01% with PCA and IG-PCA techniques, respectively. In k-NN classifier, the highest classification accuracy of 77.39% is obtained with 30 features selected through PCA and 82.98% with 22 features selected through IG-PCA technique. The parameters resulting in optimal classification accuracies consist of $C = 17$ and $\sigma = 0.58$ for SVM classifier, 15 hidden neurons for ANN classifier and $k = 20$ for k-NN classifier.

Reduced Feature Vector Using GA: In the fourth experiment, GA and IG-GA feature selection methods are used in order to reduce the dimensionality of the original

feature vector. GA searches for optimal set of features by assessing the search results based on an evaluation function, which measures fitness of the selected features for the classification (Raymer et al. 2000). The GA parameters used in the present work are given in Table 4.2; these parameters are determined empirically. SVM attained the highest classification accuracy of 85.06% and 89.02% with 22 and 18 features obtained through GA and IG-GA techniques, respectively. The ANN classifier achieved an optimal classification accuracy of 84.51% and 89.18% with 30 and 26 features obtained through GA and IG-GA techniques, respectively. The k-NN classifier resulted in best classification accuracy of 79.31% with 26 features obtained by GA method and 84.39% with 22 features obtained by IG-GA technique. The parameters resulting in optimal classification accuracies consist of $C = 12$ and $\sigma = 0.50$ for SVM classifier, 21 hidden neurons for ANN classifier and $k = 15$ for k-NN classifier. It is observed

Table 4.2: Genetic Algorithm Parameters

Parameter	**Value**
Population Size	50
Selection Technique	Roulette Wheel
Cross Over Type	Two Point Cross Over
Cross Over Rate	0.9
Mutation Operator	Bit Inversion
Mutation Rate	0.001
No. of Generations	500

from the above experiments that SVM, ANN and k-NN classifiers performed more effectively with the reduced feature vector when compared to the complete feature vector. Classifiers attained better accuracy with the combination of feature selection and feature ranking when compared to using the feature selection alone for selecting a subset of features. This is because feature ranking helps in eliminating irrelevant features and then the feature selection technique removes redundant features from relevant features resulting in the feature vector consisting of a small number of highly distinguishable features. Among IG-ICA, IG-PCA and IG-GA techniques, the IG-ICA technique resulted in the highest classification accuracy with all the classifiers.

This is because of the ability of ICA to capture the essential structure of the data by giving statistically independent features, whereas PCA and GA give a global compact representation of the data.

In order to evaluate the effectiveness of 3D features, similar experiments are carried out on 550 3D tumor models and here also the highest classification accuracies are obtained with the IG-ICA technique. Table 4.3 and Table 4.4 shows the classification performance achieved with 2D and 3D features selected through IG-ICA technique, respectively. The classification performance is shown in terms of sensitivity, specificity, accuracy and area under ROC curve (Az). Both 2D and 3D features obtained almost similar classification accuracies in classifying brain tumor as benign or malignant. Thus, 2D features are considered in the further experiments. It can be observed from Table 4.3 and Table 4.4 that accuracies of SVM, ANN and k-NN are different. This is because each learning model captures different properties of the data, and thus their error regions differ. SVM, ANN and k-NN attained the highest classification accuracy of 96.42%, 94.18% and 89.09% with 14, 10 and 18 features, respectively. Comparison of the classifier performance shows that SVM classifier achieves the highest classification performance. This is due to the ability of SVM in finding a separating hyper plane based on the structural risk minimization principle to maximize the margin between two classes, whereas other classifiers are based on the minimization of empirical risks.

Table 4.3: Brain Tumor Classification Performance with 2D Features

Classifier	**Performance**	**No. of Features**						
		6	10	14	18	22	26	30
SVM	Sensitivity (%)	94.44	95.55	97.03	96.66	95.92	95.18	94.81
	Specificity (%)	86.42	91.78	95.71	95.71	95.35	90.35	90.35
	Accuracy (%)	90.36	93.63	96.42	96.16	95.63	92.82	92.51
	Az	0.901	0.930	0.961	0.953	0.947	0.926	0.917
ANN	Sensitivity (%)	94.81	96.29	95.92	95.18	93.70	92.59	92.22
	Specificity (%)	87.50	92.14	90.71	88.57	87.14	83.92	82.85
	Accuracy (%)	91.18	94.18	93.27	91.96	90.39	88.28	87.50
	Az	0.905	0.940	0.929	0.916	0.898	0.881	0.872

Continued on next page

Table 4.3 – *Continued from previous page*

Classifier	**Performance**	**No. of Features**						
		6	10	14	18	22	26	30
k-NN	Sensitivity (%)	92.59	93.33	94.44	95.18	95.55	94.18	92.92
	Specificity (%)	77.14	78.57	80.0	83.21	81.07	79.04	76.42
	Accuracy (%)	84.69	85.93	87.09	89.09	88.18	87.27	84.54
	Az	0.842	0.855	0.868	0.890	0.879	0.871	0.842

Table 4.4: Brain Tumor Classification Performance with 3D Features

Classifier	**Performance**	**No. of Features**						
		6	10	14	18	22	26	30
SVM	Sensitivity (%)	94.81	95.55	97.03	96.66	96.66	95.55	94.81
	Specificity (%)	90.35	91.78	95.71	96.07	94.28	90.35	90.35
	Accuracy (%)	90.90	93.63	96.42	96.25	95.61	92.95	92.51
	Az	0.903	0.930	0.961	0.962	0.949	0.918	0.917
ANN	Sensitivity (%)	94.81	96.29	95.92	95.18	93.70	92.59	92.96
	Specificity (%)	88.92	92.14	90.71	88.92	87.14	83.92	83.21
	Accuracy (%)	91.96	94.18	93.27	92.05	90.39	88.28	88.13
	Az	0.918	0.940	0.929	0.921	0.898	0.881	0.879
k-NN	Sensitivity (%)	92.96	93.33	94.44	95.18	95.55	94.18	93.33
	Specificity (%)	78.57	78.57	80.0	83.21	81.42	82.59	76.78
	Accuracy (%)	85.77	85.93	87.09	89.09	88.20	87.23	84.60
	Az	0.854	0.855	0.868	0.890	0.881	0.871	0.844

Ensemble Classifier Performance

The ensemble classifier for the proposed CAD system consists of SVM, ANN and k-NN classifiers to predict the class of the given tumor. In order to improve the classification accuracy of the CAD system, individual decisions of all three classifiers (SVM, ANN and k-NN) are combined using majority voting rule (Kittler et al. 1998).

This combination in ensemble classifier performed better than the best performed single classifier (e.g. SVM with an accuracy of 96.42%). The confusion matrix of the ensemble classifier is illustrated in Table 4.5. All 270 malignant brain tumors are correctly classified, whereas 5 benign brain tumors are misclassified in a set of 280 benign brain tumors.

Table 4.5: Confusion Matrix of Ensemble Classification of Brain Tumors

	Predicted Class	
Actual Class	Benign	Malignant
Benign	275	5
Malignant	0	270

The performance measures computed from the confusion matrix of ensemble classifier are shown in Table 4.6. The ensemble classifier can predict well the malignant

Table 4.6: Performance of Ensemble Classifier in Brain Tumor Classification

Performance Metrics	**Classifier Performance**
Sensitivity	100%
Specificity	98.21%
Accuracy	99.09%
Az	0.991

category of brain tumor (Sensitivity: 100%). This is important from the diagnostic viewpoint as the false classification of malignant brain tumor has very serious consequences for patients. However, 5 benign tumors are incorrectly classified resulting in 98.21% specificity. This is due to the difficulty in capturing the boundary and shape features of these tumors. Overall, the classification accuracy is improved by 3% based on the multiple classifier fusion, when compared to the best performance of the single classifier (e.g., SVM with an accuracy of 96.42%). This proves the validity of using an ensemble classifier in the characterization of the brain tumor.

Further, the performance of the ensemble classifier is evaluated with features extracted from manually and automatically segmented tumors. Figure 4.7 shows the ROC curves of the ensemble classifier with manual and automatic brain tumor segmentations. The manual segmentation of brain tumor is performed by two experienced (R1 and R2) and two inexperienced (R3 and R4) radiologists. The automatic brain tumor segmentation is performed by the proposed segmentation technique based on MFCM clustering. The performance of the ensemble classifier is evaluated by area under ROC curve (Az). In order to investigate the classification performance for the manual segmentation, features are extracted from brain tumors that are delineated by radiologists R1, R2, R3 and R4. The ensemble classification of brain tumors resulted in Az value of 0.991 with automatic segmentation, and 0.995, 0.995, 0.786, 0.731 with manual segmentation by radiologists R1, R2, R3, and R4, respectively. This indicates that the difference between the brain tumor classification obtained based on automatic and experienced radiologists' segmentations is negligible. The classification of tumors segmented by inexperienced radiologists shows the poor performance due to the imperfect delineation of tumor boundary.

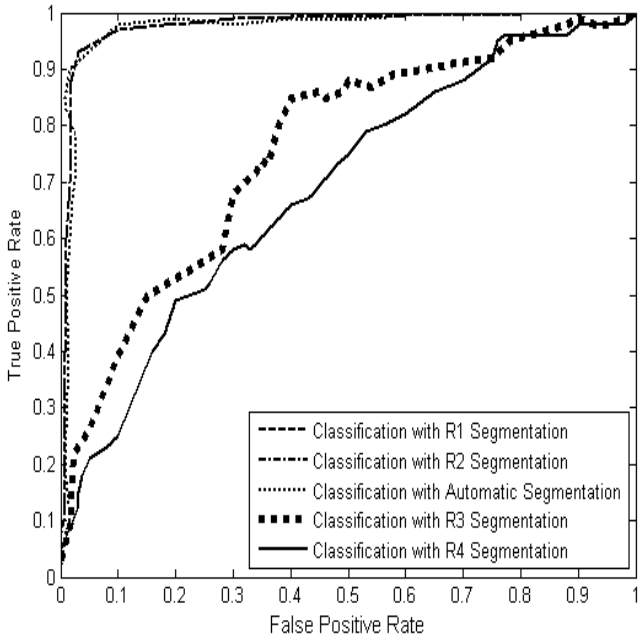

Figure 4.7: ROC Curves of Ensemble Classifier With Manual and Automatic Segmentation of Brain Tumors

Classification Performance of Radiologists

In another experiment, all four radiologists have been asked to visually analyze the brain tumor on 550 representative MRI slices and give their decision on the type of tumor. Table 4.7 shows the classification performance of the radiologists evaluated with respect to the ground truth. Here, the ground truth for the tumor classifications is defined based on the histopathological analysis of biopsy samples of 550 tumors. The experienced radiologists R1 and R2 obtained classification accuracy of 79.09% and 78.54%, respectively. The inexperienced radiologists R3 and R4 attained classification accuracy of 62.72% and 66.90%, respectively. There is not much difference in classification results of expert radiologists, whereas the classification difference existed between experienced and inexperienced radiologists. However, the classification performance of all the radiologists is poor when compared to that of the proposed CAD system.

Table 4.7: Brain Tumor Classification Performance of Radiologists

Performance Metrics	**Classification Performance(%)**			
	R1	**R2**	**R3**	**R4**
Sensitivity	75.02	74.28	57.14	63.57
Specificity	83.13	82.96	68.51	70.37
Accuracy	79.09	78.54	62.72	66.90
Az	0.772	0.769	0.618	0.694

Computation Time

The mean computation time required for processing the representative slice of the brain tumor in each phase of the CAD system is shown in Figure 4.8. The feature extraction stage is more time consuming as multi-resolution analysis of features is carried out to achieve better discrimination ability. The brain tumor characterization with reduced feature set takes about 4 to 5 sec, whereas the brain tumor characterization with the complete feature vector takes about 18 sec. Thus, the integration of the ensemble classifier with the two-level feature selection consisting of IG and ICA techniques has resulted in the reduction of computation time by 72.22%.

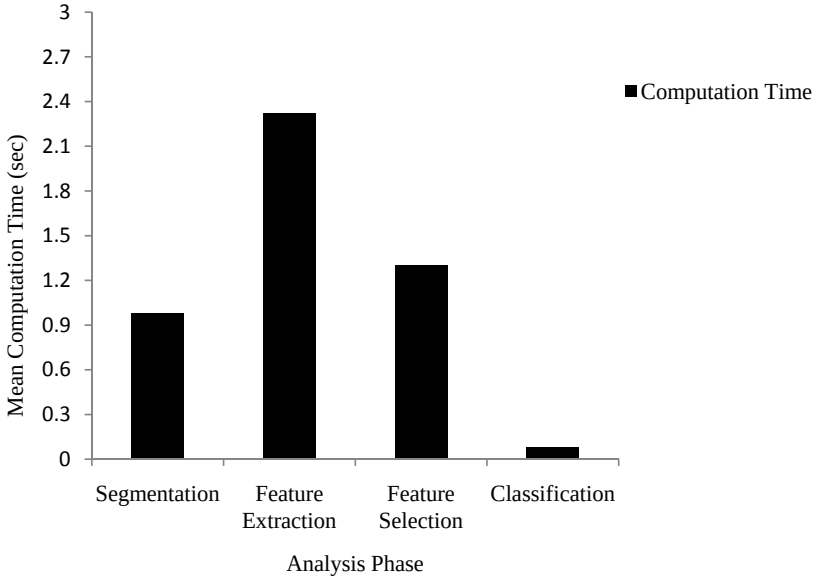

Figure 4.8: Time Taken by Different Phases of CAD of Brain Tumor

4.2.2 Liver Tumor Classification Results

The liver tumor classification experiments are carried out on a dataset consisting of non-contrast-enhanced abdominal CT images of 487 patients (female: 235, male: 252). Among 487 patients, 247 patients were diagnosed with benign tumor and 240 patients with malignant tumor based on histopathological analysis of biopsy samples. The detailed description of the datasets is already given in Section 2.8. The feature selection is performed on the features extracted from all 487 cases and the reduced feature set is used to train the individual classifiers of an ensemble classifier. The LOO-based validation is used to train and test the classifiers.The LOO-based validation is performed on a set of 487 2D representative CT images. Each classifier is trained using 486 CT images in the set and then tested on the remaining single CT image using the initialized value of the parameter. This is repeated 487 times such that each image in the set is used once as the test data. The average accuracy of these 487 iterations is used to estimate the generalization accuracy of the classifier for the parameter value used, and the parameter value which resulted in the highest estimated accuracy is chosen as the optimal value. This procedure provides unbiased estimation of the classifier performance and also avoids overtraining of the classifier,

because the classifier is trained with features of 486 cases and the remaining one case used for testing is unknown to the classifier.

Feature Selection and Classification

In order to determine the features leading to optimal classification performance, four types of experiments are performed, based on the complete 216-dimensional feature

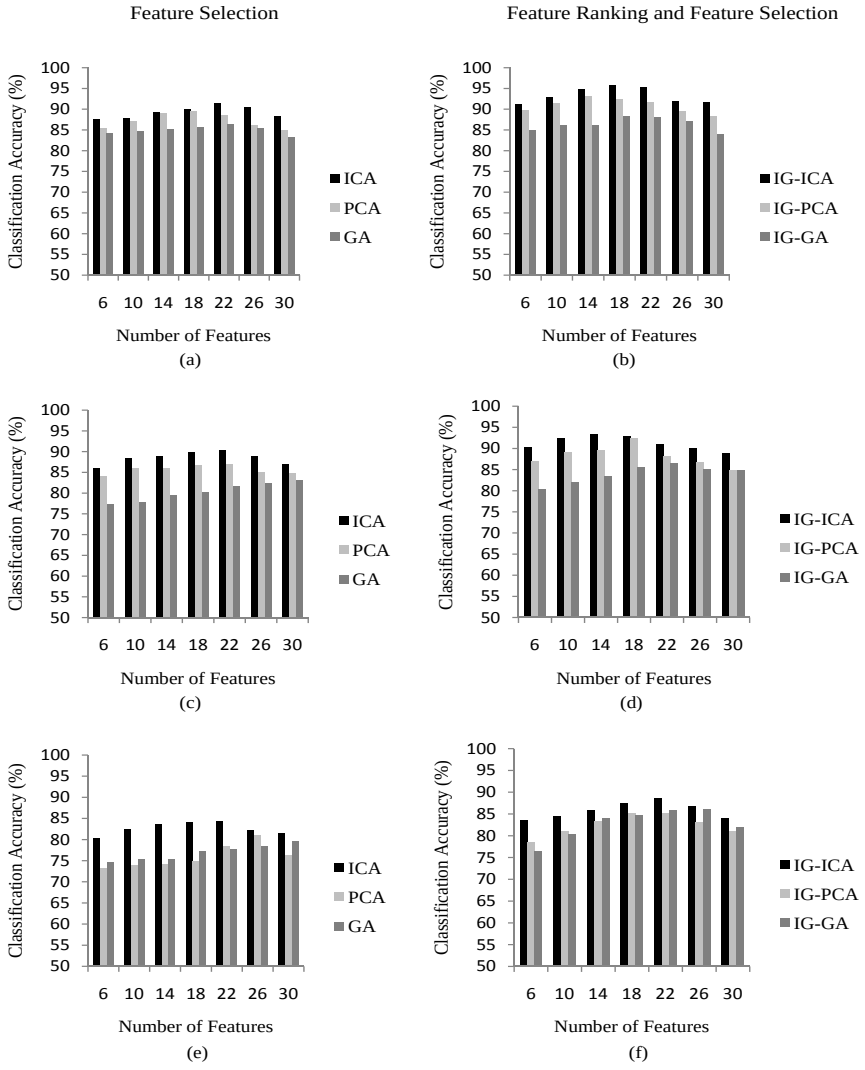

Figure 4.9: Liver Tumor Classification Performance of Individual Classifiers versus Feature Subset Dimensionality: (a)(b) SVM Classifier (c)(d) ANN classifier (e)(f) k-NN Classifier.

vector consisting of 2D features, and the reduced feature vectors produced by the application of feature selection techniques (ICA, PCA and GA). Further, these feature selection techniques are combined with IG-based feature ranking (IG-ICA, IG-PCA, and IG-GA). For each classifier, the classification accuracies obtained by LOO validation are shown in Figure 4.9. Further details about experiments on input feature vector are presented as follows:

Complete Feature Vector: In the first experiment, each classifier is trained with the complete 216-dimensional feature vector containing features extracted from non-contrast-enhanced abdominal CT images. Classification accuracy of 78.02% is achieved by SVM classifier with its parameters set as: $C = 21$ and $\sigma = 0.75$. ANN achieved classification accuracy of 75.97% with 22 hidden neurons. Classification accuracy of 74.94% is achieved by k-NN with the number of neighbors $k = 25$.

Reduced Feature Vector Using ICA: In the second experiment, feature selection is carried out for SVM, ANN and k-NN classifiers using ICA and IG-ICA techniques. In SVM classification, the highest classification accuracy of 91.37% and 95.68% is achieved with 22 and 18 features obtained by ICA and IG-ICA techniques, respectively. ANN classifier resulted in the best classification accuracy of 90.34% with 22 features obtained through ICA and 93.42% with 14 features obtained through IG-ICA techniques. In k-NN, the highest classification accuracy of 82.13% and 88.70% is obtained using 26 and 22 features selected through ICA and IG-ICA techniques, respectively. The parameters resulting in optimal classification accuracies consist of $C = 8$ and $\sigma = 0.07$ for SVM classifier, 10 hidden neurons for ANN classifier and the number of neighbors $k = 10$ for k-NN classifier.

Reduced Feature Vector Using PCA: Experiments similar to ICA method are also performed with PCA and IG-PCA techniques. PCA transforms the high-dimensional input feature space into a lower dimensional feature space using eigenvectors corresponding to the largest eigenvalues of the covariance matrix (Fukunaga 1990). SVM attained the highest classification accuracy of 89.52% and 93.01% with 18 and 14 features obtained through PCA and IG-PCA techniques, respectively. For ANN, 22 and 18 features led to the highest classification accuracy of 87.06% and 92.40% with PCA and IG-PCA techniques, respectively. k-NN obtained the highest

classification accuracy of 81.10% with 26 features selected through PCA and 85.21% with 22 features selected through IG-PCA technique. The parameters resulting in optimal classification accuracies consist of $C = 18$ and $\sigma = 0.55$ for SVM classifier, 16 hidden neurons for ANN classifier and $k = 12$ for k-NN classifier.

Reduced Feature Vector Using GA: In the fourth experiment, GA and IG-GA feature selection methods are used in order to reduce the dimensionality of the original feature vector. GA searches for optimal set of features by assessing the search results based on an evaluation function, which measures fitness of the selected features for the classification (Raymer et al. 2000). The GA parameters used for the feature selection are given in Table 4.8; these parameters are determined empirically. SVM classifier attained the highest classification accuracy of 86.24% and 88.29% with 22 and 18 features selected by GA and IG-GA techniques, respectively. ANN classifier achieved an optimal classification accuracy of 83.16% and 86.44% with 30 and 22 features obtained through GA and IG-GA techniques, respectively. k-NN classifier resulted in the highest classification accuracy of 79.67% with 30 features obtained by GA and 86.03% with 26 features obtained by IG-GA technique. The parameters resulting in optimal classification accuracies consist of $C = 16$ and $\sigma = 0.48$ for SVM classifier, 13 hidden neurons for ANN classifier and $k = 20$ for k-NN classifier.

Table 4.8: Parameters of Genetic Algorithm

Parameter	**Value**
Population Size	30
Selection Technique	Roulette Wheel
Cross Over Type	Two Point Cross Over
Cross Over Rate	0.8
Mutation Operator	Bit Inversion
Mutation Rate	0.001
No. of Generations	450

It is observed that SVM, ANN and k-NN classifiers performed more effectively with the reduced feature vector when compared to the complete feature vector. Clas-

sifiers attained better accuracy with the combination of feature selection and feature ranking when compared to using the feature selection alone for selecting a subset of features. This is because feature ranking helps in eliminating irrelevant features and then the feature selection technique removes redundant features from relevant features resulting in the feature vector consisting of a small number of highly distinguishable features. Among IG-ICA, IG-PCA and IG-GA technique, the IG-ICA technique resulted in the highest liver tumor classification accuracy with all the classifiers.

Table 4.9 and Table 4.10 shows the classification performance achieved with 2D and 3D features selected through IG-ICA technique, respectively. Both 2D and 3D features obtained almost similar classification accuracies in classifying liver tumor as benign or malignant. Thus, 2D features are considered in the further experiments. SVM, ANN and k-NN attained the highest classification accuracy of 95.68%, 93.42% and 88.70% with 18, 14 and 22 features, respectively. Comparison of the classifier accuracies shows that SVM classifier achieves the highest liver tumor classification accuracy.

Table 4.9: Liver Tumor Classification Performance with 2D Features

Classifier	**Performance**	**No. of Features**						
		6	10	14	18	22	26	30
SVM	Sensitivity (%)	92.08	93.33	94.16	95.00	94.58	92.50	92.08
	Specificity (%)	90.28	92.30	95.14	96.35	95.95	91.49	91.09
	Accuracy (%)	91.17	92.81	94.66	95.68	95.27	91.99	91.58
	Az	0.910	0.922	0.943	0.954	0.951	0.916	0.915
ANN	Sensitivity (%)	91.25	90.00	90.83	88.33	87.50	87.08	85.83
	Specificity (%)	89.47	94.73	95.95	97.57	94.73	93.11	91.90
	Accuracy (%)	90.34	92.40	93.42	93.01	91.17	90.14	88.91
	Az	0.901	0.924	0.933	0.930	0.908	0.907	0.882
k-NN	Sensitivity (%)	87.50	87.91	88.75	89.58	90.41	90.00	87.08
	Specificity (%)	79.75	81.37	82.99	85.42	87.04	83.80	80.97
	Accuracy (%)	83.57	84.59	85.83	87.47	88.70	86.85	83.98
	Az	0.831	0.843	0.857	0.870	0.886	0.862	0.833

Table 4.10: Liver Tumor Classification Performance with 3D Features

Classifier	**Performance**	**No. of Features**						
		6	10	14	18	22	26	30
SVM	Sensitivity (%)	92.08	93.33	95.00	95.00	94.58	92.50	92.08
	Specificity (%)	90.28	92.30	94.73	96.35	95.95	91.49	91.09
	Accuracy (%)	91.17	92.81	94.86	95.68	95.27	91.99	91.58
	Az	0.910	0.922	0.945	0.954	0.951	0.916	0.915
ANN	Sensitivity (%)	91.66	90.00	90.83	88.33	87.50	87.08	85.83
	Specificity (%)	89.47	94.73	95.95	97.57	94.73	93.11	91.90
	Accuracy (%)	90.55	92.40	93.42	93.01	91.17	90.14	88.91
	Az	0.903	0.924	0.933	0.930	0.908	0.907	0.882
k-NN	Sensitivity (%)	87.50	87.91	87.50	89.58	90.41	90.00	87.08
	Specificity (%)	79.75	81.37	83.40	85.42	87.04	83.80	80.97
	Accuracy (%)	83.57	84.59	85.53	87.47	88.70	86.85	83.98
	Az	0.831	0.843	0.855	0.870	0.886	0.862	0.833

Ensemble Classifier Performance

In order to improve the classification accuracy of the CAD system, individual decisions of all three classifiers (SVM, ANN and k-NN) in the ensemble classifier are combined using majority voting rule (Kittler et al. 1998). The confusion matrix of the ensemble classifier is illustrated in Table 4.11. All 240 malignant liver tumors are correctly classified, whereas 7 benign brain tumors are misclassified in a set of 247 benign liver tumors. The performance measures computed from the confusion matrix of

Table 4.11: Confusion Matrix of Ensemble Classification of Liver Tumors

	Predicted Class	
Actual Class	Benign	Malignant
Benign	240	7
Malignant	0	240

ensemble classifier are shown in Table 4.12. The combination of classifiers in an ensemble classifier resulted in the classification accuracy of 98.56%. The sensitivity of 100% is obtained with ensemble classifier, this means that the ensemble classifier can predict well the malignant category of the liver tumor. However, 7 benign tumors are incorrectly classified resulting in specificity of 97.16%. This is due to the difficulty in capturing boundary and shape features of these tumors. Overall, the classification accuracy is improved by 3% based on the multiple classifier fusion, when compared to the best performance of the single classifier (e.g. SVM with an accuracy of 95.68%). This proves the validity of using ensemble classifier in tissue characterization of brain tumor.

Table 4.12: Performance of Ensemble Classifier in Liver Tumor Classification

Performance Metrics	**Classifier Performance**
Sensitivity	100%
Specificity	97.16%
Accuracy	98.56%
Az	0.989

Figure 4.10 shows the ROC curves of the ensemble classifier with manual segmentation and proposed automatic segmentation techniques. The manual segmentation of liver tumor is performed by two experienced (R1 and R2) and two inexperienced (R3 and R4) radiologists. The automatic liver tumor segmentation is performed by the proposed segmentation technique based on automatic region growing. To investigate the classification performance for the manual segmentation, features are extracted from liver tumors that are delineated by radiologists R1, R2, R3 and R4. The ensemble classification of liver tumors resulted in Az value of 0.989 with automatic segmentation and 0.990, 0.990, 0.753, 0.745 with manual segmentation by radiologists R1, R2, R3 and R4, respectively. It can be observed that the liver tumor classification based on automatic and experienced radiologists' segmentations are almost similar. The classification of tumors segmented by inexperienced radiologists shows the poor performance due to the imperfect delineation of tumor boundary.

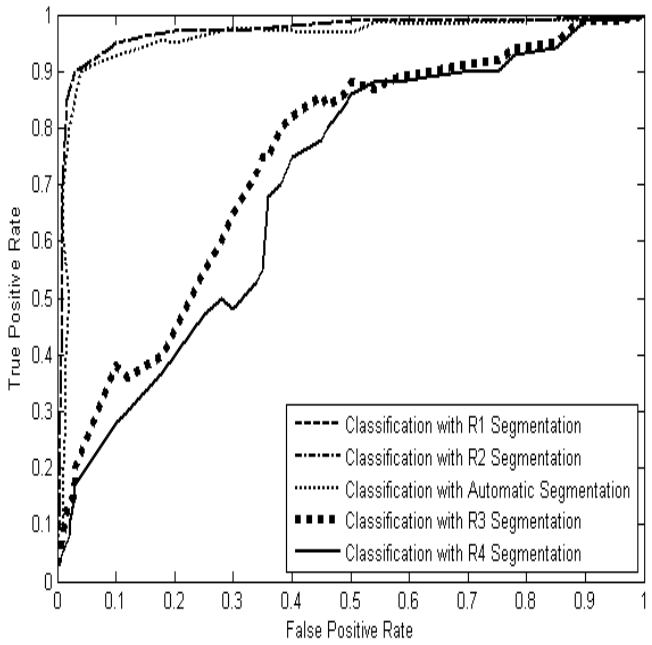

Figure 4.10: ROC Curves of Ensemble Classifier With Manual and Automatic Segmentation of Liver Tumors

Classification Performance of Radiologists

In another experiment, all four radiologists have been asked to visually analyze the liver tumor on 487 representative CT slices and give their decision on the type of tumor. Table 4.13 shows the classification performance of the radiologists evaluated with respect to the ground truth, which is defined based on histopathological analysis of biopsy samples of 487 tumors. The experienced radiologists R1 and R2 obtained classification accuracy of 72.68% and 70.43%, respectively. The inexperienced radiologists R3 and R3 attained classification accuracy of 63.65% and 61.19%, respectively. There is not much difference in classification results of expert radiologists due to their experience in interpreting liver CT images, whereas classification difference existed between experienced and inexperienced radiologists. However, the classification performance of all the radiologists is poor when compared to that of the proposed CAD system. This is because the visual analysis of the CT images cannot capture the fine details of the tumor, whereas the proposed automatic CAD system analyzes the information in the CT image using effective image processing techniques and hence results in accurate tumor classification results.

Table 4.13: Liver Tumor Classification Performance of Radiologists

Performance Metrics	**Classification Performance (%)**			
	R1	**R2**	**R3**	**R4**
Sensitivity	71.66	68.75	60.41	58.33
Specificity	73.68	72.06	66.80	64.77
Accuracy	72.68	70.43	63.65	61.19
Az	0.702	0.694	0.665	0.628

Computation Time

The mean computation time required for processing the representative slice of the liver tumor in each phase of the CAD system is shown in Figure 4.11.

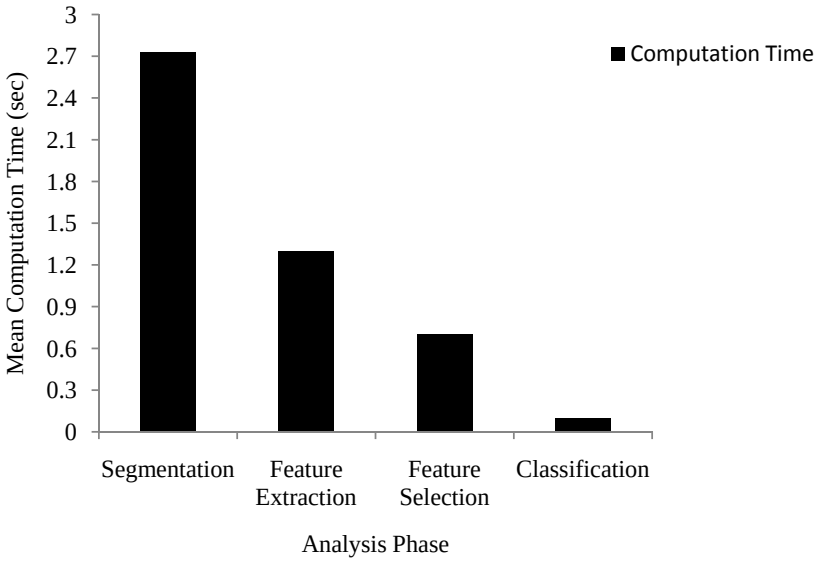

Figure 4.11: Time Taken by Different Phases of CAD of Liver Tumor

The feature extraction stage is more time consuming as multi-resolution analysis of features is carried out to achieve better discrimination ability. The liver tumor characterization with reduced feature set takes about 4 to 5 sec, whereas the tumor

characterization with complete feature vector takes about 12 sec. Thus, the integration of the ensemble classifier with the two-level feature selection has resulted in the reduction of computation time by 52.33%.

4.3 Summary

This chapter presented the proposed tumor classification scheme for determining the type of brain/liver tumor as benign or malignant. The proposed scheme represented the tumor characteristics with a set of significant features, selected discriminating features with two-level feature selection and classified the given tumor using ensemble classifier. The experimental results demonstrated that both 2D and 3D features are equally effective in characterizing the brain/liver tumor as benign or malignant. The two-level feature selection technique which combines feature ranking and selection methods proved to be more effective when compared to using feature selection alone. The ensemble classifier helped to improve the tumor classification accuracy by avoiding a biased decision. The ensemble classifier obtained 99.09% accuracy, 98.21% specificity and 100% sensitivity for classification of brain tumors, and it obtained 98.56% accuracy, 97.16% specificity and 100% sensitivity for classification of liver tumors. Further, the inclusion of feature selection made the classification scheme more efficient when compared to using high-dimensional feature vector.

Chapter 5

Content-Based Image Retrieval for Diagnosis of Tumor

The proposed CAD system consists of tumor detection, classification, content-based image retrieval (CBIR) and 3D reconstruction methods for effective and efficient analysis of brain and liver tumors. The CBIR retrieves similar pathology bearing tumor images from the database in response to query image by comparing the visual contents of the images. CBIR is an important component of CAD system, since it assists the radiologist to make an accurate tumor diagnostic decision based on the retrieved images. Hence, in this chapter, effective and efficient CBIR methods are proposed for assisting the radiologist in the brain/liver tumor diagnosis. Precisely, an attempt has been made to fulfill the third objective of the research work and to overcome the limitations of the existing CBIR methods discussed in Section 2.5. The research contributions towards the development of CBIR methods are as follows:

- Elimination of the semantic gap by developing a hierarchical CBIR framework that effectively identifies the similarity between images.
- Developing CBIR methods robust to misalignments of images based on image rotation correction/rotation invariant features.
- Developing an efficient indexing structure called as Cluster with IG-ICA and KD-tree (CIKD) for fast retrieval of images from the database.
- Developing modified k-means clustering with automatic identification of the number of clusters and initial cluster centers for partitioning the features in the database.

5.1 Proposed Framework

Figure 5.1 shows the framework of the proposed CBIR methods for the diagnosis of brain/liver tumor as benign or malignant. It consists of two phases: database building (off-line) and query processing (on-line) phases.

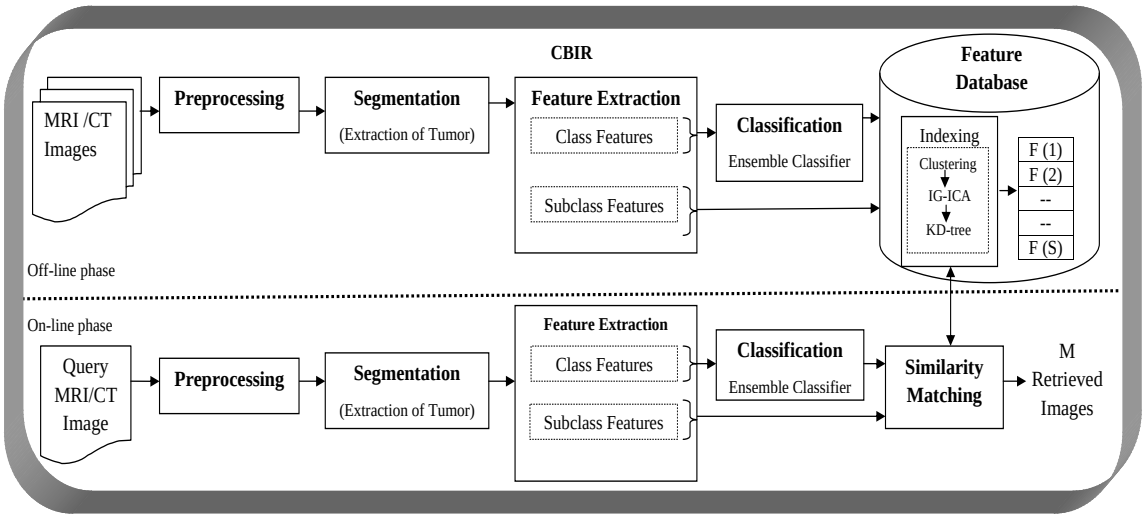

Figure 5.1: Framework of the Proposed CBIR Methods

In the off-line phase, the MRI images of brain tumors / CT images of liver tumors stored in the image database are preprocessed to improve the quality of images. Next, the tumor is segmented on MRI/CT images using proposed segmentation methods as discussed in Chapter 3. Tumors belonging to the same class (benign/malignant) differ by severity, density, and other such factors. Hence, not all pairs of images within one class have equivalent perceptual similarity; that is tumor subclasses exist. Therefore, the segmented tumor is represented using the class and subclass feature vectors. The most discriminating class features are selected based on IG-ICA feature selection technique. The selected features are fed to the ensemble classifier consisting of SVM, ANN and K-NN classifiers to obtain the class label as benign or malignant. Finally, the class label along with the subclass features is stored in the feature database.

Similarly in the online phase, a query image of the brain/liver tumor is preprocessed and segmented. Next, the segmented tumor is represented using class and subclass features. Then, based on the class label, the subclass features of the query image are compared with the subclass features in the database using the Euclidian

and Chi-square distances. The database is indexed using the proposed CIKD indexing technique and the most similar pathology bearing brain/liver images are retrieved.

The following two CBIR methods are proposed based on the framework shown in Figure 5.1 for brain/liver tumor diagnosis. These two methods differ in the technique used to handle the misalignment of images for accurate retrieval of images, and are discussed in Section 5.2 and Section 5.3, respectively.

- CBIR based on image rotation correction.
- CBIR based on rotation invariant features.

5.2 CBIR Based on Image Rotation Correction

MRI/CT images may be misaligned due to movement of the patient during scanning. The rotation changes the features of the image, and hence finding similarity between images becomes difficult. Thus, in this proposed CBIR method, the misaligned image is restored to its standard position using the proposed rotation correction technique in the preprocessing step as discussed in Chapter 3. Then, the class and subclass features of the segmented tumor are extracted and most similar images are retrieved from the database using similarity matching. The various steps of the proposed CBIR method are detailed below.

5.2.1 Preprocessing

Prior to segmentation, the quality of MRI/CT images is enhanced by image denoising based on the median and Laplacian filters, image contrast enhancement using histogram equalization, and rotation correction of misaligned image using the proposed rotation correction technique. The T1-weighted and T2-weighted MRI images of the brain are co-registered using the FLIRT registration tool (Jenkinson and Smith 2001) as discussed in Chapter 3.

5.2.2 Segmentation

After preprocessing, the input image is segmented in order to extract the tumor region for further analysis. If the input image is the MRI image of the brain, then the image is segmented using the proposed brain tumor segmentation technique based on

Modified Fuzzy C-Means (MFCM) clustering. If the input image is the abdominal CT image of the liver, then the image is segmented using the proposed liver tumor segmentation method based on automatic region growing. The brain and liver tumor segmentation methods are already discussed in Chapter 3.

5.2.3 Feature Extraction

The feature extraction step is used to describe characteristics of the segmented tumor by extracting its various features. In the proposed CBIR method, the segmented tumor is represented using the class and subclass features extracted from the representative slice of the tumor. Given a set of slices, the slice containing the largest cross-sectional area of the tumor is chosen as a representative slice of the tumor, since it contains the maximum possible information of the tumor. In case of brain tumor analysis, a representative slice is selected from both T1-weighted post-contrast and T2-weighted MRI images of the brain, and in case of liver tumor analysis, a representative slice is chosen from a set of non-contrast-enhanced abdominal CT images of the liver. The details of the tumor class and subclass features are given below.

Tumor Class Representation: The features that represent the class of the tumor as benign or malignant are extracted from the wavelet decomposed 2D image using global shape, image histogram, GLCM, wavelet energy and fractal dimension. Then, the most discriminating class features are selected based on the IG-ICA feature selection technique as discussed in Chapter 4.

Tumor Subclass Representation: In order to represent the subclass of the tumor, the following local shape and texture features are extracted from the representative slice of the tumor.

Shape Feature Extraction

The local shape of the tumor is represented using Wavelet-based Fourier Descriptors (WFD) (Kunttu et al. 2006) as they help in analyzing the local shape features of the tumor. Let the boundary coordinates of the tumor be $B(n) = \{(x(n), y(n)), n = 0, 1, ..., L-1\}$ as shown in Figure 5.2.

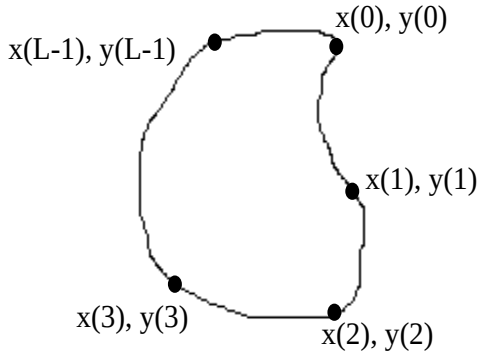

Figure 5.2: Boundary Points of the Tumor

In order to extract WFD, the shape signature $S(n)$ of the boundary points is computed using the centroid distance function as given in Equation (5.1).

$$S(n) = [(x(n) - x_c)^2 + (y(n) - y_c)^2]^{\frac{1}{2}} \tag{5.1}$$

Where,

$$x_c = \frac{1}{L}\sum_{n=0}^{L-1} x(n),\ y_c = \frac{1}{L}\sum_{n=0}^{L-1} y(n) \tag{5.2}$$

Where, $x(n)$ and $y(n)$ represent the x and y coordinates of the n^{th} boundary point, respectively. x_c and y_c represent the x and y coordinates of the of the shape centroid, respectively.

Then, the shape signature is normalized by sampling K boundary points based on equal arc length.

$$n = n + \frac{P}{K} \tag{5.3}$$

$$U(t) = S(n), t = 0, 1, ..., K - 1 \tag{5.4}$$

Where, P is the boundary perimeter and $U(t)$ is the normalized shape signature.

Next, the wavelet transform is applied to $U(t)$ as given in Equation (5.5). In the present work, Mexican hat wavelet is used as it is gives effective representation of the shape details (Yadav et al. 2007).

$$C_a(b) = \frac{1}{\sqrt{|a|}} \int_R U(t)\varphi(\frac{t-b}{a})dt \tag{5.5}$$

Where, $C_a(b)$ are wavelet coefficients at the scale a and position b. After the wavelet transform, WFD are obtained by applying Fourier transform to wavelet coefficients and it is given by,

$$a_n = \frac{1}{N}\sum_{b=0}^{N-1} C_a(b) exp(-j2\pi b/N) \tag{5.6}$$

The Fourier coefficients a_n are called Fourier Descriptors (FDs) of the shape and the first coefficient (FD_0) of FDs is ignored in order to make the shape representation invariant to the boundary starting point. Further, the area of the tumor A is computed based on the number of pixels in the tumor region. Finally, the shape of the tumor is represented by the shape feature vector SFV consisting of the tumor area and FDs as given below:

$$SFV = [A, FD_1, FD_2.....FD_{N-1}]. \tag{5.7}$$

Texture Feature Extraction

Local texture of the tumor is extracted using Gabor filter and Edge Histogram Descriptor (EHD), which are provided by the MPEG-7 standard (Manjunath et al. 2001). These features provide perceptual representation of the image texture and thus help in retrieving most similar images from the database. The Gabor filter extracts the homogeneous texture of the image and EHD represents the local distribution of edges in the image.

Gabor Filter: Texture analysis of the brain/liver tumor is performed by applying a bank of Gabor filters on the tumor image. The 2-D Gabor function $g(x, y)$ is given by,

$$g(x,y) = \frac{1}{2\pi\sigma_x\sigma_y} exp\left[-\frac{1}{2}\left(\frac{x^2}{\sigma_x^2} + \frac{y^2}{\sigma_y^2}\right) + 2\pi jWx\right] \tag{5.8}$$

where, W is the modulation frequency and σ_x^2 and σ_y^2 represent the variance in x and y directions, respectively. A set of self-similar Gabor functions, $g_{mn}(xy)$ are obtained by dilation and rotation of mother Gabor filter using the following generating function:

$$g_{mn}(x,y) = a^{-2m} g(x', y'), a \geq 1 \tag{5.9}$$

$$x' = a^{-m}(xcos(\theta) + ysin(\theta)),\ y' = a^{-m}(-xsin(\theta) + ycos(\theta)) \tag{5.10}$$

where $\theta = \frac{n\pi}{N}$, $m = 0, 1...M-1$, $n = 0, 1, ..N-1$ and a is the scale factor. The parameters M and N specify the total number of scales and orientations, respectively. Based on the experiments, four scales ($M = 4$) and six orientations ($N = 6$) are chosen to describe the tumor texture. Texture features of an image $I(x, y)$ are obtained by convolution of $I(x, y)$ with the Gabor filter g_{mn}(x,y):

$$G_{mn}(x, y) = I(x_1, y_1)g_{mn}(x - x_1, y - y_1) \tag{5.11}$$

The mean (μ_{mn}) and the standard deviation (σ_{mn}) of the filtered images are used to construct a feature vector and these are given by,

$$\mu_{mn} = \frac{1}{P}\sum_x\sum_y |G_{mn}(x, y)| \tag{5.12}$$

$$\sigma_{mn} = \sqrt{\frac{1}{P}\sum_x\sum_y (|G_{mn}(x, y)| - \mu_{mn})^2} \tag{5.13}$$

where, P is the total number of image pixels. The Gabor feature vector GFV for M scales and N orientations is given by,

$$GFV = [\mu_{00}, \sigma_{00}, \mu_{01}, \sigma_{01}.....\mu_{(M-1)}, \sigma_{(N-1)}] \tag{5.14}$$

Edge Histogram Descriptor: EHD represents the local distribution of edges on five different orientations: vertical, horizontal, 45^0 anti-diagonal, 135^0 diagonal and non-directed. The EHD is computed by dividing an image into 4×4 non-overlapping blocks as shown in Figure 5.3.

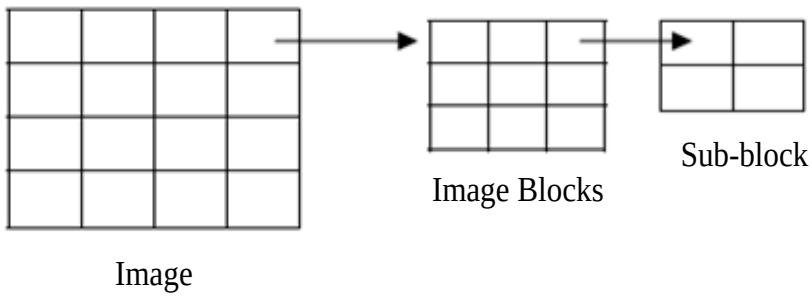

Figure 5.3: Image Partitioning for EHD Computation

This partitioning yields 16 equal sized sub-images. Each sub-image is divided into a number of 3×3 image blocks and each image block is divided into 4 sub-blocks for abstracting the edge histogram. The edge histogram information is obtained by applying five types of edge detectors defined by MPEG-7 on each sub-block as shown in Figure 5.4. This computation results in an edge histogram with $16 \times 5 = 80$ bins.

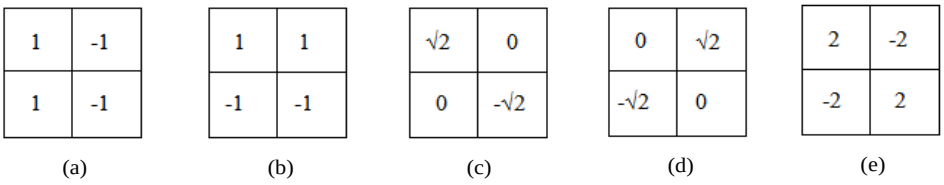

Figure 5.4: Edge Detection Operators: (a) Vertical (b) Horizontal (c) 45^oAnti-diagonal (d) 135^oDiagonal (e) Non-directional

The EHD feature vector EFV consists of bins of the edge occurrence histogram as given below:

$$EFV = [B_1, B_2.....B_{80}] \tag{5.15}$$

Finally, the brain and liver tumor is represented by 268 and 134 subclass features, respectively.

5.2.4 Classification

The classification stage determines the type of the brain/liver tumor as benign or malignant based on selected features. Class features of the tumor selected using IG-ICA technique are fed to the ensemble classifier consisting of SVM, ANN and k-NN classifiers for identifying the type of tumor as benign or malignant. The individual decisions of these classifiers are combined using the majority voting rule (Kittler et al. 1998) as discussed in Chapter 4.

5.2.5 Similarity Matching

Similarity matching identifies the similarity between the query image and images in the database based on the distance measure. In the present research work, the following similarity measures are used to measure the similarity between subclass features of the query image and database images belonging the same tumor class.

- The shape similarity $DS(x, y)$ between two images x and y is given by the Euclidian distance:

$$DS(x,y) = \sqrt{(A^x - A^y)^2 + (\sum_{i=1}^{N-1}(FD_i^{(x)} - FD_i^{(y)})^2)} \tag{5.16}$$

  where, A and FD represent the area and Fourier descriptors of the tumor, respectively.

- The texture similarity $DTG(x, y)$ between two images x and y, with their texture feature vectors obtained by Gabor filter is measured using the Euclidian distance $d_{mn}(x, y)$:

$$DTG(x,y) = \sum_m \sum_n d_{mn}(x,y) \tag{5.17}$$

$$d_{mn}(x,y) = \sqrt{(\mu_{mn}(x) - \mu_{mn}(y))^2 + (\sigma_{mn}(x) - \sigma_{mn}(y))^2} \tag{5.18}$$

  where, μ_{mn} and σ_{mn} are mean and standard deviation of the Gabor filtered image at scale m and orientation n.

- The texture similarity $DTE(x, y)$ between two images x and y, with their texture feature vectors obtained by EHD is given by the Chi-square distance $\chi^2(x, y)$:

$$DTE(x,y) = \chi^2(x,y) = \sum_{k=1}^{K} \frac{[B_x(k) - B_y(k)]^2}{[B_x(k) + B_y(k)]} \tag{5.19}$$

  where, $B_x(k)$ and $B_y(k)$ are k^{th} EHD histogram bins of the images x and y, respectively.

All the similarity measures are normalized and fused to form a single similarity measure as given below:

$$D(x,y) = DS(x,y) + DTG(x,y) + DTE(x,y) \tag{5.20}$$

In order to retrieve M most relevant images from the database, the calculated distances are sorted in the ascending order. Further, the top M distances are selected and the corresponding images are retrieved.

5.2.6 Feature Database Indexing Technique

Instead of exhaustively matching the features of the query image with all features in the database, the preferred approach is to use indexing for faster retrieval of images from the database. Accordingly, in the present research work, an indexing method called CIKD is proposed for efficient processing of Nearest Neighbor (NN) queries as shown in Figure 5.5. In order to reduce the search space, the CIKD technique partitions the subclass features into different clusters using the proposed modified k-means clustering. Further, the dimensionality of the feature vectors in each cluster is reduced using IG-ICA feature selection technique as features are correlated at the local, rather than at the global level. Then within each cluster, the features are indexed using a KD-tree as KD-tree provides a nearest neighbor search with $O(log_2 N)$ efficiency on low-dimensional feature vectors (Javier et al. 2012).

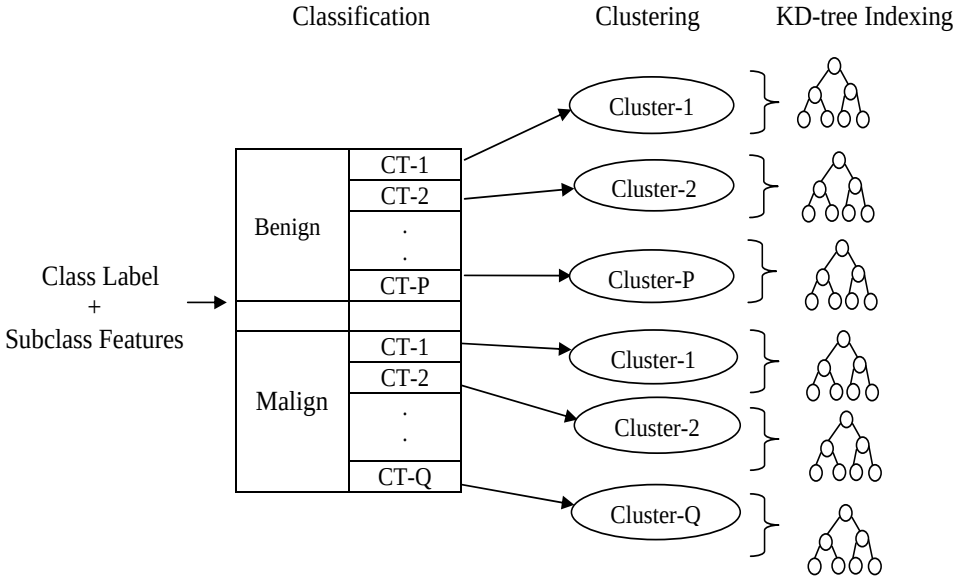

Figure 5.5: Feature Database Index Structure

Given a query image q, its class label is used to assign q to the group of benign or malignant tumor features. Then, the similarity of q to clusters in the database is measured by computing the distance using similarity measure $D(q, CT)$ between the query subclass features and each cluster center CT. The query image is considered as most similar to the cluster with the closest center, and then the query is projected onto the subspace in the nearest cluster. Finally, the M-nearest neighbor search is

performed on the KD-tree to obtain a subset of M images nearest to the query image q. The subset contains all the tumor images satisfying (for all $i \in M$),

$$\| q - i \| < \| q - n \|, \text{for all } n \in (DB - M) \tag{5.21}$$

where $\| \, . \, \|$ is a distance measure and DB represents a set of images in the database.

The KD-tree is a binary search tree which is built from the given feature set by recursively partitioning the tree into two halves at each level. This partitioning is based on the median of the dimension having the largest variance. For example, Figure 5.6 shows the KD-tree built for the given set of features: $\{(7,2)(5,4)(9,6)(2,3)(4,7)(8,1)\}$. In order to search M-nearest neighbors, the query image is first compared with the root node of the tree. If the partitioning dimension of the query image is less than that of the root node, then the left sub-tree is searched for M-nearest neighbors. Otherwise, the right sub-tree is searched. Thus, KD-tree reduces the search time by almost eliminating half of the tree during the searching process.

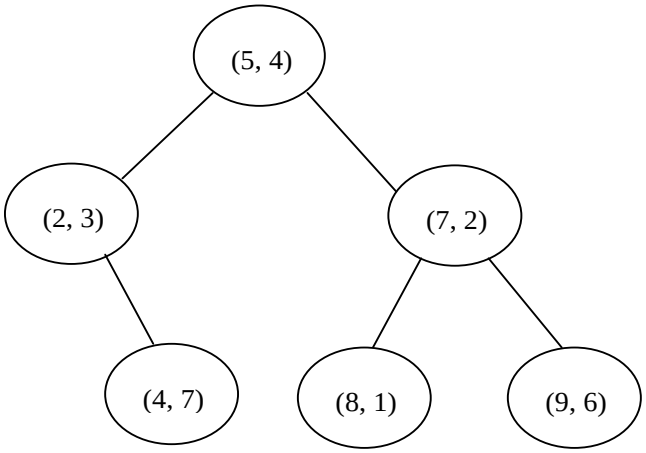

Figure 5.6: KD-tree Construction

5.2.7 Modified K-Means Clustering

The proposed CIKD indexing structure makes use of the proposed modified k-means clustering to partition the subclass features into different clusters. The main drawback of the k-means clustering (MacQueen 1967) is, it requires the user to input the number

of clusters and initial cluster centers. Hence, the results of k-means clustering are sensitive to the given clusters and their centers (Bishnu and Bhattacherjee 2012). In order to overcome these drawbacks, we propose the modified k-means clustering with automatic determination of the number of clusters and initial cluster centers in the given dataset.

Determining Number of Clusters

The optimal number of clusters is determined in the given dataset based on the fusion of several validity indices $V = [V_1, V_2, ...V_r]$ value instead of single validity index. This is because there is no universally best cluster validity index, since the validity index outperforms other validity indices in a particular situation or depending on the shape of clusters (Arbelaitz et al. 2013).

In order to determine the number of clusters, the k-means clustering algorithm (MacQueen 1967) is run on the set of n features with the number of clusters (c) varied between $C_{min} = 2$ and $C_{max} = \sqrt{n}$ (Bezdek and Pal 1998). At the end of each run, clusters of the dataset are evaluated using Dunn, Davies-Bouldin and Jagota indices, which are defined as follows.

- *Dunn Index*: The Dunn Index DI is defined as the ratio of the minimal inter-cluster distance to maximal intra-cluster distance (Dunn 1974) and it is computed by,

$$DI = \min_{1 \le i \le c} \left\{ \min_{1 \le j \le c, j \ne i} \left\{ \frac{d(i,j)}{\max_{1 \le k \le c} d'(k)} \right\} \right\} \tag{5.22}$$

  where, $d(i,j)$ represents the distance between centers of clusters i and j, and $d'(k)$ measures the distance between the pair of elements in cluster k. The clustering algorithm that produces clusters with the highest Dunn index is considered as the best algorithm.

- *Davies-Bouldin Index*: The Davies-Bouldin index DBI is defined as the ratio of the sum of within-cluster (intra-cluster) scatter to between-cluster (inter-cluster) separation (Davies and Bouldin 1979), and it is computed by,

$$DBI = \frac{1}{c} \sum_{i=1}^{c} \max_{i \ne j} \left\{ \frac{\mu_i + \mu_j}{d(K_i, K_j)} \right\} \tag{5.23}$$

where, c is the number of clusters, K_i and K_j represent the center of the cluster i and j, respectively. u_i is the average distance of all elements in the cluster i to center K_i, u_j is the average distance of all elements in the cluster j to center K_j, and $d(K_i, K_j)$ is the distance between centers K_i and K_j. The clustering algorithm that produces a collection of clusters with the smallest Davies-Bouldin index is considered as the best algorithm.

- *Jagota Index*: The Jagota index JI measures the compactness of clusters (Jagota 1991) and it is computed by,

$$JI = \sum_{i=1}^{c} \frac{1}{|C_i|} \sum_{x \in C_i} d(x, K_i) \tag{5.24}$$

where, $|C_i|$ is the number of data items in the cluster i, c is the number of clusters and K_i is the center of i^{th} cluster. The clustering algorithm with the smallest Jagota index is considered as the best algorithm.

After calculating the values of validity indices, min-max normalization (Han et al. 2011) is performed to scale these values to the range [0, 1] as given below:

$$v_i^{'} = \frac{v_i - min_A}{max_A - min_A}(new\_max_A - new\_min_A) + new\_min_A \tag{5.25}$$

where, min_A and max_A are the minimum and maximum values of an attribute A. min-max normalization maps the value, v_i, of an attribute A to $v_i^{'}$ in the range $[new\_min_A, new\_max_A]$.

The maximum value of Dunn index, and minimum values of Davies-Bouldin and Jagota indices indicates the best clustering solution. Thus to have consistency, we have used $(1 - DI)$ to make a minimum value of the Dunn index as an indicator of the best clustering. Then, the values of cluster validity indices of each run are combined by computing the median. Finally, the number of clusters corresponding to the minimum fused index value is considered as the optimal number of clusters.

The complete steps of the proposed algorithm for determining the number of clusters are given in Algorithm 5.1. Since, the Algorithm 5.1 runs the k-means clustering algorithm $C_{max} = \sqrt{n}$ times, its time complexity is $O(\sqrt{n}tcn)$. Where, t is the number of iterations required by the k-means algorithm to converge, c is the number of clusters, and n is the number of subclass feature sets.

Algorithm 5.1 Estimate_Clusters

Input: Set of n Tumor subclass features.

Output: Number of clusters c in the feature set.

1: Choose the range of clusters with C_{min} and C_{max}.
2: **for** $c = C_{min}$ to C_{max} **do**
3: Initialize c cluster centers.
4: Apply K-means algorithm to update the membership matrix and the cluster centers (c).
5: Test for convergence. If not converged go to step 4.
6: Compute value of validity indexes $V(c) = [V_1, V_2...V_r]$.
7: **end for**
8: Normalize values of validity indexes in V.
9: Combine the normalized values using median-based decision fusion to obtain single index, $I(c)$.
10: Choose number of clusters that give optimum value of index, $I(c)$.

Cluster Center Initialization

Clustering is considered as optimal if it minimizes the intra-cluster distance and maximizes the inter-cluster distance. Thus, in the present research work, the initial centers are selected based on the maximum distance. For a given dataset $S = 0, 1..., n-1$, a distance $D(i, j)$ is computed between every pair of elements i and j in the given dataset S. For given c clusters, the first two cluster centers chosen are the data items that have maximum distance $D(i, j)$. Next, these data items are removed from the dataset S, and then the distance is calculated between the remaining data item and the selected cluster centers. The data item that is farthest from its nearest cluster is chosen as the next cluster center and it is removed from the dataset S. This process is repeated until c cluster centers are chosen. The complete steps of the proposed algorithm for automatically initializing the cluster centers is given in Algorithm 5.2. The Algorithm 5.2 has a time complexity of $O(n^2) + O(nc)$. Where, n^2 is the number of distance computations made between all n feature sets. nc is the number of distance computation made between n feature sets and c cluster centers.

Like the k-means clustering algorithm, the modified k-means clustering algorithm also partitions the given dataset based on the distance from the cluster center. But, it begins with automatic determination of the number of clusters and initial cluster centers instead of random initialization as given in Algorithm 5.3.

Algorithm 5.2 ClusterCenter_Init

Input: Number of clusters c, Set of n tumor subclass features.

Output: Cluster centers $\{C_1, C_2, ...C_k\}$.

1: Let S = 0,1,...n-1 represent the data set.
2: For each $(i, j) \in S^2$, compute distance $D(i, j)$
3: $(i^*, j^*) = \arg\max_{(i,j) \in S^2} D(i, j)$
$C_1 = i^*$
$C_2 = j^*$
$S = S - \{i^*\} - \{j^*\}$
4: **repeat**
5: For each $h \in S$, compute $dist(h, \{C_1, C_2, ...C_k\})$.
6: Choose the data item that is farthest from the nearest cluster as the next cluster center.
7: $C(k + 1) = farthest\_item.$
8: $S = S - \{farthest\_item\}$.
9: **until** $k \neq Number\ of\ clusters$

Algorithm 5.3 Modified k-Means Clustering

Input: Set of n tumor subclass features.

Output: Set of c clusters of the subclass features.

1: Determine number of clusters in the given feature set using Algorithm 5.1.
2: Let c be the number of clusters determined by Algorithm 5.1.
3: Select c initial cluster centers $K = [K_1, K_2, ..., K_c]$ using Algorithm 5.2.
4: Calculate distance between each data point and cluster centers.
5: Assign each data point to its closest cluster center.
6: Recalculate the new cluster centers.

$$K_i = \frac{1}{n_i} \sum_{i=1}^{n_i} x_i \tag{5.26}$$

Where, x_i and n_i are the data point and number of data points in the i^{th} cluster, respectively.

7: Recalculate the distance between each data point and new cluster centers.
8: If no data point is reassigned to the clusters, then STOP. Otherwise, repeat from step 5.

5.2.8 Experimental Results and Discussion

In order to test the performance of the proposed CBIR method, several experiments are carried out on brain and liver tumor datasets. The ground truth for the CBIR experiments is defined based on histopathological analysis of biopsy samples of tumors. The performance of the proposed CBIR method is measured in terms of effectiveness and efficiency. The effectiveness of the CBIR method for retrieving the most similar images from the database is quantified using standard performance metrics, namely Precision and Recall. These metrics are computed as given below.

$$Precision(P) = \frac{No.\ of\ relevant\ images\ retrieved}{No.\ of\ images\ retrieved} \times 100 \tag{5.27}$$

$$Recall(R) = \frac{No.\ of\ relevant\ images\ retrieved}{No.\ of\ relevant\ images\ in\ the\ database} \times 100 \tag{5.28}$$

In order to calculate P and R, all the images in the database are considered as query images and for each query image the number of retrieved images M is varied. Then, the values of P and R are averaged at each value of M over all queries to obtain the effectiveness of the CBIR method. The retrieval efficiency is measured in terms of the amount of time required to retrieve most similar images from the database using the proposed indexing technique. The CBIR results of brain and liver tumors are given in the following sections.

CBIR Results of Brain Tumor

The brain tumor retrieval experiments are carried out on a database consisting of T1-weighted post-contrast and T2-weighted brain tumor MRI images of 820 patients (female: 382, male: 438). Among 820 patients, 420 patients were diagnosed with benign tumor and 400 patients with malignant tumor based on histopathological analysis of biopsy samples. The details of the dataset are already given in Section 2.8. The retrieval effectiveness and efficiency of the proposed CBIR method in retrieving most similar brain tumor images from the database are detailed below.

Retrieval Effectiveness

In order to test the robustness of the proposed CBIR method, some of the images in the dataset are rotated by $10^o, 15^o, 20^o$ and 25^o in clockwise and anti-clockwise direc-

tions. Given a query image, the CBIR system extracts the class and subclass features of the tumor and obtains the class label using class features with ensemble classifier. The subclass features of the query image are compared with subclass features of the tumor images in the database with the same class label using the similarity measure $D(x, y)$, which is defined in Section 5.2.5. The retrieved images are ordered based on their similarity to the query image. Figure 5.7 shows the top 11 most similar brain tumor images retrieved along with the patient's identification number PID in response to the query image. Based on the PID, the radiologist can refer the diagnosis reports of the patient for more detailed analysis of the tumor characteristics, such as severity, prescribed treatment, etc. The retrieved images and their diagnostic reports help the radiologist to make a diagnostic decision about the given query MRI image of the brain tumor.

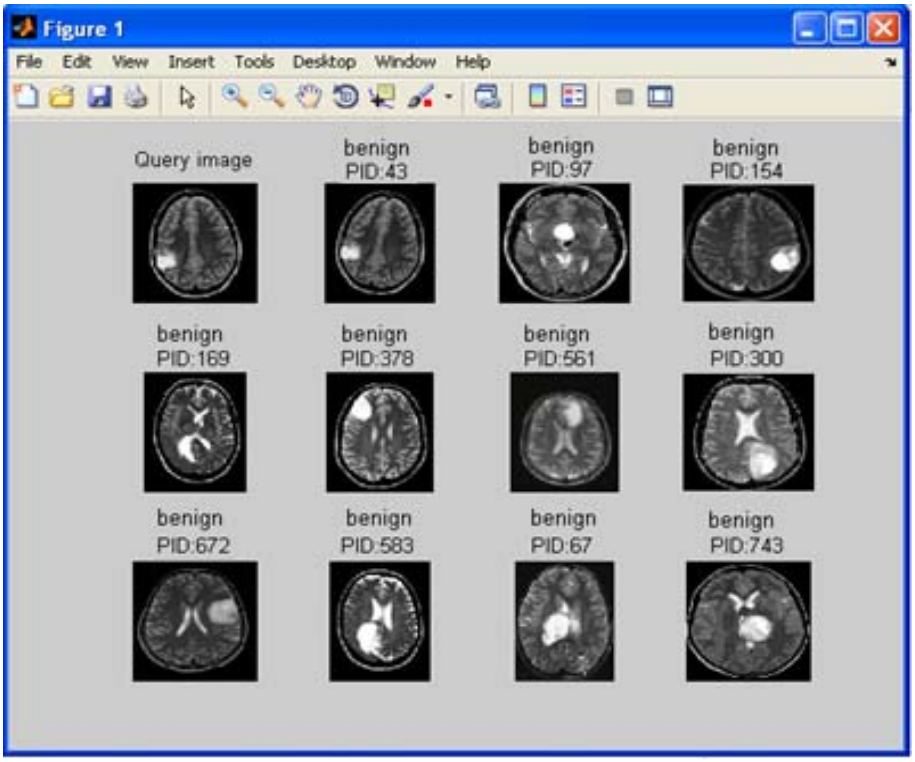

Figure 5.7: Brain Tumor Retrieval Results

In the classification stage, the ensemble classifier consisting of SVM, ANN and k-NN classifiers is used to classify the brain tumor as benign or malignant based on the class features selected by IG-ICA. Table 5.1 shows the confusion matrix of the

tumor classifications obtained by the ensemble classifier. All the malignant tumors are correctly classified, whereas 5 benign tumors are misclassified as malignant tumors. Further, the classification performance measures that are discussed in Section 4.2 are

Table 5.1: Ensemble Classification of Brain Tumor

	Predicted Class	
Actual Class	Benign	Malignant
Benign	415	5
Malignant	0	400

computed based on the confusion matrix of the ensemble classifier as shown in Table 5.2. The correct classification of malignant tumors resulted in 100% sensitivity and incorrect classification of benign tumors resulted in 98.80% specificity. Hence, the overall classification accuracy obtained by the ensemble classifier is 99.39%.

Table 5.2: Performance Measures of Ensemble Classification of Brain Tumor

Performance Metrics	**Classifier Performance**
Sensitivity	100%
Specificity	98.80%
Accuracy	99.39%
Az	0.991

The shape description of the tumor based on Wavelet-based Fourier Descriptors (WFD) gives a large set of Fourier coefficients. Further, the number of boundary points of the tumor may not be equal due to the varying sizes of the tumor, and this creates problem in similarity matching. In order to estimate the number of Fourier coefficients necessary for shape matching, we carried out an experiment with 10 to 30 WFDs, which are selected based on equal arc length normalization. With 10 or 20 WFDs we could obtain the global description of the object, but finer details were missing. Whereas an optimal tumor shape description is obtained with 30 WFDs, and therefore 30 WFDs are used for the tumor retrieval.

The effectiveness of the WFD in representing tumor shape details is evaluated by comparing it with other state-of-the-art shape descriptors based on a Precision-Recall

graph (P-R graph) as shown in Figure 5.8. WFD and Curvature Scale Space (CSS) (Mokhtarian et al. 1999) are contour-based shape descriptors, whereas a Zernike moment descriptor (ZMD) and Grid Descriptors (GD) (Lu and Sajjanhar 1999) are region-based shape descriptors. ZMD (Manjunath et al. 2001) is more effective (P: 90%, R: 95.12%) in retrieving similar shapes when compared to CSS (P: 81.02%, R: 93.10%) and GD (P: 72.98%, R: 93%). However, ZMD loses the important perceptual meaning. The highest retrieval effectiveness is obtained with WFD (P: 98.16%, R: 97.35%) as it applies Fourier transform on the wavelet coefficients. Further, WFDs are much easier to derive, match, normalize, and more compact compared to other shape descriptors.

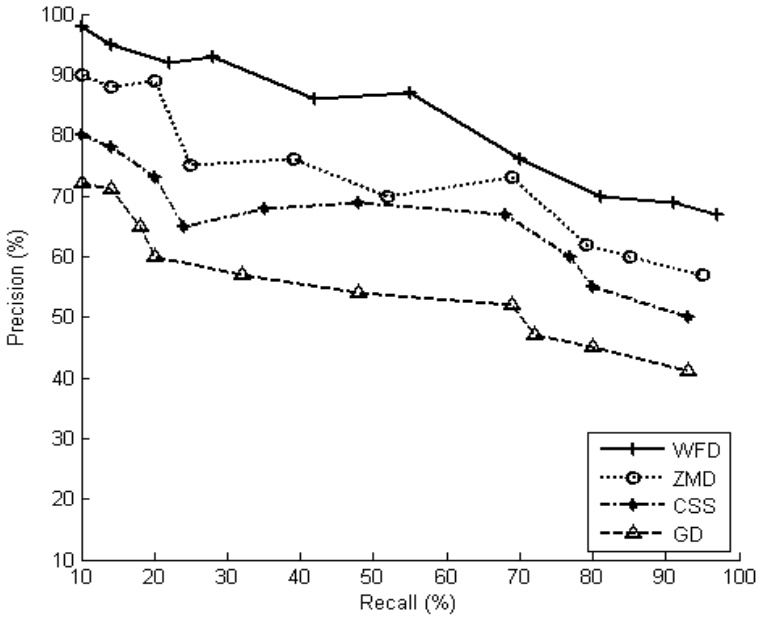

Figure 5.8: Performance Comparison of Shape Descriptors in CBIR of Brain Tumor

The MPEG-7 Gabor filter and EHD describe homogeneous and non-homogeneous texture of the tumor. The performance of Gabor filter and EHD is compared with other texture descriptors, such as Gray Level Co-occurrence Matrix (GLCM) (Haralick et al. 1973) and Tamura (Tamura et al. 1978). The performance comparison of these texture features, and the combination of texture and shape features for representing the tumor subclass is given in Table 5.3. It is observed that the retrieval accuracy improves when shape descriptor WFD is combined with texture descriptors.

The GLCM and Tamura texture features show poor performance when compared to Gabor and EHD. Whereas the performance of Gabor and EHD is almost similar, and these texture descriptors perform better when used together for representing the subclass of the tumor. The proposed combination of shape and texture features extracted using WFD, Gabor filter and EHD achieves the highest Precision and Recall of 98.16% and 97.35%, respectively.

Table 5.3: Performance Comparison of Feature Descriptors in CBIR of Brain Tumors

Feature Descriptors	**Precision (%)**	**Recall (%)**
Gabor Filter	92.52	88.41
EHD	90.11	93.53
GLCM	85.62	83.0
Tamura	82.18	79.31
Gabor Filter+WFD	95.0	94.86
EHD+WFD	94.72	95.20
GLCM+WFD	92.55	88.53
Tamura+WFD	90.60	88.15
Gabor Filter+EHD+WFD(Proposed)	98.16	97.35

The comparison of shape and texture similarity measures is shown in Figure 5.9.

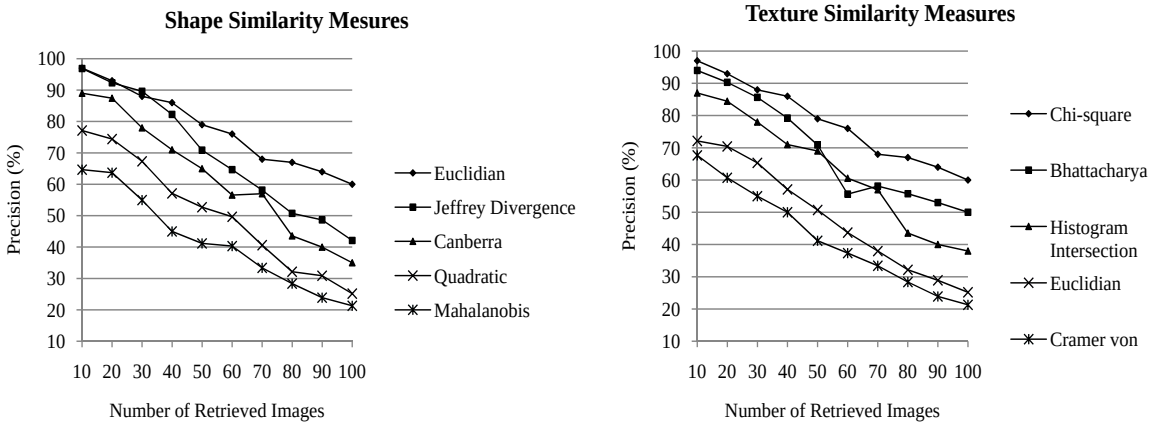

Figure 5.9: Performance Comparison of Similarity Measures in CBIR of Brain Tumors

In addition to tumor features, the feature similarity measure also has a vital effect on the retrieval results. Thus, we experimented with various similarity measures to evaluate their performance in retrieving similar brain tumor shapes and textures as shown in Figure 5.9. It is found that Euclidian and Chi-square distances give good retrieval performance when used for comparing shape and texture features, respectively. Thus, in the present work, Euclidian and Chi-square distances are used as shape and texture similarity measures, respectively.

In order to provide fast retrieval results, the proposed CIKD indexing method prunes the search space by clustering subclass features based on the modified k-means clustering algorithm. The modified k-means clustering algorithm makes use of the proposed Algorithm 5.1 and Algorithm 5.2 for determining the number of clusters and initial cluster centers, respectively. The performance of these algorithms is tested on brain tumor dataset as well as on three standard datasets (Iris, Wine, Glass) from UCI[1] machine learning repository. Table 5.4 shows the number of clusters determined in the MRI benign brain tumor dataset by the proposed algorithm (Algorithm 5.1).

Table 5.4: Estimation of Number of Clusters in Benign Brain Tumor Dataset

No. of Clusters	**Cluster Validity Indices**			**Index Fusion**
	Dunn	**Davies-Bouldin**	**Jagota**	
2	0.85	0.83	0.69	0.83
3	0.80	0.59	0.72	0.72
4	0.68	0.27	0.53	0.53
5	0.38	0.24	0.19	0.24
6	0.16	0.20	0.21	0.20
7	**0.06**	**0.09**	**0.17**	**0.09**
8	0.08	0.14	0.20	0.14
9	0.15	0.21	0.23	0.19
10	0.18	0.27	0.25	0.25

In the experiments, the number of clusters is varied between $C_{min} = 2$ and $C_{max} = \sqrt{n}$, where n indicates the number of features to be clustered. For simplicity, only

[1] *University of California, Irvine*

10 entries are shown in the Table 5.4. The clustering results obtained in each run of the k-means algorithm are evaluated using Dunn, Davies-Bouldin and Jagota index and the values of these indices are fused by computing the median. The minimum fused index value indicates the optimal number of clusters. The algorithm identifies 7 clusters in the benign brain tumor dataset as shown in Table 5.4. Based on the similar experiments, 5 clusters are identified in the malignant brain tumor dataset. Table 5.5 shows the number of clusters estimated by Algorithm 5.1 in the UCI dataset. It is observed that the algorithm correctly identifies the number of clusters in the datasets.

Table 5.5: Estimation of Number of Clusters in UCI Datasets

Dataset	**Number of Data Points**	**Number of Known Clusters**	**Number of Estimated Clusters**
Iris	150	3	3
Wine	178	3	3
Glass	214	6	6

Further, the effectiveness of the proposed algorithm (Algorithm 5.2) for determining initial cluster centers is measured in terms of average Cluster Center Proximity (CCP) (Khan and Ahmad 2004) as shown in Table 5.6. The value of CCP indicates the difference between the actual and initial cluster centers.

Table 5.6: Comparison of Cluster Center Initializations

Dataset	**CCP**	
	Random Initialization	**Proposed Initialization**
Iris	0.76	0.24
Wine	0.27	0.05
Glass	0.48	0.19
Benign Brain Tumor	0.62	0.10
Malignant Brain Tumor	0.45	0.07

The CCP is computed by,

$$CCP = \frac{1}{K \times m} \sum_{s=1}^{K} \sum_{j=1}^{m} |\frac{f_{sj} - C_{sj}}{f_{sj}}| \tag{5.29}$$

where, f_{sj} and C_{sj} indicate j^{th} attribute value of the actual cluster center and initial cluster center, respectively. It is observed from Table 5.6 that proposed algorithm estimates initial cluster centers nearer to actual cluster centers when compared to random initialization in both UCI and brain tumor datasets.

Retrieval Efficiency

The CBIR method makes use of the proposed CIKD indexing technique for fast retrieval of images. Let N and D be the number of feature vectors and their original dimensions, respectively. Let C be the number of feature clusters, and $N^{(h)}$ and D' be the number of feature vectors in cluster h ($h = 1, 2...C$) and their reduced dimensions, respectively.

The proposed CIKD indexing technique computes the distance between the given query image and cluster centers of the subclass features based on the similarity measure. It takes constant amount of time to compare features of the query image with cluster center. Thus, the time taken for computing the distance between the query image and C cluster centers of dimension D is given as follows.

$$\begin{aligned} T &= \sum_{i=1}^{C} \sum_{j=1}^{D} 1 \\ &= \sum_{i=1}^{C} (D - 1 + 1) \\ &= D(C - 1 + 1) \\ &= DC \end{aligned} \tag{5.30}$$

Hence, the time complexity of computing the distance between the query image and all cluster centers is $O(DC)$. After computing the distances, the smallest distance is determined among C distances in order to find the closest cluster center. The comparison between two distances takes a constant amount of time, and accordingly the time taken to make C distance comparisons is given in Equation 5.31.

$$\begin{aligned} T &= \sum_{i=1}^{C} 1 \\ &= C - 1 + 1 \\ &= C \end{aligned} \tag{5.31}$$

Thus, the time complexity of finding the smallest distance is $O(C)$. The cluster center having the smallest distance is considered as the closest to the query image.

The query image is assigned to corresponding cluster and executed on the KD-tree with the reduced dimension in order to find the most similar images. If the KD-tree consists of only one node, then one comparison is made with that node. If the KD-tree consists of N nodes, then on the average, the search for the most similar images in the KD-tree is only in the half of the tree. Therefore, in this case, the total number of comparisons is $T(\frac{N}{2})$ plus one comparison for identifying the partitioning dimension. Thus, the recurrence relation for the search in KD-tree of N nodes can be expressed as:

$$T(N) = \begin{cases} 1 & \text{if } N = 1 \\ T(\frac{N}{2}) + 1 & \text{otherwise} \end{cases} \tag{5.32}$$

The above equation can be solved by considering $N = 2^k$.

$$\begin{aligned} T(\frac{N}{2}) &= T(2^{k-1}) + 1 \\ &= T(2^{k-2}) + 1 + 1 \\ &= T(2^{k-2}) + 2 \\ &= T(2^{k-3}) + 3 \\ &\cdots \\ &= T(2^{k-k}) + k \\ &= T(1) + k = k \\ &= 1 + k = 1 + log_2 N \approx log_2 N \end{aligned} \tag{5.33}$$

The feature vectors in the KD-tree are with reduced dimension D' and, hence the time complexity of searching the KD-tree for most similar images is $O(D' log_2 N)$. The total time complexity of CIKD indexing is $O(DC) + O(C) + O(D' log_2 N^{(h)})$.

Table 5.7 shows the comparison of time complexity of different indexing methods for processing nearest neighbor queries. The exhaustive indexing is a brute force ap-

Table 5.7: Comparison of Database Indexing Techniques

Indexing Method	**Exhaustive** Indexing	**Cluster-based** Indexing	**CIKD** (Proposed)
Time Complexity	$O(DN)$	$O(DC) + O(C) + O(D'N^{(h)})$	$O(DC) + O(C) + O(D'log_2N^{(h)})$

proach and compares subclass features of the query image with subclass features of all images in the database. Hence, it has a time complexity of $O(DN)$ and consumes more time to retrieve similar tumor images from the database.The cluster-based indexing reduces the search time by comparing subclass features of the query image with subclass features of all the images in the cluster closest to the query image. Hence, it has a time complexity of $O(DC) + O(C) + O(D'N(h))$ and performs better than exhaustive search. The proposed CIKD method takes $O(DC) + O(C) + O(D'log_2N^h)$ and performs better than exhaustive and cluster-based methods, since it has a combination of modified k-means clustering, IG-ICA and KD-tree. The use of clustering and IG-ICA feature selection prunes the search space by limiting the query to lower dimensional space of the closest cluster instead of searching the entire database. Also, the KD-tree gives good search performance of log_2N in lower dimensional space. Thus, the proposed indexing method narrows down the search space and thus accelerate the retrieval task. The CIKD method takes about 2-3 sec to retrieve most similar images from the database in response to the query image.

CBIR Results of Liver Tumor

This section discusses the results of the CBIR experiments carried on the liver tumor database consisting of abdominal CT images of 764 patients. Among 764 patients, 380 patients were diagnosed with benign tumor and 384 patients with malignant tumor based on histopathological analysis of biopsy samples. The details of the dataset are already given in Section 2.8. Experiments similar to brain tumor also performed on a liver tumor database. The effectiveness and efficiency of the proposed CBIR

method in retrieving most similar liver tumor images from the liver tumor database are detailed below.

Retrieval Effectiveness

To test the robustness of the proposed CBIR method, some of the images in the dataset are rotated by $10^o, 15^o, 20^o$ and 25^o in clockwise and anti-clockwise directions. Given a query image, the CBIR system extracts the class and subclass features of the tumor and obtains the class label using class features with ensemble classifier. The subclass features of the query image are compared with subclass features of the tumor images with the same class label in the database using the similarity measure $D(x, y)$, which is defined in Section 5.2.5. The retrieved images are ordered based on their similarity to the query image. Figure 5.10 shows the top 11 most similar liver tumor images which are retrieved along with the patient's identification number PID in response to the query image.

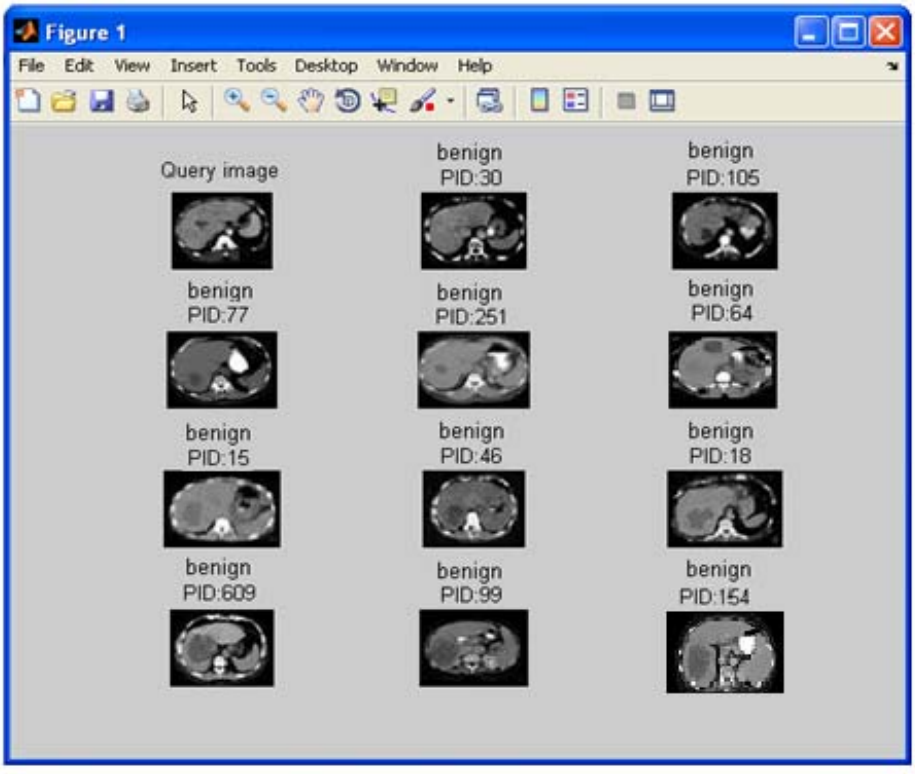

Figure 5.10: Liver Tumor Retrieval Results

Based on the PID, the radiologist can refer the diagnostic reports of the patient for more detailed analysis of the tumor with respect to severity, prescribed treatment, etc. It can be seen that both the query image and the retrieved images are benign. This shows that the CBIR method effectively retrieves most similar images from the database in response to the query image. The retrieved images and their diagnosis reports help the radiologist to make a diagnostic decision about the given query CT image of the liver tumor.

In the classification stage, the ensemble classifier consisting of SVM, ANN and k-NN classifiers is used to classify the liver tumor as benign or malignant based on the class features. Table 5.8 shows the confusion matrix of the tumor classifications obtained by the ensemble classifier. It is observed that all the malignant tumors are correctly classified, whereas 7 benign tumors are misclassified as malignant tumors. The classification performance of the ensemble classifier is measured in terms

Table 5.8: Ensemble Classification of Liver Tumors

	Predicted Class	
Actual Class	Benign	Malignant
Benign	373	7
Malignant	0	384

of sensitivity, specificity and accuracy as discussed in Section 4.2. The performance measures computed based on the confusion matrix of ensemble classifier are shown in Table 5.9. The correct classification of malignant tumors resulted in 100% sensitivity and incorrect classification of benign tumors resulted in 98.15% specificity. Hence, the overall classification accuracy obtained by the ensemble classifier is 99.08%.

Table 5.9: Performance Measures of Ensemble Classification of Liver Tumors

Performance Metrics	**Classifier Performance**
Sensitivity	100%
Specificity	98.15%
Accuracy	99.08%
Az	0.989

The shape description of the liver tumor based on Wavelet-based Fourier Descriptors (WFD) gives a large set of Fourier coefficients. Further, the number of boundary points of the tumor may not be equal due to the varying sizes of the tumor, and this creates problem in similarity matching. Thus, based on the experiments, 30 WFDs are considered optimal for the liver tumor retrieval. These 30 WFDs are selected from the boundary points based on equal arc length normalization.

The effectiveness of the WFD in representing the shape of liver tumors is evaluated by comparing it with other state-of-the-art shape descriptors based on a Precision-Recall graph (P-R graph) as shown in Figure 5.11. WFD and Curvature Scale Space (CSS) (Mokhtarian et al. 2005) are contour-based shape descriptors, whereas a Zernike Moment Descriptor (ZMD) and Grid Descriptors (GD) (Lu and Sajjanhar 1999) are region-based shape descriptors. ZMD (Manjunath et al.2001) is more effective (P: 92.12%, R: 94%) in retrieving the similar shape when compared to CSS (P: 77.03%, R: 92.13%) and GD (P: 70%, R: 92.13%). However, ZMD loses the important perceptual meaning. The highest retrieval effectiveness is obtained with WFD (P: 97.83%, R: 97.02%) as it applies Fourier transform to the wavelet coefficients.

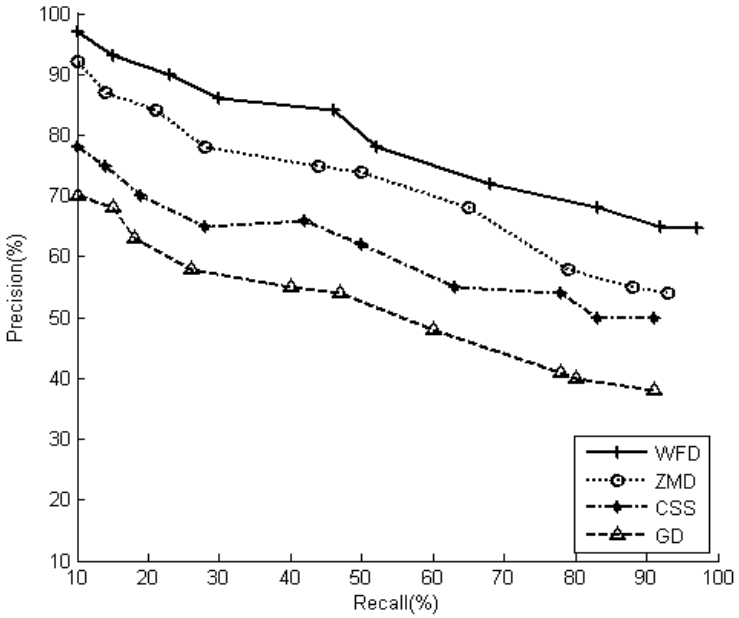

Figure 5.11: Performance Comparison of Shape Descriptors in CBIR of Liver Tumors

The MPEG-7 Gabor filter and EHD describe homogeneous and non-homogeneous texture of the tumor. The performance of Gabor filter and EHD is compared with other texture descriptors, such as Gray Level Co-occurrence Matrix (GLCM) (Haralick et al. 1973) and Tamura (Tamura et al. 1978). The performance comparison of these texture features, and the combination of texture and shape features for representing the tumor subclass is given in Table 5.10. It is observed that the retrieval accuracy improves when shape descriptor WFD is combined with texture descriptors. The GLCM and Tamura texture features show poor performance when compared to Gabor and EHD. Whereas the performance of Gabor and EHD is almost similar, and these texture descriptors perform better when used together for representing the subclass of the tumor. The proposed combination of shape and texture features extracted using WFD, Gabor filter and EHD achieves the highest Precision and Recall of 98.83% and 97.02%, respectively.

Table 5.10: Performance Comparison of Feature Descriptors in CBIR of Liver Tumors

Feature Descriptors	**Precision (%)**	**Recall (%)**
Gabor Filter	94.17	88.41
EHD	90.26	89.33
GLCM	83.58	80.14
Tamura	82.02	80.09
Gabor Filter+WFD	94.91	93.67
EHD+WFD	92.43	90.22
GLCM+WFD	92.55	88.53
Tamura+WFD	86.52	88.15
Gabor Filter+EHD+WFD(Proposed)	97.83	97.02

In addition to tumor features, the feature similarity measure also has a vital effect on the retrieval results. Thus, we experimented with various similarity measures to evaluate their performance in retrieving similar liver tumor shapes and textures as shown in Figure 5.12. It is found that Euclidian and Chi-square distances give good retrieval performance when used for comparing liver tumor shape and texture features, respectively, and thus these distances are used in the present work.

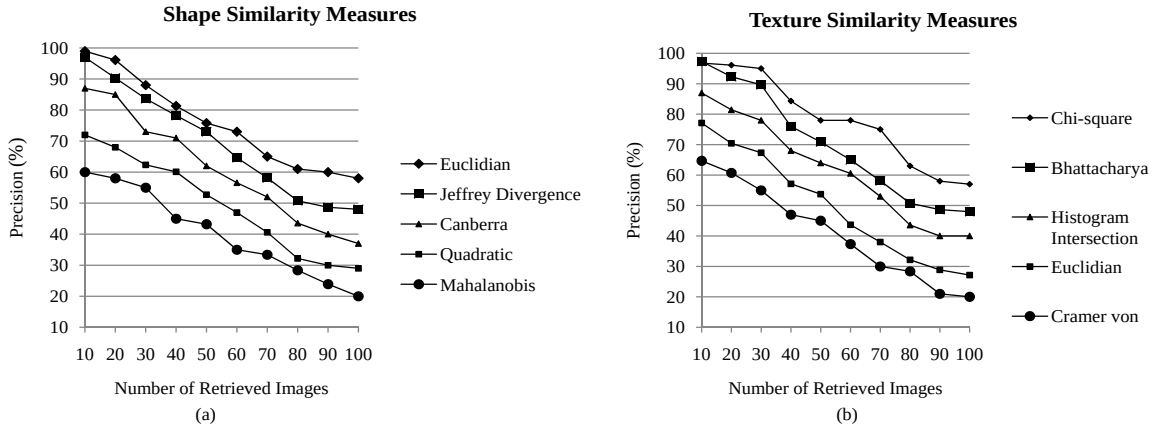

Figure 5.12: Comparison of Similarity Measures in CBIR of Liver Tumors

In order to provide faster retrieval results, the proposed CIKD indexing method prunes the search space by clustering subclass features based on the modified k-means clustering algorithm. The modified k-means clustering algorithm makes use of the proposed algorithms (Algorithm 5.1 and Algorithm 5.2) for determining the number of clusters and initial cluster centers, respectively.

Table 5.11 shows the number of clusters determined in the CT benign liver tumor dataset by the proposed algorithm (Algorithm 5.1). In the experiments, the number of clusters is varied between $C_{min} = 2$ and $C_{max} = \sqrt{n}$, where n indicates the number of features to be clustered. For simplicity, only 10 entries are shown in the Table 5.11. The clustering results obtained in each run of the k-means algorithm are evaluated using Dunn, Davies-Bouldin and Jagota index and the values of these indices are fused by computing the median. The minimum fused index value indicates optimal clustering. The algorithm identifies 4 clusters in the benign liver tumor dataset as shown in Table 5.11. Based on the similar experiments, 5 clusters are identified in the malignant liver tumor dataset.

Further, the effectiveness of the proposed algorithm (Algorithm 5.2) for determining initial cluster centers is measured in terms of average Cluster Center Proximity (CCP), which gives the difference between the actual and initial cluster centers. The CCP is computed using Equation (5.29). Table 5.12 shows the comparison between the effectiveness of random and proposed cluster center initializations. It is observed that the proposed algorithm (Algorithm 5.2) estimates initial cluster centers nearer

to actual cluster centers when compared to random initialization in both benign and malignant liver tumor datasets.

Table 5.11: Estimation of Number of Clusters in Benign Liver Tumor Dataset

No. of Clusters	**Cluster Validity Indices**			**Index Fusion**
	Dunn	**Davies-Bouldin**	**Jagota**	
2	0.36	0.21	0.23	0.23
3	0.10	0.15	0.14	0.14
4	**0.06**	**0.03**	**0.11**	**0.06**
5	0.13	0.11	0.20	0.13
6	0.18	0.23	0.26	0.23
7	0.23	0.37	0.33	0.33
8	0.30	0.45	0.35	0.35
9	0.35	0.49	0.41	0.41
10	0.46	0.55	0.43	0.46

Table 5.12: Comparison of Cluster Center Initializations in Liver Tumor Dataset

Dataset	**CCP**	
	Random Initialization	**Proposed Initialization**
Benign Liver Tumor	0.36	0.06
Malignant Liver Tumor	0.38	0.14

Retrieval Efficiency

Similar to the brain tumor retrieval, the proposed CIKD indexing technique is also more efficient in retrieving liver tumor images from the database when compared to the exhaustive search and cluster based indexing methods. The liver tumor retrieval based on CIKD has a time complexity of $O(DC) + O(C) + O(D'log_2N^{(h)})$ due to the combination of modified k-means clustering, IG-ICA feature selection and KD-tree. The N and D are the number of feature vectors and their original dimensions,

respectively. C is the number of feature clusters, and $N^{(h)}$ and D' are the number of feature vectors in cluster h ($h = 1, 2...C$) and their reduced dimensions, respectively.

5.3 CBIR Based on Rotation Invariant Features

MRI/CT images may be misaligned due to movement of the patient during scanning. The rotation changes the features of the image, and hence finding similarity between images becomes difficult. Thus, in this proposed CBIR method, the tumor characteristics in the misaligned image are represented using rotation invariant features. Then, most similar images are retrieved from the database using similarity matching. The various steps of the proposed CBIR method are detailed below.

5.3.1 Preprocessing

Prior to segmentation, the quality of MRI/CT images is enhanced by image denoising based on the median and Laplacian filters, image contrast enhancement using histogram equalization, and rotation correction of misaligned image using the proposed rotation correction technique. The T1-weighted and T2-weighted MRI images of the brain are co-registered using the FLIRT registration tool (Jenkinson and Smith 2001) as discussed in Chapter 3.

5.3.2 Segmentation

After preprocessing, the input image is segmented in order to extract the tumor region for further analysis. If the input image is the MRI image of the brain, then the image is segmented using the proposed brain tumor segmentation technique based on Modified Fuzzy C-Means (MFCM) clustering. If the input image is the abdominal CT image of the liver, then the image is segmented using the proposed liver tumor segmentation method based on automatic region growing. The brain and liver tumor segmentation methods are already discussed in Chapter 3.

5.3.3 Feature Extraction

In the proposed CBIR method, the segmented tumor is represented using the extracted class and subclass features from the tumor representative slice. In case of

brain tumor analysis, a representative slice is selected from both T1-weighted post-contrast and T2-weighted MRI images of the brain, and in case of liver tumor analysis, a representative slice is chosen from a set of non-enhanced abdominal CT images of the liver. The details of the tumor class and subclass features are given below.

Tumor Class Representation: The features that represent the class of the tumor as benign or malignant are extracted from the wavelet decomposed 2D image using global shape, image histogram, Gray Level Co-occurrence Matrix (GLCM), wavelet energy and fractal dimension as discussed in Chapter 4. The features extracted using global shape and image histogram are rotation invariant. But, other features such as GLCM, wavelet energy and fractal dimension are sensitive to image rotations, and thus these are made rotation invariant as follows.

- The GLCM obtained at four angles ($0^o, 45^0, 90^0$ and 135^o) is made rotation invariant by constructing symmetric GLCM such that $M_{0^o}^T = M_{180^o}, M_{45^o}^T = M_{225^o}, M_{90^o}^T = M_{270^o}, M_{135^o}^T = M_{315^o}$ and the features extracted from these matrices are averaged over the four angles (Eleyan and Demirel 2011).
- In order to make the wavelet energy feature invariant to rotation, the HL (horizontal) and LH (vertical) sub-bands in each level of decomposition are grouped together by taking the average of the energy features extracted from HL and LH sub-bands (Manthalkar et al. 2003).
- The fractal dimension which describes the irregularity of tumor boundary is made rotation invariant by applying central projection transform on the tumor boundary to generate a unique boundary, and then the fractal dimension of the generated boundary is calculated (Tao et al. 2001).

The most discriminating class features are selected based on the IG-ICA feature selection technique as discussed in Chapter 4.

Tumor Subclass Representation: In order to represent the subclass of the tumor, the following local shape and texture features are extracted from the representative slice of the tumor.

Shape Feature Extraction

The local shape of the tumor is described using rotation invariant wavelet-based Fourier Descriptors (WFD) (Kunttu et al. 2006). The WFDs are extracted using the procedure as discussed in Section 5.2.3. But, the extracted WFDs are made rotation invariant. That is in the first step, shape signature of the boundary is obtained based on the centroid distance of the boundary points. Next, the shape signature is normalized based on the equal arc length. Then, the wavelet transform is applied to the shape signature. Finally, the Fourier transform is applied on the wavelet coefficients to get a set of Fourier coefficients describing the tumor shape. These Fourier coefficients are known as FDs and they are denoted as $FD_1, FD_2, ...FD_{N-1}$. The extracted FDs of the tumor are made invariant to rotation by ignoring the phase information. The area A of the tumor is calculated based on the number of pixels in the tumor in order to retrieve the tumors of similar size. The complete shape feature vector SFV, representing the shape of the tumor is given as:

$$SFV = [A, FD_1, FD_2.....FD_{N-1}]. \tag{5.34}$$

Texture Feature Extraction

The local texture of the tumor is extracted using the proposed rotation invariant modified uniform LBP operator. The basic LBP operator proposed by Ojala et al. (2002) is a gray scale and rotation invariant operator that characterizes the local texture of the image. LBP provides computational simplicity and high texture discriminating power, and hence it has proven useful in describing medical images such as mammogram (Oliver et al. 2007), MRI volumes (Unay and Ekin 2008), and pap smear images (Plissiti et al. 2011). Therefore, in the present work, LBP is considered as the suitable operator for local texture analysis of MRI and CT images. The LBP operator labels each pixel with a binary code by thresholding relative gray values of its circularly symmetric neighbors. Formally, the gray scale and rotation invariant LBP is defined as:

$$LBP^{ri}_{P,R} = min\left\{ROR(LBP_{P,R}, i)|i = 0, 1, 2, ..., P-1\right\} \tag{5.35}$$

where, P is the total number of neighbors located in a radius R, and $ROR(LBP_{P,R}, i)$ performs a circular bitwise right shift on a P-bit binary pattern $LBP_{P,R}$ for i times.

The binary code $LBP_{P,R}$ is computed based on the neighbors as given by,

$$LBP_{P,R} = \sum_{p=0}^{P-1} s(g_p - g_c), s(x) = \begin{cases} 1, x \geq 0 \\ 0, x < 0 \end{cases} \tag{5.36}$$

where, g_c and g_p are the gray value of the center and neighbor pixels, respectively. LBP code computation is shown in Figure 5.13 with $P = 8$ and $R = 1$. After the LBP code 10101101 is computed, the center pixel value is replaced with the corresponding rotation invariant LBP code, 01011011.

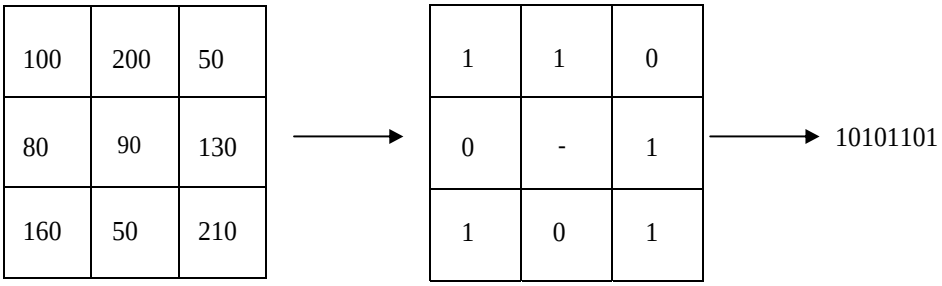

Figure 5.13: LBP Code Computation

When the whole image is coded with the values of $LBP^{ri}_{P,R}$, the texture distribution in the image is represented using the histogram of $LBP^{ri}_{P,R}$ values. The LBP histogram contains the number of occurrences of each LBP in the image. It was observed by Ojala et al. (2002) that about 70% of the patterns in the image were uniform patterns in which the number of 0/1 transitions was at most 2. (e.g., Pattern 00001111 is uniform and pattern 10001110 is non-uniform). Thus, they proposed another rotation invariant texture description operator known as uniform LBP which is given by,

$$LBP^{riu2}_{P,R} = \begin{cases} \sum_{p=0}^{P-1} s(g_p - g_c), U(LBP_{P,R}) \leq 2 \\ P + 1, \text{otherwise} \end{cases} \tag{5.37}$$

$$U(LBP_{P,R}) = |s(g_{p-1} - g_c) - s(g_0 - g_c)| + \sum_{p=1}^{P-1} |s(g_p - g_c) - s(g_{p-1} - g_c)| \tag{5.38}$$

where, $LBP^{riu2}_{P,R}$ is the uniform LBP operator and U represents the number of 0/1 transitions in the binary pattern. According to Equation (5.37), if the binary pattern

generated is uniform, then $LBP^{riu2}_{P,R}$ value is computed by adding bit values in the binary pattern. Otherwise, miscellaneous label $P+1$ is assigned. Thus, $LBP^{riu2}_{P,R}$ can generate $P+2$ distinct binary patterns. For example, $LBP_{8,1}$ can generate 10 distinct binary patterns. After the LBP codification of the image, a histogram with $P+2$ bins is built to represent the image texture. In the histogram, $P+1$ bins contain uniform patterns and all non-uniform patterns are put in one single bin.

The drawback of $LBP^{riu2}_{P,R}$ is its inability to analyze flat areas on the image, where all gray values of neighbor pixels are nearly same and they fluctuate near the gray value of the center pixel. The flat area problem is illustrated in Figure 5.14. Here, all gray values of pixels are near 166 and they have homogeneous distribution. Thus, the binary pattern is a random value of 0 and 1.

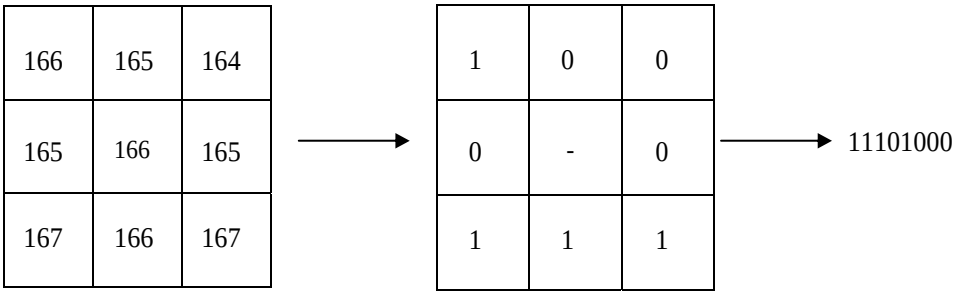

Figure 5.14: Flat Area Representation with LBP Code

In the present work, the above problem is solved by modifying $LBP^{riu2}_{P,R}$ as:

$$LBP^{riu2mod}_{P,R} = \begin{cases} \sum_{p=0}^{P-1} s(g_p - g_c + \alpha), U(LBP_{P,R}) \leq 2 \\ P+1, \text{otherwise} \end{cases} \tag{5.39}$$

where, α is a small constant, which changes the difference in pixel values without affecting the discriminating ability of LBP operator. This change makes the LBP operator work effectively even in flat areas of the image.

Another drawback of $LBP^{riu2}_{P,R}$ is that it cannot describe the image texture completely as all non-uniform patterns are put in one bin. Thus in the present work, the image texture is described effectively by assigning non-uniform patterns to the bins of uniform patterns based on the similarity measure given below.

$$D^{min}_{ROR}(LBP_{P,R}) = min\{D_{ROR}(LBP_{P,R}, LBP^{uniform}_{P,R}), allLBP^{uniform}_{P,R}\} \tag{5.40}$$

Where,

$$D_{ROR}(X,Y) = min\{\phi(ROR(X,i),Y), i = 0..P-1\} \tag{5.41}$$

$$\phi(X,Y) = \sum_{i=0}^{P-1} |X_i - Y_i| \tag{5.42}$$

Here, $LBP_{P,R}^{uniform}$ and $LBP_{P,R}$ represent uniform and non-uniform patterns, respectively. $ROR(X,i)$ is a circular bitwise right shift of the P-bit number X for i times. X_i and Y_i correspond to the bit values of the P-bit numbers X and Y, respectively. The role of the similarity measure in assigning non-uniform pattern to the bin of uniform pattern is explained as follows:

Let X and Y be the non-uniform and uniform patterns. In order to assign a non-uniform pattern to the closest bin of the uniform pattern, the distance D_{ROR} is computed between X and each uniform pattern. The D_{ROR} performs circular bitwise right shift of X, and then computes the distance between X and Y based on the number of bit differences ϕ. This circular shift and distance computation is repeated $P-1$ times, and the minimum distance is considered as the distance between X and Y. This whole procedure is repeated with non-uniform pattern X and each uniform pattern Y. Finally, X is assigned to the closest bin of Y based on the minimum distance D_{ROR}. For example, given a non-uniform pattern 00000011 and two uniform patterns {00001011, 00101011}, a non-uniform pattern 00000011 is assigned to the histogram bin of uniform pattern 00001011, since it is at a lesser distance compared to the uniform pattern 00101011.

The subclass shape and texture features extracted from the tumor region are combined into a feature vector to represent the subclass of the tumor. The brain tumor is represented with feature vector consisting of 94 features extracted from T1 and T2-weighted images. The liver tumor is represented with a feature vector consisting of 47 features extracted from the abdominal CT image.

5.3.4 Similarity Matching

In the present research work, the following similarity measures are used to measure the similarity between subclass features of the query image and subclass features of images in the database belonging to a same class.

- The shape similarity $DS(x, y)$ between two images x and y is given by the Euclidian distance:

$$DS(x,y) = \sqrt{(A^x - A^y)^2 + (\sum_{i=1}^{N-1}(FD_i^{(x)} - FD_i^{(y)})^2)} \tag{5.43}$$

  where, A and FD represents the area and Fourier descriptors of the tumor, respectively.

- The texture similarity $DTE(x, y)$ between two images x and y, with their texture feature vectors obtained by LBP is given by the Chi-square distance $\chi^2(x, y)$:

$$DTE(x,y) = \chi^2(x,y) = \sum_{k=1}^{K} \frac{[B_x(k) - B_y(k)]^2}{[B_x(k) + B_y(k)]} \tag{5.44}$$

  where, $B_x(k)$ and $B_y(k)$ are k^{th} LBP histogram bins of the images x and y, respectively.

All the similarity measures are normalized and fused to form a single similarity measure as given below:

$$D(x,y) = DS(x,y) + DTG(x,y) \tag{5.45}$$

In order to retrieve M most relevant images from the database, the calculated distances are sorted in the ascending order. Further, the top M distances are selected and the corresponding images are retrieved.

5.3.5 Feature Database Indexing Technique

In order to provide fast retrieval of images, the subclass features in the database are indexed using the proposed CIKD indexing technique as discussed in Section 5.2.6. The CIKD indexing technique prunes the search space by partitioning the subclass features in the database into different clusters using the proposed modified k-means clustering algorithm. The dimensionality of each cluster is reduced separately using IG-ICA feature selection technique. Then within each cluster, the features are indexed using a KD-tree.

5.3.6 Experimental Results and Discussion

In order to test the performance of the proposed CBIR method based on rotation invariant features, experiments are carried out on a brain and liver tumor datasets. The ground truth for the CBIR experiments is obtained based on histopathological analysis of biopsy samples of tumors. The performance of the proposed CBIR method is measured in terms of effectiveness and efficiency. The effectiveness of the CBIR method for retrieving the most similar images from the database is quantified using standard performance metrics, namely Precision and Recall as already discussed in Section 5.2.8. In the present method, the tumor classification performances are the same while the retrieval performances are different when compared to the CBIR method based on rotation correction. This is because the class features are similar and subclass features are different in both the methods. The retrieval efficiency is measured in terms of amount of time required to retrieve most similar images from the database using the proposed indexing technique. The CBIR results of brain and liver tumors are given below.

CBIR Results of Brain Tumor

The brain tumor retrieval experiments are carried out on a database consisting of T1-weighted post-contrast and T2-weighted brain MRI images of 820 patients (female: 382, male: 438). Among 820 patients, 420 patients were diagnosed with benign tumor and 400 patients with malignant tumor based on histopathological analysis of biopsy samples. The details of the dataset are already given in Section 2.8. The retrieval effectiveness and efficiency of the proposed CBIR method in retrieving most similar brain tumor images from the database are detailed below.

Retrieval Effectiveness

In order to test the robustness of the proposed CBIR method with respect to rotation, some of the images in the database are rotated by $10^o, 15^o, 20^o$ and 25^o in both clockwise and anti-clockwise directions. Table 5.13 shows the similarity scores, which are obtained by computing distance between original MRI image and its corresponding rotated MRI image based on the similarity measure $D(x, y)$.

The Average Similarity Score (ASC) is computed with respect to each angle. Image rotation changes the texture and shape patterns of the tumor. But, due to the

Table 5.13: Similarity Scores Between the Original and Rotated MRI Images

Rotation Angle	**Average Similarity Score (ASC)**
-10^o	0.00
-15^o	0.00
-20^o	0.00
-25^o	0.01
10^o	0.00
15^o	0.00
20^o	0.02
25^o	0.02

use of rotation invariant features to represent the shape and texture of the tumor, the original and rotated images are considered similar (ASC = 0.00) in most of the rotation angles. However, small difference is shown with some of the rotation angles, such as -25^o, 20^0, and 25^0.

In the classification stage, the ensemble classifier consisting of SVM, ANN and k-NN classifiers is used to classify the brain tumor as benign or malignant based on the class features. Table 5.14 shows the confusion matrix of the brain tumor classifications obtained by the ensemble classifier. All the malignant tumors are correctly classified, whereas 5 benign tumors are misclassified as malignant tumors. The same 5 benign tumors shown in Table 5.1 (Section 5.2) are misclassified due to the difficulty in capturing boundary and shape features of these tumors.

Table 5.14: Classifications of Brain Tumors by Ensemble Classifier

	Predicted Class	
Actual Class	Benign	Malignant
Benign	415	5
Malignant	0	400

Further, the classification performance measures are shown in Table 5.15. The correct classification of malignant tumors resulted in 100% sensitivity and incorrect classification of benign tumors resulted in 98.80% specificity. Hence, the overall classification accuracy obtained by the ensemble classifier is 99.39%.

Table 5.15: Performance of Ensemble Classification of Brain Tumors

Performance metrics	**Classifier performance**
Sensitivity	100%
Specificity	98.80%
Accuracy	99.39%
Az	0.991

The subclass features of the tumor are extracted using rotation invariant WFD and proposed modified rotation invariant uniform LBP operator $LBP^{riu2mod}_{P,R}$. The number of boundary points of tumors in the database is not equal, and hence this creates problem in similarity matching. Therefore, based on experiments, 30 boundary points are selected using equal arc length normalization. This helps in representing the tumor shape with equal number of WFDs. Further, $LBP^{riu2mod}_{P,R}$ operator is tested with different values of (P, R). The computing speed of (8, 1),(16, 2),(24, 3) is 0.0824 sec, 1.53241 sec, 3.7563 sec, respectively and the corresponding retrieval accuracy is 94.04%, 97.62% and 91%, respectively. The larger the value of (P, R), the larger the computation time of feature extraction. Therefore $(P, R) = (16, 2)$ is chosen, since it is acceptable to have more powerful texture descriptor with a slight increase of the computational cost.

Table 5.16 shows the performance comparison of the modified rotation invariant uniform LBP operator $LBP^{riu2mod}_{P,R}$ with the existing LBP operators, such as $LBP^{ri}_{P,R}$ and $LBP^{riu2}_{P,R}$ (Ojala et al. 2002) for $P = 16$ and $R = 2$. The $LBP^{ri}_{P,R}$ generates a large number of histogram bins and shows poor retrieval performance as it is sensitive to noise. The $LBP^{riu2}_{P,R}$ improves the performance of $LBP^{ri}_{P,R}$ by considering uniform patterns in the image. However, its retrieval performance is not much effective as uniform patterns are given more importance than non-uniform patterns. It is observed that the proposed operator $LBP^{riu2mod}_{P,R}$ performs better than the other LBP operators due to the distribution of non-uniform patterns among the bins of uniform patterns.

Table 5.16: Performance Comparison of LBP Operators in CBIR of Brain Tumors

LBP Operator	**Number of Histogram Bins**	**Precision**	**Recall**
$LBP^{ri}_{P,R}$	243	91.35%	88.59%
$LBP^{riu2}_{P,R}$	18	93.12%	94.31%
$LBP^{riu2mod}_{P,R}$	17	97.62%	97.18%

Figure 5.15 shows the comparison of the proposed CBIR method with shape-based (WFD) and texture-based (LBP) retrieval in terms of precision and recall graph. It is seen that proposed method achieves the highest retrieval precision of 97.62% and recall of 97.18% as a combination of more robust shape and texture features (WFD + LBP) is used. The shape or texture features alone do not represent the tumor characteristics completely. Hence, CBIR based on such features gives low precision and recall rates.

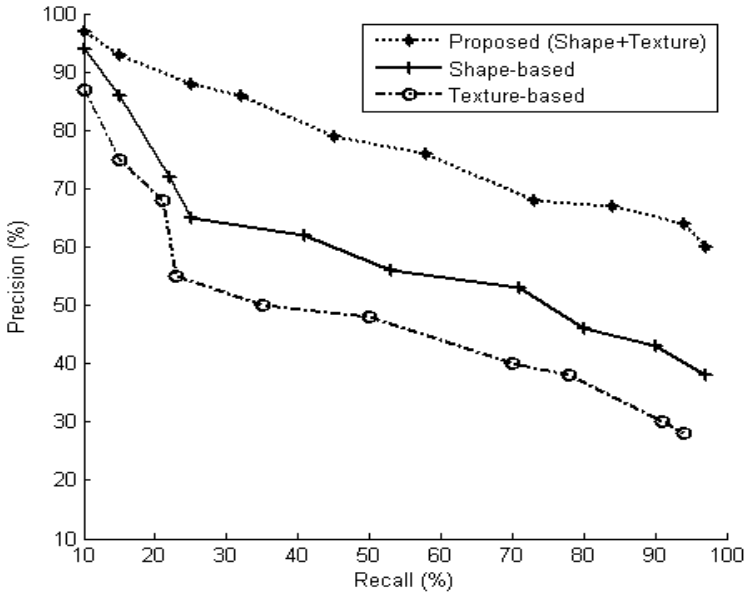

Figure 5.15: Comparison of Feature Descriptors in CBIR of Brain Tumors

In order to provide fast retrieval results, the proposed CIKD indexing method prunes the search space by clustering subclass features of the brain tumor based on

the modified k-means clustering algorithm. The modified k-means clustering algorithm makes use of the proposed algorithms (Algorithm 5.1 and Algorithm 5.2) for determining number of clusters and initial cluster centers, respectively. Based on the minimum fused validity index value, the Algorithm 5.1 identifies 7 and 5 clusters in the benign and malignant brain tumor dataset, respectively.

Further, the effectiveness of the proposed algorithm (Algorithm 5.2) for determining initial cluster centers is measured in terms of average Cluster Center Proximity (CCP), which gives the difference between the actual and initial cluster centers. The CCP is computed using Equation (5.29) as discussed in Section 5.2.8. Table 5.17 shows the comparison between the effectiveness of random and proposed cluster center initializations. It is observed that the proposed algorithm estimates initial cluster centers nearer to actual cluster centers when compared to random initialization in both benign and malignant brain tumor datasets.

Table 5.17: Comparison of Cluster Center Initializations in Brain Tumor Dataset

Dataset	**CCP**	
	Random Initialization	**Proposed Initialization**
Benign Brain Tumor	0.76	0.11
Malignant Brain Tumor	0.48	0.13

Retrieval Efficiency

The proposed CIKD indexing technique provides fast retrieval of liver tumor images based on modified k-means clustering, IG-ICA feature selection technique, and KD-tree. The brain tumor retrieval based on CIKD has a time complexity of $O(DC) + O(C) + O(D'log_2N^{(h)})$ as discussed in section 5.2.8. The N and D are the number of feature vectors and their original dimensions, respectively. C is the number of feature clusters, and $N^{(h)}$ and D' are the number of feature vectors in cluster h ($h = 1, 2...C$) and their reduced dimensions, respectively.

CBIR Results of Liver Tumor

This section discusses the results of the CBIR experiments carried on a database consisting of abdominal CT images of 764 patients. Among 764 patients, 380 patients were diagnosed with benign liver tumor and 384 patients with malignant liver tumor based on histopathological analysis of biopsy samples. The details of the dataset are already given in Section 2.8. Experiments similar to brain tumor are also performed on a liver tumor dataset. The effectiveness and efficiency of the proposed CBIR method in retrieving most similar liver tumor images from the liver tumor database are detailed below.

Retrieval Effectiveness

In order to test the robustness of the proposed CBIR method with respect to rotation, some of the images in the database are rotated by $10^o, 15^o, 20^o$ and 25^o in both clockwise and anti-clockwise directions. Table 5.18 shows the similarity scores, which are obtained by computing distance between original CT image and its corresponding rotated CT image based on the similarity measure $D(x, y)$. The average similarity

Table 5.18: Similarity Scores Between the Original and Rotated CT Images

Rotation Angle	**Average Similarity Score (ASC)**
-10^o	0.00
-15^o	0.00
-20^o	0.00
-25^o	0.01
10^o	0.00
15^o	0.01
20^o	0.00
25^o	0.04

score is computed with respect to each angle. Image rotation changes the texture and shape patterns of the tumor. But, due to the use of rotation invariant features to represent the shape and texture of the tumor, the original and rotated images

are considered similar (ASC = 0.00) in most of the rotation angles. However, small difference is shown with some of the rotation angles, such as -25^o, 15^0, and 25^0.

In the classification stage, the ensemble classifier consisting of SVM, ANN and k-NN classifiers is used to classify the liver tumor as benign or malignant based on the class features. Table 5.19 shows the confusion matrix of the liver tumor classifications obtained by the ensemble classifier. All the malignant tumors are correctly classified, whereas 7 benign tumors are misclassified as malignant tumors. The same 7 benign tumors shown in Table 5.8 (Section 5.2) are misclassified due to the difficulty in capturing boundary and shape features of these tumors. Further, the classification performance measures that are discussed in Section 4.2 are shown in Table 5.20. The correct classification of malignant tumors resulted in 100% sensitivity and incorrect classification of benign tumors resulted in 98.15% specificity. Hence, the overall classification accuracy obtained by the ensemble classifier is 99.08%.

Table 5.19: Classifications of Liver Tumors by Ensemble Classifier

	Predicted Class	
Actual Class	Benign	Malignant
Benign	373	7
Malignant	0	384

Table 5.20: Performance of Ensemble Classification of Liver Tumors

Performance metrics	**Classifier performance**
Sensitivity	100%
Specificity	98.15%
Accuracy	99.08%
Az	0.989

The subclass features of the liver tumor are extracted using rotation invariant WFD and proposed modified rotation invariant uniform LBP operator $LBP^{riu2mod}_{P,R}$. The number of boundary points of tumors in the database is not equal, and hence this creates problem in similarity matching. Therefore, based on experiments, 30

boundary points are selected using equal arc length normalization. This helps in representing the tumor shape with equal number of WFDs. Further, based on the experiments, the values of P and R are chosen as $(P, R) = (16, 2)$.

Table 5.21 shows the performance comparison of the modified rotation invariant uniform LBP operator $LBP^{riu2mod}_{P,R}$ with the existing LBP operators, such as $LBP^{ri}_{P,R}$ and $LBP^{riu2}_{P,R}$ (Ojala et al. 2002) for $P = 16$ and $R = 2$. The $LBP^{ri}_{P,R}$ generates a large number of histogram bins and shows poor retrieval performance as it is sensitive to noise. The $LBP^{riu2}_{P,R}$ improves the performance of $LBP^{ri}_{P,R}$ by considering uniform patterns in the image. However, its retrieval performance is not much effective as uniform patterns are given more importance than non-uniform patterns. It is observed that the proposed operator $LBP^{riu2mod}_{P,R}$ performs better than the other LBP operators due to the distribution of non-uniform patterns among the bins of uniform patterns for complete texture analysis.

Table 5.21: Performance Comparison of LBP Operators in CBIR of Liver Tumors

LBP Operator	**Number of Histogram Bins**	**Precision**	**Recall**
$LBP^{ri}_{P,R}$	243	90.07%	88.36%
$LBP^{riu2}_{P,R}$	18	92.41%	91.69%
$LBP^{riu2mod}_{P,R}$	17	97.18%	95.67%

Figure 5.16 shows the comparison of the proposed CBIR method with shape- and texture-based retrieval in terms of Precision and Recall graph. It is seen that proposed method achieves the highest retrieval precision of 97.18% and recall of 95.67% as a combination of more robust shape and texture features is used. The shape or texture features alone do not represent the tumor characteristics completely. Hence, CBIR based on such features gives low precision and recall rates.

In order to provide fast retrieval results, the proposed CIKD indexing method prunes the search space by clustering subclass features based on the modified k-means clustering algorithm. The modified k-means clustering algorithm makes use of the proposed algorithms (Algorithm 5.1 and Algorithm 5.2) for determining the number of clusters and initial cluster centers, respectively. The Algorithm 5.1 identifies 4 and 5 clusters in the benign and malignant liver tumor dataset.

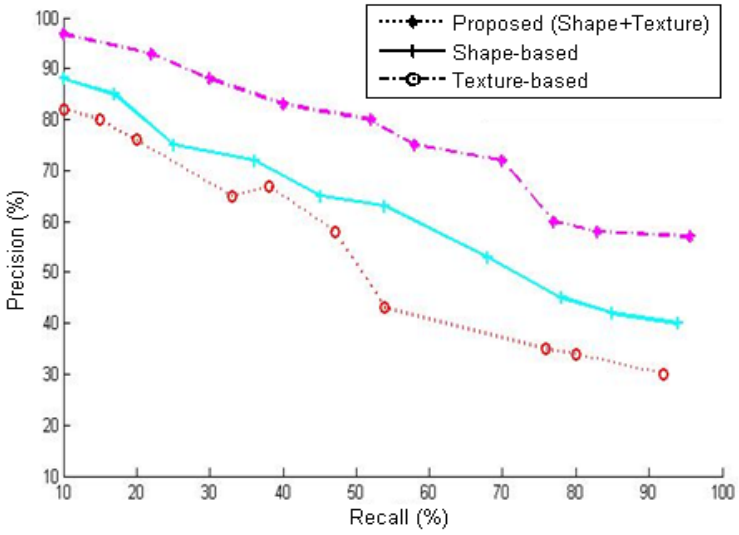

Figure 5.16: Comparison of Feature Descriptors in CBIR of Liver Tumors

Further, the effectiveness of the proposed algorithm (Algorithm 5.2) for determining initial cluster centers in a set of liver tumor subclass features is measured in terms of average Cluster Center Proximity (CCP), which gives the difference between the actual and initial cluster centers. The CCP is computed using Equation (5.29) as discussed in Section 5.2.8. Table 5.22 shows the comparison between the effectiveness of random and proposed cluster center initialization. It is observed that the proposed algorithm estimates initial cluster centers nearer to actual cluster centers when compared to random initialization in both benign and malignant liver tumor datasets.

Table 5.22: Comparison of Cluster Center Initializations in Liver Tumor Datasets

Dataset	**CCP**	
	Random Initialization	**Proposed Initialization**
Benign Liver Tumor	0.53	0.09
Malignant Liver Tumor	0.45	0.11

Retrieval Efficiency

The proposed CIKD indexing technique provides fast retrieval of liver tumor images based on modified k-means clustering, IG-ICA feature selection technique, and KD-tree. The liver tumor retrieval based on CIKD has a time complexity of $O(DC) + O(C) + O(D'log_2N^{(h)})$ as discussed in section 5.2.8. The N and D are the number of feature vectors and their original dimensions, respectively. C is the number of feature clusters, and $N^{(h)}$ and D' are the number of feature vectors in cluster h ($h = 1, 2...C$) and their reduced dimensions, respectively.

5.4 Summary

This chapter discussed the two CBIR methods based on image rotation correction and rotation invariant features, respectively for retrieval of most similar images from the database in response to query image of brain/liver tumor. The experimental results showed that the proposed CBIR methods are robust to misalignment of images due to use of rotation correction technique and rotation invariant features, respectively. Also, both the proposed CBIR methods achieve high precision and recall rates due to the use of effective shape and texture descriptors of the tumor. The CBIR method based on image rotation correction obtained $P = 98.16\%$, $R = 97.35\%$ and $P = 97.83\%$, $R = 97.02\%$ in brain and liver tumors retrieval, respectively. Whereas the CBIR method based on rotation invariant features obtained $P = 97.62\%$, $R = 97.18\%$ and $P = 97.18\%$, $R = 95.67\%$ in the brain and liver tumors retrieval, respectively. Thus, the CBIR method based on image rotation correction is more effective than CBIR method based on rotation invariant features.

Also, the CBIR methods proved to be efficient by providing fast retrieval of images from the database based on the proposed CIKD indexing technique. The modified k-means clustering with automatic initialization of a number of clusters and their centers provided superior results compared to random initialization. Hence, the combination of effective feature descriptors and indexing technique makes the CBIR methods effective and efficient in retrieval of most similar brain and liver tumor images from the database. Therefore, the proposed CBIR methods can assist the radiologist in the accurate diagnosis of brain and liver tumors based on the relevant cases.

Chapter 6

3D Reconstruction of Tumor

The proposed CAD system consists of tumor detection, classification, CBIR and 3D reconstruction methods for effective and efficient analysis of brain and liver tumors. The 3D reconstruction method builds the 3D model of the brain/liver tumor, and then computes its volume for assisting the radiologist in determining the stage of cancer. A set of 2D cross-sectional images of the brain/liver tumor generated by MRI/CT imaging techniques cannot accurately represent the structure of the tumor. Whereas 3D visualization of the tumor enables the radiologist to understand the structure, topology and the stage of the tumor; thus helps in planning the treatment. Hence, an accurate 3D model of the tumor should be reconstructed from the set of 2D parallel cross-sectional images of the tumor. Accordingly, in this chapter, an effective and efficient 3D reconstruction scheme for building the 3D model of brain/liver tumor is proposed. Precisely, an attempt has been made to fulfill the fourth objective of the research work and overcome the limitations of the existing 3D reconstruction methods discussed in Section 2.5. The research contributions towards the development of the 3D reconstruction scheme are as follows:

- Developing an enhanced shape-based interpolation algorithm for estimating the missing slices in a given set of brain/liver tumor slices.
- Developing the mesh simplification algorithm for reducing the number of triangles in the 3D surface mesh of the brain/liver tumor without degrading the model quality.

The proposed 3D reconstruction scheme incorporating the above contributions in building the 3D model of the brain/liver tumor is detailed as follows:

6.1 Proposed Methodology

Figure 6.1 shows the various steps in the proposed 3D reconstruction scheme for building the 3D model and computing the volume of brain/liver tumor.

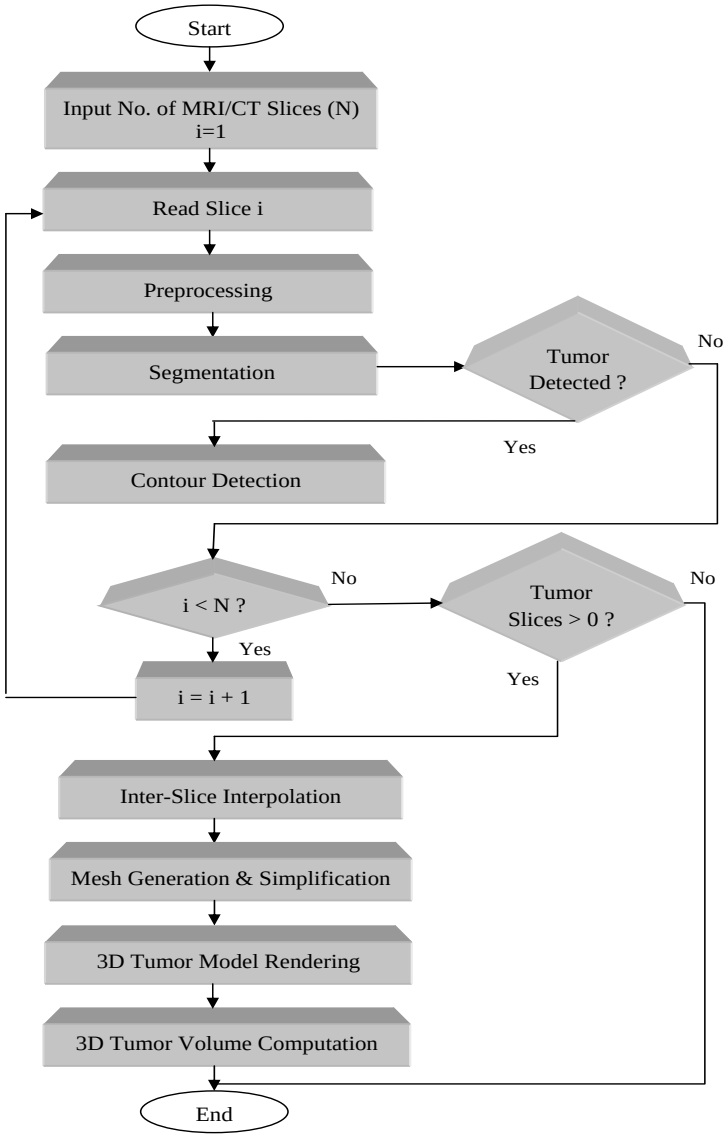

Figure 6.1: Flowchart of the Proposed 3D Tumor Reconstruction Scheme

In the first step, the MRI/CT image of the brain/liver slice (cross section) is preprocessed to improve the quality of the image. Next, the tumor is detected on each abnormal slice using the proposed brain/liver tumor segmentation methods. Then,

the normal slices are eliminated from the set and only abnormal slices are retained for further processing. In order to provide the smooth surface, the gap between the slices is filled by the proposed enhanced shape-based interpolation technique. In the next step, the contours of tumors on abnormal slices are connected so as to generate a 3D surface mesh of the tumor using the marching cubes (MC) algorithm. The large number of triangles in the surface mesh is reduced by the proposed mesh simplification algorithm. The realistic effects are added to the tumor by shading the generated mesh using Phong lighting and shading model. Finally, the volume of the tumor is computed from a set of abnormal slices. The various steps of the proposed 3D reconstruction scheme are detailed below.

6.1.1 Preprocessing

Prior to segmentation, the quality of MRI/CT images is enhanced by image denoising based on the median and Laplacian filters, image contrast enhancement using histogram equalization, and rotation correction of misaligned image using the proposed rotation correction technique as discussed in Chapter 3.

6.1.2 Segmentation

After preprocessing, the input image is segmented in order to extract the tumor region for further analysis. If the input image is the MRI image of the brain, then the image is segmented using the proposed brain tumor segmentation technique based on Modified Fuzzy C-Means (MFCM) clustering. If the input image is the abdominal CT image of the liver, then the image is segmented using the proposed liver tumor segmentation technique based on automatic region growing. The brain and liver tumor segmentation techniques are already discussed in Chapter 3.

6.1.3 Enhanced Shape-Based Interpolation Algorithm

After segmentation, slices of the segmented tumor are stacked up to form the volume data in the 3D space as shown in Figure 6.2. Generally, MRI and CT imaging devices provide a limited number of slices of the organ being scanned, and hence the distance between the slices is larger than the distance between the pixels in the slice. The surface reconstructed with these slices is inaccurate and contains artifacts. Thus, in

the present research work, an enhanced shape-based interpolation method is proposed in order to estimate missing slices in a given set of MRI/CT slices of the brain/liver tumor.

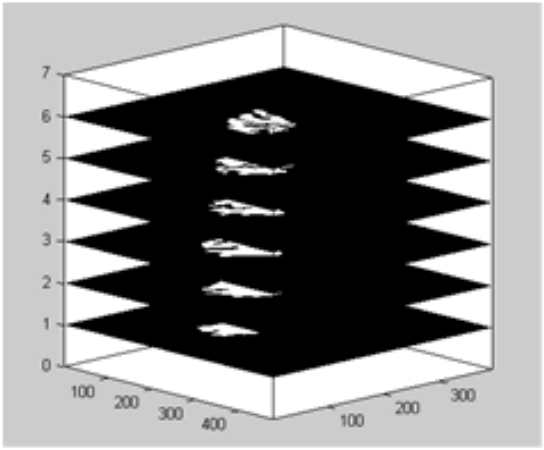

Figure 6.2: Stack of Tumor Slices

The original shape-based interpolation method proposed by Raya and Udupa (1990) converts the segmented binary image into a gray scale image using a city-block Distance Transform (DT), which assigns to every point in the binary image a gray level equal to its shortest city-block distance from the boundary of the object. Then, the intermediate slice is estimated by linearly interpolating the distances on two consecutive slices. Finally, the interpolated image is converted to a binary image by threhsolding at zero. This method accurately captures the geometry of the tumor on the slices but it suffers from the following drawbacks:

- It computes DT based on the city-block distance, which provides a bad approximation to the Euclidian distance.

- It produces inaccurate interpolation results whenever there is a drastic shift in the tumor position on the consecutive slices.

In order to overcome the drawbacks of shape-based interpolation, an enhanced shape-based interpolation method is proposed and its details are given below.

In 3D space, each voxel consists of 26 neighbors: 6 neighbors joined by a plane, 12 neighbors joined by a line and 8 neighbors joined by a point. Let $d1$, $d2$ and $d3$

be the local distances to neighbors joined by a plane, line and point, respectively. The exact distance between the two voxels, $P_1(x_1, y_1, z_1)$ and $P_2(x_2, y_2, z_2)$, can be calculated using the Euclidian distance $D_e(P1, P2)$ as given below.

$$D_e(P_1, P_2) = \sqrt{(x_2 - x_1)^2 + (y_2 - y_1)^2 + (z_2 - z_1)^2} \tag{6.1}$$

The Euclidian distances to three kinds of neighbors of a voxel are: $d1 = 1$, $d2 = \sqrt{2}$ and $d3 = \sqrt{3}$. The Euclidian DT is a global operation, since for each non-boundary voxel it calculates the Euclidian distance to all boundary voxels and assigns the shortest distance to the non-boundary voxel. Therefore, Euclidian DT of the image requires $O(N^2)$ operations, where N is the total number of voxels in the image. Hence, to reduce the computational complexity, the original shape-based interpolation method (Raya and Udupa 1990) makes use of city-block DT, which computes the DT based on n-neighbors. That is, it approximates the global distance by propagating the local distances between neighboring voxels. Hence, the number of operations required to calculate DT are reduced to $O(N)$. However, the city-block DT does not provide a good approximation to the Euclidian distance (Borgefors 1986). This is because, the city-block distance metric $D_c(P_1, P_2)$ measures the distance between two points $P_1(x_1, y_1, z_1)$ and $P_2(x_2, y_2, z_2)$ by the number of horizontal/vertical steps required to traverse (P_1, P_2) as given in Equation (6.2). Since, city-block distance considers only 6 neighbors joined by a plane, the local distances to neighbors of a voxels are: $d1 = 1$, $d2 = d3 = \infty$. However, the local distance to neighbors connected by a line and point can be obtained by 2 and 3 horizontal/vertical steps, respectively, Hence, the city-block distance overestimates the Euclidian distance.

$$D_c(P_1, P_2) = |x_2 - x_1| + |y_2 - y_1| + |z_2 - z_1| \tag{6.2}$$

Hence in the present research work, another n-neighbor distance called chamfer distance (Borgefors 1986) is used to provide a good approximation to Euclidian distance and accelerate the computation of DT. The chamfer distance metric considers the local distances to three kinds of neighbors of a voxel as: $d1 = 1$, $d2 = \sqrt{2}$ and $d3 = \sqrt{3}$. Therefore, it better approximates the Euclidian distance when compared to city-block distance. The chamfer DT makes use of the masks shown in Figure 6.3.

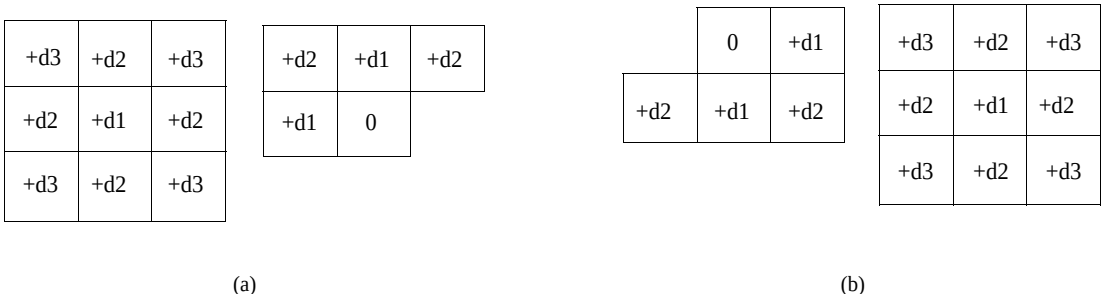

Figure 6.3: Masks for Computing Chamfer Distance Transform: (a) Forward mask (b) Backward Mask

In order to compute chamfer DT two passes over the image are necessary: forward and backward passes. In the forward pass the mask shown in Figure 6.3(a) is moved over the slice image in the 3D space left to right, top to bottom, and front to back. In the backward pass the mask shown in Figure 6.3(b) is moved over the slice image in the 3D space right to left, bottom to top, and back to front. In each position, the sum of the local distance in each mask voxel and the value of the voxel it covers is computed, and the new value of the voxel covered by the zero voxel is the minimum of these sums.

Another problem with shape-based interpolation is, it produces inaccurate results whenever there is a drastic shift in the tumor position on consecutive slices. In order to overcome this problem, the centers of the tumors on consecutive slices are aligned before interpolation. This results in gradual changes in both shape and spatial position of the tumor in interpolated slices.

The proposed enhanced shape-based interpolation algorithm based on the chamfer DT and tumor center alignment is given in Algorithm 6.1. First, tumors on consecutive slices are translated to align the tumor center with that of the slice. Then, shape-based interpolation is performed with chamfer DT to estimate the missing slice. After estimating the new slice, the tumors in the slices used for interpolation are translated back to their original positions and their centers are used to determine the center of the tumor on the newly estimated slice. Finally, the tumor on the new slice is translated to the new position defined by the computed center of the tumor.

Algorithm 6.1 Slice_Interpolation

Input: Two consecutive slices a and b of tumor.

Output: Estimated slice e between slices a and b.

1: Compute the center C of the consecutive slices a and b.

2: Compute the centers C_s and C_t of the tumor region R_s and R_t on slice a and b respectively.

3: Translate R_s and R_t to align the centers C_s and C_t on the line passing through the centers of the slices.

4: Perform shape-based interpolation.

- Compute a distance transform for slice a and b.

$$D(x,y,z) = \begin{cases} 0, & (x,y,z) \in BO \\ +d(x,y,z), & (x,y,z) \in O \\ -d(x,y,z), & (x,y,z) \notin O \end{cases} \tag{6.3}$$

  Where, $D(x,y,z)$ represents chamfer DT of point (x,y,z) on slice $z = a, b$. O and BO represent the region and boundary of the tumor, respectively.

- Interpolate distance values on slice a and b to estimate distance values on slice e.

$$D(x,y,e) = D(x,y,a) + \frac{e-a}{b-a}(D(x,y,b) - D(x,y,a)) \tag{6.4}$$

- Convert gray scale image into a binary image by thresholding at zero.

$$I(x,y,e) = \begin{cases} 1, & D(x,y,e) \geq 0 \\ 0, & D(x,y,e) < 0 \end{cases} \tag{6.5}$$

5: Restore R_s and R_t to their original positions.

6: Compute new center for the tumor on the newly interpolated slice e.

$$C_e = C_s + \frac{e-a}{b-a}(C_t - C_s) \tag{6.6}$$

7: Translate new tumor region R_z on slice e to a new location using the corresponding center C_e.

6.1.4 3D Surface Mesh Generation

The 3D surface mesh generation involves joining the tumor contours on the consecutive slices using polygonal structures to reconstruct the 3D surface mesh of the tumor. In present research work, 3D mesh of the tumor has been reconstructed using Marching Cubes (MC) algorithm proposed by Lorensen and Cline (1987) as it provides high quality surfaces.

The MC algorithm operates on a logical cube created from eight voxels; four voxels from each of the two adjacent slices as shown in Figure 6.4. It processes one cube at a time and determines the intersection of the surface with the cube. During this processing, the vertices of the cube are set to 1, if their value is greater than or equal to the isovalue of the surface and otherwise they are set to 0. The vertex with value 1 is considered as inside the surface and the vertex with value 0 is considered as outside the surface. The surface intersects those edges of the cube where one vertex is inside the surface and the other one is outside the surface.

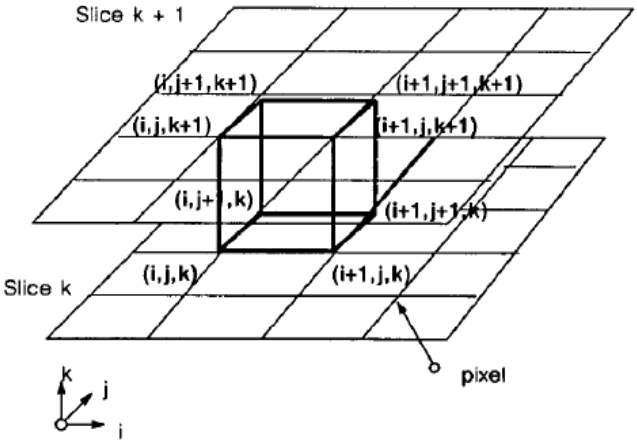

Figure 6.4: Marching Cube

Since, each of the eight vertices of a cube can be in two states, inside or outside the surface, $2^8 = 256$ cube-surface intersection patterns are possible. However, the MC algorithm considers most of these patterns as topologically equivalent by complementary and rotational symmetry. Hence, 256 cube-surface intersection patterns are reduced to 15 patterns (Lorensen and Cline 1987) as shown in Figure 6.5. The dark circle at the vertices of the cube denotes vertices inside the surface.

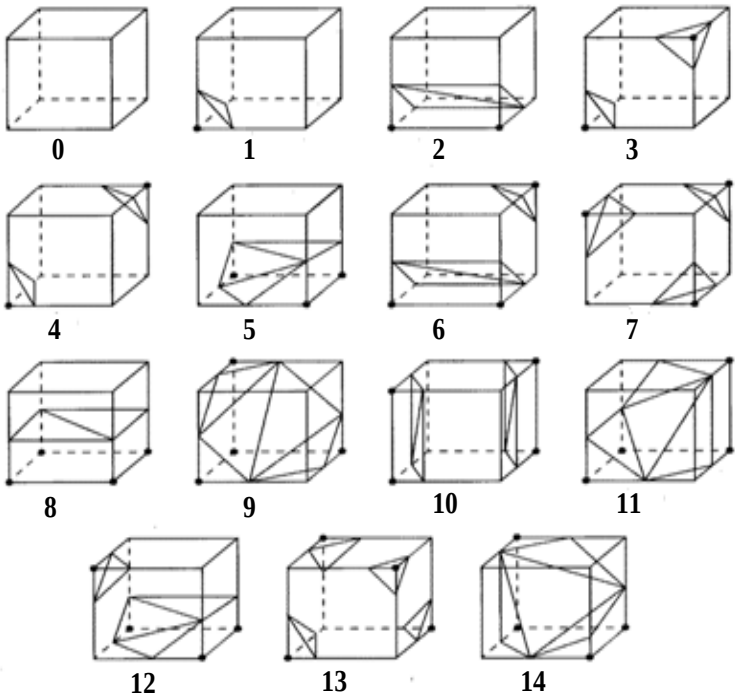

Figure 6.5: Cube-Surface Intersection Patterns

The problem with these 15 patterns is that there is a possibility of ambiguous faces, and hence holes will appear on the reconstructed surface. An ambiguous face is the one which has a cube-surface intersection point in each of its four edges as shown in Figure 6.6. In this case, the topologically correct connection of intersection points becomes ambiguous and in turn leads to the creation of holes in the reconstructed surface (Dürst 1988).

Figure 6.6: Ambiguous Faces

The hole appears on the reconstructed surface whenever a complement pattern is connected to the regular pattern by an ambiguous face. For example, the hole can be seen in Figure 6.7, where a cube with pattern 3 shares a face with the complement of pattern 6, and the shared face is the place where the hole appears. It is observed that

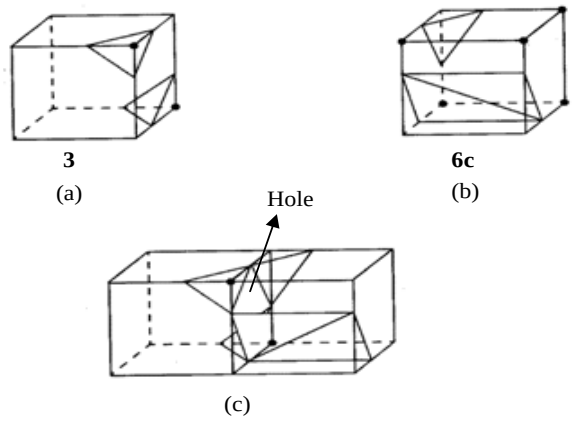

Figure 6.7: Hole on the Shared Face: (a) Pattern 3 (b) Complement of Pattern 6 (c) Hole in the Joined Patterns

only patterns 3, 6, 7, 10, 12 and 13 have ambiguous face, and hence modification is required only for these patterns. In order to solve the hole problem in these patterns, the additional six patterns (Figure 6.8) proposed by Montani et al. (1994) are added to the list of basic 15 patterns; these additional patterns are complements of patterns 3, 6, 7, 10, 12 and 13. Thus, total 21 (15 + 6) patterns are considered to identify cube-surface intersection for the 3D tumor reconstruction.

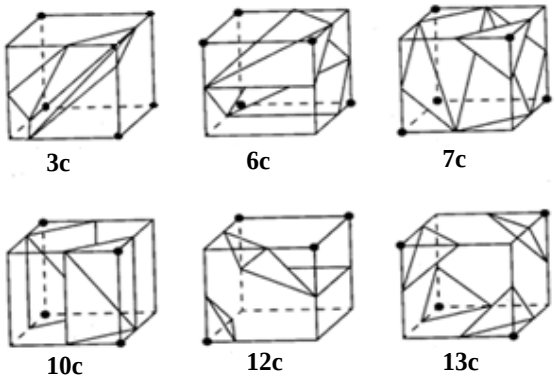

Figure 6.8: Additional Patterns to Solve the Hole Problem

The 21 cube-surface intersection patterns are incorporated into the lookup table called as edge table and an eight bit index (vertex-index) for each pattern in the edge table is created based on the state (0/1) of the vertex as shown in Figure 6.9. The edge table is referred using the vertex-index to determine the edges intersected by the surface. The midpoint of the intersected cube's edge is considered as the location of the intersection, since the segmented image is in binary. Another lookup table, known as triangle table is referred using the same vertex-index to determine the set of triangles generated by the intersected edges.

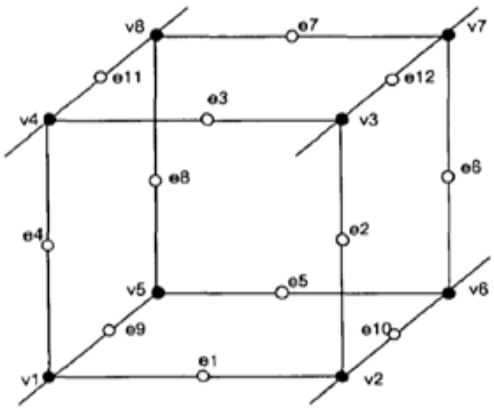

Vertex-Index =	v7	v6	v5	v4	v3	v2	v1	v0

Figure 6.9: Computation of Vertex-Index

6.1.5 3D Surface Mesh Simplification

Mesh simplification reduces the number of triangles in the reconstructed mesh. The MC algorithm results in a large number of triangles in the reconstructed mesh of the tumor, due to processing of small sized cubes. Hence, the mesh simplification algorithm is needed for reducing the number of triangles in the mesh, and thereby accelerating the rendering phase of the tumor. Among the existing mesh simplification algorithms, QSlim (Garland and Heckbert 1997) and Memoryless Simplification (MS) (Lindstrom and Turk 1998) are identified as the best algorithms with respect to producing high quality simplified mesh models. But, both of these algorithms cannot preserve important shape features such as highly curved regions, since their error

metric is based on distance to the plane and volume loss, respectively. In order to overcome these drawbacks, in the present work, a mesh simplification algorithm is proposed, which iteratively collapses edges based on the error metric consisting of curvature, volume loss and shape of adjacent triangles of the edge. Curvature factor helps in identifying flat and curved regions in the mesh, and thus mesh simplification can be performed in the flat regions while preserving the details of highly curved regions. The volume loss measure in the error metric helps in preserving the shape of the original model, whereas the shape of adjacent triangles of the collapsed edge helps in avoiding skinny triangles, which do not contribute much to the mesh geometry.

The proposed algorithm has a two-phase greedy approach to simplifying the mesh. In the first phase, priorities are assigned to internal vertices based on their curvature. In the second phase, the edges of the highest priority vertex are analyzed and the edge that causes minimum geometric deviation is collapsed. Table 6.1 shows the notations used in the proposed mesh simplification algorithm.

Table 6.1: Notations Used in the Mesh Simplification Algorithm

Symbol	**Description**
v_i	Vertex of mesh M
e_{ij}	Edge of mesh M connecting vertices (v_i, v_j). v_i and v_j are the start and end vertices of e_{ij}
t	Triangular face of M with a set of edges $\{e_{ij}, e_{jk}, e_{ki}\}$ and vertices $\{v_i, v_j, v_k\}$
T_{v_i}	Set of triangles incident on vertex v_i
$T_{e_{ij}}$	Set of triangles incident on edge e_{ij}
E_{v_i}	Set of edges incident on vertex v_i
N_{v_i}	Set of vertices in the neighbor of vertex v_i

During the edge collapse operation, the start point (v_i) of an edge is moved to the position of the end point (v_j) and the adjacent triangles of the edge are eliminated as shown in Figure 6.10. Removal of boundary vertices may distort the shape of the mesh, and hence edge collapse operation is performed only on internal vertices.

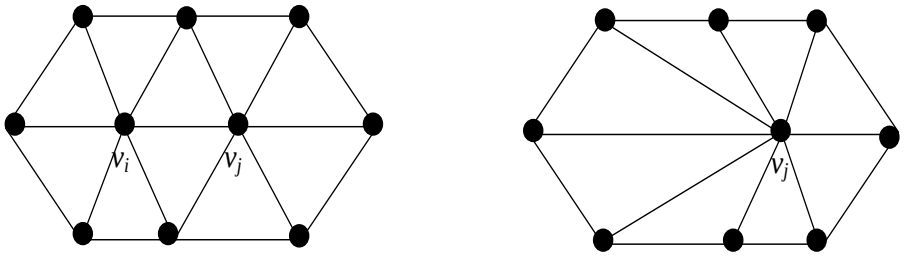

Figure 6.10: Edge Collapse Operation

The two phases of the proposed mesh simplification algorithm are detailed below.

Phase-I: Assignment of Vertex Priority

In this phase, internal vertices of the mesh are prioritized based on the curvature at a vertex in order to collapse more edges in flat regions and retain details of highly curved regions. The curvature at a vertex v_i is defined by using the mean and Gaussian curvatures (Dyn et al. 2001) as given below:

$$Curvature(v_i) = \sqrt{2H^2 - K} \tag{6.7}$$

where, H and K represent mean and Gaussian curvatures at a vertex, respectively and they are defined by the following equations:

$$K = \frac{2\pi - \sum_{j=1}^{n} \alpha_j}{\frac{1}{3}A} \tag{6.8}$$

$$H = \frac{\frac{1}{4}\sum_{j=1}^{n} \parallel e_j \parallel \beta_j}{\frac{1}{3}A} \tag{6.9}$$

where, n is the number of adjacent triangles around vertex v_i and A is the sum of the areas of the adjacent triangles around a vertex v_i. α denotes the angle between two successive edges around vertex v_i. $\parallel e_j \parallel$ and β denote the length and dihedral angle of an edge e_j connected to vertex v_i, respectively.

After calculating the curvature, internal vertices of the mesh are ordered based on the curvature. Vertex with the highest curvature is given the least priority and

a vertex with the least curvature is given the highest priority. After assigning the priorities, vertices are maintained in a heap with highest priority vertex at the top.

Phase-II: Edge Collapse

The sharp features of the surface cannot be preserved by considering only the curvature of the vertex because the edge collapse operation also changes the shape of the adjacent triangles. Thus, the highest priority vertex is eliminated by collapsing the edge ($e_{ij} \in E_{v_i}$) that causes minimum geometric distortion in its local neighborhood; this edge is referred to as optimal edge (h_o). In order to find h_o, the volume loss measure proposed by Lindstrom and Turk (1998), and the changes in shape of the adjacent triangles are considered. An edge collapse $e_{ij} : (v_i, v_j) \rightarrow v_j$ causes each triangle $t \in T_{v_i}$ to sweep out a tetrahedron volume defined by the four vertices (v_i, v_1, v_2, v_j) as illustrated in Figure 6.11.

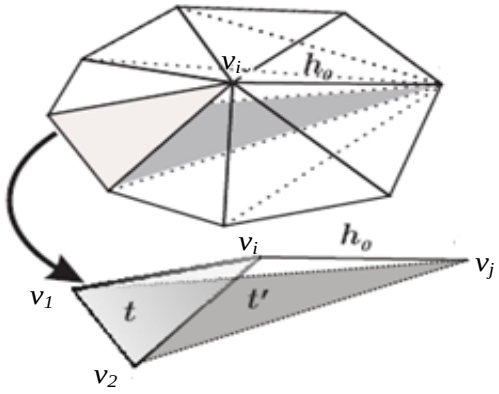

Figure 6.11: Volume Loss Caused by Edge Collapse Operation

The volume $V(t)$ of the tetrahedron represents the volume loss or the geometric deviation of the mesh due to the movement of triangle $t(v_1, v_2, v_i)$ and it is given by,

$$V(t) = \frac{1}{6}|(v_1 - v_i) \cdot ((v_2 - v_i) \times (v_j - v_i))| \tag{6.10}$$

The geometric deviation S(t) introduced by the change in the triangle shape (Wang et al. 2009) is defined by,

$$S(t) = \frac{4\sqrt{3}A}{l_1^2 + l_2^2 + l_3^2} \tag{6.11}$$

where, l_1, l_2, l_3 are the lengths of the edges and A is the area of the triangle t. $S(t)$ takes values in the range [0 1], where 1 indicates equilateral triangle and 0 indicates the collinear triangle. Finally, the total cost of collapsing an edge is given by,

$$Collapse\_Cost(e_{ij}) = \sum_{t \in T_{v_i}} V(t)(1 - S(t)) \tag{6.12}$$

For each edge $e_{ij} \in E_{v_i}$, $Collapse\_Cost(e_{ij})$ is computed and the edge that has minimum $Collapse\_Cost(e_{ij})$ is considered as an optimal edge h_o. The proposed mesh simplification algorithm is summarized in Algorithm 6.2.

Algorithm 6.2 Mesh_Simplification

Input: Mesh with a set of T triangles, V vertices, and E edges; Percentage of simplification $P\%$.

Output: Simplified mesh with reduced sets T, V and E.

1: Compute curvature at each internal vertex v_i using Equation (6.7).

2: Compute the curvature threshold Th.

$$Th = \frac{\sum_{i=1}^{n} Curvature(v_i)}{n} \tag{6.13}$$

3: Form a set of candidate vertices CV for mesh simplification.
For each $v_i \in V$, if $Curvature(v_i) < Th$, then put v_i in the candidate set CV.

4: Insert all the candidate vertices into the heap with highest priority vertex at the top.

5: Perform edge collapse by selecting an optimal edge of the vertex.

- Remove top vertex from the heap.
- For each edge $e_{ij} \in E_{v_i}$, compute $Collapse\_Cost(e_{ij})$ using Equation (6.12).
- Select the optimal edge $h_o \in E_{v_i}$ based on the minimum $Collapse\_Cost$.

$$Collapse\_Cost(h_o) = min\{Collapse\_Cost(e_{ij}) | e_{ij} \in E_{v_i}\} \tag{6.14}$$

- Collapse $h_o : (v_i, v_j) \rightarrow v_j$, by eliminating triangles incident on the edge (v_i, v_j) and substituting v_j for every occurrence of v_i in the left over triangles in T_{v_i}. Update sets T, V, E

6: For each $v_i \in N_{v_i}$, compute its curvature, and if it is less than the threshold then put it in candidate set CV and update heap.

7: Repeat steps 5 to 6 until $P\%$ reduction of faces (triangles) is achieved or the candidate set is empty.

6.1.6 3D Surface Rendering

In the final step of 3D reconstruction, realistic effects are added to the surface of the 3D model by applying the Phong lighting and shading model (Foley et al. 1996). Lighting model finds the intensity at a point on the surface using the vertex normal, and the shading model applies the lighting model at each point on the surface to shade the entire surface. The Phong lighting model considers diffuse, specular and ambient reflections for identifying the intensity (I) at each point on the surface as given below:

$$I = k_a I_a + k_d I_l (N.L) + k_s I_l (V.R)^{n_s} \tag{6.15}$$

where k_a, k_d and k_s denote ambient, diffuse and specular reflection coefficients whose values lie in the range [0 1] based on the reflective property of the surface. I_a and I_l represent intensity of ambient light and point light source, respectively. N is the unit normal surface vector and L is the unit vector directed toward the point light source. V and R are unit vectors in the viewing and specular reflection directions, respectively, and the parameter n_s indicates the type of surface.

In order to shade the mesh, a unit normal (N) is calculated at each vertex of the mesh by taking the average of adjacent triangle normals as given below:

$$N = \frac{(n_1 + n_2 + ... + n_k)}{k} \tag{6.16}$$

where, n_i is a unit normal vector of an adjacent triangle of a vertex and it is computed by,

$$n_i = \frac{(P_1 - P_3) \times (P_2 - P_3)}{\parallel (P_1 - P_3) \times (P_2 - P_3) \parallel} \tag{6.17}$$

where, (P_1, P_2, P_3) are the vertices of a triangle. The unit normal computed at each vertex of the mesh are used for identifying the intensity at each point on the surface.

In the present work, the Phong shading model is used as it gives more realistic shadings compared to the Gouroud shading model. It shades the given surface by linearly interpolating the vertex unit normal. The normals along the polygon edges are obtained by interpolating vertex normals of the edge. Then the normals across the polygon scan line are obtained by interpolating the starting and ending normal of the scan line as shown in Figure 6.12. Once all normals are computed, Phong lighting model is applied along each scan line to calculate intensities on the surface.

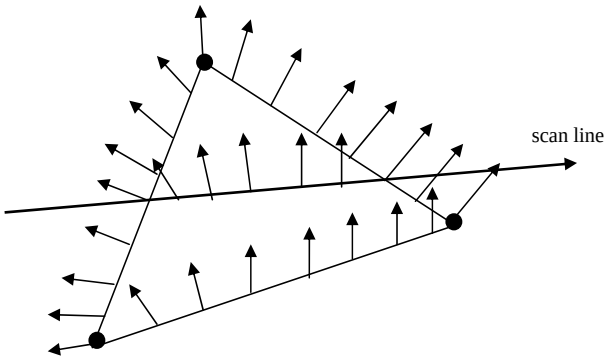

Figure 6.12: Interpolation of Vertex Normals

6.1.7 3D Tumor Volume Computation

The volume of the tumor is the vital information that can be extracted from the 3D model of tumor for determining the stage/severity of the cancer and treatment planning. In the present work, the tumor region is detected automatically on each abnormal slice based on the proposed segmentation method, and then the tumor volume is estimated by considering the slice thickness, inter-slice gap and area of the tumor on each abnormal slice.

$$Tumor\_Volume = (Interslice\_Gap + Slice\_Thickness) * (\sum_{i=1}^{n} A_i) \tag{6.18}$$

Where, n indicates the total number of abnormal slices, and A is area of tumor on each abnormal slice. The area of the tumor is computed by considering the pixels in the tumor region as given below:

$$A_i = No.\ of\ pixels\ in\ the\ tumor\ region\ on\ slice\ i * Pixel\_Dimension \tag{6.19}$$

6.2 Experimental Results

The performance of the 3D reconstruction of brain/liver tumor is measured in terms of effectiveness and efficiency. The effectiveness of the proposed enhanced shape-based interpolation technique is verified by estimating a known slice. In this procedure, three consecutive slices S_i, S_{i+1}, S_{i+2} are taken from the set of brain/liver slices; slices S_i and S_{i+2} are considered as input to the proposed interpolation algorithm for

estimating slice S'_{i+1}. The estimated slice S'_{i+1} is compared with the original slice S_{i+1} using the overlap-based error measure, which is defined as the ratio of the wrongly estimated pixels with respect to the area of the reference slice (S_{i+1}) as given below:

$$\varepsilon(S_{i+1}, S'_{i+1}) = \frac{card(S_{i+1} \triangle S'_{i+1})}{card(S_{i+1})} \tag{6.20}$$

where, $\triangle$ is the symmetric difference and *card* is the cardinal function. The effectiveness of the proposed mesh simplification algorithm is measured by evaluating the quality of the simplified mesh of the tumor using Symmetric Hausdorff Distance (SHD). It estimates the mesh simplification error by measuring the distance between the original and simplified mesh. The SHD is defined using the following equation:

$$SHD(M1, M2) = max\left(\max_{v \in M1} d_v(M2), \max_{v \in M2} d_v(M1)\right) \tag{6.21}$$

where, M1 and M2 are the original and simplified meshes of the tumor. $d_v(M2)$ is the minimum distance from vertex v of mesh $M1$ to the closest vertex of mesh $M2$, and $d_v(M1)$ is the minimum distance from vertex v of mesh $M2$ to the closest vertex of mesh $M1$.

The efficiency of the proposed 3D reconstruction scheme is measured in terms of the amount of time required for reconstructing the 3D model of the tumor from a set of abnormal slices. The 3D reconstruction results of the brain and liver tumors are given Section 6.2.1 and Section 6.2.2, respectively.

6.2.1 3D Brain Tumor Reconstruction Results

This section discusses the results of the experiments carried out on T2-weighted MRI images of 550 patients (benign: 280, malignant: 270). The scan of each patient produced a set of 22 slices having a thickness of 5 mm. The detailed description of the dataset is already given in Section 2.8. The 3D reconstruction experiments are carried out on T2-weighted MRI images because the T2-weighted MRI image provides better contrast between tumor, edema and other regions of the brain when compared to T1-weighted post-contrast MRI image. Thus, T2-weighted MRI image helps in effective segmentation of the tumor for accurate 3D reconstruction of the tumor.

Effectiveness of 3D Reconstruction Scheme

The MRI scan of the brain produces a set of slices containing normal (without tumor) and abnormal slices (with tumor) as shown in Figure 6.13.

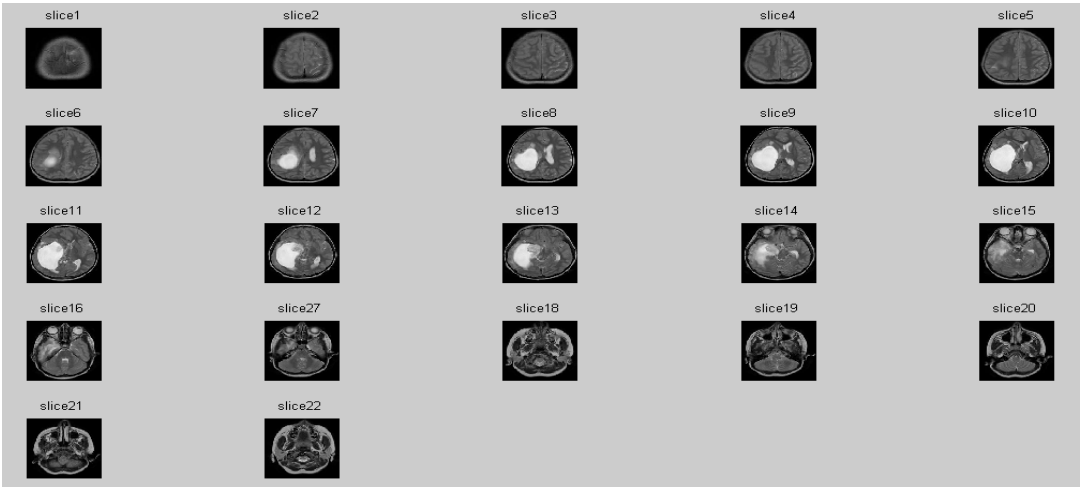

Figure 6.13: Set of Brain Slices obtained by MRI Scan

The abnormal slices are identified from the given set of brain MRI slices and the tumor is segmented on each abnormal slice using the proposed segmentation method based on MFCM clustering as shown in Figure 6.14.

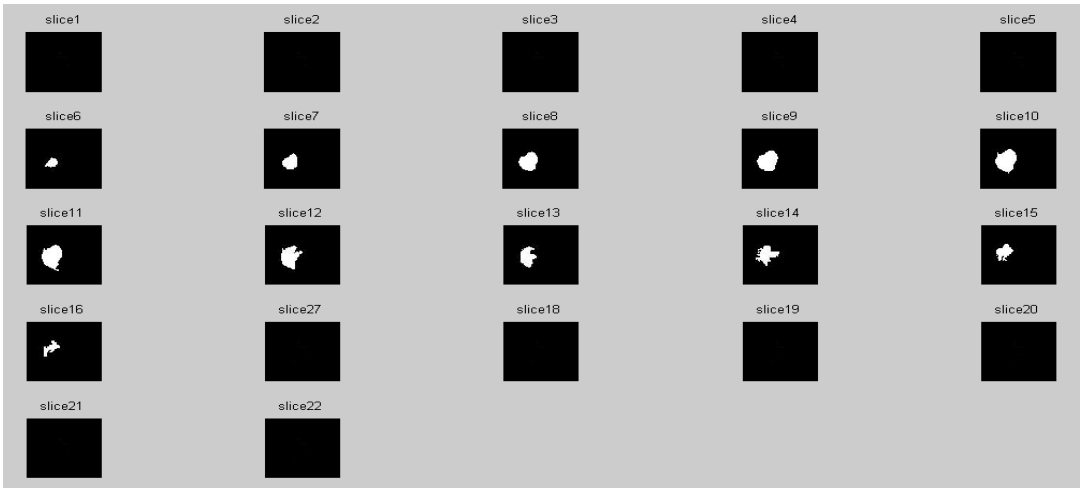

Figure 6.14: Set of Brain Tumor Segmented Slices

After the tumor segmentation, 2D tumor contours are arranged exactly in real spatial positions; this forms the volume data of the tumor. The x and y coordinates of a pixel in the 3D space are the row and the column numbers of the corresponding pixel in the 2D image matrix, and the z coordinate of the pixel is determined by the MRI slice number. Then x, y, and z coordinates are used to index the 3D matrix containing multiple images of the tumor to plot the volume data in the 3D space as shown in Figure 6.15. The stacking of the tumor contours in the 3D space is shown in Figure 6.15(a) and Figure 6.15(b) shows the missing slices estimated by applying the proposed enhanced shape-based interpolation technique on the sequential slices shown in Figure 6.15(a).

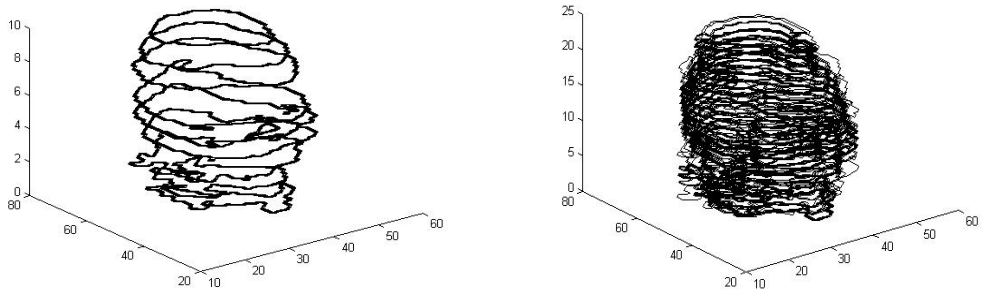

Figure 6.15: Tumor Contours:(a) Before Interpolation (b) After Interpolation

Table 6.2 shows the performance comparison of three interpolation methods in estimating missing slices: LG-linear gray level interpolation, SO-original shape-based interpolation, SE-enhanced shape-based interpolation (proposed method) in terms of overlap-based error(ε). Four sets of tumor slices $\{S_i, S_{i+1}, S_{i+2}\}$ are taken from each of the 550 cases in the dataset. Slices S_i and S_{i+2} are given as input to the interpolation method to estimate slice S'_{i+1}. Next, the overlap-error is computed with S_{i+1} and S'_{i+1}. It is observed that the LG interpolation method gives the worst performance with $\varepsilon < 12\%$, since it cannot capture the geometrical details of the tumor. The SO method captures the geometrical details of the tumor, but it gives ineffective results as it is dependent on city-block DT and it cannot handle drastic shifts of the tumor regions. Hence, SO method shows moderate performance with $\varepsilon < 9\%$. The proposed SE method outperforms ($\varepsilon < 5\%$) other interpolation methods, since it captures well the geometry of the tumor based on chamfer DT and center alignment of tumors.

The error ($\varepsilon < 5\%$) may lead to small artifacts in the 3D surface of the tumor and hence some features of the tumor may get distorted.

Table 6.2: Performance Comparison of Interpolation Methods

Dataset	**Slices**	**Overlap-Based Error(ε%)**		
	$\{S_i, S_{i+1}, S_{i+2}\}$	**LG**	**SO**	**SE**
MRI	6, 7, 8	6.91	5.22	4.03
	9, 10, 11	8.07	6.24	3.91
	11, 12, 13	11.17	8.79	3.33
	14, 15, 16	5.38	2.93	2.77

After the Inter-slice interpolation, surface mesh of the brain tumor is reconstructed using the MC algorithm. In order to reduce the number of triangles, the mesh is simplified using the proposed mesh simplification algorithm. The effectiveness of the proposed mesh simplification algorithm is demonstrated by presenting images of simplified models and error graphs. Figure 6.16 shows the simplified meshes and the corresponding rendered 3D models of the brain tumor along with the percentage of faces simplified (P%) and the number of faces retained in the simplified model. In order to analyze the effectiveness, the original model is simplified at different levels (40%, 60%, 80%). It is observed that even at 60% reduction the simplified model retains the sharp features of the original model, and the simplified model gets distorted when the reduction is more than 70%.

The quality of the simplified models of the brain tumor generated by the proposed mesh simplification algorithm is evaluated using symmetric Hausdorff distance (SHD) between original and simplified models of the tumor. Figure 6.17 shows the comparison of the proposed method with other state-of-the-art mesh simplification methods such as QSlim (Garland and Heckbert 1997), MS (Lindstrom and Turk 1998), and FSIMP (Hussain 2008). This comparison is based on average SHD computed with respect to simplified tumor models of all 550 cases in the dataset.

It is observed that the proposed method is more effective ($SHD < 0.6\ mm$) when compared to other methods as it is based on selecting edge contractions with minimum effect on curvature, volume and shape of adjacent triangles. The mesh simplification error $SHD < 0.6\ mm$ may lead to small variations in the tumor volume

and difficulty in estimating the stage of cancer. The FSIMP selects the vertex and its edge for removal based on the curvature, but simplified models are not of good quality ($SHD < 0.8\ mm$) because of the significant volume loss. The QSlim and MS

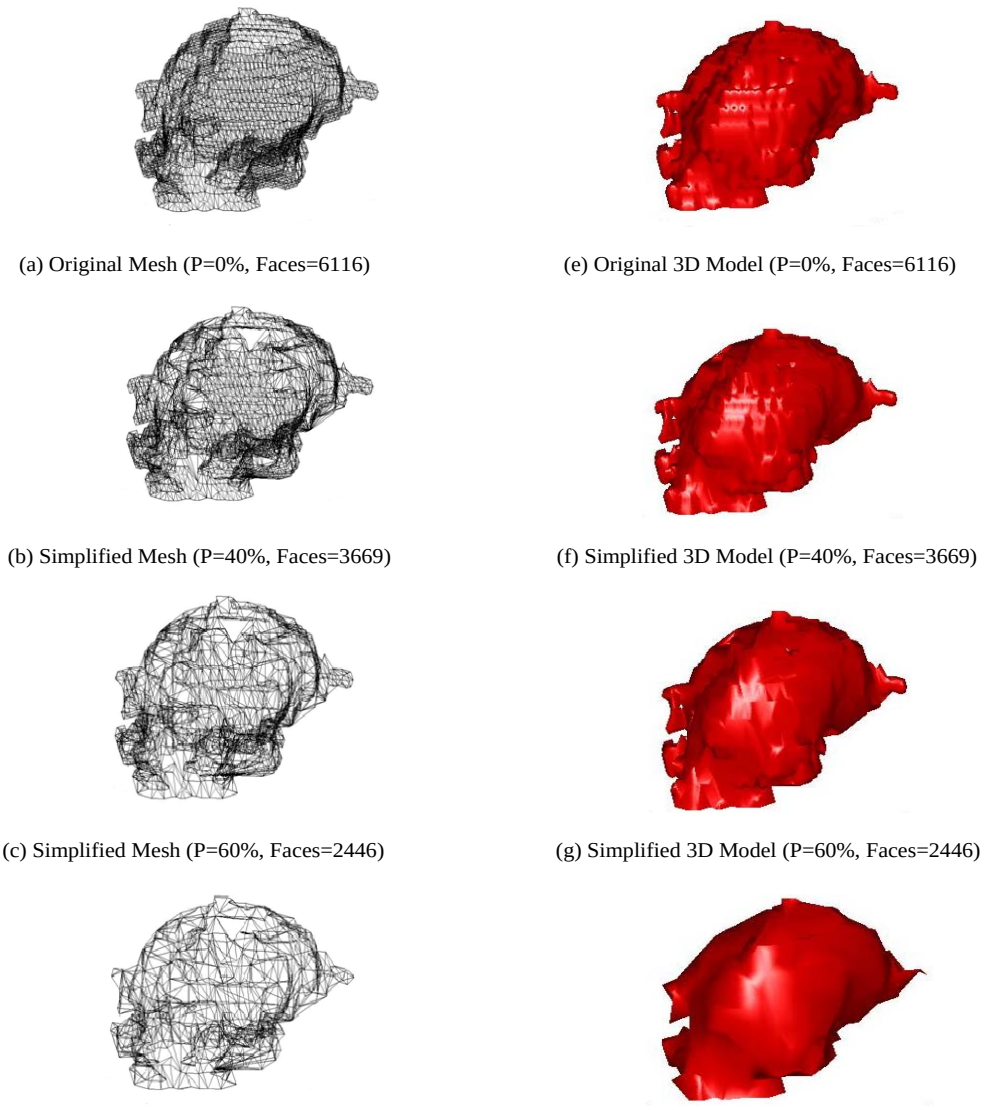

(a) Original Mesh (P=0%, Faces=6116)

(e) Original 3D Model (P=0%, Faces=6116)

(b) Simplified Mesh (P=40%, Faces=3669)

(f) Simplified 3D Model (P=40%, Faces=3669)

(c) Simplified Mesh (P=60%, Faces=2446)

(g) Simplified 3D Model (P=60%, Faces=2446)

(d) Simplified Mesh (P=80%, Faces=1223)

(h) Simplified 3D Model (P=80%, Faces=1223)

Figure 6.16: Mesh Simplification of Brain Tumor

methods perform mesh simplification using the error metrics based on the distance of a vertex to the plane and volume loss, respectively. These methods do not consider the curvature of the mesh and hence cannot preserve the sharp details of the mesh

in the simplified models. Therefore, QSlim and MS methods show poor performance with $SHD < 1\ mm$ and $SHD < 1.12\ mm$, respectively.

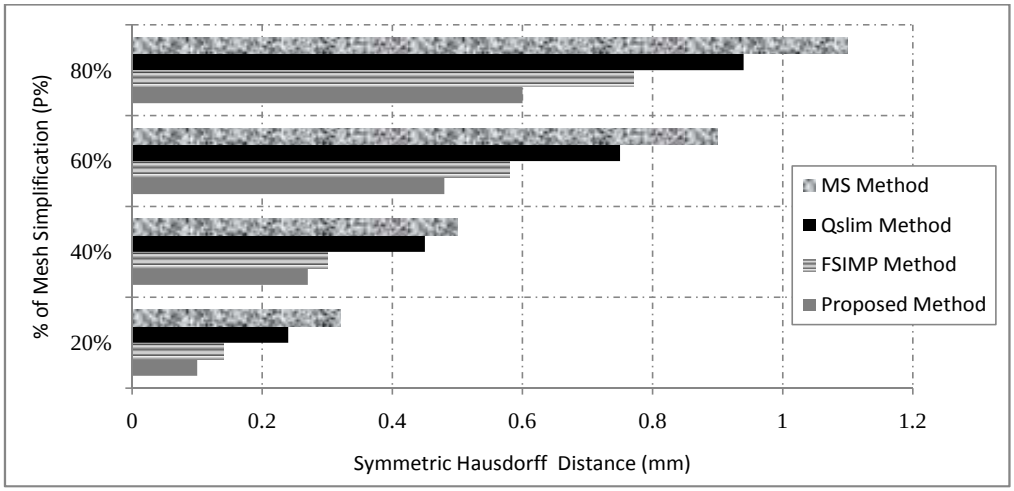

Figure 6.17: Comparison of Mesh Simplification Methods with SHD

The mean volume of the tumor obtained by manual (radiologist) and proposed automatic methods are 12359 mm^3 and 12312 mm^3, respectively. The reconstructed 3D model of the tumor can also be rotated so that the radiologist can analyze the structure of the tumor thoroughly. The two views of the 3D brain tumor are shown in Figure 6.18. The surface of the brain can also be reconstructed using the proposed 3D

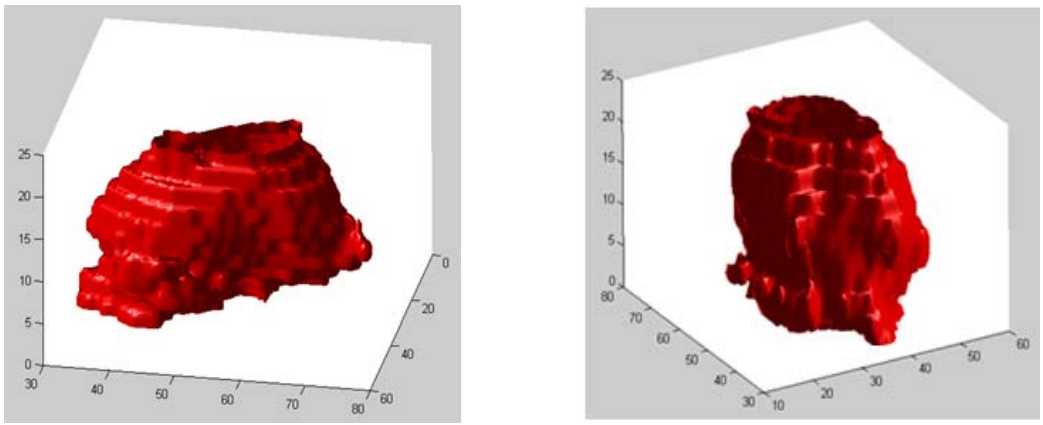

Figure 6.18: Two Views of the 3D Brain Tumor Obtained by Rotation

reconstruction approach, but by considering the brain region instead of the tumor.

Using the proposed approach, various types of cuts can also be performed on the brain by the radiologist to understand the tumor growth as shown in Figure 6.19. The traverse cut shown in Figure 6.19(a) helps the radiologist to determine the location of the tumor in the brain. The longitudinal cut shown in Figure 6.19(b) helps the radiologist to understand the growth and complexity of the tumor.

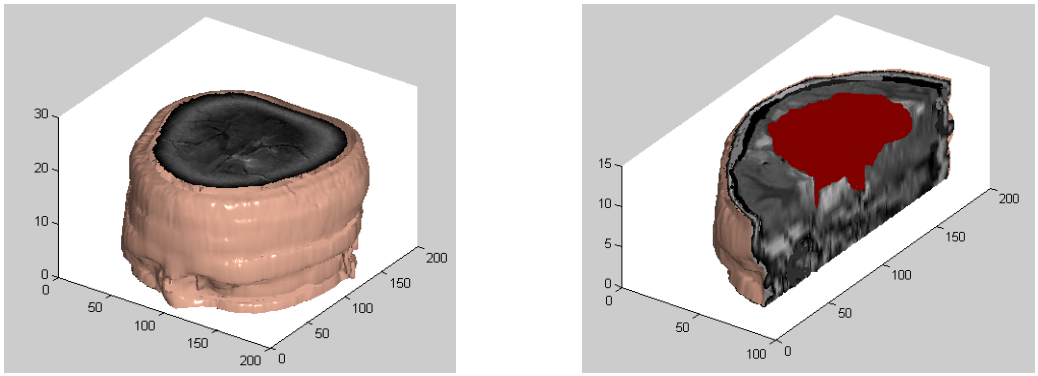

(a) (b)

Figure 6.19: Cuts of the 3D Brain (a) Traverse Cut (b) Longitudinal Cut

Efficiency of the 3D Reconstruction Scheme

This section discusses the time complexity of the proposed 3D reconstruction scheme. The 3D reconstruction of brain tumor consists of various phases such as segmentation, inter-slice interpolation, mesh generation, mesh simplification and rendering. The following list of notations is used for computing time complexity of the proposed 3D reconstruction scheme.

- Let G be the number of gray levels in the image histogram, C be the number of clusters in the brain region, I be the number of iterations required for the clustering algorithm to converge.
- Let N be the total number of pixels in the image and D be the number of cubes processed in the 3D reconstruction of the tumor mesh.
- Let V, E and R be the number of vertices, edges, triangles in the original mesh, respectively. R' be the reduced set of triangles in the simplified mesh.

The segmentation phase detects the tumor on abnormal slice using the proposed segmentation method based on MFCM clustering, and hence its time complexity is $O(ICG)$ as discussed in Chapter 3.

The proposed enhanced shape-based interpolation algorithm has a time complexity of $O(N)$ as it computes the chamfer Distance Transform (DT) by making two passes over the image. The marching cubes (MC) algorithm processes D cubes to generate the 3D surface mesh of the tumor and hence it has a time complexity of $O(D)$.

The time complexity of the proposed mesh simplification algorithm is dependent on the heap data structure used to maintain a set of vertices for mesh simplification. The heap is built with V vertices and hence the time complexity of building the heap is $O(V)$. During the mesh simplification, V deletions are performed on the heap. In order to delete a single vertex from the heap, the root vertex is exchanged with $(V-1)^{th}$ vertex, and the heap is recreated for $(V-1)$ vertices. The recreation of the heap is dependent on the height of the tree and hence the time complexity to recreate heap for $(V-1)$ vertices is $2log_2(V-1)$. The time complexity $T(V)$ for V deletions is computed based on heaps of diminishing sizes from V to 2 as given below.

$$\begin{aligned} T(V) &\leq 2log_2(V-1) + 2log_2(V-2) + ... + 2log_2 1 \\ &\leq 2\sum_{i=1}^{V-1} log_2 i \\ &\leq 2\sum_{i=1}^{V-1} log_2(V-1) \\ &\leq 2(V-1)log_2(V-1) \\ &\leq 2Vlog_2V \end{aligned} \tag{6.22}$$

Therefore, the time complexity for V deletions from the heap is $O(Vlog_2V)$. The overall time complexity of heap creation and deletion with V vertices is $[O(V) + O(Vlog_2V)] \approx O(Vlog_2V)$.

During the mesh simplification, the edges of the vertices in the flat regions are eliminated from the mesh and hence the number of triangles is reduced from R to R' in the simplified mesh. The simplified mesh with a reduced set of triangles is input to the rendering phase, which processes these triangles to shade the surface of the mesh. Hence, the time complexity of the rendering phase is $O(R')$. The radiologist's time in

the analysis of 3D tumor is reduced by 60%, since the proposed mesh simplification algorithm can remove 60% of the triangles from the mesh without any distortion. The time complexity of different phases of the 3D reconstruction scheme is summarized in Table 6.3.

Table 6.3: Time Complexity of Different Phases of 3D Reconstruction of Brain Tumor.

3D Reconstruction Phase	**Time Complexity**
Segmentation	$O(ICG)$
Interpolation	$O(N)$
Mesh Generation	$O(D)$
Mesh Simplification	$O(Vlog_2V)$
Rendering	$O(R')$

The MFCM clustering used in the segmentation phase is efficient as it clusters the image based on the gray levels in the image histogram instead of pixels in the image. Unlike the city-block distance in the original shape-based interpolation method (Raya and Udupa 1990), the chamfer distance in the proposed enhanced shape-based interpolation provides a good approximation to the Euclidian distance, and also has a lesser time complexity ($O(N)$) when compared to that of the Euclidian DT ($O(N^2)$). Further, the proposed mesh simplification algorithm is more efficient when compared the state-of-the art mesh simplification algorithms such as QSlim (Garland and Heckbert 1997) and MS (Lindstrom and Turk 1998). This is because the proposed algorithm iteratively selects the vertex with least curvature and collapses its optimal edge, and hence it has a time complexity of $O(Vlog_2V)$, whereas the QSlim and MS algorithms perform mesh simplification by selecting the edge that causes minimum geometric deviation, and hence their time complexity is $O(Elog_2E)$. The rendering phase of the proposed 3D reconstruction scheme is also accelerated, since the mesh with a reduced set of triangles R' is given as input to the rendering phase.

6.2.2 3D Liver Tumor Reconstruction Results

This section discusses the results of the 3D reconstruction experiments carried out on non-contrast-enhanced abdominal CT images of 487 patients (benign:247, malig-

nant:240). The detailed description of the dataset is already given in Section 2.8.

Effectiveness of 3D Reconstruction Scheme

The CT scan of the liver produces a set of 32 slices containing normal (without tumor) and abnormal slices (with tumor) as shown in Figure 6.20. The liver tumor is segmented on each abnormal slice as shown in Figure 6.21.

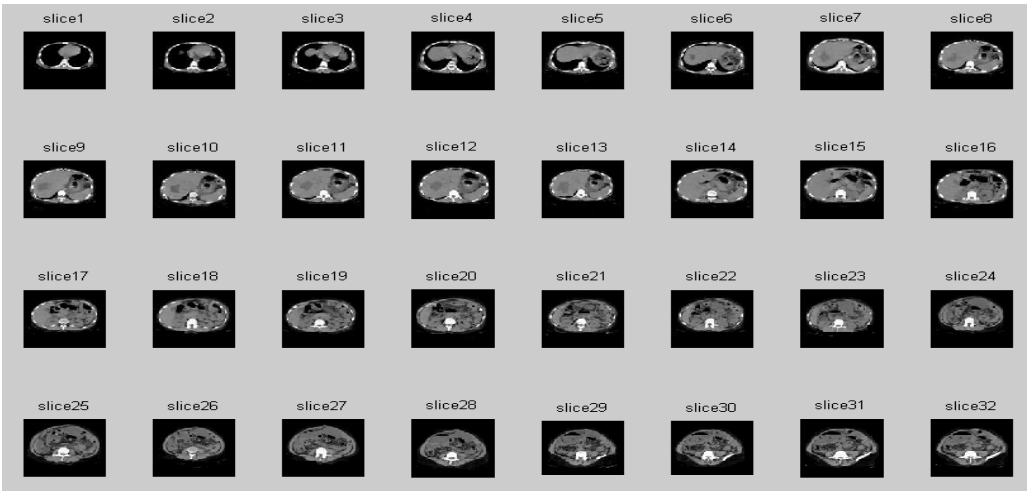

Figure 6.20: Set of Liver Slices obtained by CT Scan

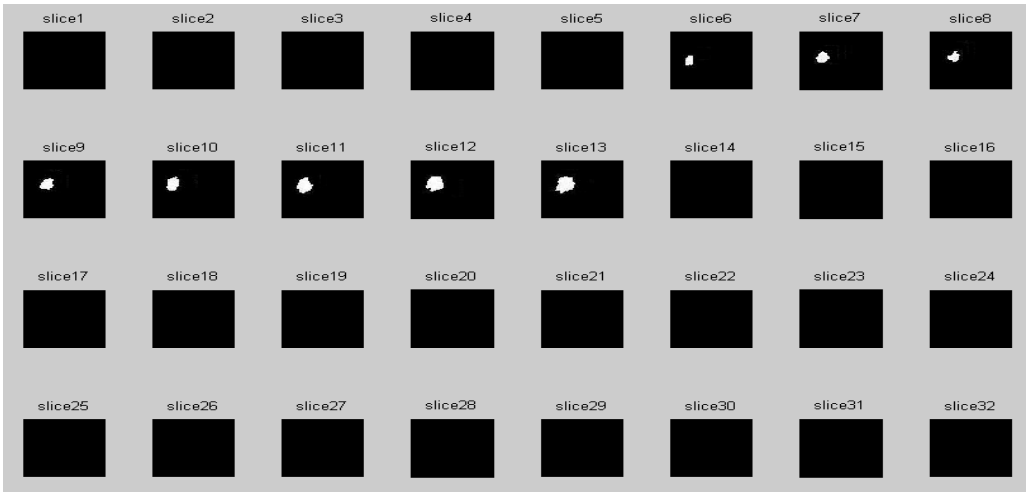

Figure 6.21: Set of Liver Tumor Segmented Slices

After the tumor segmentation, a volume data is formed in the 3D space by arranging 2D tumor contours exactly in real spatial positions. Then, missing slices in the volume data are estimated using the proposed enhanced shape-based interpolation technique. The effectiveness of the proposed enhanced shape-based interpolation is evaluated using overlap-based error measure, which is computed using Equation (6.20). Table 6.4 shows the comparison of the effectiveness of three interpolation methods: LG-linear gray level interpolation, SO-original shape based interpolation, SE-enhanced shape-based interpolation (proposed method). Four sets of liver tumor slices $\{S_i, S_{i+1}, S_{i+2}\}$ are taken from each of the 487 cases in the dataset. Slices S_i and S_{i+2} are given as input to the interpolation method to estimate slice S'_{i+1}. Next, the overlap-error is computed with S_{i+1} and S'_{i+1}.

Table 6.4: Comparison of Interpolation Methods

Dataset	**Slices**	**Overlap-Based Error(ε%)**		
	$\{S_i, S_{i+1}, S_{i+2}\}$	**LG**	**SO**	**SE**
CT	6,7,8	7.05	6.54	3.33
	8,9,10	6.67	3.12	1.07
	10,11,12	11.17	8.79	4.19
	11,12,13	13.35	9.48	4.36

It is observed that the LG interpolation method gives the worst performance with $\varepsilon < 14\%$, since it cannot capture the geometrical details of the tumor. The SO method captures the geometrical details of the tumor, but it gives ineffective results as it is dependent on city-block DT and it cannot handle drastic shifts of the tumor regions. Hence, SO method shows moderate performance with $\varepsilon < 10\%$. The proposed SE method outperforms ($\varepsilon < 5\%$) other interpolation methods, since it captures well the geometry of the tumor based on chamfer DT and center alignment of tumors. The error ($\varepsilon < 5\%$) may lead to small artifacts in the 3D surface of the tumor and hence some features of the tumor may get distorted.

The effectiveness of the proposed mesh simplification algorithm is demonstrated by presenting images of simplified models and error graphs. Figure 6.22 shows the simplified meshes and the corresponding rendered 3D models of liver tumors along with the percentage of faces simplified (P%) and the number of faces retained in the

simplified model. In order to analyze the effectiveness, the original model is simplified at different levels (40%, 60%, 80%). It is observed that even at 60% reduction the simplified model retains the sharp features of the original model, and the simplified model gets distorted when the reduction is more than 70%.

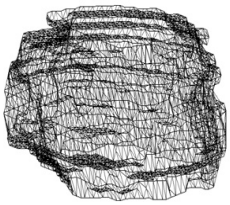

a. Original Mesh (P=0%, Faces=4794)

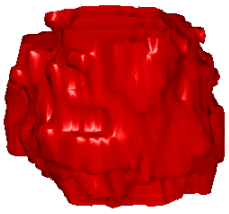

e. Original 3D Model (P=0%, Faces=4794)

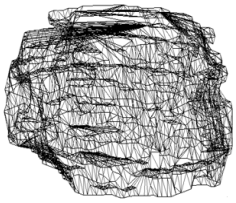

b. Simplified Mesh (P=40%, Faces=2876)

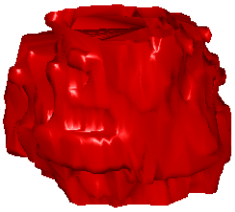

f. Simplified 3D Model (P=40%, Faces=2876)

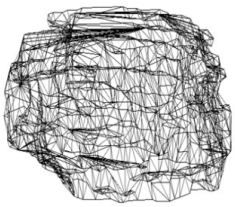

c. Simplified Mesh (P=60%, Faces=1917)

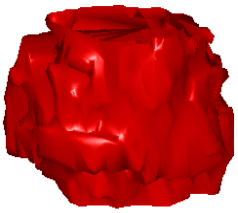

g. Simplified 3D Model (P=60%, Faces=1917)

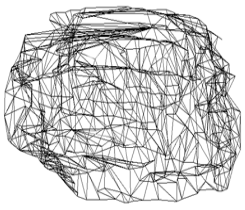

d. Simplified Mesh (P=80%, Faces=958)

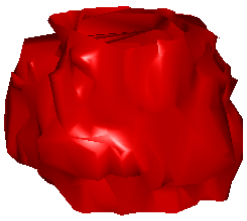

h. Simplified 3D Model (P=80%, Faces=958)

Figure 6.22: Mesh Simplification of Liver Tumor

The quality of the simplified models of the liver tumor generated by the proposed mesh simplification algorithm is evaluated using symmetric Hausdorff distance (SHD)

between original and simplified models of the tumor. Figure 6.23 shows the comparison of the proposed method with other state-of-the-art mesh simplification methods such as QSlim (Garland and Heckbert 1997), MS (Lindstrom and Turk 1998), and FSIMP (Hussain 2008). This comparison is based on average SHD computed with respect to simplified tumor models of all 487 cases in the dataset.

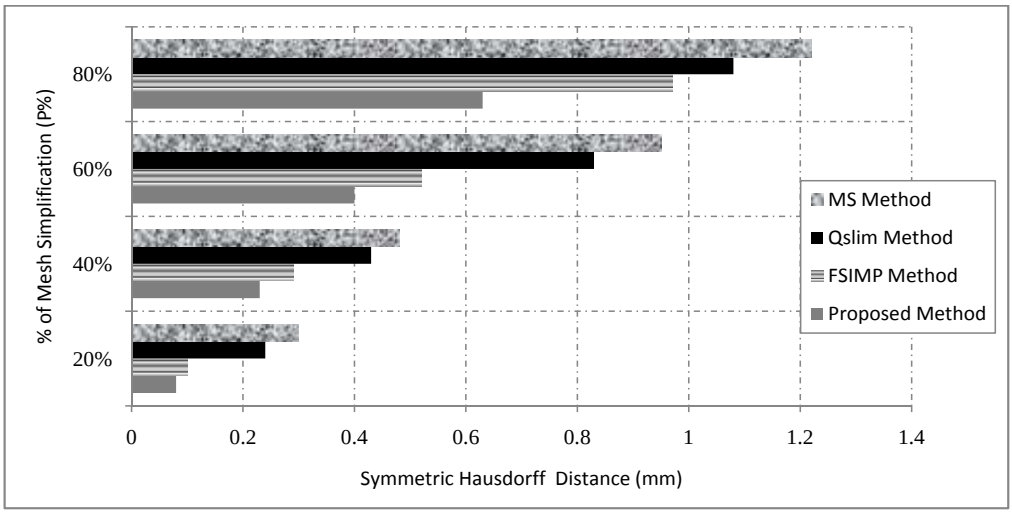

Figure 6.23: Comparison of Mesh Simplification Methods

It is observed that the proposed method is more effective ($SHD < 0.7\ mm$) when compared to other methods as it is based on selecting edge contractions with minimum effect on curvature, volume and shape of adjacent triangles. The mesh simplification error $SHD < 0.7\ mm$ may lead to small variations in the tumor volume and difficulty in estimating the stage of cancer. The FSIMP selects the vertex and its edge for removal based on the curvature, but simplified models are not of good quality ($SHD < 1\ mm$) because of the significant volume loss. The QSlim and MS methods perform mesh simplification using the error metrics based on the distance of a vertex to the plane and volume loss, respectively. These methods do not consider the curvature of the mesh, and hence cannot preserve the sharp details of the mesh in the simplified models. Therefore, QSlim and MS methods show poor performance with $SHD < 1.1\ mm$ and $SHD < 1.3\ mm$, respectively.

The mean volume of the tumor obtained by manual (radiologist) and proposed automatic methods are 10657 mm^3 and 10415 mm^3, respectively. Thus, the volume obtained by the proposed method is close to the radiologist's result. The proposed

method of volume computation is automatic, and hence efficient. Whereas in the manual method radiologist marks the tumor on each abnormal slice to compute the volume based on the slice gap and thickness, and hence manual method is tedious and time consuming. The reconstructed 3D model of the liver tumor can also be rotated so that the radiologist can analyze the structure of the tumor thoroughly, and the two views of the 3D liver tumor are shown in Figure 6.24. The surface of the liver can also be reconstructed using the proposed 3D reconstruction approach, but by considering the liver region instead of the tumor region. The radiologist can perform various types of cuts on the liver based on the proposed 3D reconstruction scheme to understand the tumor growth as shown in Figure 6.25. The traverse cut

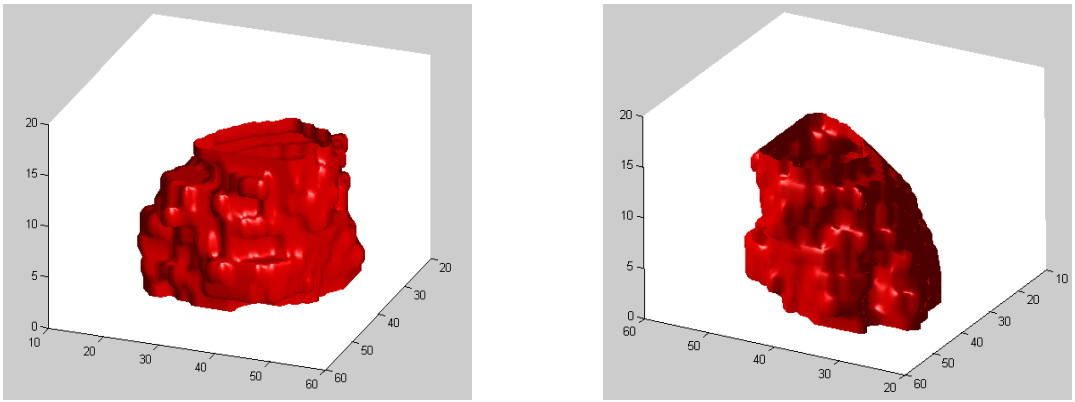

Figure 6.24: Two Views of the 3D Liver Tumor Obtained by Rotation

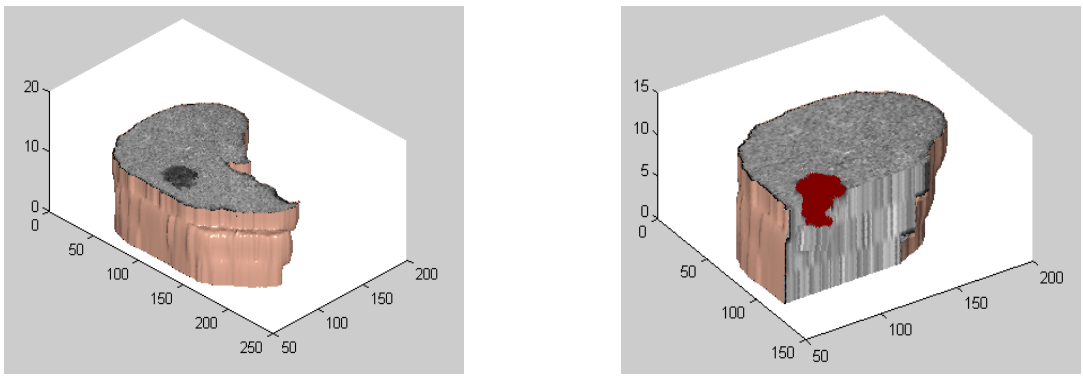

(a) (b)

Figure 6.25: Cuts of the 3D Liver (a) Traverse Cut (b) Longitudinal Cut

shown in Figure 6.25(a) helps the radiologist to determine the location of the tumor in the liver. The longitudinal cut shown in Figure 6.25(b) helps the radiologist to understand the growth and complexity of the tumor.

Efficiency of the 3D Reconstruction Scheme

This section discusses the time complexity of the proposed 3D reconstruction scheme. The 3D reconstruction of liver tumor consists of various phases such as segmentation, inter-slice interpolation, mesh generation, mesh simplification and rendering. The following list of notations is used in the computation of time complexity of the proposed 3D reconstruction scheme for liver tumor.

- Let G be the number of gray levels in the image, C be the number of clusters in the liver region, I be the number of iterations required for clustering algorithm to convergence. M be the total number of pixels in the tumor region. H and W be the height and width of the neighborhood of each pixel, respectively.
- Let N be the total number of pixels in the image. D be the number of cubes processed in the 3D reconstruction of the tumor mesh.
- Let V, E and R be the number of vertices, edges, triangles in the original mesh, respectively. R' be the reduced set of triangles in the simplified mesh.

The time complexity of different phases of the 3D reconstruction scheme is summarized in Table 6.5.

Table 6.5: Time Complexity of Different Phases of 3D Reconstruction of Liver Tumor

3D Reconstruction Phase	**Time Complexity**
Segmentation	$O(ICG) + O(MHW)$
Interpolation	$O(N)$
Mesh Generation	$O(D)$
Mesh Simplification	$O(Vlog_2V)$
Rendering	$O(R')$

The segmentation phase detects the liver tumor on abnormal slice using the proposed segmentation method based on the automatic region growing algorithm, and

hence its time complexity is $O(ICG)+O(MHW)$ as discussed in Chapter 3. All other phases have time complexity similar to that of the brain tumor reconstruction phases and these time complexities are already discussed in Section 6.2.1. The proposed 3D reconstruction scheme improves the efficiency of segmentation, interpolation, mesh simplification and rendering phases, and thus helps in building the 3D model of the tumor in less amount of time. Overall, the radiologist's time in the analysis of 3D tumor is reduced by 60%, since the proposed mesh simplification algorithm can remove 60% of the triangles from the mesh without any distortion.

6.3 Summary

This chapter discussed the proposed 3D reconstruction scheme for building the 3D model of the tumor and for computing the tumor volume. The proposed enhanced shape-based interpolation and mesh simplification algorithms improve the effectiveness and efficiency of the 3D reconstruction scheme. The experimental results demonstrated that the proposed enhanced shape-based interpolation method is effective in estimating brain/liver tumor slices with the error (ε) less than 5%, and it is also efficient as it is dependent on n-neighbor chamfer distance transform. The proposed mesh simplification method is able to retain the curved regions in the simplified mesh even at 60% reduction in the number of triangles of the mesh and it is also efficient as it collapses the edges of vertices only in the flat regions of the mesh. Further, the mesh simplification algorithm helped to accelerate the rendering phase by generating a 3D model with less number of triangles. Thus, the proposed 3D reconstruction scheme can assist the radiologist in building the accurate 3D model of the brain/liver tumor in less amount of time.

Chapter 7

Conclusion and Future Work

The accurate diagnosis of brain and liver tumors is crucial for effective treatment of the patient. The needle biopsy provides confirmed diagnosis of the tumor, but it is an invasive technique. Further, the diagnosis of the tumor by the radiologist based on visual analysis is time consuming, subjective and inaccurate. Therefore, the CAD system is essential to assist the radiologist in fast and accurate diagnosis of the cancer. But, the existing CAD methods do not provide the automation, accuracy and efficiency required in the medical domain. Hence, the research work in this thesis is directed towards the development of an automatic, effective and efficient CAD system for detection, classification, CBIR and 3D reconstruction of brain and liver tumors.

The first set of contributions of this thesis attempts to address the tumor detection problem by proposing automatic, effective and efficient segmentation techniques for detection of brain and liver tumors on MRI and CT images, respectively. The segmentation technique based on Modified Fuzzy C-means (MFCM) clustering algorithm is proposed to detect the brain tumor on the MRI image. The proposed MFCM clustering algorithm is effective as it automatically determines the initial cluster centers, performs clustering based on fuzzy membership matrix and contains an effective objective function to provide compact and well separated clusters. The MFCM clustering algorithm is also efficient as it performs clustering based on the gray level histogram instead of pixels in the image. The segmentation technique based on the automatic region growing algorithm is proposed to detect the liver tumor on the abdominal CT image. The proposed automatic region growing algorithm automatically determines the seed point and threshold by combining MFCM clustering algorithm with the region growing algorithm. Thus, the proposed technique is effective and

efficient. The experimental results show that the proposed segmentation techniques achieve good agreement with the gold standard and these techniques are also more efficient when compared to the existing tumor segmentation techniques. However, there is a scope for further improvement of the proposed segmentation techniques as given below:

- The computational efficiency of the MFCM clustering algorithm can be further improved by developing a parallel MFCM clustering algorithm, since the computation of cluster centers and member matrix is sequential and time consuming.
- The automatic region growing algorithm grows the region by analyzing all neighborhood pixels of each seed pixel, and thus the region growing process is time consuming. Hence, the proposed automatic region growing algorithm can be further made computationally efficient by parallelizing the region growing steps.
- The proposed MFCM clustering and automatic region growing algorithms could not effectively detect the boundary of the tumor region in case of blurred edges. Hence, these algorithms can be combined with edge detection or deformable model approaches to detect an exact boundary of the tumor region.

The second set of contributions of this thesis targets for effective and efficient tumor classification scheme for identifying the type of brain/liver tumor as benign or malignant. In the proposed scheme, the characteristics of the tumor are represented by extracting significant features of the tumor such shape, texture and boundary features. In order to provide the effective and efficient classification, the dimensionality of the feature vector is reduced using the proposed two-level feature selection technique consisting of Information Gain (IG) based feature ranking and Independent Component Analysis (ICA) based feature selection methods. The effectiveness of the tumor classification is further improved by using the proposed ensemble classifier consisting of three classifiers: Support Vector Machine (SVM), Artificial Neural Network (ANN) and k-Nearest Neighbor (k-NN). The experimental results show that the ensemble classifier achieves more accurate tumor classifications when compared to single classifiers and radiologists. Further, the proposed scheme is efficient as it uses reduced feature vector rather than a complete feature vector of the tumor. In future, the proposed tumor classification scheme can be enriched to handle the following issues:

- Investigate and quantify the features extracted from other imaging modalities (such as magnetic resonance spectroscopy and ultrasonogrphy) and fuse them with the features employed in the present work to improve the classification accuracy.
- More extensive training using larger datasets is expected to further improve the generalization ability of the proposed classification scheme.
- The tumor classification performed by SVM, ANN and k-NN classifiers in the ensemble is sequential and hence these classifications can be parallelized to further improve the classification efficiency.

The third set of contributions of this thesis aim for Content-Based Image Retrieval (CBIR) of brain and liver tumor images from the database to assist the radiologist in the diagnosis of brain and liver tumors based on relevant cases. In this direction two effective and efficient CBIR methods are proposed based on image rotation correction and rotation invariant features. The semantic gap problem in CBIR is addressed by using a hierarchical CBIR framework with separate set of features for representing the class and subclass of the tumor. An efficient indexing structure called as CIKD is proposed for fast retrieval of images from the database. The proposed modified k-means clustering algorithm effectively clusters the tumor features in the database by automatically identifying the number of clusters and initial cluster centers. The experimental results demonstrate that the proposed CBIR methods are robust to misalignment of images, and also accurate and efficient in retrieving similar pathology bearing tumor images from the database. The proposed CBIR methods can be augmented to incorporate the following challenges through future research:

- The accuracy of the CBIR can be further improved by combining visual and text features such as the image descriptions provided by the physician in the diagnostic reports.
- The proposed CBIR methods are meant for specific imaging modality such as MRI of the brain and CT of the liver. Thus, the proposed methods can be extended to work for database consisting of the brain and liver tumor images obtained from different imaging modalities.

The fourth set of contributions of this thesis attempt to develop effective and efficient 3D reconstruction scheme for building the 3D model of the brain/liver tumor

to assist the radiologist in understanding the complexity of the tumor and planning the treatment. The 3D reconstruction scheme consists of the proposed enhanced shape-based interpolation algorithm for estimating the missing slices of the tumor. This algorithm overcomes the drawback of the original shape-based interpolation algorithm by including chamfer distance transform and center alignment in the interpolation process. The 3D surface mesh of the tumor is generated using the marching cubes algorithm. In order to accelerate the rendering phase for interactive medical applications, the number of triangles in the reconstructed mesh is reduced using the proposed mesh simplification algorithm. The experimental results demonstrate that the proposed shape-based interpolation is more effective and efficient when compared to the existing interpolation techniques. The proposed mesh simplification algorithm preserves the sharp details of the mesh in the simplified models, and hence it is superior when compared to the existing mesh simplification algorithms. The further investigation should focus on the following issues:

- The marching cubes (MC) algorithm is computationally expensive due to the sequential processing of small sized cubes for reconstructing the 3D mesh of the tumor. Hence, the MC algorithm should be parallelized to improve the efficiency.
- The mesh generated by the MC algorithm is piecewise linear approximation to the original surface, and thus the reconstructed surface consists of staircase artifacts. Hence, the quality of the reconstructed surface can be improved by smoothing the generated mesh.
- The visual attributes like intensity, texture and viewing parameters can be included in the proposed mesh simplification scheme to perform appearance preserving and view-dependent simplification.

Finally, the future work is needed to evaluate how effective are the proposed techniques (segmentation, classification, CBIR and 3D reconstruction) when used by the radiologist in the analysis of brain and liver tumors. This evaluation helps to determine the usefulness of the proposed CAD system in the clinical environment. It also helps to determine the diagnosis accuracy when the entire diagnosis process is automated and there is no involvement of the radiologist. Thus physicians can determine whether their accuracy and efficiency is improved with the support of the CAD system.

To summarize, this thesis proposes automatic, effective and efficient solutions to the problems related to computer-aided tumor detection, classification, CBIR and 3D reconstruction for providing the assistance to the radiologist in the accurate and fast diagnosis of brain and liver tumors.

Appendix 1

Graphical User Interface

The graphical user interface (GUI) is a human-computer interface that allows the users to communicate with the applications using windows, menus, image and symbols rather than text commands. In this appendix, we present the easy-to-use and user-friendly GUI designed to provide an interaction with the developed CAD system for the diagnosis of brain and liver tumors. The radiologist can access various tumor analysis tasks such as tumor detection, classification, Content-Based Image Retrieval (CBIR) and 3D reconstruction through the GUI.

Figure 7.1 shows the main window of the GUI for CAD system. The radiologist can select the type of task which he/she wants to perform on the liver/brain tumor.

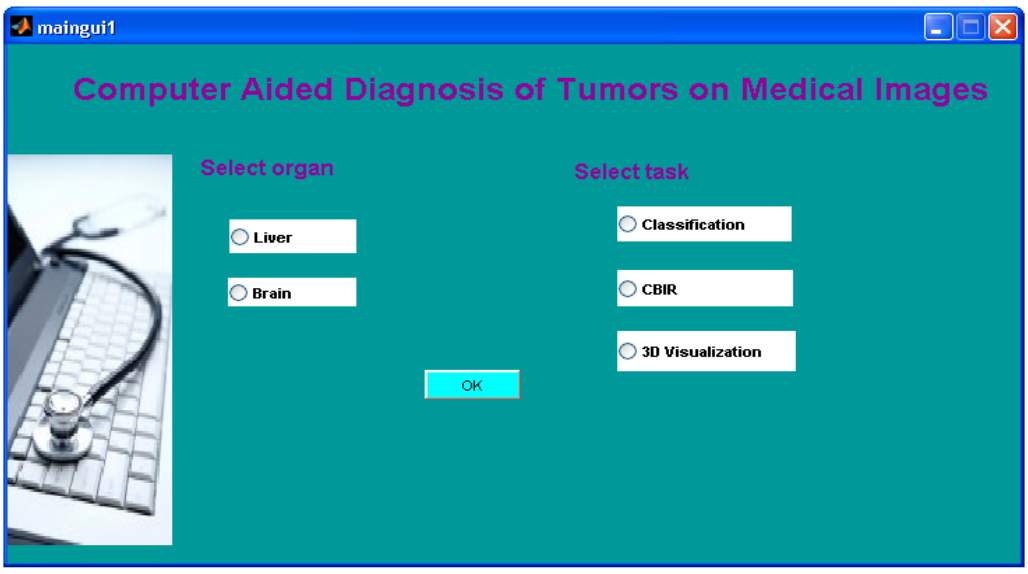

Figure 7.1: Main Window of the GUI for CAD System

Based on the selection, the corresponding window of the tumor analysis task will be opened. The output obtained from the task provides second opinion to the radiologist for making diagnostic decisions. The details of the GUI for the different modules of the CAD system are given below.

Tumor Detection and Classification

When the radiologist selects the brain and classification task, the window shown in Figure 7.2 will be opened. Here the radiologist can choose the image of the slice in which he/she wants to detect the tumor or identify the type of detected tumor as benign or malignant. If the slice chosen is normal, then the message is displayed indicating that the slice is normal and does not contain tumor. Otherwise, the region of the tumor on the abnormal slice is detected and marked on the image. The type of the tumor is displayed as benign or malignant when the classify button is clicked as shown in Figure 7.2. Similar operations can be performed by selecting the liver in the main window of the GUI.

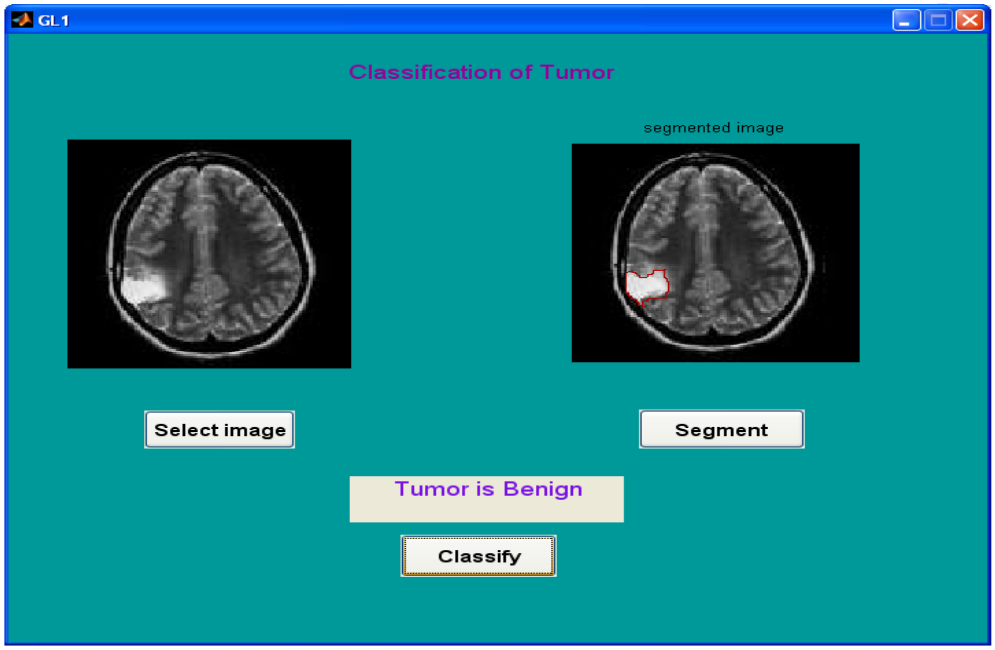

Figure 7.2: GUI for Tumor Segmentation and Classification

Content Based Image Retrieval of Tumor

Figure 7.3 shows the GUI for the CBIR system along with the retrieved brain images. It can be seen that the query image and retrieved images contain the benign tumor. With the help of a GUI, the user can select a query image and the number of images to be retrieved from the database. The retrieved images are ranked by degree of similarity to the query image. The top 12 most similar images are retrieved and displayed along with the patient data in response to the query image as shown in Figure 7.3. Further, the retrieval results can be refined for detailed analysis based on the age and gender of the patient. Then, the radiologist can study the characteristics of the retrieved tumors and also refer diagnostic report to know the severity and prescribed treatment of the corresponding cases. All these parameters assist the radiologist in the diagnosis of the brain tumors. Similar operations can be performed by selecting the liver in the main window of the GUI.

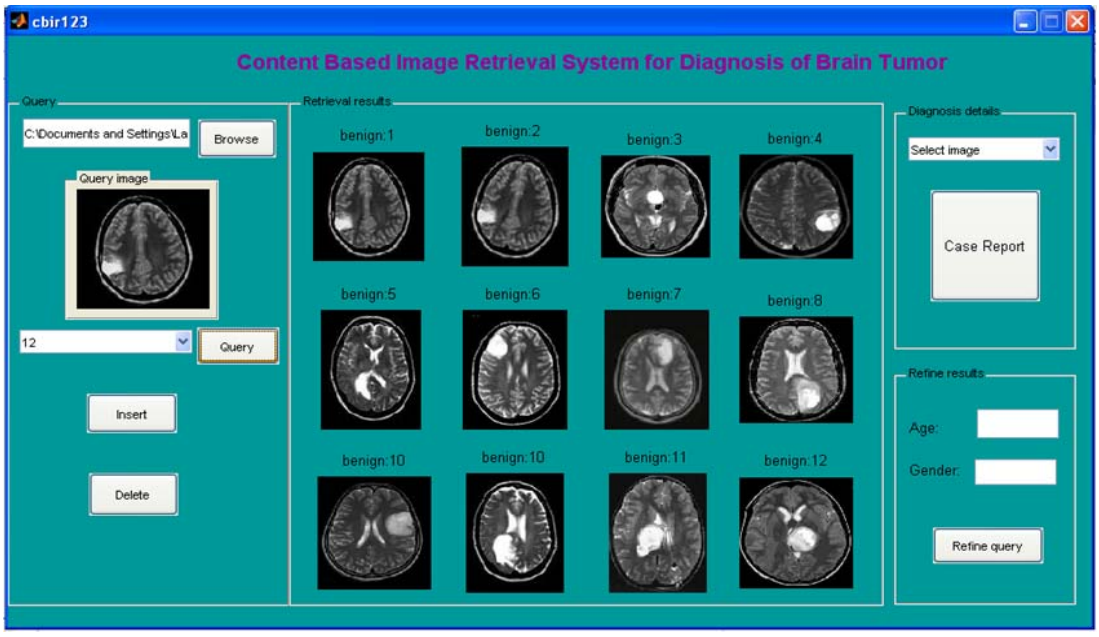

Figure 7.3: GUI for Content-Based Image Retrieval

3D Reconstruction of Tumor

The GUI for the 3D reconstruction of brain/liver tumor provides the facility for the radiologist to view the 3D model of the tumor and rotate the 3D model to have

multiple views of the tumor as shown in Figure 7.4. In order to determine the stage of cancer, the radiologist can measure the volume of the 3D tumor on clicking the volume button. The radiologist can also cut the brain/liver surface by selecting traverse or longitudinal cut in the GUI. These cuts help the radiologist to understand the complexity and growth of the tumor in the brain/liver.

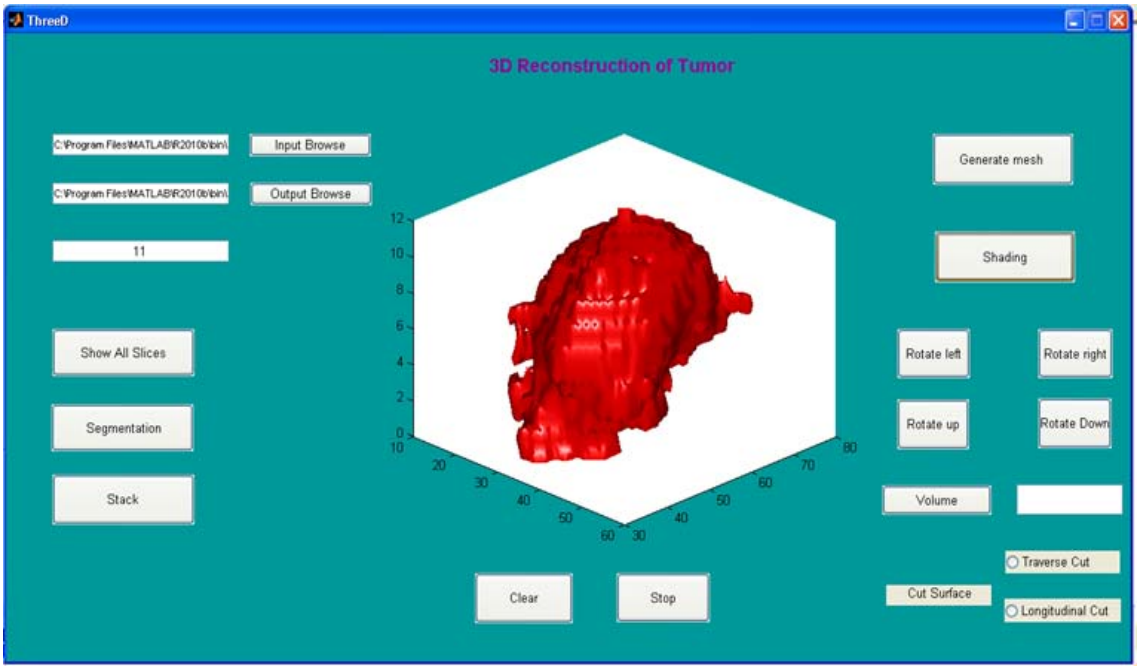

Figure 7.4: GUI for 3D Reconstruction of Tumor

Bibliography

Abbasi, S., Mokhtarian, F., and Kittler, J. (1999). "Curvature scale space image in shape similarity retrieval". *Multimedia Systems*. 7:467–476.

Acharyya, M., De, R. K., and Kundu, M. K. (2003). "Extraction of features using M-band wavelet packet frame and their neuro-fuzzy evaluation for multitexture segmentation". *IEEE Transactions on Pattern Analysis and Machine Intelligence*. 25:1639–1644.

Adams, R. and Bischof. L. (1994). "Seeded region growing". *IEEE Transaction on Pattern Analysis and Machine Intelligence*. 16:641–647.

Agarwal, P., Sardana, H. K., and Jindal, G. (2009). "Content based medical image retrieval:Theory,gaps and future directions". *Graphics, Vision and Image Processing*. 9:27–37.

Ahmadian, A., Mostafa, A., Abolhassani, M. D., and Alam, N. R. (2004). "A method for texture classification of ultrasonic liver images based on Gabor wavelet". *Proc. of International Conference on Signal Processing, IEEE*. 971–974.

Akilandeswari, U., Nithya, R., and Santhi, B (2012). "Review on feature extraction methods in pattern classification". *European Journal of Scientific Research*. 71:265–272.

Albu, A. B., Beugeling, T., and Laurendeau, D. (2008). "A morphology-based approach for interslice interpolation of anatomical slices from volumetric images". *IEEE Transaction on Biomedical Engineering*. 55:2022–2038.

Alia, O. M., Mandava, R., Ramachandran, D., and Aziz, M. E. (2009). "Hormony search-based cluster initialization for fuzzy c-means segmentation of MR images". *Proc. of IEEE Region 10 Conference (TENCON 2009)*. 1–6.

Al-Zoubi, M. B., Hudaib, A., and Al-Shboul, B. (2007). "A Fast Fuzzy Clustering Algorithm". *Proc. of WSEAS International Conference on Artificial Intelligence, Knowledge Engineering and Databases, ACM*. 28–32.

Amruta, A., Gole, A., and Karunakar, Y (2010). "A systematic algorithm for 3D reconstruction of MRI based brain tumors using morphological operators and bicubic interpolation". *Proc. of International Conference on Computer Technology and Development, IEEE*. 305–309.

Arbelaitz, O., Gurrutxaga, I., Muguerza, J., and Pérez, J. M. (2013). "An extensive comparative study of cluster validity indices". *Pattern Recognition*. 46:243–256.

Archip, N., Rohling, R., Dessenne, V., Erard, P. J., and Nolte. L. P. (2006). "Anatomical structure modeling from medical images". *Computer Methods and Programs in Biomedicine*. 82:203–215.

Arizmendi, C., Vellido, A., and Ramero, E. (2011). "Binary classification of brain tumors using discrete wavelet transform and energy criteria". *Proc. IEEE Latin American Symposium on Circuits and Systems*. 1–4.

Arun, K. S. and Menon, H. P. (2009). "Content based medical image retrieval by combining roation invariant contourlet features and fourier descriptors". *International Journal of Recent Trends in Engineering*. 2:35–39.

Babu, G. P. and Murty, M. N. (1993). "A near-optimal initial seed value selection in k-means means algorithm using a genetic algorithm". *Pattern Recognition Letters*. 14:763–769.

Bauer, S., Nolte, L. P., and Reyes, M. (2011). "Fully automatic segmentation of brain tumor images using support vector machine classification in combination with hierarchical conditional random field regularization". *Proc. of International Conference on Medical Image Computing and Computer Assisted Intervention (MICCAI 2011), LNCS, Springer*. 6893:354–361.

Bay, H., Ess, A., Tuytelaars, T., and Gool, L. V. (2008). "Speeded-up robust features (SURF)". *Computer Vision and Image Understanding*. 110:346–359.

Beucher, S. and Meyer, F. (1992). "The morphological approach to segmentation: the watershed transformation". *Mathematical Morphology in Image Processing, CRC Press*. 433–481.

Bezdek, J. C. (1981). "Pattern recognition with fuzzy objective function algorithms". *New York: Plenum Press*.

Bezdek, J. C. and Pal, N. R. (1998). "Some new indexes of cluster validity". *IEEE Transaction on Systems, Man and Cybernetics*. 28:301–315.

Bhat, S. and Kunte, S. R. (2010). "Mixed model based on watershed and active contour algorithm for brain tumor segmentation". *Proc. of International Conference on Advances in Recent Technologies in communication and Computing, IEEE*. 398–400.

Bian, S. and Wang, W. (2007). "On diversity and accuracy of homogeneous and heterogeneous ensembles". *International Journal of Hybrid Intelligent Systems*. 4:103–128.

Bishnu, P. S. and Bhattacherjee, V. (2012). "Software Fault Prediction Using Quad Tree-Based K-Means Clustering Algorithm". *IEEE transaction on Knowledge and Data Engineering*. 24:1146–1150.

Boissonnat, J. D., Pons J. P., and Yvinec, M. (2009). "From segmented images to good quality meshes using Delaunay refinement". *Emerging Trends in Visual Computing, LNCS, Springer*. 5416:13–37.

Borgefors, G. (1986). "Distance transformations in digital images". *Computer Vision, Graphics and Image Processing*. 34:344–371.

Bourne, R. (2010). "Fundamentals of digital Imaging in Medicine". *Springer*. 161–164.

Burger and Burge (2008). "Digital Image Processing". *Springer*. 106–108.

Bushberg, J. T., Seibert, J. A., Leidholdt, E. M., and Boone, J. M. (2002). "The essential physics of medical imaging". *2nd Edition, Lippincott Williams & Wilkins*.

Cai,W., Chen,S., and Zhang ,D. (2007). "Fast and Robust fuzzy c-means clustering algorithms incorporating local information for image segmentation". *Pattern Recognition*. 40:825–838.

Cannon, R. L., Dave, J. V., and Bezdek, J. C. (2010). "Efficient implementation of the fuzzy c-means clustering algorithms". *IEEE Transactions on Pattern analysis and Machine Intelligence*. 8:248–255.

Castro, A., Bóveda, C., and Arcay, B. (2007). "A new method for the initialization of clustering algorithms based on histogram analysis". *IASTED International Conference on Visualization, Imaging and Image Processing, ACM*. 176–181.

Chen, S. Y., Lin, W. C., Liang C.C., and Chen, C.T. (1990). "Improvement on dynamic elastic interpolation technique for reconstructing 3-D objects from serial cross sections". *IEEE Trnasaction on Medical Imaging*, 9:71–83.

Choudhary, A., Moretto, N., Ferrarese, F. P., and Zamboni, G. A. (2008). "An Entropy Based Multi-Thresholding Method for Semi-Automatic Segmentation of Liver Tumors". *Proc. of Workshop on 3D Segmentation in the Clinic: A Grand Challenge II, Liver Tumor Segmentation, MICCAI 2008*.

Clavien, P. A. (2011). "Malignant liver tumors: Current and Emerging Therapies". *3rd Edition, John Wiley & Sons*.

Cobbold, R. S. C. (2007). "Foundations of biomedical ultrasound". *Oxford University Press*.

Cobzas, D., Birkbeck, N., Schmidt, M., Jagersand, M., and Murtha, A. (2007). "3D Variational brain tumor segmentation using a high dimensional feature set". *Proc. of IEEE International Conference on Computer Vision(ICCV'07)*, 1–8.

Cook, L. J., Cook, and Freedman, J. (2011). "Neuroanatomy". *4th Edition, Elsevier Health Sciences*.

Corso, J. J., Sharon, E., Dube, S., El-Saden, S., Sinha, U., and Yuille, A. (2008). "Efficient multi-level brain tumor segmentation with integrated Bayesian model classification". *IEEE Transaction on Medical Imaging*. 27:629–640.

Crossingham, J. L., Jenkinson, J., Woolridge, N., Gallinger, S., Tait, G. A., and Moulton, C.-A. E. (2009). "Interpreting three-dimensional structures from two-dimensional images: a web-based interactive 3D teaching model of surgical liver anatomy". *HPB*. 11:523–528.

Crossman, A. R. and Neary, D. (2010). "Neuroanatomy". *4th Edition, Elsevier Health Sciences*.

Davis, L. S. (1981). "Polarograms: A new tool for image texture analysis". *Pattern Recognition*. 13:219–223.

de Vargas, R. R., Bedregal, B. R. C., and Palmeira, E. S. (2011). "A comparative study between K-Means,FCM and ckMeans algorithms". *Proc. of Workshop on Theoretical Computer Science (WEIT 2011), IEEE*. 32–38.

Davies, D. L. and Bouldin, D. W. (1979). "A cluster separation measure". *IEEE Transaction on Pattern analysis and Machine Intelligence*. PAMI-1:224–227.

DeVita, V. T., Lawrence, T. S., and Rosenberg, S. A. (2012). "Cancer: Principles and Practice of Oncology: Primer of the Molecular Biology of Cancer". *Lippincott Williams & Wilkins*.

Dietrich, C. A., Scheidegger, C. E., Schreiner, J., Comba, J. L. D., Nedel, L. P., and Silva, C. T. (2009). "Edge transformations for Improving Mesh Quality of Marching Cubes". *IEEE Trnasaction on Visualization and Computer Graphics*. 15:150–159.

Doi, K. (2007). "Computer aided diagnosis in medical imaging: historical review, current status and future potential". *Computerized Medical Imaging and Graphics*. 31:198–211.

Dongxiang, C. and Tiankun, L. (2009). "Iterative quadtree decomposition segmentation of liver MR image". *Proc. of International Conference on artificial Intelligence and Computational Intelligence, IEEE*. 527–529.

Dube, S., El-Saden, S., Cloughesy, T. F., and Sinha, U. (2006). "Content based image retrieval for MR image studies of brain tumors". *Proc. of IEEE International conference of the Engineering in Medicine and Biology Society (EMBS 2006)*. 3337–3340.

Dunn, J. C. (1974). "A fuzzy relative of the isodata process and its use in detecting compact and well separated clusters". *Journal of Cybernetics*. 3:32–57.

Dürst, M. J. (1988). "Additional reference to marching cubes". *Computer Graphics*. 22:72–73.

Dyn, N., Hormann, K., Kim, S. J., and Levin, D. (2001). "Optimizing 3D triangulations using discrete curvature analysis". *Mathematical Methods for Curves and Surfaces*. 135–146.

Eleyan, A. and Demirel, H. (2011). "Co-occurrence matrix and its statistical features as a new approach for face recognition". *turkish Journal of Electrical Engineering and Computer Sciences*. 19:97-107.

Emmanuel, M., Ramesh Babu, D. R., Potdar, G. P., Sonkamble, B. A., and Game, P. (2007). "Content-based medical image retrieval". *Proc. of International Conference on Information and Communication Technology in Electrical Sciences (ICTES 2007), IEEE*. 712–717.

Fan, J., Zeng, G., Body, M., and Hacid,M. S. (2005). "Seeded region growing: an extensive study". *Pattern Recognition Letters*. 26:1139–1156.

Fang, Y. and Wang, J. (2012). "Selection of the number of clusters via the bootstrap method". *Computational Statistics and Data Analysis*. 56:468–477.

Fauzi, M. F. A. and Wan Ahmad, W. S. H. M. (2008). "Efficient block based matching for content based retrieval of CT head images". *Proc. of IEEEWorkshop on Multimedia Signal Processing*. 142–147.

Fazel Zarandi, M. H., Zarinbal, M., and Izadi, M. (2011). "Systematic image processing for diagnosing brain tumors: A type-II fuzzy expert system approach". *Applied Soft Computing*. 11:285–294.

Foley, J. D., Van Dam, A., Feiner, S. K., and Hughes, J. F. (1996). "Computer graphics : principles and practice". 2^{nd} *Edition, Addison-Wesley*.

Frakes, D. H., Dasi, L. P., Pekkan, K., Kitajima, H. D., Sundareswaran, K., Yoganathan, A. P., and Smith, M. J. T. (2008). "A new method for registration-based medical image interpolation". *IEEE Transaction on Medical Imaging*. 27:370–377.

Franc, M. and Skala, V. (2002). "Fast algorithm for triangular mesh simplification based on vertex decimation". *Proc. of International conference on Computational Science (ICCS 2002), LNCS, Springer*. 42–51.

Freedman, J. (2009). "Brain Cancer:Current and Emerging Trends in Detection and Treatment". *The Rosen Publishing Group*.

Freeman, H. (1961). "on the encoding of arbitrary geometric configurations". *IRE Transaction on Electronic Computers*. EC-10:260-268.

Fujita, H., You, J., Li, Q., Arimura, H., Tanaka, R., Sanada, S., Niki, N., Lee, G., Hara, T., Fukuoka, D., Muramatsu, C., Katafuchi, T., Iinuma, G., Miyake, M., Arai, Y., and Moriyama, N. (2010). "State-of-the-art computer aided detection/diagnosis (CAD)". *Proc. of International Conference on Medical Biometrics (ICMB 2010), LNCS, Springer*, 6165:296–305.

Fukunaga, K. (1990). "Introduction to statistical pattern recognition". 2^{nd} *Edition, Academic Press*.

Garland, M., Heckbert, P. S. (1997). "Surface simplification using quadric error metrics". *Proc. of ACM SIGGRAPH conference on Computer graphics and interactive techniques*. 209–216.

Georgiadis, P. Cavouras, D., Kalatzis, I., Daskalakis, A., Kagadis, G. C., Sifaki, K., Malamas, M., Nikiforidis, G., and Solomou, E. (2008). "Improving brain tumor characterization on MRI by probabilistic neural network and non-linear transformation of textural features". *Computer Methods and Programs in Biomedicine*. 89:24–32.

Gerig, G., Jomier, M., and Chakos, M. (2001). "Valmet: a new validation tool for assessing and improving 3D object segmentation". *Proc. of MICCAI 2001, LNCS, Springer*. 2208:516–523.

Ghanavati, S., Li, J., Liu, T., Babyn, P. S., Doda, W., and Lampropoulos, G. (2012). "Automatic brain tumor detection in magnetic resonance images". *Proc. of IEEE Internation Symposium on biomedical Imaging*. 574–577.

Gonzalez, R. C. and Woods, R. E. (2009). "Digital Image Processing". 3^{rd} *Edition, Pearson Education*.

Goshtasby, A., Turner, D. A., and Ackerman, L. V. (1992). "Matching tomographic slices for interpolation". *IEEE Transaction on Medical Imaging*. 11:507–516.

Gouraud, H. (1971). "Continous shading of curved surfaces". *IEEE Transaction on Computers*. C-20:623–629.

Greenberg, H. S., Chandler, W. F., and Sandler, H. M. (1999). "Brain tumors". *Oxford University Press*.

Guo, J. F., Cai, Y. L., and Wang, Y. P. (1995). "Morphology based interpolation for 3D medical image reconstruction". *Computerized Medical Imaging and Graphics*. 19:267–279.

Guyon,I. and Elisseeff, A. (2003). "An introduction to variable and feature selection". *The Journal of Machine Learning Reasearch*. 3:1157–1182.

Hamarneh,G. and Li, X. (2009). "Watershed segmentation using prior shape and appearance knowledge". *Image and Vision Computing*. 27:59–68.

Han, J., Kamber, M., and Pei, J. (2011). "Data Mining: Concepts and Techniques". 3^{rd} *Edition, Elsevier*.

Haralick, R. M., Shanmugam, K., and Dinstein, I. (1973). "Texture features for image classification". *IEEE Transaction on Systems, Man and Cybernetics*. 3:610–621.

Hashemi, R. H., Bradley, W. G., and Lisanti, C. J. (2012). "MRI: The basics". *3rd Edition, Lippincott Williams and Wilkins*, 41:87–109.

Haskell, C. M. (2001). "Cancer treatment". *W.B. Saunders Company*.

Haykin, S. O. (2009). "Neural networks and Learning Machines". 3^{rd} *Edition, Pearson Education*.

Hemanth, D. J., Selvathi, D., and Anitha. J. (2009). "Effective fuzzy clustering algorithm for abnormal MR brain image segmentation". *Proc. of IEEE International Advance Computing Conference (IACC 2009*. 609–614.

Hoppe, H., DeRose, T., Duchamp, T., McDonald, J., and Stuetzle, W. (1993). "Mesh optimization". *Proc. of ACM SIGGRAPH conference on Computer graphics and interactive techniques*. 19–26.

Huang, Y. L., Chen, J. H., and Shen, W. C. (2006). "Diagnosis of hepatic tumors with texture analysis in nonenhanced computed tomography images". *Academic Radiology*, 13:713–20.

Huo, J., Okada, K., Kim, H. J., Pope, W. B., Goldin, J. G., Alger, J. R., and Brown, M. S. (2009). "CADrx for GBM brain tumors: predicting treatment response from changes in diffusion weighted MRI". *Algorithms*, 2:1350–1367.

Hussain. M. (2008). "Fast decimation of polygonal models". *Proc. of International Symposium on Advances in Visual Computing (ISVC 2008)*. 119–128.

Hyvärinen, A. (1999). "Fast and robust fixed-point algorithms for independent component analysis". *IEEE Transactions on Neural Networks*. 10:626–634.

Iftekharuddin, K. M., Jia, W., and Marsh, R. (2003). "Fractal analysis of tumor in brain MR images". *Machine Vision and Applications*. 13:352–362.

Insu, P., Shirani, S., and Capson, D. W. (2006). "Mesh simplification using area-based distortion measure". *Journal of Mathematical Modelling and Algorithms*. 5:309–329.

Jafari-Khouzani, K., Soltanian-Zadeh, H., Elisevich, K., and Patel, S. (2004). "Comparison of 2D and 3D wavelet features for TLE lateralization". *Proc. of SPIE, Medical Imaging 2004: Physiology, Function, and Structure from Medical Images*. 5369:593–601.

Jagota, A. (1991). "Novelty detection on a very large number memories stored in hopified-style network". *Proc. of International Conference on Neural Networks (IJCCN-91), IEEE*.

Javier, H., Jordi, N., and Marc, S. (2012). "Kd-tree and the real disclosure risks of large statistical databases". *Information Fusion*. 13:260–273.

Jemal, A., Bray, F., Center, M. M., Ferlay, J., Ward, E., and Forman, D. (2011). "Global cancer statistics". *CA: A Cancer Journal for Clinicians*, 61:69–90.

Jenkinson, M. and Smith, S. (2001). "A global optimization method for robust affine registration of brain images". *Medical Image Analysis*. 5:143–156.

Jiang, X. (2011). "Linear Subspace Learning-Based Dimensionality Reduction". *IEEE Signal Processing Magazine*. 28:16–26.

Juang, L. H. and Wu, M. N. (2010). "MRI brain lesion image detection based on color-converted K-means clustering segmentation". *Measurement*. 43:941–949.

Kassimi, M. A. and Elbeqqali, O. (2011). "3D model retrieval based on semantic and shape indexes". *International Journal of Computer Science Issues*. 8:172–181.

Keys, R. G. (1981). "Cubic convolution interpolation for digital image processing". *IEEE Transaction on Acoustics, Speech and Signal Processing*. 29:1153–1160.

Khan, S. S. and Ahmad, A. (2004). "Cluster center initialization algorithm for K-means clustering". *Pattern Recognition Letters*. 25:1293-1302.

Kim, T. Y., Son, J., and Kim, K.G. (2011). "The recent progress in quantitative medical image analsis for computer aided diagnosis systems". *Healthcare Informatics Research*. 17:143–149.

Kim, H. C., Pang, S., Je, H. M., Kim, D., and Bang, S.Y. (2003). "Constructing support vector machine ensemble". *Pattern Recognition*. 36:2757–2767.

Kittler, J., Hatef, M., Duin, R. P. W., and Matas, J. (1998). "On combining classifiers". *IEEE Transactions on Pattern Analysis and Machine Intelligence*. 20:226–238.

Klein, R., Schilling, A., and Strasser, W. (2000). "Reconstruction and simplificationof surfaces from contours". *Graphical Models*. 62:429–443.

Kopec, D., Kabir, M. H., Reinharth, D., Rothschild, O., and Castiglione, J.A. (2003). "Human errors in medical practice:systematic classification and reduction with automated information systems". *Journal of Medical Systems*, 27:297–313.

Kothari, R. and Pitts, D. (1999). "On finding the number of clusters". *Pattern Recognition Letters*. 20:405–416.

Kothavi, R. (1995). "A study of cross-validation and bootstrap for accuracy estimation and model selection". *Proc. of International Joint conference on Artificial Intelligence*. 1137–1143.

Krishnamurthy, C., Rodriguez, J. J., and Gillies, R. J. (2004). "Snake-based liver lesion segmentation". *Proc. of IEEE symposium on Image Analysis and Interpretation*. 187–191.

Kumar, V., Sachdeva, J., Gupta, I., Khandelwal, N., and Ahuja, C. K. (2011). "Classification of Brain tumor using PCA-ANN". *Proc. of World Congress on Information and Communication Technologies*. 1079–1083.

Kunttu, I., Lepisto, L., Rauhamaa, J., and Visa, A. (2006). "Multiscale fourier descriptors for defect image retrieval". *Pattern Recognition Letters*. 27:123-132.

Lee, C. C., Chung, P. C., and Tsai, H. M. (2003). "Identifying abdominal organs from CT image series using a multimoule contextual neural network and spatial fuzzy rules". *IEEE Trnsaction on Information Technology in Biomedicine*. 7:208–217.

Lee, C. H., Varshney, A., and Jacobs, D. W. (2005). "Mesh saliency". *ACM Transactions on Graphics*. 24:659–666.

Lehmann, T. M., Gonner, C., and Spitzer, K. (1999). "Survey: Interpolation methods in medical image processing". *IEEE Transaction on Medical Imaging*. 18:1049–1075.

Li, G., Wang, W., Ding, G, Zou, Y., and Wang, K. (2012). "The edge collapse algorithm based on the iteration in mesh simplification". *Proc. of International-conference on Computer and Information Science (ACIS 2012), IEEE*. 356–360.

Liao, S. X. and Panlak, M. (1997). "Image analysis with zernike moment descriptors". *Proc. of IEEE conference on Electrical and Computer Engineering*. 700–703.

Liao, X., Reutens, D., and Yang, Z. (2011). "Morphology-based interslice interpolation using local intensity information for segmentation". *Proc. of International Conference on biomedical Engineering and Informatics (BMEI 2011)*. 384–389.

Likas, A., Vlassis, N., and Verbeek, J. J. (2003). "The global k-means clustering algorithm". *Pattern Recognition*. 36:451–461.

Lin, W. C., Liang, C. C., and Chen, C. T. (1988). "Dynamic elastic interpolation for 3-D medical image reconstruction from cross sections". *IEEE Transaction on Medical Imaging*. 7:225–232.

Linde, Y., Buzo, A., and Gray, R. M. (1980). "An algorithm for vector quantizer design". *IEEE Transactions on Communications*. 28:84–95.

Lindstrom, P. and Turk, G. (1998). "Fast and memory efficient polygonal simplification". *Proc. of Conference on Visualization, IEEE*. 279–286.

Liu, J., Wang, Z., and Zhang, R. (2009). "Liver cancer CT image segmentation methods based on watershed algorithm". *Proc. of International conference on computational Intelligence and Software Engineering, IEEE*. 1–4.

Liu, J., Chen, J., Liu, X., Chun, L., Tang, T., and Deng, Y. (2011). "Mass segmentation using a combined method for cancer detection". *BMC Systems Biology*, 5:1–9.

Lorensen, W. E. and Cline, H. E. (1987). "Marching cubes: a high resolution 3-D surface construction algorithm". *Computer Graphics*, 4:163–169.

Low, K. L. and Tan, T. S. (1997). "Model simplification using vertex-clustering". *Proc. of Symposium on Interactive 3D Graphics, ACM* , 75–82.

Lowe, D. G. (2004). "Distinctive image features from scale-invariant key points". *International Journal of Computer Vision*, 60:91–110.

Lu, G. (2002). "Techniques and data structures for efficient multimedia retrieval based on similarity". *IEEE Transaction on Multimedia*, 4:372–384.

Lu, R., Marziliano, P., Thng, C. H. (2005). "Liver tumor volume estimation by semi-automatic segmentation method". *Proc. of IEEE International Conference on Engineering in Medicine and Biology Society*. 3296–3299.

Lu, G. J. and Sajjanhar, A. (1999). "Region-based shape representation and similarity measure suitable for content-based image retrieval". *Multimedia Systems*. 7:165–174.

MacQueen, J. B. (1967). "Some methods for classification and analysis of multivariate observation". *Proc. of 5th Berkeley symposium on Mathematical Statistics and Probability, University of California Press*. 281–297.

Mala, K., Sadasivam, S., and Alagappan, S. (2006). "Neural network based texture analysis of liver tumor from computed tomography images". *International Journal of Biomedical and Life Sciences*. 2:33–40.

Mandelbrot, B. B. (1983). "The fractal geometry of nature". *Freeman, Newyork*.

Manjunath, B. S., Ohm, J.-R, Vasudevan, V. V., and Yamada, A. (2001). "Color and texture descriptors". *IEEE Transaction on Circuits and Systems for Video Technology*. 11:703–715.

Manthalkar, R., Biswas, P. K., and Chatterji, B. N. (2003). "Rotation and scale invariant texture features using discrete wavelet packet transform". *Pattern Recognition Letters*. 24:2455-2462.

Martin-Landrove, M., Pereira, D., Caldeira, M. E., Itriago, S., and Juliac, M. (2007). "Fractal analysis of tumoral lesions in brain". *Proc. of IEEE International Conference on Engineering in Medicine and Biology Society (EMBS 2007)*. 1306–1309.

Masala, G. L., Golosio, B., and Oliva, P. (2013). "An improved marching cubes algorithm for 3D data segmentation". *Computer Physics Communications*. 184: 777–782.

Meijering, E. H. W. (2000). "Spline interpolation in medical imaging: comparison with other convolution-based approaches". *Proc. of European Signal Processing Conference (EUSIPCO 2000)*. 151–159.

Menze, B. H., Leemput, K. V., Lashkari, D., Weber, M. A., Ayache, N., and Golland, P. (2010). "A generative model for brain tumor segmentation in multi-modal images". *Proc. of MICCAI 2010, LNCS, Springer*. 151–159.

Meyers. D., Skinner, S., and Sloan, K. (1992). "Surfaces from contours". *ACM Transactions on Graphics*. 11:228–258.

Mingqiang, Y., Kidiyo, K., and Joseph, R. (2008). "A survey of shape feature extraction techniques". *Pattern Recognition, Peng-Yeng Yin (Ed.)*. 43–90.

Moltz, J. H., Bornemann, L., Dicken, V., and Peitgen, H. O. (2008). "Segmentation of Liver Metastases in CT scans by adaptive thresholding and morphological processing". *Proc. of Workshop on 3D Segmentation in the Clinic: A Grand Challenge II, Liver Tumor Segmentation Challenge. MICCAI 2008*.

Montani, C., Scateni, R., and Scopigno, R. (1994). "A modified look-up table for implicit disambiguation of marching cubes". *The Visual Computer, Springer*. 10:353–355.

Moon, N., Bullitt, E., Leemput, K. V., and Gerig, G. (2002). "Model-based brain and tumor segmentation". *Proc. of International Conference on Pattern Recognition, IEEE*. 528–531.

Morgiri, S. and Sgallari, F. (2004). "3-D long bone reconstruction based on level sets". *Computerized Medical Imaging and Graphics*. 28:377–390.

Mougiakakou, S. G., Valavanis, I. K., Nikita, A., and Nikita, K. S. (2007). "Differential diagnosis of CT focal liver lesions using texture features, feature selection and ensemble driven classifiers". *Artificial Intelligence in Medicine*. 41:25–37.

Muller, H., Michoux, N., Bandon, D., and Geissbuhler, A. (2004). "A review of content-based image retrieval systems in medical applications-clinical benefits and future directions". *International Journal of Medical Informatics*. 73:1–23.

Murugavalli,S. and Rajamani,V. (2006). "A high speed parallel fuzzy c-mean algorithm for brain tumor segmentation". *International Journal on Bioinformatics and Medical Engineering*. 6:29–34.

Napel, S. A., Beaulieu, C. F., Rodriguez, C., Cui, J., Xu, J., Gupta, A., Korenblum, D., Greenspan, H., Ma, Y., and Rubin, D. L. (2010). "Automated retrieval of CT images of liver lesions on the basis of image similarity: method and preliminary results". *Radiology*. 256:243–252.

Newman, T. S. and Yi, H. (2006). "A survey of marching cubes algorithm". *Computers and Graphics*. 30:854-879.

Ng, H. P., Ong, S. H., Foong, K. W. C., Goh, P. S., and Nowinski, W. L. (2006). "Medical image segmentation using k-means clustering and improved watershed algorithm". *Proc. of IEEE Symposium on Image Analysis and Interpretation*, 61–65.

Ojala, T., Pietikainen, M., and Maenpaa, T. (2002). "multiresolution gray-scale and rotation invariant texture classification with local binary patterns". *IEEE Trnasaction on Pattern Analysis and Machine Intelligence*, 24:971–987.

Oliva, J. M., Perrin, S., and Conquillart, S. (1996). "3D reconstruction of complex polyhedral shapes from contours using a simplified generalized voronoi diagram". *Computer Graphics Forum*, 15:397–408.

Oliver, A., Llado, X., Freixenet, J., and Marti, J. (2007). "False positive reduction in mammographic mass detection using local binary patterns". *Proc. of International conference on Medical Image Processing and Computer-Assisted Intervention (MICCAI-07*. 286–293.

Otsu, N. (1979). "A threshold selection method from gray-level histogram". *IEEE Transactions on Systems, Man and Cybernetics*. 9:62–66.

Pan, M., Yang, X., and Tang, J. (2012). "Research on interpolation methods in medical image processing". *Journalof Medical Systems*, 36:777–807.

Park, S. J. Seo, K. S., and Park, J. A. (2005). "Automatic Hepatic Tumor Segmentation Using Statistical Optimal Threshold". *Proc. of International Conference on Computational Science (ICCS 2005), LNCS, Springer*. 3514:934–940.

Penney, G. P., Schnabel, J. A., Rueckert, D., Viergever, M. A., and Niessen, W. J. (2004). "Registration-based interpolation". *IEEE Transaction on Medical Imaging*. 23:922–926.

Phong, B. T. (1975). "Illumination of computer generated pictures". *communications of the ACM*. 18:311–317.

Plissiti, M. E., Nikou, C., and Charchanti, A. (2011). "Combining shape, texture and intensity features for cell nucei extraction in pap smear images". *Pattern Recognition Letters*. 32:838–853.

Ponti, M. P. (2011). "Combining classifiers: from the creation of ensembles to the decision fusion". *Proc. of SIBGRAPI Conference on Graphics, Patterns, and Images Tutorials (SIBGRAPI-T), IEEE*. 1–10.

Poonguzhali, S. and Ravindran, G. (2006). "A Complete Automatic Region Growing Method for Segmentation of Masses on Ultrasound Images". *Proc. of International Conference on Biomedical and Pharmaceutical Engineering, IEEE*. 88–92.

Portar, P. and Canagarajah, N. (1997). "Robust rotation invariant texture classification: wavelet, gabor filter and GMRF based schemes". *IEE Proc. Vision, Image and Signal Processing*. 144:180–188.

Prasad, M., Sowmya, A., and Koch, I. (2008). "Efficient feature selection based on independent component analysis". *International Journal of Computational Intelligence and Applications*. 7:447–468.

Prastawa, M., Bullitt, E., Ho, S., and Gerig, G. (2004). "A brain tumor segmentation framework based on outlier detection". *Medical Image Analysis*. 8:275–283.

Priyadarshini, S. and Selvathi, D. (2012). "Survey on segmentation of liver from CT images". *Proc. of IEEE International Conference on Advanced Communication Control and Computing Technologies (ICACCCT)*. 234–238.

Pudil, P., Novovicova, J., and Kittler, J. (1994). "Floating search methods in feature selection". *Pattern Recognition Letters*. 15:1119–1125.

Qi, Y., Xiong,W., Leow,W.K., Tian,Q., Zhou,J., Liu,J., Han,T., Venkatesh,S.K., and Wang,S.C. (2008). "Semi-automatic segmentation of liver tumors from CT scans using Bayesian rule-based 3D region growing". *Proc. of workshop on 3D segmentation in the clinic: a grand challenge, MICCAI 2008*.

Quellec, G., Lambard, M., Cazuguel, G., Roux, C., and Cochener, B. (2011). "Case retrieval in medical databases by fusing heterogeneous information". *IEEE Transactions on Medical Imaging*. 30:108–118.

Raya, S. P. and Udupa, J. K. (1990). "Shape-based interpolation of multidimensional objects". *IEEE Transactions on Medical Imaging*. 9:32–42.

Raymer, M. L., Punch, W. F., Goodman, E. D., Kuhn, L.A., and Jain, L. C. (2000). "Dimensionality reduction using genetic algorithms". *IEEE Transaction on Evolutionary computation*. 4: 164–171.

Rahman, M.M., Bhattacharya, P., and Desai, B.C. (2007). "A framework for medical image retrieval using machine learning and statistical similarity matching techniques with relevance feedback". *IEEE Transaction on Information Technology in Biomedicine*. 11:58–69.

Roslan, R., Jamil, N., and Mahmud, R. (2011). "Skull stripping magnetic resonance images brain images: region growing versus mathematical morphology". *International Journal of Computer Information Systems and Industrial Management Applications*. 3:150–158.

Rossignac, J. and Borrel, P. (1993). "Multi-resolution 3D approximations for rendering complex scenes". *Modeling in Computer Graphics: Methods and Applications*. 455–465.

Saeys, Y., Iñza, I., and Larrañaga, P. (2007). "A review of feature selection techniques in bioinformatics". *Bioinformatics*. 23:2507–2517.

Scheppach, W., Bresalier, R. S., and Tytgat, G. H. (2004). "Gastrointestinal and liver tumors". *Springer*.

Schroeder, W. J., Zarge, J. A., and Lorensen, W. E (1992). "Decimation of triangle meshes". *Computer Graphics*. 26:65–70.

Seeram, E. (2010). "Computed Tomography: physical principles and recent technical advances". *Journal of Medical Imaging and Radiation Sciences*, 41:87–109.

Seo, K. S. (2005). "Automatic hepatic tumor segmentation using composite hypotheses. Image Analysis and Recognition". *Proc. of International Conference on Image Analysis and Recognition (ICIAR 2005), LNCS, Springer*, 3656:922–929.

Shahabi, C. and Safar, M. (2007). "An experimental study of alternative shape-based image retrieval techniques". *Multimedia Tools and Applications* . 32:29–48.

Shang, C. and Barnes, D. (2010). "Combining support vector machines and information gain ranking for classification of mars mcmurdo panorama images". *Proc. IEEE International Conference on Image Processing*. 1061–1064.

Shen, J., Shen, W., and Shen, D. (2000). "On geometric and orthogonal moments". *International Journal of Pattern Recognition and Artificial Intelligence*. 14:875–894.

Shih, F. Y. (2010). "Image processing and mathematical morphology: fundamentals and applications". *CRC Press*.

Shih, M. Y. and Tseng, D. C.(2000). "Versatile surface model reconstruction from serial planar contours". *Proc. of IEEE International Conference on Engineering in medicine and Biology Society (EMBS 2000)*. 2910–2913.

Showalter, C., Clymer, B. D., Richmond, B., and Powell, K. (2005). "Three-dimensional texture analysis of cancellous bone cores evaluated at clinical CT resolutions". *Osteoporosis International*. 17:259–266.

Song, Y., Huang, J., Zhou, D., Zha, H., and Giles, C. L. (2007). "IKNN: informative k-nearest neighbor pattern classification". *Proc. of European Conference on Principles and Practice of Knowledge Discovery in Databases (PKDD 2007), LNCS, Springer*. 4702: 248–264.

Sporns, O. (2011). "Networks of the brain". *MIT Press*.

Stoitsis, J., Valavanis, I., Mougiakakou, S. G., Golemati, S., Nikita, A., and Nikita, K. S. (2006). "Computer aided diagnosis based on medical image processing and artificial intelligence methods". *Nuclear Instruments and Methods in Physics Research Section A: Accelerators, Spectrometers, Detectors and Associated Equipment*, 569:591–595.

Suganya, R. and Rajaram, S. (2012). "Content Based Image Retrieval of Ultrasound Liver Diseases Based on Hybrid Approach". *American Journal of Applied Sciences* . 9:938–945.

Taheri, S., Ong, S. H., and Chong, V. (2010). "Level-set segmentation of brain tumors using a threshold-based speed function". *Image and Vision Computing*. 28:26–37.

Tamura, H., Mori, S., and Yamawaki, T. (1978). "Textural features corresponding to visual perception". *IEEE Transaction on Systems, Man and Cybernetics*. 8:460–473.

Tan, X. and Triggs, B. (2007). "Enhanced local texture feature sets for face recognition under difficult lighting conditions". *Proc. of International Workshop on Analysis and Modeling of Faces and Gestures (AMFG 2007), LNCS, Springer*. 4778:168–182.

Tao, Y., Ioerger, T. R., and Tang, Y. Y. (2001). "Extraction of rotation invariant signature based on fractal geometry". *Proc. of International Conference on Image Processing, IEEE*. 1090–1093.

Taylor, S. A, Brittenden, J., Lenton, J., Lambie, H., Goldstone, A., Wylie, P. N., Tolan, D., Burling, D., Honeyfield, L., Bassett, P., and Halligan, S. (2009). "Influence of computer-aided detection false-positives on reader performance and diagnostic confidence for CT colonography". *Americal Journal of Roentgenology*, 192:1682–1689.

Taheri,S., Ong,S.H., and Chong,V. (2010). "Level-set segmentation of brain tumors using a threshold-based speed function". *Image and Vision Computing*. 28:26–37.

Teague, M. R. (1980). "Image analysis via the general theory of moments". *Journal of Optical Society of America*. 70:920–930.

Traina, A. G. M., Balan, A. G. R., Bortolotti, L. M., and Traina, C. (2004). "Content-based image retrieval using approximate shape of objects". *Proc of IEEE Symposium on computer-Based Medical Systems (CBMS 2004)*, 91–96.

Trpovski Z. (2008). "Content based image retrieval: From pixels to semantics". *Proc. of Symposium on Neural Network Applications in Electrical Engineering, IEEE*, 7–12.

Tsang, W., Corboy, A., Lee, K., Raicu, D., and Furst, J. (2005). "Texture-based image retrieval for computerized Tomography databases". *Proc. of IEEE Symposium on Computer-Based Medical Systems*, 593–598.

Unay, D. and Ekin, A. (2008). "Intensity versus texture for medical image search and retrieval". *Proc. of IEEE International symposium on Biomedical Imaging: From Nano to Macro*. 241–244.

Vapnik, V. (2005). "Universal learning technology: support vector machines". *NEC Journal of Advanced Technology*. 2:137–144.

Venkatachalam. P. A, Mohd Hani. A. F, Ngah. U. K, and Lim Eng Eng. (2004). "Processing of abdominal ultrasound images using seed based region growing method". *Proc. of International Conference on Intelligent Sensing and Information Processing, IEEE*. 57–62.

Verma, R. Zacharaki, E. I., Ou, Y., Cai, H., Chawla, S., Lee, S. K., Melhem, E. R., Wolf, R., and Davatzikos, C. (2008). "Multiparametric tissue characterization of brain neoplasms and their recurrence using pattern classification of MR images". *Academic Radiology*. 15:966–977.

Wang, L., Li, J., and Hagiwara, I. (2009). "A topology preserved mesh simplification algorithm". *World Congress on Computer Science and Information Engineering, IEEE*. 698–702.

Węgliński, T. and Fabijańska, A. (2011). "Brain tumor segmentation from MRI data sets using region growing approach". *Proc. of International Conference on Prospective Technologies and Methods in MEMS Design (MEMSTECH 2011), IEEE*. 185–188.

Wels, M., Carneiro, G., Aplas, A., Huber, M., Hornegger, J., and Comaniciu,D. (2008). "A discriminative model-constrained graph cuts approach to fully automated pediatric brain tumor segmentation in 3-D MRI". *Proc. of International Conference on Medical Image Computing and Computer Assisted Intervention (MICCAI 2008), LNCS, Springer*. 5241:67–75.

Wu, J., Poehlman, S., Noseworthy, M. D., and Kamath, M. V. (2009). "Texture feature based automated seeded region growing in abdominal MRI segmentation". *Journal on Biomedical Science and Engineering*. 2:1-8.

Wu, P., Xie, K., Zheng, Y., and Wu, C. (2012). "Brain tumor classification based on 3D shape". *Advances in FCCS, AISC, Springer*, 160:277–283.

Wu, Y., Chang, E. Y., Chang, K. C. C., and Smith, J. R. (2004). "Optimal multimodal fusion for multimedia data analysis". *Proc. of ACM International Conference on Multimedia*. 572–579.

Wu, Y. T., Shyu, K. K., Jao, C. W., Wang, Z. Y., Soong, B. W., Wu, H. M., and Wang, P. S. (2010). "Fractal dimension analysis for quantifying cerebellar morphological change of multiple system atrophy of the cerebellar type (MSA-C)". *Neuroimage*. 49:539–551.

Xie, K., Yang, J., Zhang, Z. G., and Zhu, Y. M. (2005). "Semi-automated brain tumor and edema segmentation using MRI". *European Journal of Radiology*. 56:12–19.

Xie, S., Guo R, Li, N., Wang, G., and Zhao, H. (2009). "Brain fMRIprocessing and classification based on combinations of PCA and SVM". *Proc. of International Joint Conference on Neural Networks (IJCNN 2009), IEEE*. 3384–3389.

Xu, J. W., Suzuki, K., Hori, M., Oto, A., and Baron, R. (2011). "Computer-aided detection of hepatocellular carcinoma in multiphase contrast-enhanced hepatic CT: a preliminary study". *Proc. SPIE 7963, Medical Imaging 2011: Computer-Aided Diagnosis*. 79630S.

Yadav, R. B., Nishchal, N. K., Gupta, A. K., and Rastogi, V. K. (2007). "Retrieval and classification of shape-based objects using Fourier, generic Fourier, and wavelet-Fourier descriptors technique: A comparative study". *Optics and Lasers in Engineering*. 45:695-708.

Yoshizawa, S., Belyaev, A., and Seidel, H. P. (2005). "Fast and robust detection of crest lines on meshes". *Proc. of ACM Symposium on Solid and Physical Modeling*. 227–232.

You, F., Hu, Q., Lu, Q., and Yao, Y. (2008). "Study on the algorithm of surface reconstruction of defective bone based on delaunay triangulation". *Proc. of 7th Asian-Pacific Conference on Medical and Biological Engineering (IFMBE), Springer*. 19:250–254.

Yu, M., Lu, Z., Feng, Q., and Chen, W. (2010). "Liver CT image retrieval based on non-tensor product wavelet". *Proc. of International Conference of Medical Image Analysis and Clinical Application (MIACA 2010)*. 67–70.

Yuan, K., Feng, S., Chen, W., Jia, S., and Xiao, P. (2008). "Diagnosis system of computer aided brain MRI using content based image retrieval". *Proc. of International Conference on Information Technology and Application in Biomedicine, IEEE*. 152–156.

Zacharaki, E. I., Kanas, V. G., and Davatzikos, C. (2011). "Investigating machine learning techniques for MRI-based classification of brain neoplasms". *International Journal of Computer Assisted Radiology and Surgery*. 6:821–828.

Zacharaki, E. I., Wang, S., Chawla, S., Soo Yoo, D., Wolf, R., Melhem, E. R., and Davatzikos, C. (2009). "Classification of brain tumor type and grade using MRI

texture and shape in a machine learning scheme". *Magnetic Resonance in Medicine*. 62:1609–1618.

Zhang, D. and Lu, G. (2002). "Shape-based image retrieval using generic Fourier descriptor". *Signal Processing: Image Communication*. 17:825–848.

Zhang, X., Fujita, H., Qin, T., Zhao, J., Kanematsu, M., Hara, T., Zhou, X., Yokoyama, R., Kondo, H., and Hoshi, H. (2008). "CAD on liver using CT and MRI". *Proc. of International Conference on Medical Imaging and Informatics (MIMI 2007), LNCS, Springer*, 4987:367–376.

Zhao, Q., Xu, M., and Franti, P. (2011). "Extending external validity measures for determining the number of clusters". *Proc. of International Conference on Intelligent System Design and Applications (ISDA 2011), IEEE*. 931–936.

Zhou, J., Xiong, W., Tian, Q., Qi, Y., liu, J.,Leow, W. K., Han, T., Venkatesh, S., and Wang, S. (2008). "Semi-automatic segmentation of 3D liver tumors from CT scans using voxel classification and propagational learning". *Proc. of Workshop on 3D Segmentation in the Clinic: A Grand Challenge II, Liver Tumor Segmentation, MICCAI 2008*.

Zhu, Y. and Yan, H. (1997). "Computerized tumor boundary detection using a Hopfield neural network". *IEEE Transaction on Medical Imaging*. 16:55–67.

Zhu, C. and Wang, R. (2012). "Local multiple petterns based multiresolution gray-scale and rotation invariant texture classification". *Information Sciences*. 187:93–108.

Zöllner, F. G., Emblem, K. E., and Schad, L. R. (2012). "SVM-based glioma grading: Optimization by feature reduction analysis". *Journal of Medical Physics*. 22:205–214.

Publications

List of Publications Based on Research Work:

International Journals

1) Megha.P.Arakeri, G. Ram Mohana Reddy, *An intelligent content-based image retrieval system for clinical decision support in brain tumor diagnosis*, International Journal of Multimedia Information Retrieval, Springer, 2, 2013, pp. 175–188. DOI:http://dx.doi.org/10.1007/s13735-013-0037-5.

2) Megha.P.Arakeri, G.Ram Mohana Reddy, *Computer-aided diagnosis system for tissue characterization of brain tumor on magnetic resonance images*, Signal, Image and Video Processing, Springer, 2013. DOI:http://dx.doi.org/10.1007/s11760-013-0456-z.

3) Megha.P.Arakeri, G. Ram Mohana Reddy, *A novel CBIR approach to differential diagnosis of liver tumor on computed tomography images*, International Conference on Modelling, Optimization and Control, Procedia Engineering, Elsevier, 38, 2012, pp. 528–536. DOI:http://dx.doi.org/10.1016/j.proeng.2012.06.066.

4) Megha.P.Arakeri, G. Ram Mohana Reddy, *Recent trends and challenges in computer aided diagnosis of liver cancer on CT abdominal images*, International Journal of Information Processing, 6, 2012, pp. 50–59.

5) Megha.P.Arakeri, G. Ram Mohana Reddy, *An effective and efficient approach to 3D reconstruction and quantification of brain tumor on magnetic resonance images*, International Journal of Signal Processing, Image Processing and Pattern Recognition, 6, 2013, pp. 111–128.

Conference Publications

1) Megha.P.Arakeri, G. Ram Mohana Reddy, *Recent advances and future potential of computer aided diagnosis of liver cancer on computed tomography images*, Proc. of Int. Conf. on Information Processing (ICIP-2011), CCIS 157, Springer, August 5-7, 2011, Bangalore, pp. 246–251. DOI:http://dx.doi.org/10.1007/978-3-642-22786-8_31.

2) Megha.P.Arakeri, G. Ram Mohana Reddy, *A comparative performance evaluation of independent component analysis in medical image denoising*, Proc. of Int. Conf. on Recent Trends in Information Technology (ICRTIT-2011), IEEE, June 3-5, 2011, Chennai, pp.770–774. DOI:http://dx.doi.org/10.1109/ICRTIT.2011.5972264.

3) Megha.P.Arakeri, G.Ram Mohana Reddy, *Efficient fuzzy clustering based approach to brain tumor segmentation on MR images*, International Conference on Computational Intelligence and Information Technology (CIIT-2011), CCIS 250, Springer, 2011, pp. 790–795, Nov 7-8, 2011, Pune. DOI:http://dx.doi.org/10.1007/978-3-642-25734-6_141.

4) Megha.P.Arakeri, G.Ram Mohana Reddy, *A hybrid algorithm for automatic and efficient segmentation of liver tumor on CT abdominal images*, Proc. of Int. Conf. on Recent Trends in Information Processing and Computing (IPC-2011), Nov 14-15, 2011, Malaysia. (Accepted)

5) Megha.P.Arakeri, G. Ram Mohana Reddy, *Medical image retrieval system for diagnosis of brain tumor based on classification and content similarity*, Proc. of IEEE INDICON 2012, pp. 416–421, December 7-9, 2012, Kochi. DOI:http://dx.doi.org/10.1109/INDCON.2012.6420654.

Brief Bio-Data

Megha. P. Arakeri
Research Scholar
Department of Information Technology
National Institute of Technology Karnataka, Surathkal
P.O.Srinivasanagar
Mangalore-575025

Permanent address

Megha. P. Arakeri $W/0$ Lakshmana,
No. 11, Durga Layout,
Vidyaranyapura, Bangalore-560097,
Karnataka.
Phone: 9008977922
Email: meghalakshman@gmail.com

Qualification

- M.Tech. Computer Science, Visvesvaraya Technological University (VTU), Karnataka, 2005.